Tidal Hydrodynamics in the Interconnected Channel Network of the Southwestern Ganges-Brahmaputra-Meghna Delta, Bangladesh

By

Rachel Louise Bain

Dissertation
Submitted to the Faculty of the
Graduate School of Vanderbilt University
in partial fulfillment of the requirements
for the degree of

DOCTOR OF PHILOSOPHY
in
Environmental Engineering

December 14, 2019

Nashville, Tennessee

Approved:
Steven Goodbred Jr., Ph.D.
James Clarke, Ph.D.
David Furbish, Ph.D.
George Hornberger, Ph.D.

ACKNOWLEDGMENTS

I am deeply grateful to my dissertation advisor, Steve Goodbred, for giving me the unparalleled opportunity to work on the Bangladesh project for so many years. Steve thought I had enrolled at Vanderbilt to study tidally-generated stratigraphy (to be fair, so did I), yet he remained enthusiastic and unfailingly optimistic throughout each of the twists and turns that led to the present dissertation topic. If a picture is worth a thousand words, then the following photo is far more descriptive than anything I could succinctly write about Steve's support of, and involvement in, this research. Thank you, Steve.

Photo of Steve dangling headfirst off the dock at Pankhali while installing the pressure sensor in October 2017.

I also owe my gratitude to Rip Hale and Carol Wilson for their mentorship and guidance, and to my committee members—David Furbish, George Hornberger, and Jim Clarke—for advice on data analysis and feedback on the dissertation contents. The Bangladesh team at Vanderbilt (including Leslie Auerbach, Kelsea Best, Liz Chamberlain, Matt Dietrich, Meagan Patrick, Jenn Pickering, Chelsea Peters, Jess Raff, Ryan Sincavage, and Chris Tasich) and the broader Vanderbilt EES community (especially Jen Bradham and Tyler Doane) also offered insight into various aspects of the research. I hope that each of the individuals mentioned in this paragraph will interpret its brevity with the understanding that nothing short of a book would adequately describe your contributions to 5+ years of personal and professional growth.

The research presented in Chapter 2 was funded by the Office of Naval Research (award N00014-11-1-0683; PI–Goodbred) and the National Science Foundation (award 1600258–Coastal SEES; PI–Goodbred). We are grateful to Carol Wilson and Paola Passalacqua for providing GIS data, to Jim Best for supplying the ADCPs, to Elizabeth Chamberlain for advice on the manuscript, and to Md. Zahangir "Titas" Alam, Mamun Hasan, Abrar Hossain, Md. Saddam Hossain, Masud Iqbal, Basudeb Kumar, Chelsea Peters, Mike Reed, Chris Tasich, and the crews of the *Bawali*, *Mawali*, and *Kokilmoni* for assisting with data collection and/or analysis. Luca Solari, Andrea D'Alpaos, and two anonymous reviewers provided feedback that greatly improved the original manuscript. The discharge, water level, and spatial datasets generated during this project are available at doi:10.6084/m9.figshare.7495904.v1.

Data collection for Chapters 3 and 4 was funded by the National Science Foundation (award 1600258–Coastal SEES; PI–Goodbred). We express our thanks to the huge team of people who made this project possible. Abdullah Al Nahian, Sourov Bijoy, Rip Hale, Md. Saddam Hossain, Anayet Karim, Basudeb Kumar, Chelsea Peters, Chris Tasich, and Carol Wilson assisted with various aspects of project design and/or field work. Peter Knappett and UNAVCO supplied the GPS units, Jewell Beasley managed the administrative arrangements for international research travel, and Nazrul Islam Bachchu of Pugmark Tours coordinated all transportation and lodging in Bangladesh. Syed Humayun Akhter, Dhiman Mondal, Mike Steckler, Chris Tasich, and Keith Williams provided technical expertise for the GPS surveys. We are also extremely grateful to the crew of the M.B. *Mawali*, who pulled three consecutive "all nighters" to deploy the instruments after an inconveniently-timed tropical depression threatened to derail the project. The data presented in these chapters will be publicly available following manuscript submission and publication.

Finally, personal thanks to all my family and friends for their unconditional love, especially Dad & Mom, Tim & Katie, Rebekah, David, and Lynn; and to my savior Jesus, whose mercies are new every morning.

TABLE OF CONTENTS

LIST OF TABLES

Table Page

LIST OF FIGURES

Figure Page

Chapter 1

Introduction

1.1 A note to the reader

While filling out a workshop application in spring 2015, I naïvely listed the title of this dissertation as *Tidal hydrodynamics in the southwestern Ganges-Brahmaputra-Meghna Delta: Implications for sediment transport*. Our primary objective at that early stage in the project was to quantify various aspects of tidal propagation through southwestern Bangladesh's tidal channel network and, by doing so, to better understand how sediment is transported through the system. In the simplest of terms, our rationale was, "The tide transports sediment. Therefore, if we can understand how the tide behaves, by extension we will know where the sediment is going." This idea was not unfounded, especially considering the literature's broad tendency to classify tidal signals as *ebb dominant* or *flood dominant* and then draw conclusions about the channel's long-term morphodynamic stability. But as the now-abridged abridged dissertation title suggests, we vastly underestimated the complexities of tidal propagation in large-scale, interconnected tidal channel systems, and the implications of this study are somewhat more modest than anticipated.

Despite these limitations, the research presented in the following chapters makes two contributions to future research in Bangladesh. The first is the high-precision, high-frequency tidal records that were collected for this project. Tidal measurements in this region are often collected by taking manual readings from a tide staff, which is a metered rod planted in the channel bed (see the paper by Chatterjee et al., 2013, for a detailed description of the methodology). Due to the manual nature of data collection, samples are never collected more frequently than once per hour during daylight hours, and it is typical for measurement to cease completely between sunrise and sunset. These records frequently contain datum shifts, as well as "spikes" where it appears the measurement was incorrectly recorded or transcribed. Additionally, vertical referencing in the study area tends to be ambiguous. There is a significant emphasis on hydrodynamic modeling to inform coastal management strategies in this region (*e.g.*, Ali et al., 2007; Bhuiyan and Dutta, 2012; Shampa, 2012; Lewis et al., 2013; Bricheno et al., 2016; Paul et al., 2016; Rahman et al., 2017; Deb and Ferreira, 2018), but such models require accurate field data for calibration and validation. The measurements collected for this study therefore fill a gap in the collective understanding of local tidal behavior by providing high-precision, high-frequency ($\Delta T \leq 10$ minutes) records which are referenced to an absolute vertical datum.

Second, by performing the analyses presented herein, we were able to identify and correct several of our early misconceptions about tidal dynamics in large-scale delta plain environments. For example, early in the project we assumed that the tidally-driven flow velocity would always be in the same direction as the water surface gradient. The reality is that the discharge may propagate against an adverse surface gradient for up to three hours in certain locations. We also thought that vertical tidal asymmetries would predict the dominant current direction (and therefore, net sediment transport), but we now know that there is little to no correlation between the vertical and horizontal tidal asymmetry due to the looping geometry of the channel network. Another early misconception was that the sharp increase in M_6 amplitude during peak platform inundation events was a consequence of frictional drag due to cross-platform flow; our data instead suggest that M_6 is generated by volume storage effects, although further analysis will be necessary to formally evaluate this phenomenon. Addressing these misconceptions has laid the groundwork for future research in the study area, which will not be stymied by incorrect assumptions.

1.2 Overview of the project

Note: An edited version of the following text was published on 17-Jul-2019 by the American Geophysical Union, ©2019 AGU, under the citation

> Bain, R.L., Hale, R.P., and Goodbred, S.L. (2019), Flow reorganization in an anthropogenically modified tidal channel network: An example from the Southwestern Ganges-Brahmaputra-Meghna Delta: *Journal of Geophysical Research–Earth Surface*, v. 124, pp. 1–19, DOI:10.1029/2018JF004996.

Tidal energy influences coastal morphology and nearshore sedimentation worldwide (Davies, 1964), with even small-amplitude tides capable of modifying river- or wave-driven transport and deposition (Dashtgard et al., 2012; Leonardi et al., 2013). In almost all shallow-water tidal environments, tidal channels are a prominent feature influencing regional morphodynamic behavior. Specifically, nonlinear frictional distortion influences the symmetry and the amplitude of the tidal waveform as it propagates upchannel. The result is an unequal duration of the rising and falling limbs, with the shorter limb necessarily displaying higher flow velocities. This has profound implications for determining the net sediment transport direction and long-term system stability (*e.g.*, Speer and Aubrey, 1985; Dronkers, 1986; Friedrichs and Aubrey, 1988; Mazda et al., 1995; Wells, 1995; Blanton et al., 2002).

Most prior research addressing flow behavior in tidal channels emphasizes two end-member cases. First, much focus has been placed on channel formation and stability in tidal wetland environments. Tidal behavior in these systems is strongly influenced by overbank exchange with the intertidal platform (*e.g.* Pethick, 1980; Blanton et al., 2002), but their short spatial scale (10^0 to 10^1 km) prevents the development of differential water surface elevations needed to drive channelized flow between adjacent tidal basins. Indeed, these studies are typically able to assume instantaneous tidal propagation across the marsh (*e.g.,* Boon, 1973; Pethick, 1980; Fagherazzi et al., 2008; Seminara et al., 2010). However, this assumption is quickly violated when considering tidal hydrodynamics in systems that span hundreds of kilometers, such as the Ganges-Brahmaputra-Meghna (GBM) tidal delta plain, where cross-system propagation times may exceed several hours and non-negligible lateral surface gradients may develop between neighboring channels.

A second tidal setting commonly addressed in the literature is the classic "funnel-shaped" estuary. In contrast to small-scale tidal wetlands, an estuarine channel may display tidal oscillations hundreds of kilometers inland from the coast, like the GBM system. However, the typically small ratio of intertidal platform to channelized area in tidal estuaries allows the simplifying assumption that platform flooding has negligible effect on the tidal hydrodynamics (*e.g.*, Todeschini et al., 2008). The number of channels in such networks also tends to be low. Among the best-studied tidal estuaries in the world (the Amazon, Columbia, Fly, Ord, Pearl, Saint Lawrence, Western Scheldt, and Yangtze), none has more than four outlets at the coast.

Here we present results from a third type of tidal environment, the tidal delta plain, which shares some attributes of tidal wetlands and estuaries but is nevertheless distinct in its governing physical processes. Like tidal wetland settings, deltas with a large vertical tidal range often display an extensive intertidal platform, making it unreasonable to neglect the effects of overbank flow when analyzing channel behavior. However, it is also unreasonable to characterize tidal delta plain dynamics using the results of marsh inundation studies due to the difference in spatial scale. Delta plains are spatially extensive and able to develop non-negligible water surface gradients along the channel profiles. Additionally, the length of coastline (200-300 km) and the total number of channel outlets ($\sim$10-20) typically exceed those of the traditional estuarine environment, creating conditions that favor the development of both along-coast and inter-channel gradients in tidal phase and amplitude. Large differences in freshwater discharge from upstream further contribute to these gradients, as many of the channels may receive no direct fluvial input. Emerging from these controls are looping structures (*e.g.*, Tejedor et al., 2015), which allow for channelized flow exchange between the delta plain's dominant channels and define a characteristic topological feature of these channel network systems.

Among of the largest (10 to 20×10^3 km^2) and most prevalent examples of these looping tidal channel networks are the south Asian mega-deltas, including the Ganges-Brahmaputra-Meghna Delta (GBMD), Indus (Giosan et al., 2006), and Ayeyarwady (Goodbred and Saito, 2012). Other examples of expansive tidal delta plains (5 to 10×10^3 km^2) with looping networks include the Orinoco in South America (Aslan et al., 2003), the Kikori-Purari in Papua New Guinea (Fagherazzi, 2008), and the Sesayap in eastern Borneo. Each of these systems is characterized by an extensive intertidal platform with highly interconnected channels, yet these systems and their corresponding morphodynamic processes have not been well studied, and many remain largely undescribed. Of these, the GBMD has perhaps received the most attention (*e.g.* Chatterjee et al., 2013; Pethick and Orford, 2013; Bricheno et al., 2016; Shaha and Cho, 2016; Hale et al., 2019a), and we build on this knowledge with the present study.

The relevant literature on this type of system includes several recent publications which characterize tidal hydrodynamics in smaller tidal delta plain environments with interconnected channels, including the $\sim$500 km^2 Berau (Buschman et al., 2010, 2013) and $\sim$1500 km^2 Mahakam Delta (Sassi et al., 2011, 2013). These results provide a conceptual framework for understanding how mass and energy propagate through looping, interconnected systems. Key findings include the observation that tides influence discharge and sediment transport tens to $>$100 km inland of the coast, and adjacent tidal channels often display contrasting hydrodynamic behavior. In this paper, we focus on the question of how hydrodynamic variation among interconnected channels influences channel stability within such looping tidal systems.

The question of deltaic channel stability is broadly relevant considering its implications for stratigraphic interpretation, navigation, and sustainable delta management, yet the mechanisms governing tidal channel network reorganization and the rate at which these mechanisms operate are poorly constrained. For example, although deltaic tidal channels tend to be less mobile than their non-tidal counterparts (Rossi et al., 2016; Hoitink et al., 2017; Lentsch et al., 2018), Fagherazzi (2008) found that tidal deltas self-organize such that a perturbation to the network will result in a sudden, widespread reorganization. Given the vulnerability of human populations residing on tidal systems and the tendency for anthropogenic activity to "perturb" deltaic environments (*e.g.*, Ericson et al., 2006; Syvitski and Saito, 2007; Syvitski et al., 2009), it is critical to evaluate the stability of tidal channel networks under present and future human influence. We consider several facets of this question throughout the following three chapters.

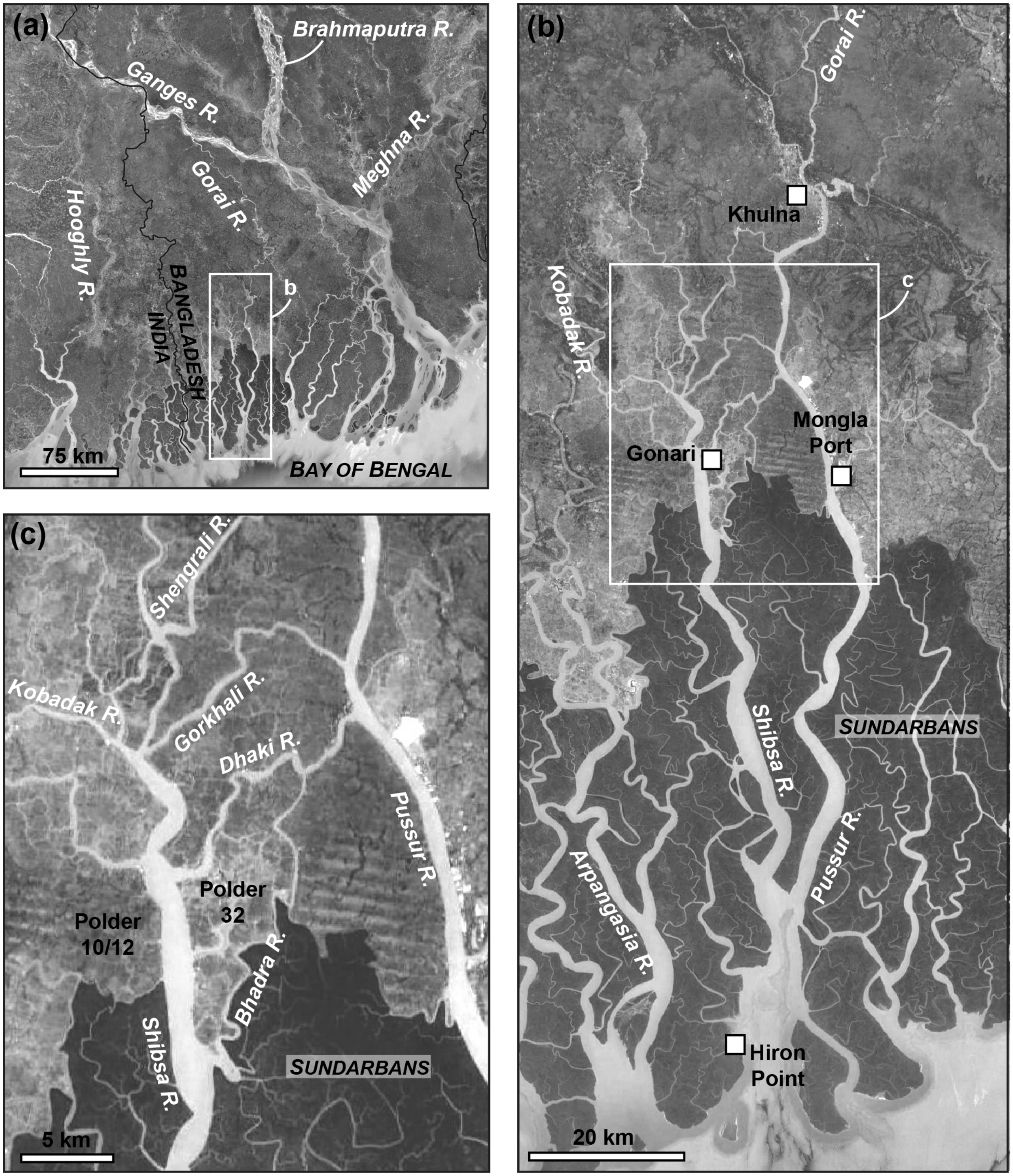

Figure 1.1: Overview map showing the study area in its larger context on the Ganges-Brahmaputra-Meghna Delta. The dark region in the southern portion of each image (southwestern portion of subplot a) is the Sundarbans Reserved Forest, a pristine intertidal mangrove environment; the lighter region to the north is embanked agricultural land that is cut off from tidal inundation. Each subplot indicates major geographical landmarks that are referenced throughout the document. In subplot (a), the black line indicates the international boundary between Bangladesh and India. All background images are undated Landsat imagery obtained via Google Earth, ©2019 TerraMetrics.

1.3 Study area

Throughout this dissertation, we examine various aspects of tidal behavior in a looping subnetwork of the GBMD tidal system (Passalacqua et al., 2013). Our primary focus is the Shibsa and Pussur Rivers, two of the primary north-south conduits for tidal discharge in southwest Bangladesh (Figure 1.1a-b). The channels initiate at an estuarine bifurcation $\sim$ 30 km north of the Bay of Bengal and then extend northwards for an additional 60 km before reconnecting via four smaller channels (from south to north, the Bhadra, Dhaki, Gorkhali, and Shengrali Rivers; Figure 1.1c). We refer to these smaller, east-west oriented channels as "transverse" channels to emphasize their role in connecting the subparallel Shibsa and Pussur Rivers. The Pussur then extends more than 150 km north as the Gorai River, a Ganges distributary with a modern monsoon-season discharge of 3000 m^3/s (Winterwerp and Giardino, 2012).

The modern spring tide range is approximately 2 meters at the coast but amplifies to $>$ 4 meters in the upper tidal basin, where the transverse channels reconnect the main channels. This particular part of the study area lies at the boundary between the Sundarbans Reserved Forest, a pristine intertidal mangrove environment covering 10,000 km^2 across Bangladesh and India, and the densely populated, embanked region to the north. The embanked area is low-lying, formerly intertidal landscape (Wilson and Goodbred, 2015) that has been cut off from tidal inundation since the 1960s and 1970s due to widespread construction of earthen embankments to form poldered islands. Confounding issues from these structures include tidal amplification (Pethick and Orford, 2013) and embankment failures (Auerbach et al., 2015), both of which illustrate the critical need to characterize regional landscape dynamics as a basis for sustainable human-landscape interactions. More generally, the extensive tidal channel network in southwestern Bangladesh provides an opportunity to broaden our fundamental knowledge of tidal propagation through spatially extensive, interconnected channels under pristine and engineered conditions.

The issues arising over the past few decades also include major navigational disruptions caused by the siltation and abandonment of channels across the study area (*e.g.*, Rahman, 2017). Wilson et al. (2017) determined that over 600 km of large, navigable waterways (formerly 100-300 meters

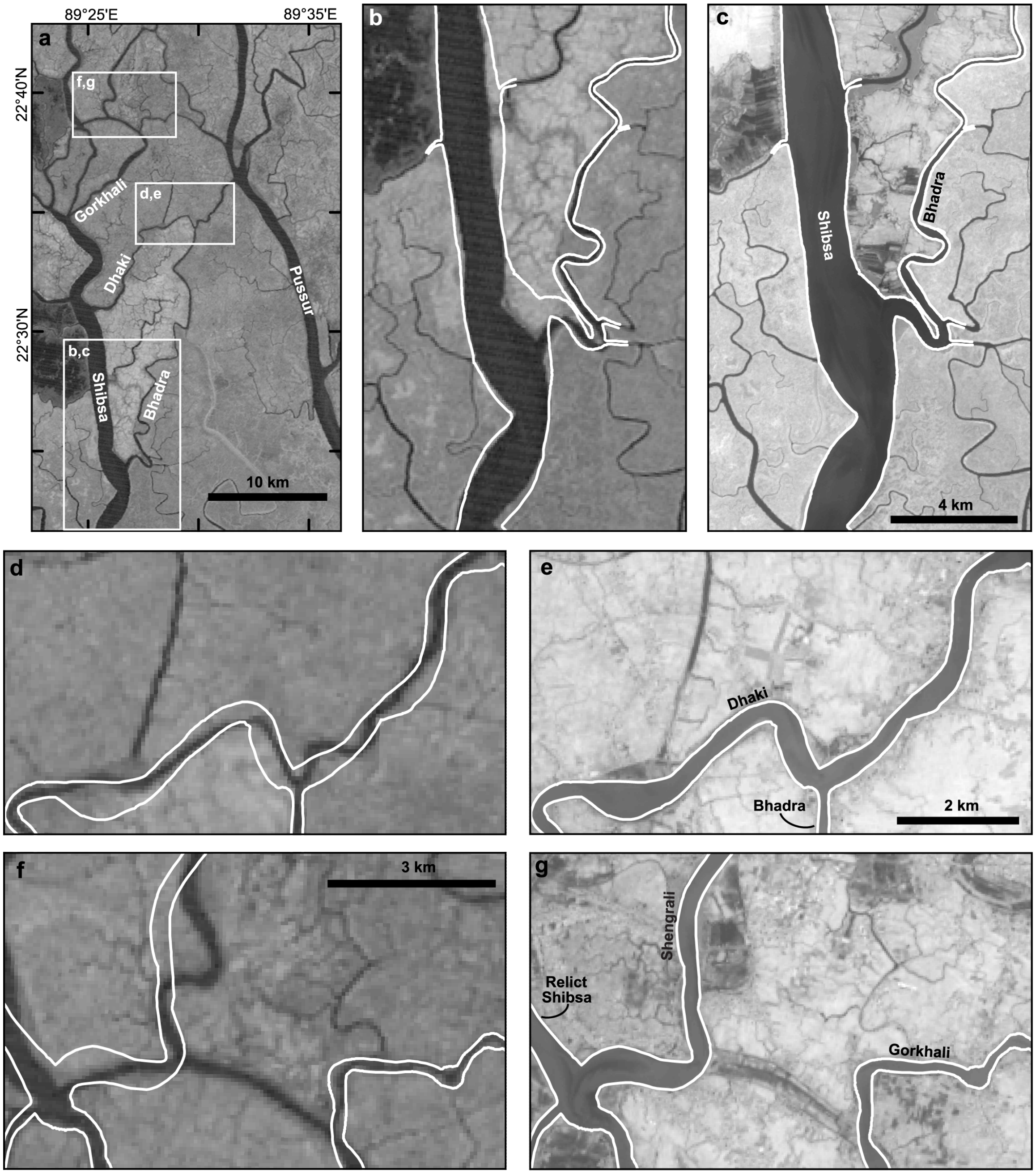

Figure 1.2: Examples of channel widening and straightening in the Shibsa, Bhadra, Dhaki, Gorkhali, and Shengrali channels. (a) Index map showing the location of frames b-g. (b-g) Paired images comparing the channel geometry on 11-Dec-1972 (Landsat 1, Band 7–NIR) on the left and 18-Feb-2017 (Landsat 8, Band 5–NIR) on the right. Both images were acquired around low water during the spring-neap transition. The white lines, which are identical in each pair of images, show the low water line on 11-Jan-2015. These were manually digitized from high-resolution Digital-Globe imagery in Google Earth. *Note: This figure was published by the American Geophysical Union in Bain et al. (2019) and is reprinted here under AGU's "Rights Granted to Authors" policy. AGU retains copyright of this figure.*

wide) have closed or infilled to <30 meters width since the 1960s. 98% of these channel closures were located in the embanked region, whereas only 2% of the infilled channels were within the pristine Sundarbans. The authors attributed this widespread channel abandonment to the polder-driven reduction in tidal prism and consequent decrease in channelized flow velocity. The paper by Hale et al. (2019a) further demonstrates the order-of-magnitude agreement between the annual suspended sediment load advected into the system from the Bay of Bengal (Rogers et al., 2013), the former rate of sedimentation on the now-embanked tidal platform (Auerbach et al., 2015; Hale et al., 2019b), and the volume of sediment required to produce such extensive channel infilling (Wilson et al., 2017).

Although narrowing and abandonment dominate the observed regional changes to the tidal channel network, a comparison of the earliest satellite imagery with the modern channel geometry reveals that some channels have actually widened and straightened over the past half-century (Wilson et al., 2017, with additional examples in Figure 1.2). Among the best examples of this behavior are several of the transverse channels connecting the Shibsa and Pussur. Ground-based observations and multibeam sonar also show prevalent bank erosion and collapse features along the length of the Dhaki and Bhadra transverse channels, as well as the nearby mainstem Shibsa (Reed, 2015). Such observations are consistent with a local increase in flow volume but deviate from the regional trend of channel infilling observed just upstream (Wilson et al., 2017). However, this change in tidal volume cannot be sourced from outside the Shibsa-Pussur tidal basin. Polder construction has eliminated 10^9 m^3 of intertidal storage volume to the north, east, and west of the study area (Pethick and Orford, 2013), and upstream discharge from the Gorai distributary has halved in the past 50 years due to some combination of Ganges water diversion at the Bangladesh-India border (Mirza, 1998; Winterwerp and Giardino, 2012; Anwar and Takewaka, 2014), land-use change in the Gorai catchment (Bharati and Jayakody, 2011), and/or naturally-occurring distributary abandonment as the Ganges migrates eastward (Allison et al., 2003). Any increase in discharge through the transverse channels connecting the Shibsa and Pussur must instead be a consequence of internal flow reorganization. Characterizing this flow reorganization and determining its underlying mechanisms are the broad goals of this dissertation.

1.4 Description of chapter contents

In Chapter 2, we present field data quantifying the volume of water conveyed by the modern transverse channels. We then analyze the modern and pre-polder channel configurations to examine how the magnitude of exchange between the Shibsa and Pussur channels has changed over the past half-century. Our specific objectives are as follows: (1) to characterize the ongoing, large-scale reorganization of a tidal channel network in the western GBMD; (2) to propose a physical mechanism driving the channels' response to anthropogenic modification of the natural system; and (3) to discuss the implications of our observations for other less-studied tidal delta plain environments. GIS-based analysis of the pre- and post-polder channel configurations indicates that polder construction eliminated a substantially larger intertidal volume from the Shibsa basin compared to the Pussur. A straightforward mass conservation argument would consequently predict that the mainstem Shibsa channel should be shoaling at a faster rate than the Pussur; however, bathymetric data suggest that the Shibsa has maintained or increased its depth even as the Pussur is experiencing major siltation issues. ADCP data collected in 2015 support the conclusion that the Shibsa has maintained its pre-polder tidal prism by expanding its tidal basin eastward into the former Pussur basin via the transverse channels.

Chapter 3 considers the hypothesis that polder-induced changes in tidal asymmetry contributed to the regional-scale system reorganization described in Chapter 2. Preliminary data collected in 2015 suggest an abrupt transition from ebb to flood asymmetry over a 10-kilometer Shibsa reach spanning the boundary between the Sundarbans and the poldered region; this is consistent with theoretical and field-based studies of other tidal systems which demonstrate a relationship between ebb asymmetry and channel-platform exchange (*e.g.*, Parker, 1984; Speer and Aubrey, 1985; Friedrichs and Aubrey, 1988; Parker, 1991; Pethick, 1994; Aucan and Ridd, 2000; Fortunato and Oliveira, 2005; Brown and Davies, 2010). Considering the often-cited association between a *flood* *asymmetric* vertical tide and a *flood dominant* horizontal tide, which favors a net inland transport of sediment, it seems plausible that a regional shift from ebb to flood dominance following polder construction drove the widespread siltation documented by Wilson et al. (2017). Such a correlation between tidal asymmetry and net sediment transport would be advantageous for predicting ongoing depositional trends within the channel network. With these ideas in mind, we collected high-frequency tide gauge data to quantify spatiotemporal variations in tidal asymmetry along the Shibsa and Pussur channels and evaluate the potential morphodynamic implications of vertical tide measurements. Our analysis indicates that although the waveform's flood asymmetry is enhanced with distance inland, and although there is a strong correlation between platform inundation depth and waveform deformation magnitude, the vertical tide never achieves an "ebb asymmetric" classification even within the Sundarbans. Further confounding these results is data demonstrating an incoherence between the vertical tidal asymmetry and the dominant horizontal current, likely due to the looping geometry of the channel network. We therefore conclude that vertical tidal records provide insufficient information for predicting the channel network's future morphodynamic stability.

Having determined that tidal asymmetry is not an accurate predictor of sediment transport in the Shibsa-Pussur system, in Chapter 4 we consider water surface gradients and their possible role in establishing preferential flow routes through the channel network. Our overarching goal for this analysis is to test a hypothesis developed at the end of Chapter 2: that polder-induced tidal amplification reduced the Pussur's gradient advantage in the vicinity of the transverse channel bifurcations, thereby forcing a larger percentage of upstream Gorai discharge into the Shibsa. We approach this problem in two steps, first by performing a momentum balance on modern-day velocity and surface gradient data to determine the relative importance of surface gradients for driving flow through the network, and second by examining a multi-decade time series of water surface gradients along the Pussur channel. The results of the momentum balance indicate that the local acceleration and quadratic friction terms are the same order of magnitude, which allows for lags of up to 3 hours between the slope and velocity reversals. When averaged over a semidiurnal period, we observe a weak correlation between mean surface gradient and mean velocity, but our data also display local deviations from this pattern which suggest that gradient does not exert a strong control on net water transport. The long-term datasets indicate a slight increase in the time-averaged surface gradient between Hiron Point and Mongla and non-negligible decrease in mean gradient between Mongla and Khulna, which does not contradict the stated hypothesis. However, in the absence of more comprehensive data, and further considering the weak relationship between flow velocity and surface gradient, we cannot draw any strong conclusions about the validity of our hypothesis from Chapter 2.

One unexpected result that arises from the analyses of Chapter 4 is an improved conceptualization of channel-platform interactions in the Sundarbans region. Although mangrove forests are often assumed to be high-friction environments, our momentum balance suggests that flow across the intertidal platform does not enhance frictional drag within the mainstem channels themselves. It is therefore reasonable to treat the channel and the platform as decoupled systems when considering frictional influences on the tidal propagation (see Speer and Aubrey, 1985; Giese and Jay, 1989; Friedrichs and Aubrey, 1994; Savenije, 2005; Savenije et al., 2008, in contrast to Pethick, 1994; Fortunato and Oliveira, 2005; Brown and Davies, 2010). However, this implies that the significant increase in M_6 overtide amplitude during spring tides cannot be attributed to quadratic friction, as is typical in other natural systems (Parker, 1984; Friedrichs and Aubrey, 1994; Orescanin et al., 2016). We conclude the dissertation by describing future research that could be undertaken to examine this and other unresolved questions arising from the projects herein.

Chapter 2

Flow reorganization in an anthropogenically modified tidal channel network: An example from the southwestern Ganges-Brahmaputra-Meghna Delta

Note: An edited version of this chapter was published on 17-Jul-2019 by the American Geophysical Union, ©2019 AGU. The paper appears as

> Bain, R.L., Hale, R.P., and Goodbred, S.L. (2019), Flow reorganization in an anthropogenically modified tidal channel network: An example from the Southwestern Ganges-Brahmaputra-Meghna Delta: *Journal of Geophysical Research–Earth Surface*, v. 124, pp. 1–19, DOI:10.1029/2018JF004996.

Abstract

We examine variations in discharge exchange between two parallel, 1-2 kilometer-wide tidal channels (the Shibsa and the Pussur) in southwestern Bangladesh over spring-neap and historical timescales. Our objective is to evaluate how large-scale, interconnected tidal channel networks respond to anthropogenic perturbation. The study area spans the boundary between the pristine Sundarbans Reserved Forest, where regular inundation of the intertidal platform maintains the fluvially-abandoned delta plain, and the anthropogenically-modified region to the north, where earthen embankments sequester large areas of formerly intertidal landscape. Estimates of tidal response to the embankment-driven reduction in basin volume, and hence tidal prism, predict a corresponding decrease in size of the mainstem Shibsa channel, yet the Shibsa is widening and locally scouring even as the interconnected Pussur channel faces rapid shoaling. Rather, the Shibsa has maintained or even increased its pre-polder tidal prism by capturing a large portion of the Pussur's

basin via several “transverse” channels that are themselves widening and deepening. We propose that an enhanced tidal setup in the Pussur and/or the elimination of an effective Shibsa-Pussur flow barrier are driving this basin capture event. These results illustrate previously unrecognized channel interactions and emphasize the importance of flow reorganization in response to perturbations of interconnected, multi-channel tidal networks that characterize several large tidal delta plains worldwide.

2.1 Methods

We quantified channel reorganization and decadal-scale discharge variation using a combination of field measurements and GIS-based calculations. Field data were collected over the two-week period from 27-Aug through 9-Sep-2015, encompassing one spring-neap cycle during peak monsoon conditions and maximum Gorai discharge.

2.1.1 TIDAL ELEVATION MEASUREMENTS

An assortment of water pressure gauges recorded high-frequency time series of the local tidal oscillations at seven locations in the Polder 32 region of southwest Bangladesh (Figure 2.1a, 2.1b). An eighth instrument at Shibsa Head failed after becoming tangled in a fishing net. The sampling interval at each site was determined by available instrument memory but did not exceed $\Delta t = 10$ minutes. We converted the raw pressure measurements to water depth using a conversion factor of 9.9 kPa/m, which is consistent with the regionally- and temporally-averaged water temperature of 30.0°C and conductivity of 32.6 mS/cm. As we were unable to survey the instruments to a common vertical datum, analysis of these datasets is limited to local tidal behavior and cannot provide absolute elevation differences between stations.

Field limitations required us to deploy six of the instruments at sites with up to 2.9 hours of subaerial exposure during spring-tide lows; only the CTD-Diver at Sutarkhali Forest Station remained continuously submerged throughout data collection. We reconstructed the missing data with a cubic spline interpolant, which outperformed several tidal constituent-based methods (*e.g.*,

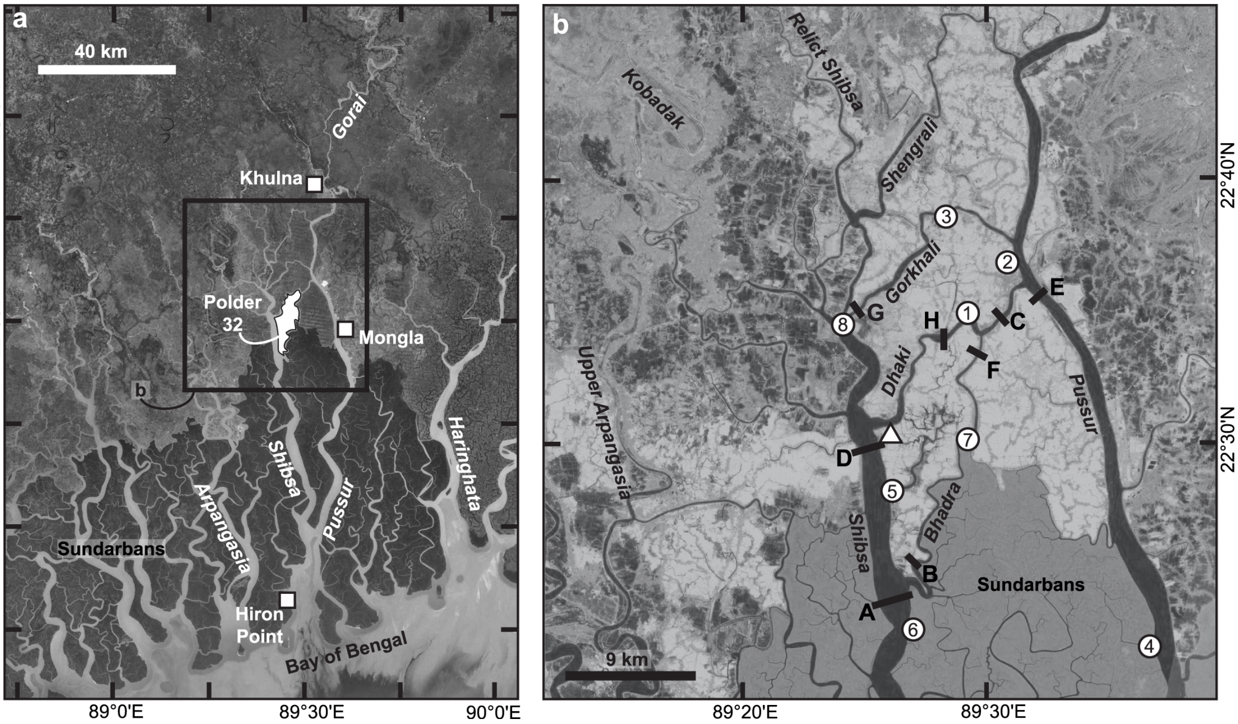

Figure 2.1: (a) Satellite image of southwest Bangladesh with major channels labeled. The dark region in the southern half of the image is the Sundarbans Reserved Forest, a pristine intertidal mangrove environment; the lighter region to the north is embanked agricultural landscape. Our study focuses on the channels surrounding Polder 32, an embanked island that suffered catastrophic flooding during Cyclone Aila in 2009. The white squares show the location of Hiron Point, Mongla, and Khulna, which were examined in an earlier study by Pethick and Orford (2013). (b) Configuration of the transverse channels connecting the Shibsa and Pussur Rivers in the Polder 32 region. The thick black lines indicate ADCP transects from the 2015 monsoon season, with letters corresponding to Table 2.1. Numbered white circles indicate sites of short-term tide gauging during the same period. The white triangle shows the location of the Gonari meteorological monitoring station. Labels are as follows: **A**–Shibsa South ADCP transect from Hale et al. (2019a); **B**–Bhadra South; **C**–Dhaki East; **D**–Shibsa North from Hale et al. (2019a); **E**–Chalna South; **F**–Bhadra North; **G**–Gorkhali West; **H**–Dhaki West; **1**–Brick Factory pressure sensor; **2**–Chalna North; **3**–Gorkhali East; **4**–Jongla Forest Station; **5**–Nalian Forest Station; **6**–Shibsa Forest Station; **7**–Sutarkhali Forest Station; **8**–failed sensor at Shibsa Head ferry ghat. Background: (a) undated Google Earth mosaic from Landsat/Copernicus, ©2018 TerraMetrics; (b) Landsat 8 imagery dated 9-Feb-2017. *Note: This figure was published by the American Geophysical Union in Bain et al. (2019) and is reprinted here under AGU's "Rights Granted to Authors" policy. AGU retains copyright of this figure.*

Pawlowicz et al., 2002; Codiga, 2011) for reconstructing the known low water elevations at Sutarkhali. The poor performance of the standard tidal analysis algorithms is partly due to the short time series duration, which in many cases was insufficient to separate the M_2 and S_2 constituents and reconstruct a spring-neap pattern. Additionally, we observe a pronounced variation in the amplitude and phase of the shallow water harmonics depending on platform inundation depth; this cannot be reproduced by an algorithm which time-averages these parameters. Section A.3 in Appendix A contains a detailed description of the cubic spline algorithm.

2.1.2 DISCHARGE MEASUREMENTS

We collected discharge data at six transects across the Bhadra, Dhaki, Gorkhali, and Pussur channels using boat-mounted Sontek M9 acoustic Doppler current profilers (ADCPs) with autonomous GPS positioning. Figure 2.1b displays the location of each ADCP transect as a thick black line. By convention, we define velocities in the downstream or ebb direction (south or southwest) as positive and velocities in the upstream or flood direction as negative. The instrument automatically extrapolated the measured velocity field to the bed and the banks using the power law velocity profile of Chen (1991) and then internally computed discharge as the flux of the velocity field through the area under the transect. To correct for systematic variation in the measured discharge for left-to-right-bank versus right-to-left-bank boat travel, we averaged the raw discharge values for each pair of consecutive, oppositely oriented transects to produce our final dataset (see Norris, 2001, but note that we are averaging two, rather than four, transects due to the rapidly changing tidal conditions in our study area). The tidal prisms Ω_{ebb} and Ω_{flood}, defined as the total volume of water passing through a transect between flow reversals, were then calculated by numerically integrating the discharge curve between its zero crossings.

Challenging local working conditions, including hazardous weather and navigational delays, prevented the ADCP surveys from encompassing a full semidiurnal tidal cycle. We estimated the missing discharge values using the extrapolation procedure from Hale et al. (2019a), which we summarize as follows. Beginning from the assumption that discharge variation is negligible between consecutive tidal oscillations, we first translated the data forward or backward in time by one semidiurnal period. We then interpolated between the original and translated measurements using a fourth-degree polynomial constrained by a systemwide mass balance of water transport over a

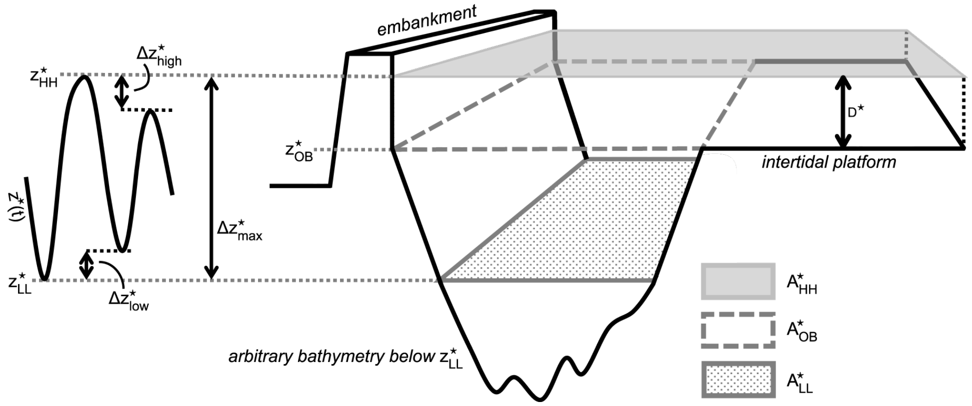

Figure 2.2: Simplified channel cross sectional geometry used for storage volume calculations. The abbreviations HH and LL refer, respectively, to the elevation of the highest high water and the lowest low water within a given channel segment. The overbank elevation is notated OB. Each channel segment is ∼2 kilometers long extending into the page. *Note: This figure was published by the American Geophysical Union in Bain et al. (2019) and is reprinted here under AGU's "Rights Granted to Authors" policy. AGU retains copyright of this figure.*

tidal cycle. For certain survey sites where this mass balance was under-constrained, we generated a suite of possible interpolating curves, and this paper reports the range of reasonable values. Additional details about this procedure, including the specific assumptions for each transect, are included in Section A.4 of Appendix A.

2.1.3 UPSTREAM BASIN VOLUME ESTIMATES: PRESENT DAY

We utilized a simplified channel cross-sectional geometry (Figure 2.2) to determine the spatial extent of the tidal basin associated with each ADCP transect. Starting with high-resolution (1 m/px) Google Earth imagery, we digitized polygons estimating the water surface area at the lowest low water ($A^\star_{\mathrm{LL}}$), at the moment of overbanking ($A^\star_{\mathrm{OB}}$), and at highest high water ($A^\star_{\mathrm{HH}}$) for 2-km-long channel segments extending upstream from the study area. The starred variables denote local measurements for a discrete channel segment. In the poldered region, we assumed that $A^\star_{\mathrm{OB}} = A^\star_{\mathrm{HH}}$. For channel segments adjacent to the Sundarbans, we defined $A^\star_{\mathrm{OB}}$ using the permanent vegetation line along the channel and estimated $A^\star_{\mathrm{HH}}$ by drawing "interfluves" separating the quasi-dendritic mangrove creek networks.

For polygons containing one of the deployed pressure gauges, the elevation time series provided local values of the peak tidal range ($\Delta z^{\star}_{\text{max}} = z^{\star}_{\text{HH}} - z^{\star}_{\text{LL}}$, where the subscripts indicate an assumed correspondence to $A^{\star}_{\text{LL}}$ and $A^{\star}_{\text{HH}}$), as well as the offset between the absolute extrema and the high and low water elevations recorded on the date of interest ($\Delta z^{\star}_{\text{low}}$ and $\Delta z^{\star}_{\text{high}}$). We linearly interpolated with along-channel distance to obtain values of $\Delta z^{\star}_{\text{max}}$, $\Delta z^{\star}_{\text{low}}$, and $\Delta z^{\star}_{\text{high}}$ at polygons between two instruments. Upstream of the study area, where we lacked direct measurements of the tidal elevation, we consulted with local fishermen to estimate $\Delta z^{\star}_{\text{max}}$ along the Kobadak, relict Shibsa, and northern Pussur channels (see Table A.1 in Appendix A for a detailed summary of these anecdotal tidal ranges).

To estimate the local vertical offset between $z^{\star}_{\text{OB}}$ and $z^{\star}_{\text{HH}}$, we assigned a maximum platform inundation depth $D^{\star}_{\text{max}} = z^{\star}_{\text{HH}} - z^{\star}_{\text{OB}}$ of 0.25 m in the Sundarbans based on in situ observations of the flooding depth. The value of $D^{\star}_{\text{max}}$ then decayed moving northwards to a value of 0 at the historical limit of tidal inundation, which we determined by comparing tidal inundation data from Abbas (1966), the upstream extent of soils with a tidal signature (Brammer, 2012), and the boundary between fluvial splay deposits and comparatively featureless topography visible on 1-arcsecond SRTM data (which approximately corresponds to the base of the upper delta fan system identified by Wilson and Goodbred, 2015). We then assumed a linear change in the value of $A^{\star}(z)$ between $z^{\star}_{\text{LL}}$ and $z^{\star}_{\text{OB}}$ to calculate the volume of water filling a given channel segment on a specified date.

2.1.4 ESTIMATES OF PRE-POLDER TIDAL VOLUMES

To estimate the volume of water moving through the system before and immediately following polder construction, we repeated the channel volume calculations described in Section 2.1.3 with several modifications to adjust for unrestricted platform flooding. The local maximum tidal range $\Delta z^{\star}_{\text{max}}$ was reduced based on the amplification trend from Pethick and Orford (2013, with details in Section A.5.3 of Appendix A). The overbank area of a given channel segment, $A^{\star}_{\text{OB}}$, was taken as the original embankment position digitized by Wilson et al. (2017), and we assumed that $A^{\star}_{\mathrm{LL}} = 0.8A^{\star}_{\mathrm{OB}}$, which is a representative ratio for the modern polygons. Because platform sedimentation has kept pace with high water amplification (Auerbach et al., 2015), we assumed that the local maximum platform inundation depths $D^{\star}$ were time-invariant over the 50-year study period. Finally, we generated Thiessen polygons from a set of points spaced at 1-km increments along the channel network to produce an estimate of $A^{\star}_{\mathrm{HH}}$ for each channel segment.

In the absence of direct (ADCP-based) tidal prism measurements collected prior to polder construction and subsequent channel infilling, we used waveform travel-time minimization to estimate whether a given channel segment flooded via the Shibsa or the Pussur. Starting from the channel network GIS shapefile generated by Passalacqua et al. (2013), we updated the channel widths and network connectivity to represent the system's pre-polder geometry. The pre-polder layout was based on a mosaic of the earliest Landsat 1 imagery, dated between 5-Nov-1972 and 20-Feb-1973, followed by careful comparison with the *khasland* (infilled channel) mapping of Wilson et al. (2017) to compensate for possible channel abandonment that may have occurred between polder construction in the 1960s and the satellite acquisition dates. For channel segments more than 10 km north of the coastline, we assumed that the average depth $\overline{d}^{\star}$ was given by

$$\overline{d}^{\star} = 0.17(w^{\star})^{0.6} \quad , \tag{2.1}$$

which is the best-fit relationship for published non-mouth tidal channel width:depth ratios (compiled from Langbein, 1963; Myrick and Leopold, 1963; Dury, 1971; Wright et al., 1973; Zeff, 1988, 1999; Schulz et al., 2015; Hale et al., 2019a, and summarized in Figure A.6). Given the tendency for tidal channels to shoal as they approach open water, Equation 2.1 produced implausibly large depths within the funnel-shaped channel mouths. We corrected for this issue by replacing depths near the coast with soundings from the Defense Mapping Agency (1991).

To produce a first-order estimate of flow paths through the channel network, we assumed that the waveform travel time $T^\star$ along each segment scales as:

$$T^\star \propto \frac{L^\star}{\sqrt{g \cdot \overline{d}^\star}} \ , \tag{2.2}$$

where $L^\star$ is the segment length and $g = 9.81$ m/s^2. We then performed a closest facility analysis in ArcMap to determine the fastest route to the Bay of Bengal for 1.2×10^4 points along the channels. This calculation applied Dijkstra's algorithm to calculate the minimum cumulative along-network travel time between the input points and any of a set of 14 points offshore from each of the 14 channel mouths bracketing the Shibsa-Pussur outlet. The 14 target points were located on the 80° M_2 cotidal line to account for the accelerated propagation rate associated with the Swatch of No Ground Canyon in the Bay of Bengal (Sindhu and Unnikrishnan, 2013).

2.2 Results

In the following sections, we characterize spring-neap variations in net water exchange before addressing how the Shibsa and Pussur tidal basins have changed in size and position since the 1960s. These data reveal complex, tidal-range dependent behavior which has been substantially modified relative to its pre-engineered state.

2.2.1 MODERN TIDAL PRISMS AND NET CIRCULATION PATTERNS

Here we evaluate our discharge measurements from the transverse channels in the context of Shibsa River discharge data from Hale et al. (2019a). The goals of this analysis are (1) to determine the flow division at channel junctions where we were unable to measure discharge directly and (2) to characterize net circulation patterns within the network under spring and neap conditions. Unlike single-inlet systems, in which the ebb and flood prisms have equal magnitude, the looping channel network topology in our study area admits the possibility of $|\Omega_{\text{ebb}}| \neq |\Omega_{\text{flood}}|$. We define the local

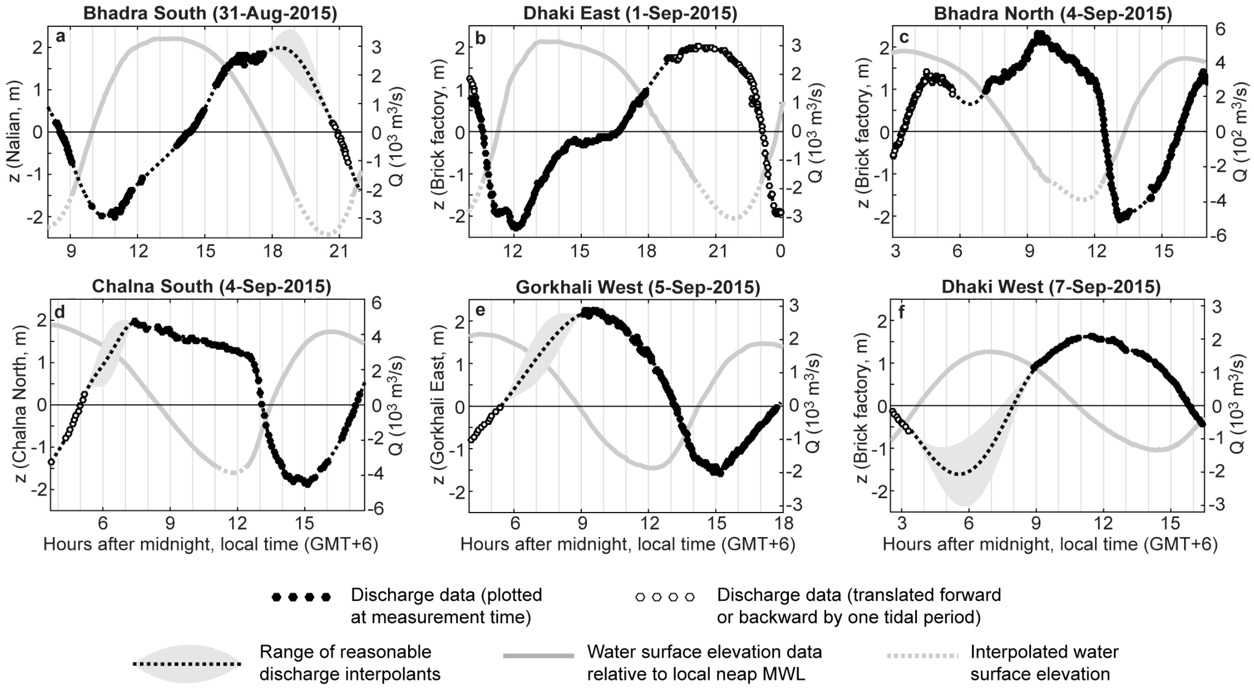

Figure 2.3: ADCP data and interpolants from six locations in the study area. Black points represent discharge values plotted at the actual time of measurement, whereas white points indicate that the measurement has been translated horizontally by one semidiurnal tidal period. Additional discharge data from this region are available in the paper by Hale et al. (2019a). *Note: This figure was published by the American Geophysical Union in Bain et al. (2019) and is reprinted here under AGU's "Rights Granted to Authors" policy. AGU retains copyright of this figure.*

net tidal prism as $\Omega_{\text{net}} = \Omega_{\text{ebb}} + \Omega_{\text{flood}}$, which is positive when $|\Omega_{\text{ebb}}| > |\Omega_{\text{flood}}|$ and negative for the opposite scenario.

During spring tides, we observe a net ebb-directed flux of water from the Pussur into the Shibsa via both the Dhaki and Bhadra Rivers (Table 2.1; Figure 2.3); however, data from Hale et al. (2019a) indicate that the Shibsa South transect conveys a net flood-directed prism of approximately -4.3×10^7 m^3. Because the channel network is effectively a closed system upstream of the study area, one or both of the Gorkhali and Shengrali channels must also be net flood-directed, delivering a combined net prism of $(-4.85 \pm 0.47) \times 10^7$ m^3 from the Shibsa into the Pussur (Figure 2.4a). Moreover, considering the upstream Gorai discharge of approximately 3000 m^3/s recorded by the Bangladesh Water Development Board (BWDB) at Gorai Railway Bridge during the study period, we estimate a net prism of $(+16.6 \pm 0.5) \times 10^7$ m^3 at Chalna South (Transect E in the Pussur; Figure 2.1b). The BWDB Gorai discharge data are provided in Appendix A.

Circulation patterns in the study area vary substantially under neap conditions (Figure 2.4b). For example, the net prism in the Gorkhali is ebb-directed during neap tides, whereas mass balance suggests a flood-directed net prism in this channel under spring-tide flow conditions. Hale et al. (2019a) likewise report a spring-to-neap reversal in net tidal prism at Shibsa South and Shibsa North. Taking the upper limit of reasonable net neap-tide values measured in the Bhadra, Dhaki, and Gorkhali and the lower bound of the net Shibsa South neap prism indicates that the Shengrali's net neap prism cannot be less than $\Omega_{\text{net}}^{\text{Sheng}} = +0.74 \times 10^7$ m^3. Due to the uncertainty in the other sites' interpolated discharge values, we are unable to more precisely constrain the value of $\Omega_{\text{net}}^{\text{Sheng}}$; however, the actual value of the Shengrali's net prism is likely larger than this reported minimum value. In contrast to the positive value of $\Omega_{\text{net}}^{\text{Sheng}}$ during neap tides, the spring tide mass balance suggests that $\Omega_{\text{net}}^{\text{Sheng}}$ is negative. To summarize, comparing the circulation patterns in Figure 2.4a and 2.4b indicates that tidal interactions between the Shibsa and the Pussur are strongly dependent on spring versus neap conditions, with the net direction of water transport reversing at several key locations. We will revisit this observation when characterizing the broader significance of our study in Section 2.3.4.

2.2.2 SPATIAL EXTENT OF MODERN TIDAL BASINS

To understand how the measured tidal prism is accommodated within the channel network, we route the ADCP-derived tidal prism magnitudes through the available upstream storage volume, which is summarized in Table 2.2. This exercise provides an estimate of the spatial boundaries of a given transect's tidal basin. Since our ultimate goal is to understand the transverse channels' morphodynamic response to post-polder flow conditions, we here focus on the basin configuration during spring tides when peak flow velocities occur. In this paper, we limit our analysis to the Shibsa North tidal prism (Hale et al., 2019a); this eliminates the uncertainty associated with possible net cross-platform exchange through the Sundarbans.

Table 2.1: Measured or estimated monsoon-season tidal prisms in the Polder 32 region. Letters in the table correspond to the transect labels in Figure 2.1b.

Spring tides

Site	Survey dates in 2015	Ebb prism, Ω_{ebb} ($\times 10^7$ m^3)	Flood prism, Ω_{flood} ($\times 10^7$ m^3)	Net prism, $\lvert\Omega_{\text{ebb}}\rvert - \lvert\Omega_{\text{flood}}\rvert$ ($\times 10^7$ m^3)	Source
A. Shibsa South	30, 31-Aug	$+47.0 \pm 1.5$	$\mathbf{-51.3}^{*}$	-4.3 ± 1.5	Hale et al. (2019a)
B. Bhadra South	31-Aug	$+4.59 \pm 0.47$	$\mathbf{-3.37}$	$+1.22 \pm 0.47$	This study
C. Dhaki East	1, 2-Sep	$\mathbf{+4.73}$	$\mathbf{-3.06}$	$\mathbf{+1.67}$	This study
D. Shibsa North	2-Sep	$\mathbf{+24.1}$	$\mathbf{-28.5}$	$\mathbf{-4.4}$	Hale et al. (2019a)
E. Chalna South[†]	(n/a)	$(+16.6 \pm 0.5) + \lvert\Omega_{\text{flood}}^{\text{ChalnaS}}\rvert$	$\Omega_{\text{flood}}^{\text{ChalnaS}}$	$+16.6 \pm 0.5$	Systemwide mass balance

Neap tides

Site	Survey dates in 2015	Ebb prism, Ω_{ebb} ($\times 10^7$ m^3)	Flood prism, Ω_{flood} ($\times 10^7$ m^3)	Net prism, $\lvert\Omega_{\text{ebb}}\rvert - \lvert\Omega_{\text{flood}}\rvert$ ($\times 10^7$ m^3)	Source
E. Chalna South	4-Sep	$+9.55 \pm 0.55$	$\mathbf{-4.43}$	$+5.12 \pm 0.55$	This study
F. Bhadra North	4-Sep	$\mathbf{+1.00}$	$\mathbf{-0.38}$	$\mathbf{+0.62}$	This study
G. Gorkhali West	5-Sep	$+4.93 \pm 0.49$	$\mathbf{-1.90}$	$+3.03 \pm 0.49$	This study
D. Shibsa North	7-Sep	$\mathbf{+18.3}$	-10.7 ± 0.6	$+7.6 \pm 0.6$	Hale et al. (2019a)
H. Dhaki West	7-Sep	$+4.02 \pm 0.06$	-2.30 ± 0.94	$+1.72 \pm 1.00$	This study
A. Shibsa South	8-Sep	$\mathbf{+26.4}$	-18.2 ± 0.6	$+8.2 \pm 0.6$	Hale et al. (2019a)

[*] Bold text in this table indicates values that were measured directly by ADCP. All other volumes were determined by interpolation and/or mass balance.

[†] Although we lack ADCP-based discharge measurements from the Chalna South transect during spring tides, balancing the known values of $\Omega_{\text{net}}^{\text{Shibsa}}$ from Hale et al. (2019a) and an upstream Gorai input of about 13.4×10^7 m^3 (*i.e.*, 3000 m^3/s over 12.42 hours; Figure A.9) requires a *net* prism of $(+16.6 \pm 0.5) \times 10^7$ m^3 at the Chalna South transect. This also constrains the minimum possible value for $\Omega_{\text{ebb}}^{\text{ChalnaS}}$ (which would occur if $\Omega_{\text{flood}}^{\text{ChalnaS}} = 0$, *i.e.*, the flow does not reverse). Details of the mass balance calculations are available in Appendix A.

Distributing the flood tidal prism of $|\Omega_{\text{flood}}^{\text{ShibN}}| = 28.5 \times 10^7$ m^3 measured at Shibsa North on 2-Sep-2015, we find that this volume not only floods the Kobadak and relict Shibsa channels to the west and north, but also completely fills the full length of the Dhaki, Gorkhali, and Shengrali channels extending eastward to the Pussur (Figure 2.5a). Moreover, a residual volume of $\sim 5.9 \times 10^7$ m^3 must flood into the mainstem Pussur channel. As a check on our calculations, we consider whether the remaining storage volume of $\sim 9.7 \times 10^7$ m^3 in the Pussur/Gorai channel upstream of Chalna South could reasonably be filled by non-Shibsa sources. Approximately 6.7×10^7 m^3 of

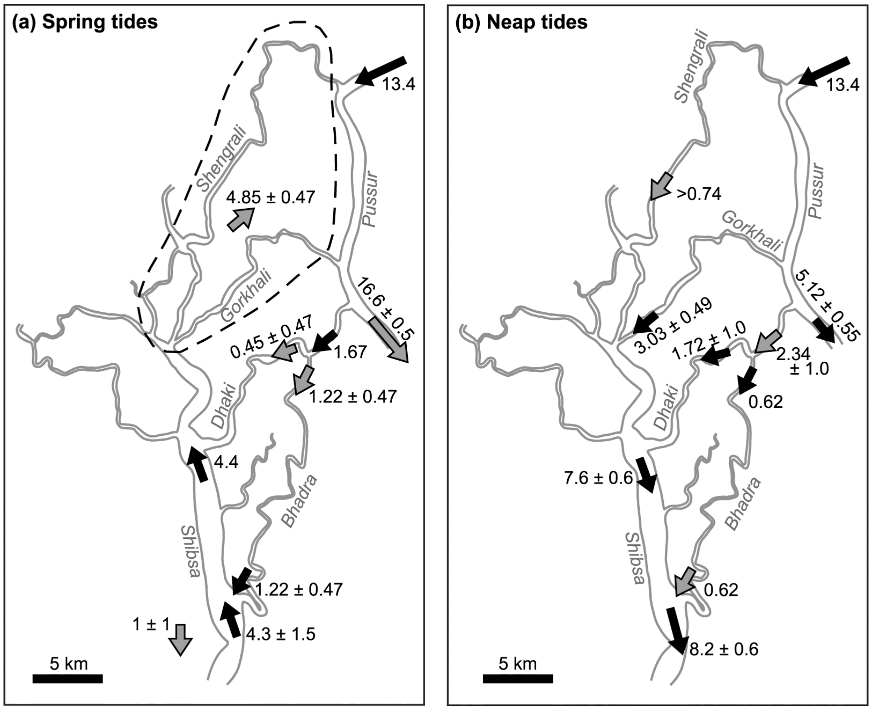

Figure 2.4: Net monsoon-season tidal prisms in the channels surrounding Polder 32 under (a) spring and (b) neap flow conditions. All numbers have units of 10^7 m^3. Black arrows indicate tidal prisms which were measured by ADCP; gray arrows are values required for systemwide mass balance. The dashed line in (a) indicates that the Gorkhali and Shengrali channels together must have a net flood-directed tidal prism of $(-4.85 \pm 0.47) \times 10^7$ m^3; however, we have insufficient data to further constrain how this flow volume is divided among the two channels. For the spring tide mass balance, we have assumed zero net discharge through the Sundarbans east of the Bhadra South ADCP transect (Transect B in Figure 2.1) and a net ebb-directed volume of $(+1 \pm 1) \times 10^7$ m^3 traveling through the Sundarbans near the Shibsa South transect (Transect A). Both assumptions are consistent with the apparent Sundarbans drainage patterns suggested by the small mangrove creeks' quasi-dendritic network geometry. *Note: This figure was published by the American Geophysical Union in Bain et al. (2019) and is reprinted here under AGU's "Rights Granted to Authors" policy. AGU retains copyright of this figure.*

Table 2.2: Storage volume between low and high water for various channel segments during the spring tide on 2-Sep-2015. The volumes were calculated based on the generalized channel geometry displayed in Figure 2.2.

Polygon description	**2-Sep** $(\mathbf{10^7\ m^3})$
Shibsa River between Shibsa South and Shibsa North	9.59
Small channel west of Nalian Forest Station and connected Sundarbans*	2.55
Bhadra River west of Bhadra South and connected Sundarbans*	2.23
Bhadra River east of Bhadra South and connected Sundarbans*	2.57
Total storage volume between Shibsa South and Shibsa North	**16.94**
Shibsa River between Shibsa North and Shibsa Head	5.39
Kobadak and Relict Shibsa bifurcates above Shibsa Head	8.07
Dhaki River	3.03
Gorkhali River	2.38
Shengrali River	3.77
Total storage volume above Shibsa North but west of Pussur	**22.64**
Pussur River between Chalna South ADCP transect and Shengrali confluence	5.51
Pussur River from Shengrali confluence to northern Khulna city limits	3.75
Gorai and tributaries from northern Khulna to upstream oscillation limit	6.62
Total storage volume in Pussur/Gorai	**15.88**

*Includes storage in main channel, mangrove creeks, and on intertidal platform during spring tides.

this volume would be filled by the 3000 m^3/s of Gorai River discharge over a 6.21-hour flooding limb (the region north of the dashed line in Figure 2.5a). The remaining volume in the Pussur would be filled by a spring-tide flood prism at Chalna South of $|\Omega_{\text{flood}}^{\text{ChalnaS}}| = 3 \times 10^7$ m^3, which is comparable in magnitude to the measured flood prism under neap conditions.

2.2.3 PRE-POLDER BASIN AREA AND TIDAL VOLUME

One goal of our study is to evaluate how the distribution of water through the modern tidal system differs from its pre-engineered configuration. To accomplish this, we first estimated the pre-polder tidal basin boundaries using waveform travel time minimization, with the results displayed in Figure 2.5b. The Shibsa River was the fastest route of tidal waveform arrival for any point between the thick white lines; outside these boundaries, the fastest path was via the Pussur to the east or the Arpangasia to the west. If we make the first-order assumption that discharge also preferentially floods any given location via the fastest travel path, then these lines serve as an estimate of the Shibsa's pre-polder flood basin boundaries. Although we have insufficient discharge data to test the validity of this assumption directly, testing the algorithm on the modern system configuration demonstrates good agreement with the ADCP-derived Shibsa-Pussur basin boundary (see Section A.6 in Appendix A for details). Moreover, we apply two geometrical arguments to evaluate the validity of our results in the following paragraphs.

First, the travel-time minimization algorithm suggests that the Shibsa-Pussur basin boundary was positioned quasi-equidistant from the two channels prior to polder construction (Figure 2.5b). To test whether the resulting size of the Pussur tidal basin is reasonable, we note that the Gorai's reported monsoon-season discharge of 5500 m^3/s in 1964 (Winterwerp and Giardino, 2012) would deliver 12.3×10^7 m^3 of water to the Pussur basin above Chalna South over a 6.21-hour rising limb. Under the assumption of negligible net discharge through the transverse channels, which is reasonable given their small pre-polder width, this entire Gorai-contributed volume would necessarily be stored somewhere in the Pussur basin. Meanwhile, the travel time minimization algorithm indicates a Pussur basin volume of 15.1×10^7 m^3 prior to poldering; this corresponds to the region east of the Shibsa basin outline in Figure 2.5b. The difference of 2.8×10^7 m^3 is the same order of magnitude as the measured Chalna South flood prism (Table 2.1), suggesting that this volume of water could reasonably enter the basin via a northwards-directed flow along the Pussur. However, even if the remaining 2.8×10^7 m^3 of water entered this region via the Shibsa (shifting the Shibsa-Pussur basin boundary slightly to the east), the Shibsa still could not have flooded into the Pussur to the extent observed under modern conditions.

Second, we apply published relationships between tidal prism and channel hydraulic geometry to test whether the travel-time minimization algorithm generates a reasonable estimate of the channels' respective basin sizes. Empirical fitting (*e.g.* O'Brien, 1931, 1969; Jarrett, 1976) and numerical models (D'Alpaos et al., 2010) support the existence of a power-law relationship between tidal prism and the channel's cross sectional area at mean water, with Ω raised to a power between 0.85 and 1.10. Although these relationships are complicated by a variety of site-specific parameters (Gao and Collins, 1994), we anticipate that published equations from non-engineered tidal

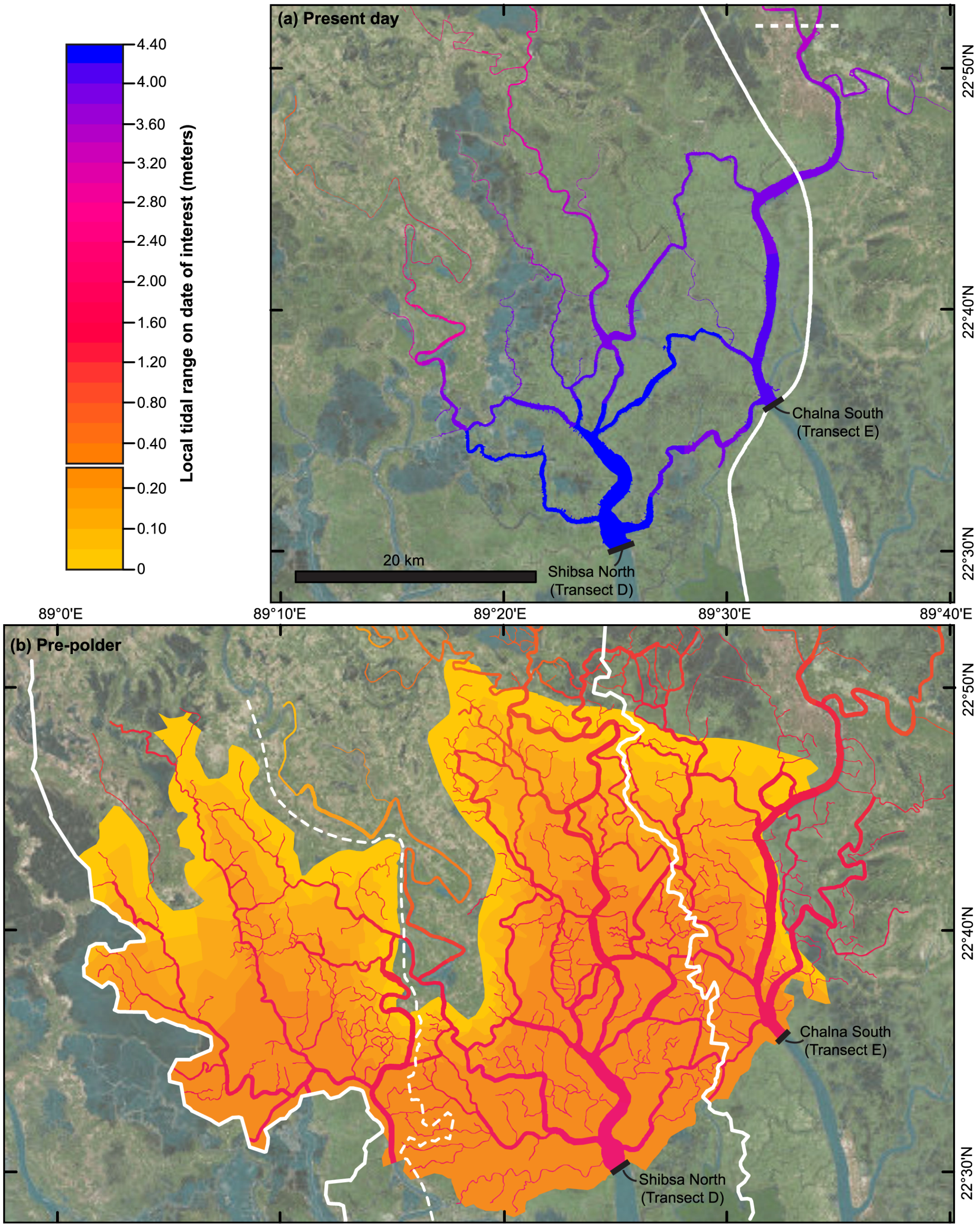

Figure 2.5: (Continued on following page.)

Figure 2.5: Map of tidal volume above the Chalna South and Shibsa North ADCP transects (a) during the midday flooding limb on 2-Sep-2015 and (b) under peak spring tide conditions for the pre-polder channel configuration. The color scale is the same for both subfigures. The thick white lines indicate estimated tidal basin boundaries. In (a), the Gorai River's discharge over a 6.21-hour flooding limb fills the volume north of the dashed white line; note that this region extends upstream to the limit of vertical oscillation at approximately 23.2°N. For (b), travel time minimization identifies the Shibsa River as the fastest route for tidal waveform travel to the upper Arpangasia basin. However, it is likely that the actual Shibsa-Arpangasia basin boundary was nearer to the dashed line due to discharge mixing from several sources. We include estimates of the Shibsa North basin volume with and without the ambiguous region west of the dashed line; this produces lower and upper bounds for the volume of water conveyed by the Shibsa River. Background: undated Terra-Color imagery, ©2018 Earthstar Geographics, obtained through ESRI/ArcMap. *Note: This figure was published by the American Geophysical Union in Bain et al. (2019) and is reprinted here under AGU's "Rights Granted to Authors" policy. AGU retains copyright of this figure.*

systems should produce a rough estimate of the expected values for the pre-polder GBMD. Applying Equation 1 to the Shibsa North transect width in the earliest Landsat imagery, we obtain a cross sectional area of 1.64×10^4 m^2; this corresponds to a predicted tidal prism between 25.0×10^7 m^3 (using the relationship for non-jettied channels from O'Brien, 1969) and 33.4×10^7 m^3 (based on Jarrett, 1976). Meanwhile, the travel-time minimization algorithm predicts a pre-polder Shibsa North basin volume of 41.6×10^7 m^3 (Table 2.3), which includes the upper reaches of the Arpangasia channel to the west. Because this is substantially higher than the values predicted by the tidal prism-inlet area relationship, we also consider the possibility that the upper Arpangasia basin (corresponding to the region west of the dashed white line in Figure 2.5b) was instead flooded by the lower Arpangasia channel. This produces a more conservative estimate of 28.6×10^7 m^3 for the pre-polder Shibsa North basin volume. Thus, we report these lower and upper limits for the Shibsa's pre-polder tidal prism, which respectively correspond to the dashed and solid white lines on the western boundary of the Shibsa tidal basin (Figure 2.5b).

2.2.4 IMMEDIATE EFFECT OF POLDER CONSTRUCTION

As a next step in the analysis, we subtract the storage volume eliminated from each channel's tidal basin using the approximate position of the embankments when they were first constructed

Table 2.3: Basin volume north of Polder 32 before and immediately after polder construction

Location	**Pre-polder basin volume ($\times 10^7$ m^3)**	**Post-polder basin volume ($\times 10^7$ m^3)***	**Volume lost ($\times 10^7$ m^3)**	**Percent change**
Shibsa Head basin	28.6	13.3	-15.3	-53%
Upper Arpangasia basin[†]	13.0	3.7	-9.3	-72%
Shibsa Head + Arpangasia	**41.6**	**17.0**	**-24.6**	**-59%**
Pussur south of Khulna	12.2	6.6	-5.6	-46%
Pussur north of Khulna	2.9	2.9	0	0%
Pussur total	**15.1**	**9.5**	**-5.6**	**-37%**

[*] Note that the “post-polder” volumes represent the immediate elimination of the tidal platform and small tidal creeks but do not include the additional, gradual loss of volume due to the khasland formation described by Wilson et al. (2017).

[†] The shortest waveform path calculations indicate that the tide propagating up the Shibsa should be the first to arrive in this basin. However, based on the system geometry observed in 1972 Landsat imagery, it is likely that this region received mixed discharge from the Shibsa and Arpangasia estuaries.

(Wilson et al., 2017). These calculations indicate a substantial but geographically varied reduction in basin volume due to poldering (Table 2.3). The Shibsa basin upstream of the Shibsa North transect lost more than half its storage volume as an immediate consequence of polder construction, reducing from a pre-polder spring tide volume of 28.6×10^7 m^3 to a post-polder volume of 13.3×10^7 m^3 (53% volume loss). These numbers assume that no Shibsa discharge was crossing the dashed white line in Figure 2.5b; however, if we do include the northern Arpangasia basin, then the volume loss increases to 59%. The Pussur's basin above the Chalna South transect lost about 37% of its volume as a direct consequence of polder construction, decreasing from 15.1×10^7 m^3 to 9.5×10^7 m^3. In summary, these pre-polder tidal volume calculations suggest that polder construction eliminated a larger basin volume in the Shibsa relative to the Pussur, which engendered several morphodynamic responses addressed below.

2.3 Discussion

The analysis of discharge and tidal range measurements, along with complementary GIS-based estimates of modern and historical basin volumes, produces three key results elucidating the channel network's response to anthropogenic modification. First, we observe that the Shibsa River's flood basin boundary has shifted eastward over the past 70 years, from a pre-polder position approximately halfway between the Shibsa and Pussur channels to the modern configuration in which the Shibsa floods a large portion of the Pussur's former basin during peak spring conditions (Figure 2.5). Specifically, of the $\sim 8.9 \times 10^7$ m^3 of tidal water (*i.e.*, total minus Gorai discharge) required to fill the modern Pussur channel above the Chalna South transect during spring tides, the Shibsa North transect supplies about 5.9×10^7 m^3. In other words, $\sim 20\%$ of the total Shibsa North flood prism of -28.5×10^7 m^3 enters the mainstem Pussur channel during the flooding limb. Second, our calculations indicate that polder construction caused a larger immediate volume reduction in the Shibsa basin compared to the Pussur basin, whether measured by absolute volume loss ($> 13.3 \times 10^7$ m^3 versus 5.6×10^7 m^3) or by percent loss ($> 53\%$ versus 37%). The first and second results both hold despite uncertainty in the precise location of the Shibsa-Arpangasia and Shibsa-Pussur basin boundaries prior to polder construction.

The third major result is the fundamentally different circulation patterns under modern spring versus neap flow conditions (Figure 2.4). During spring tides, there is a net flux of tidal volume from the Shibsa into the Pussur. Moreover, the entire volume of freshwater contributed from the Gorai River, along with any additional (unmeasured) flood prism at the Chalna South transect, must ebb out of the system via the Pussur channel. In contrast, there is a net flux of water from the Pussur into the Shibsa during neap tides, with a magnitude equivalent to $\sim 60\%$ of the Gorai input from upstream. We discuss the physical significance and broader implications of these three results in the following sections.

2.3.1 THE CONUNDRUM OF BASIN VOLUME REDUCTION GENERATING INCREASED DISCHARGE EXCHANGE

Recent literature highlights the systemwide response to polderization in the GBMD, including tidal range amplification (Pethick and Orford, 2013), accelerated relative elevation loss within the polders (Auerbach et al., 2015), and rapid channel infilling in the upper tidal basins (Wilson et al., 2017). The contemporaneity of polder construction and bank retreat in the transverse channels

(Reed, 2015; Wilson et al., 2017) suggests that localized channel widening may be yet another distinct response to these large-scale anthropogenic landscape modifications. Considering the power law relationship between tidal prism and channel cross-sectional area (*e.g.*, O'Brien, 1931; Jarrett, 1976; Gao and Collins, 1994; D'Alpaos et al., 2010) and a second power law relationship between channel width and depth (Equation 2.1), we posit that the widening of the transverse channels over the past half-century reflects a substantial increase in discharge exchange between the Shibsa and Pussur Rivers via the transverse channels.

Despite these seemingly robust observations, establishing a causative link between polder construction and the enhanced discharge exchange is not intuitive due to strong positive feedbacks between storage volume reduction and channelized flow velocity. For example, to explain why 600 km of major channels were progressively infilled and abandoned after polder construction, Wilson et al. (2017) applied the following mass-conservation argument. First, disconnecting these tidal channels from their intertidal platform dramatically reduced the volume of water required to fill the upstream basins. This reduction in basin volume subsequently drove a decrease in mean channelized flow velocities, in addition to eliminating the velocity surge associated with bank overtopping (Pethick, 1980). The resulting decline in sediment transport capacity led to rapid channel siltation, particularly in the blind upstream channels. In summary, this sequence of responses generated a strong positive feedback between tidal prism reduction, a continuing decline in local tidal discharge, and channel infilling and abandonment only 10 km upstream of the Polder 32 region (Figure 2.1).

Reasoning from this morphodynamic feedback pattern, the tidal prism reduction in the Shibsa and Pussur basins (Table 2.3) should have decreased flow velocities in both channels and consequently induced sedimentation in the adjoining transverse channels. Instead, we observe the opposite: a significant widening and scouring of the transverse channels, consistent with an increase in discharge. Moreover, considering that the Shibsa basin lost a larger percentage of its volume to poldering, the consequences of polder construction should be more pronounced; *i.e.*, we would expect siltation to be enhanced in the mainstem Shibsa channel relative to the mainstem

Pussur channel. We instead observe that the main Shibsa channel is widening and scouring near Polder 32 (Figure 1.2; see also Figure A.1 in Appendix A for examples of bathymetry), whereas deep-draft shipping along the Pussur faces major disruption due to rapid shoaling (*e.g.*, Rahman, 2017).

Post-polder tidal range amplification within and upstream of the study area (Pethick and Orford, 2013) could be an alternative mechanism for the observed scouring and widening. For example, amplification of sufficient magnitude could enable the channels to maintain their pre-polder tidal prisms by substituting vertical volume between the embankments for horizontal volume on the intertidal platform. Under this scenario we would expect amplification-generated scouring to be regionally prominent. However, Pethick and Orford (2013) document tidal amplification along the entire Pussur channel, which is noteworthy for its long-term shoaling and interruption of deep-draft shipping. Consequently, there arises neither evidence nor intuition that tidal-range amplification has been a direct cause of the observed bank erosion and channel widening along the Shibsa, Dhaki, Gorkhali, and Shengrali channels.

The possibility remains that the observed expansion of the transverse channels is a consequence of naturally-occurring distributary network morphodynamics. For example, changes to the system's boundary conditions (*e.g.*, sea-level rise in the Bay of Bengal, changes in sediment input, or migration of fluvial distributaries outside of the tidal region) or natural tidal channel competition could also drive flow reorganization. The results of prior studies allow us to eliminate most of these possibilities. First, Wilson et al. (2017) observed that over the $\sim$50-year period since polder construction, 98% of all channel closures occurred in the embanked region of the study area, with only 2% in the Sundarbans. This suggests that the rate of natural channel network migration and reorganization is low enough to be negligible over the time period of interest. Additionally, Pethick and Orford (2013) documented a tidal range increase of only 5.6 mm/year at the coastal station of Hiron Point (Figure 2.1a) between 1990 and 2011, in comparison to 16.5 mm/year at Mongla and 28.8 mm/year at Khulna. This indicates that the observed tidal amplification is largely generated by internal modifications to the system rather than by sea level rise in the Bay of Bengal. The mass of sediment imported into the study area has also remained relatively constant over the period of interest (Rogers et al., 2013; Auerbach et al., 2015; Hale et al., 2019a). Among the system's boundary conditions, the only significant change is the reduction in the Gorai's monsoon-season freshwater discharge from 5500 m^3/s in 1964 to 3000 m^3/s in 2015 (Winterwerp and Giardino, 2012). We evaluate the possible influence of upstream Gorai abandonment in Section 2.3.3.

2.3.2 RELEVANCE OF DISTRIBUTARY BIFURCATION DYNAMICS TO TIDAL NETWORK BEHAVIOR

Having demonstrated that basin volume reduction, tidal amplification, and natural network reorganization are unlikely causes of the observed channel widening and scouring, the remaining possibility is that the direct effects of polder construction documented by Pethick and Orford (2013) and Wilson et al. (2017) have forced a reorganization of tidal discharge partitioning among the channels. To explore this idea, we first suggest that the transverse channels effectively behave as "distributaries" for the bidirectional flow exchanged between the Shibsa and Pussur, and we thus turn to the rich literature on channel bifurcation dynamics to provide context for our measurements. Flow patterns at our study area's channel junctions are complicated by tidal influence, in contrast to the better-studied case of unidirectional distributary behavior; however, universal parameters governing flow division at bifurcations are still relevant for understanding the GBMD system.

Given the economic, engineering, and geological significance of deltaic distributaries, considerable effort has been devoted to identifying the parameters that influence morphological stability at bifurcations. These include the width ratio of the two downstream branches (Edmonds and Slingerland, 2008; Kleinhans et al., 2011; Bolla Pittaluga et al., 2015), a gradient advantage making one bifurcate the preferential flow route (Marra et al., 2014), climate-driven changes in basinwide discharge (Edmonds et al., 2010), and secondary flow structures produced by meanders or bedforms upstream of the bifurcation (Kleinhans et al., 2011; Miori et al., 2012; Sassi et al., 2013). Tidal energy further influences bifurcation behavior by inhibiting sediment deposition in non-dominant distributaries (Kästner et al., 2017), modulating discharge partitioning among the downstream branches (Buschman et al., 2010; Sassi et al., 2011; Zhang et al., 2017), and introducing baroclinically-driven circulation between the bifurcates if the system is poorly-mixed (Kim and Voulgaris, 2005; Buschman et al., 2013; Shaha and Cho, 2016). However, the relative influence of these parameters varies with local network geometry and other system-specific factors such as bed roughness. In the following section, we apply these authors' findings to develop two hypotheses that may explain cause of internal flow reorganization in our study area.

2.3.3 ALTERNATIVE HYPOTHESES EXPLAINING POST-POLDER SHIBSA BASIN EXPANSION

Our first hypothesis is based on the results of Sassi et al. (2011), who combined field data with a numerical model to quantify river-tide interactions in the bifurcating Mahakam Delta. The authors determined that river discharge in the Mahakam is preferentially allocated to the shorter, deeper bifurcate in the absence of tides, but the introduction of tidal oscillations produces a setup in the dominant branch that reduces its gradient advantage and forces a larger-than-expected fraction of the discharge from upstream into the longer bifurcate. By analogy, we hypothesize that post-polder tidal range amplification (Pethick and Orford, 2013) enhanced the tidal setup in the Pussur and forced a greater percentage of Gorai freshwater discharge into the Shibsa. The consequent increase in discharge scoured the beds of the Dhaki and Gorkhali channels and prevented significant sedimentation in the Shibsa. This generated a disparity in the waveform propagation times along these channels, with the present-day Shibsa and Pussur displaying mean celerity values of 11.2 m/s and 8.1 m/s, respectively, over the distance between Hiron Point and the transverse channels. The faster tidal propagation along the Shibsa thus enables its continued dominance over the Pussur.

However, other results from the Berau and Mahakam deltas suggest that under certain conditions, an increase in tidal energy will *enhance* a bifurcation's discharge inequality in favor of the already-dominant channel (Buschman et al., 2010; Zhang et al., 2017). If these results are more representative of the pre-polder GBMD study area, then the first hypothesis may be invalid. As an alternative, we consider the possibility that changes in the Shibsa-Gorai discharge interaction (rather than the Pussur-Gorai discharge interaction, as in the previous paragraph) were the primary cause of flow reorganization. Table 2.3 indicates that even before polder construction, the spring tide flood basin above Shibsa North was considerably larger (28.6 to 41.6 $\times$ 10^7 m^3) than the basin above the Chalna South transect (15.1 $\times$ 10^7 m^3). If we make the simplifying assumption of no net discharge through the transverse channels, then the maximum tidal prism at Shibsa North was identical to its basin volume, while the maximum ebb prism at Chalna South transect was $\sim$ 27.4 $\times$ 10^7 m^3 (*i.e.*, the 15.1 $\times$ 10^7 m^3 filling the basin during the flooding limb plus an additional 12.3 $\times$ 10^7 m^3 of Gorai discharge entering the system from upstream during the 6.21-hour ebbing limb). This disparity in pre-polder basin size is reflected in our estimated values of mean pre-polder celerity between Hiron Point and the transverse channels: 12.0 m/s in the Shibsa versus 11.8 m/s in the Pussur. Our second hypothesis considers that despite the Shibsa's favorable pre-polder celerity, an opposing influx of Gorai discharge into the transverse channels formerly prevented the Shibsa's tidal discharge from intruding into the Pussur. The subsequent decline in Gorai discharge eliminated this discharge-related "barrier" between the Shibsa and the Pussur, allowing the Shibsa basin to expand eastward into the Pussur channel despite its greater loss of tidal volume due to polder construction. Analogous behavior has been reported in the Yangtze Delta (Zhang et al., 2017), where the wet season river discharge prevents the tidal intrusion that occurs under lower flow conditions.

The paucity of long-term discharge and tidal range records from the study area prevents us from testing these hypotheses directly. The opposing results of Sassi et al. (2011) versus Buschman et al. (2010) and Zhang et al. (2017) illustrate that the tidal effect at a bifurcation is strongly dependent on system-specific flow parameters. Moreover, the two proposed hypotheses are not mutually exclusive. Given the complexity of the GBMD tidal channel network (Passalacqua et al., 2013), it is plausible that the combined effects of polder construction (leading to an enhanced tidal setup in the Pussur during the monsoon season) and declining freshwater discharge from the Gorai (eliminating the barrier between the Shibsa and the Pussur during the dry season) operated simultaneously to expand the transverse channels.

2.3.4 THE BROADER SIGNIFICANCE OF TIDAL BASIN CAPTURE

The literature presents numerous examples of channel avulsion events in which bed aggradation and/or mouth progradation drives channel relocation to a more hydraulically favorable position (see the review by Kleinhans et al., 2013, and references therein), including instances of tidal channel avulsions (Hood, 2010; Pierik et al., 2018). Although our observation of transverse channel flow expansion and Pussur abandonment has avulsion-like characteristics, we avoid reference to a Gorai River "avulsion" from the Pussur into the Shibsa based on the results in Figure 2.4. These data indicate that although approximately 60% of the Gorai discharge ebbs through the Shibsa River during monsoon-season neap tides, the entire Gorai-contributed volume must ebb via the Pussur during monsoon-season spring tides. The Pussur is thus still the dominant conduit for conveying Gorai discharge to the Bay of Bengal under peak flow conditions. This is further supported by observations of a ~ 40 cm tidal setup of the Pussur above the Shibsa during the 2014 monsoon season (Shaha and Cho, 2016), which indicates that the Gorai still most strongly influences the Pussur's behavior.

Instead, we find that our results are conceptually similar to the tidal flat channel competition model of Toffolon and Todeschini (2006). These authors found that nearby channels in a small-scale tidal flat setting may exist stably if the system is unperturbed. However, introducing a small perturbation to the initially-stable system will introduce a positive feedback in which one channel continues to deepen and capture the other channels' intertidal basins. There are several notable differences between these results and our data, including the substantial variation in spatial scale. Moreover, Toffolon and Todeschini (2006) examined isolated channels expanding their basins across the intertidal platform, whereas the channels in our study area are interconnected, and the captured basin volume is positioned inside the channels between the low and high water elevations. However, the broad idea of perturbation-induced tidal basin capture appears relevant to both small-scale tidal wetland and large-scale tidal delta plain settings, although further study is required to examine the specific parameters that govern this behavior in other large-scale systems.

Regardless of the driving mechanism, the results presented herein highlight the unpredictable response of a large-scale tidal channel network to anthropogenic landscape modification. Whereas an isolated tidal channel should shoal in response to a reduction in basin volume (*e.g.*, O'Brien, 1931; Jarrett, 1976; Gao and Collins, 1994; D'Alpaos et al., 2010), we observed certain channels widening and deepening in our study area. This is a consequence of the inherent complexity of distributary bifurcation dynamics, nonlinear river-tide interactions, and variable tidal phasing among the network branches. In addition to its theoretical significance, this behavior has practical implications for human welfare, one of which was already realized when widening along the Dhaki and Shibsa channels eroded the embankments protecting Polder 32 (Figure 2.1a). It was along these margins that five embankment breaches occurred during Cyclone Aila in 2009 (Auerbach et al., 2015). Given that many of the polders in southwest Bangladesh lie well below mean high water, local bank erosion in response to network reorganization substantially enhances the region's flooding risk.

2.4 Conclusion

Large-scale embankment construction in the southwestern GBMD during the 1960s and 1970s has driven a regional decline in tidal prism and discharge. However, our observations of local bank retreat and scouring suggest a counterintuitive increase in discharge through several east-west oriented, distributary-type channels connecting the Shibsa and the Pussur Rivers. GIS-based analysis of the earliest Landsat imagery indicates that embankment construction had the immediate effect of eliminating between 53% and 59% of the tidal basin volume above Shibsa North versus 37% of the tidal basin volume above Chalna South in the Pussur. Because a tidal channel's hydraulic geometry is closely related to its basin volume, it is reasonable to predict shoaling in both channels, with this effect being somewhat greater in the Shibsa due to its greater initial basin volume loss. Prior studies document rapid sedimentation and abandonment in both the mainstem Pussur and in numerous tidal creeks in the former Shibsa basin (Wilson et al., 2017). However, the mainstem Shibsa has maintained its pre-polder basin volume by expanding its basin eastward into the pre-polder Pussur basin.

We interpret our data as a local "basin-capture" event driven by polder-induced tidal amplification and changes to the interactions between tidal currents and Gorai River discharge. These results have serious implications for regional flood vulnerability, especially considering that channels experiencing a local discharge increase have an enhanced risk of embankment failure. Of course, non-anthropogenic forcings including sea-level rise, variations in sediment supply, channel mouth progradation, and lateral channel migration can also drive changes in channel network morphology. However, the spatial distribution of observed channel abandonment (98% of all channel closures occur in the embanked region, with only 2% in the pristine Sundarbans mangrove forest; Wilson et al., 2017) increases our confidence that the Shibsa's expansion into the Pussur basin and the associated widening of the transverse channels is dominantly a product of anthropogenic landscape modifications.

More broadly, our study suggests that interconnected tidal networks worldwide may respond unpredictably to perturbations because flow patterns are able to reorganize as the channels respond to changing boundary conditions. The western GBMD is morphodynamically analogous to several other minimally-studied, large-scale tidal delta plain environments, including the Ayeyarwady, Indus, Kikori-Purari, Mahakam, Orinoco, and Sesayap. Due to loops in these systems' channel networks, results from better-studied single-channel estuaries have limited relevance for these systems. Recognizing the complex interacting processes that construct and maintain these systems will be invaluable for interpreting responses to previous or ongoing landscape change. Moreover, future tidal delta plain management strategies necessitated by high rates of effective sea level rise should anticipate the possibility of rapid channel reorganization.

Chapter 3

Interpretation of tidal asymmetry in a large scale, looping channel network

Note: In this chapter, all references to "Bain et al. (2019)" also indicate the paper in Chapter 2.

3.1 Abstract

Nonlinear tidal distortion in shallow water environments has received considerable attention in the literature for two reasons: first, because the shape of the waveform provides insight into the local physical controls on tidal behavior, and second, because waveform asymmetry often has implications for net sediment transport and the system's long-term morphodynamic development. In this chapter, we quantify spatiotemporal waveform asymmetry variations in a subnetwork of the Ganges-Brahmaputra-Meghna Delta's expansive tidal channel network system. An array of 10 pressure sensors collected high-frequency tidal records along the interconnected Shibsa and Pussur Rivers in southwestern Bangladesh from October 2017 to March 2018, spanning the transition from monsoon to dry-season conditions. The data indicate that shallow-water deformation tends to increase with distance upchannel, although there are local deviations from the regional trend which may be a product of superimposed tidal signals arriving at the sensor via different routes through the network. Intertidal platform inundation enhances the magnitude of waveform deformation; however, the vertical tide remains flood asymmetric even during peak platform inundation events, which is contrary to the often-cited idea that platform inundation generates ebb asymmetric tides.

In many natural systems, flood asymmetric water surface elevations are associated with flood dominant current speeds, allowing researchers to predict net sediment transport and long-term morphodynamic stability from a vertical tidal record. To test whether such a correlation exists in the Shibsa-Pussur channel system, we calculated velocity time series from the ADCP datasets presented in Chapter 2 and compared these records with the vertical tidal signal. This analysis indicates an incoherence between the vertical tidal asymmetry and the dominant horizontal current,

likely due to loops in the channel network. Vertical tidal records therefore provide insufficient information for predicting the channels' future depositional behavior.

3.2 Introduction

3.2.1 MOTIVATION

In the previous chapter, we detailed an introductory study quantifying the volume of water stored in localized areas of the Shibsa-Pussur channel network in southwestern Bangladesh. The primary focus of that study was tidal range, *i.e.*, the vertical distance between low and high water, because this was the necessary information for calculating the volume of water filling a given channel reach. However, while collecting those preliminary data in August/September 2015 (see Hale et al., 2019a; Bain et al., 2019), we observed unexpected waveform behavior at several monitoring sites. During spring tides, the tide appears ebb asymmetric at Shibsa Forest Station (F.S.) but slightly flood asymmetric at Nalian, even though the stations are separated by less than 10 river kilometers (Figure 3.1). This abrupt deformation causes high water to occur 45 minutes *earlier* at the upstream station. Moreover, high water at Jongla precedes high water at Shibsa F.S. by over one hour, despite the Shibsa River's greater celerity (Pethick, 2012; Bain et al., 2019) and the comparable distance from Hiron Point (70 river kilometers for Shibsa F.S. versus 69 river kilometers for Jongla). North of Polder 32, the spring tides become strongly flood asymmetric. During neap tides, waveform asymmetry is weaker, and the high water timing is correlated with distance from the coast and relative channel depth.

Our study area is positioned in a region that has experienced rapid and often detrimental changes to the landscape over the past half-century, including tidal amplification (Pethick and Orford, 2013), siltation of formerly navigable channels (Wilson et al., 2017), accelerated elevation loss in the embanked agricultural regions (Auerbach et al., 2015), local bank retreat and collapse (Reed, 2015), and reorganization of tidally-driven flow patterns (Bain et al., 2019). For a detailed introduction to these anthropogenically-generated landscape changes, we direct the reader to the dissertation introduction in Section 1.3. Unfortunately, it is costly and time-prohibitive to collect

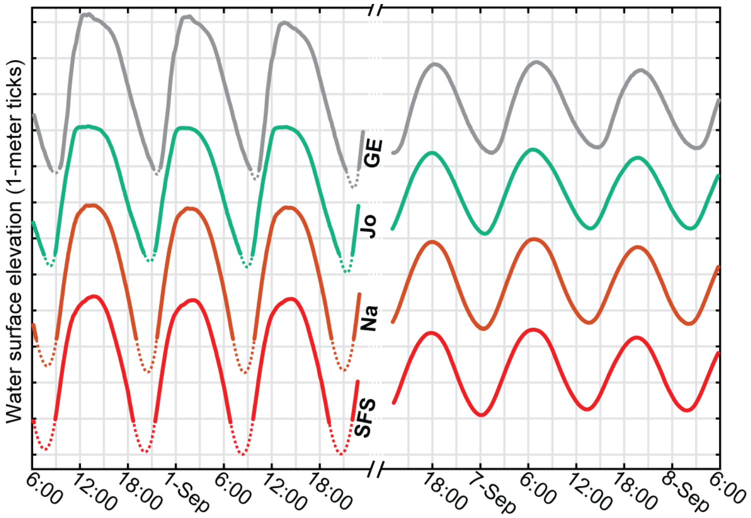

Figure 3.1: Time series of water surface elevation data from Shibsa F.S., Nalian, Jongla, and Gorkhali East in August/September 2015, as described in Hale et al. (2019a) and Bain et al. (2019). The data are vertically offset for visual clarity. Dashed lines indicate interpolation during periods of subaerial exposure. All times are local (GMT+6); note the break in the horizontal axis to allow comparison of the waveform shape at peak spring (left) and peak neap (right) conditions. A map of instrument locations is shown in Figures 2.1 or 3.3.

additional discharge and sediment transport data that would allow us to predict the system's future morphological trajectory. Vertical tidal records, in contrast, are vastly simpler to obtain and allow greater spatiotemporal coverage of the channel network.

Since tidal asymmetry and net sediment transport are known to be strongly correlated in other natural systems (*e.g.* Friedrichs and Aubrey, 1988; Pethick, 1994; Mazda et al., 1995; Bolle et al., 2010; Brown and Davies, 2010; Li et al., 2012; Toublanc et al., 2015; Pritchard and Green, 2017; Li et al., 2018), we here consider whether an analysis of tidal asymmetry has utility for understanding the landscape's resilience (or non-resilience) to future anthropogenic change in the GBMD. Our goal for this chapter is therefore to isolate and characterize the mechanisms of tidal deformation in the Shibsa-Pussur channel network and examine whether this deformation has long-term morphodynamic implications. We specifically address the following three questions:

1. How does large-scale overbank flooding of the intertidal platform influence waveform behavior?

2. To what extent does waveform interaction between the channels influence tidal propagation?
3. Is there an association between vertical and horizontal tidal asymmetry that elucidates trends in sedimentation and channel network evolution?

3.2.2 MECHANISMS AND METRICS OF SHALLOW-WATER TIDE DEFORMATION

In dominantly semidiurnal systems, it is common to approximate the shape of the tidal waveform by the relative phase and amplitude of M_2 (the lunar semidiurnal constituent; period $T_{\mathrm{M2}} =$ 12.42 hours) and its second harmonic, M_4, using the metrics

$$\mathcal{R}_{2,4} = \frac{A_{\mathrm{M4}}}{A_{\mathrm{M2}}} \quad \text{and} \quad \Delta\phi_{2,4} = 2\phi_{\mathrm{M2}} - \phi_{\mathrm{M4}} \tag{3.1a-b}$$

(Speer and Aubrey, 1985; Friedrichs and Aubrey, 1988). Here A and ϕ refer to the amplitude and phase, respectively, of the subscripted vertical tidal constituent. The value of $\Delta\phi_{2,4}$ characterizes waveform asymmetry, with $0 < \Delta\phi_{2,4} < 180°$ indicating *flood asymmetry* (*i.e.*, a shortening of the rising limb relative to the falling limb; Figure 3.2) and $180° < \Delta\phi_{2,4} < 360°$ indicating *ebb asymmetry*. For a given value of $\Delta\phi_{2,4}$, the associated value of $\mathcal{R}_{2,4}$ quantifies the strength of the deformation.

In a single-channel system, shortening the duration of one of the tidal limbs necessitates an increase in current speeds in order to conserve mass. Consequently, the literature often associates flood asymmetric vertical tides with *flood dominant* currents and ebb asymmetric vertical tides with *ebb dominant* currents, and the terms are used interchangeably. Because this chapter focuses on a multi-channel system where there is no guarantee of mass conservation through a given channel cross section (Bain et al., 2019), we limit ourselves to the terms *flood asymmetric* and *ebb asymmetric* unless we can verify that the vertical and horizontal asymmetry are in the same direction.

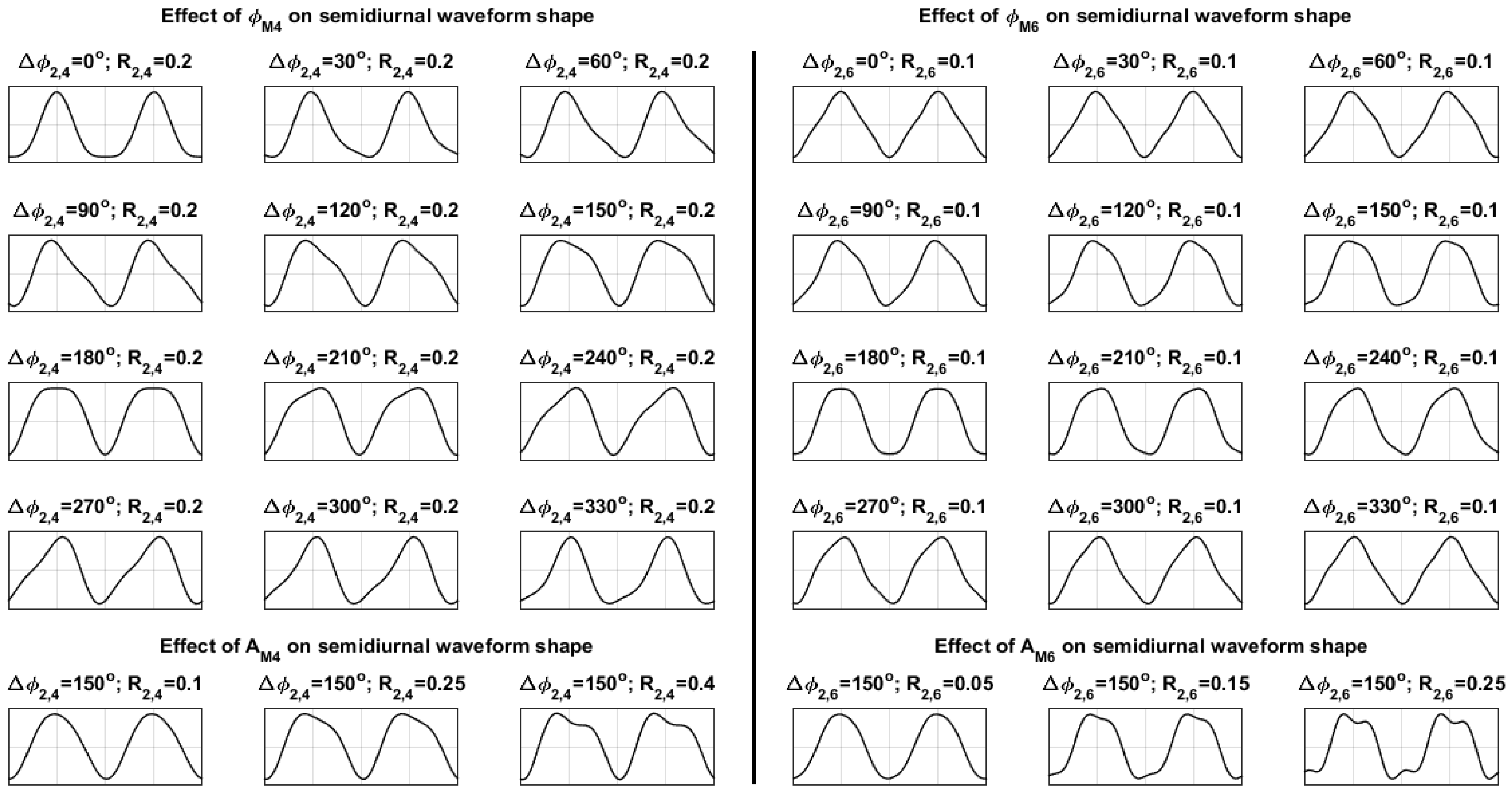

Effect of ϕ_{M4} on semidiurnal waveform shape

$\Delta\phi_{2,4}$=0°; $R_{2,4}$=0.2

$\Delta\phi_{2,4}$=30°; $R_{2,4}$=0.2

$\Delta\phi_{2,4}$=60°; $R_{2,4}$=0.2

$\Delta\phi_{2,4}$=90°; $R_{2,4}$=0.2

$\Delta\phi_{2,4}$=120°; $R_{2,4}$=0.2

$\Delta\phi_{2,4}$=150°; $R_{2,4}$=0.2

$\Delta\phi_{2,4}$=180°; $R_{2,4}$=0.2

$\Delta\phi_{2,4}$=210°; $R_{2,4}$=0.2

$\Delta\phi_{2,4}$=240°; $R_{2,4}$=0.2

$\Delta\phi_{2,4}$=270°; $R_{2,4}$=0.2

$\Delta\phi_{2,4}$=300°; $R_{2,4}$=0.2

$\Delta\phi_{2,4}$=330°; $R_{2,4}$=0.2

Effect of A_{M4} on semidiurnal waveform shape

$\Delta\phi_{2,4}$=150°; $R_{2,4}$=0.1

$\Delta\phi_{2,4}$=150°; $R_{2,4}$=0.25

$\Delta\phi_{2,4}$=150°; $R_{2,4}$=0.4

Effect of ϕ_{M6} on semidiurnal waveform shape

$\Delta\phi_{2,6}$=0°; $R_{2,6}$=0.1

$\Delta\phi_{2,6}$=30°; $R_{2,6}$=0.1

$\Delta\phi_{2,6}$=60°; $R_{2,6}$=0.1

$\Delta\phi_{2,6}$=90°; $R_{2,6}$=0.1

$\Delta\phi_{2,6}$=120°; $R_{2,6}$=0.1

$\Delta\phi_{2,6}$=150°; $R_{2,6}$=0.1

$\Delta\phi_{2,6}$=180°; $R_{2,6}$=0.1

$\Delta\phi_{2,6}$=210°; $R_{2,6}$=0.1

$\Delta\phi_{2,6}$=240°; $R_{2,6}$=0.1

$\Delta\phi_{2,6}$=270°; $R_{2,6}$=0.1

$\Delta\phi_{2,6}$=300°; $R_{2,6}$=0.1

$\Delta\phi_{2,6}$=330°; $R_{2,6}$=0.1

Effect of A_{M6} on semidiurnal waveform shape

$\Delta\phi_{2,6}$=150°; $R_{2,6}$=0.05

$\Delta\phi_{2,6}$=150°; $R_{2,6}$=0.15

$\Delta\phi_{2,6}$=150°; $R_{2,6}$=0.25

Figure 3.2: Examples of how A_{M4}, ϕ_{M4}, A_{M6}, and ϕ_{M6} influence the shape of the M_2 waveform. Each subplot spans two semidiurnal periods along the horizontal axis.

Several studies (Bolle et al., 2010; Orescanin et al., 2016) additionally characterize waveform shape using the relative amplitude and phase of the M_6 tide, which is the third harmonic of M_2:

$$\mathcal{R}_{2,6} = \frac{A_{\mathrm{M6}}}{A_{\mathrm{M2}}} \quad \text{and} \quad \Delta\phi_{2,6} = 3\phi_{\mathrm{M2}} - \phi_{\mathrm{M6}} \ . \tag{3.2a-b}$$

As shown in Figure 3.2, the addition of M_6 to M_2 produces a symmetrical deformation of both tidal limbs, which results in either a narrowing or a broadening of both high and low water.

Beyond simply characterizing waveform geometry, the deformation metrics defined in Equations 3.1a-b and 3.2a-b elucidate the physical controls on flow behavior. Flood asymmetry is generally associated with long, shallow channels lacking intertidal flats, whereas ebb asymmetry tends to develop in systems with a large intertidal storage zone. Parker (1984, 1991) calculated the Fourier expansion of each term in the shallow water equations to identify the mechanisms of M_4 and M_6 deformation. When applied to data from the Delaware estuary, this analysis indicated that nonlinear advection of mass and momentum generate approximately 80% of total M_4 energy, with the remaining 20% being produced by per-unit-volume frictional dissipation. In qualitative language, when the ratio of tidal range to mean depth is near 1, there is a non-negligible variation in the flow depth at low versus high water. The resulting time-variable celerity generates a flood asymmetry as the waveform crest propagates inland faster than the trough. Meanwhile, the frictional dissipation per unit volume of water is greatest at low tide, further reducing the celerity of the trough and favoring flood asymmetry (see also Dronkers, 1986).

However, in systems with a large intertidal platform, the waveform crest may propagate more slowly than the trough, which generates an ebb asymmetry in waveform shape. The literature discusses several possible mechanisms for this behavior. First, certain authors note that the width-averaged flow depth may actually be *smaller* at high water than at low water if the intertidal region is sufficiently large (Pethick, 1994; Fortunato and Oliveira, 2005; Brown and Davies, 2010). The wave celerity $(gh)^{1/2}$ (with h representing the cross-sectionally averaged depth) is therefore reduced at high water, allowing an ebb asymmetry to develop. Within this school of thought, it has also been suggested that enhanced frictional drag generated by the inundation of a vegetated intertidal region further slows the propagation of the crest (Pethick, 1994). The alternative interpretation is that the intertidal platform stores water but does not convey momentum (Dronkers, 1964; Speer, 1984; Speer and Aubrey, 1985; Giese and Jay, 1989; Friedrichs and Aubrey, 1994; Savenije, 2005; Savenije et al., 2008; Mariotti and Fagherazzi, 2011), and the generation of an ebb asymmetric waveform is due to volume loss and/or the addition of a momentum sink term in the equations of motion. Regardless of which proposed mechanism is most accurate, the association between platform inundation and an ebb asymmetry (generated by the M_4 overtide) is well established.

The mechanisms of the M_6 overtide generation are poorly understood in comparison to M_4. Friedrichs and Aubrey (1994) noted that hydrodynamic models struggle to accurately reproduce M_6 behavior; however,

> "[t]here is little doubt that the friction term is the major source of M_6 production within semidiurnal tidal channels." (Friedrichs and Aubrey, 1994, p. 3328)

Le Provost (1991) identified $v|v|$ in the expression for quadratic friction (where $v = v(x,t)$ is the cross-sectionally averaged flow velocity) as the primary source of sextadiurnal deformation, and several field studies attribute the M_6 signal exclusively to bed friction (Snyder et al., 1979; Blanton et al., 2002). Qualitatively, if we assume that the values of $|v_{\text{ebb}}|$ and $|v_{\text{flood}}|$ are approximately equal, then $v|v|$ will achieve equal peak magnitudes during both the rising and the falling limbs. This leads to a symmetrical distortion of the M_2 signal that is mathematically characterized by the M_6 overtide. The analyses of Parker (1984, 1991) indicate that M_6 can also be produced by nonlinear interactions between M_2 and M_4 via the mass and momentum advection terms of the shallow water equations. However, modeling results from China's Daya Bay suggest that approximately 60% of M_6 energy is generated by quadratic friction (Song et al., 2016), and Orescanin et al. (2016) justify interpreting M_6 as a product of friction by stating that M_6 generation via interactions between M_2 and M_4 is "relatively small" in comparison.

3.2.3 RESEARCH EVALUATING TIDAL BEHAVIOR IN "LOOPING", MULTI-INLET SYSTEMS

Although several prior studies address tidal behavior in interconnected channels, we are unaware of any studies explicitly addressing how the interaction of multiple waveforms influences the behavior of shallow water overtides and thus the total waveform shape. For example, Waterhouse et al. (2011) modeled the propagation of diurnal and semidiurnal waveforms entering the Florida Intracoastal Waterway via separate inlets, but the study did not consider the behavior of high-frequency overtides. Warner et al. (2003) used the relative magnitude of the terdiurnal and quarterdiurnal shallow water tidal species to identify the position of a bathymetric anomaly in a multi-inlet tidal marsh in the San Francisco Bay region; however, the paper does not examine how the bathymetrically-generated vertical tide deformation *differs* from what might be observed in a single-channel system with comparable bathymetric features. Similarly, Orescanin et al. (2016) quantified systematic changes in M_2, M_4, and M_6 for a two-inlet system near Martha's Vineyard, Massachusetts, but did not comment on how interactions between the two waveforms affect the shape of the vertical tidal signal. We build on these studies in this paper by evaluating how waveform interactions between connected channels may influence the shape of the total observed tidal signal.

3.3 Methods

3.3.1 FIELD MEASUREMENTS

The primary source of field data for this study is an array of 10 pressure sensors (an assortment of HOBO Loggers and Schlumberger CTD-Divers) deployed in the Polder 32 region of southwest Bangladesh from October 2017 through mid-March 2018. A map of the instrument locations is shown in Figure 3.3. All sites had a sampling interval of $\Delta t = 10$ minutes. As summarized in Table 3.1, five of the instruments were continuously submerged throughout the five month recording period. The remaining five instruments have maximum exposure periods ranging from 50 minutes (at Sutarkhali) to 5 hours (Kobadak at Paikgachha). As described in Section B.1.2 in Appendix A,

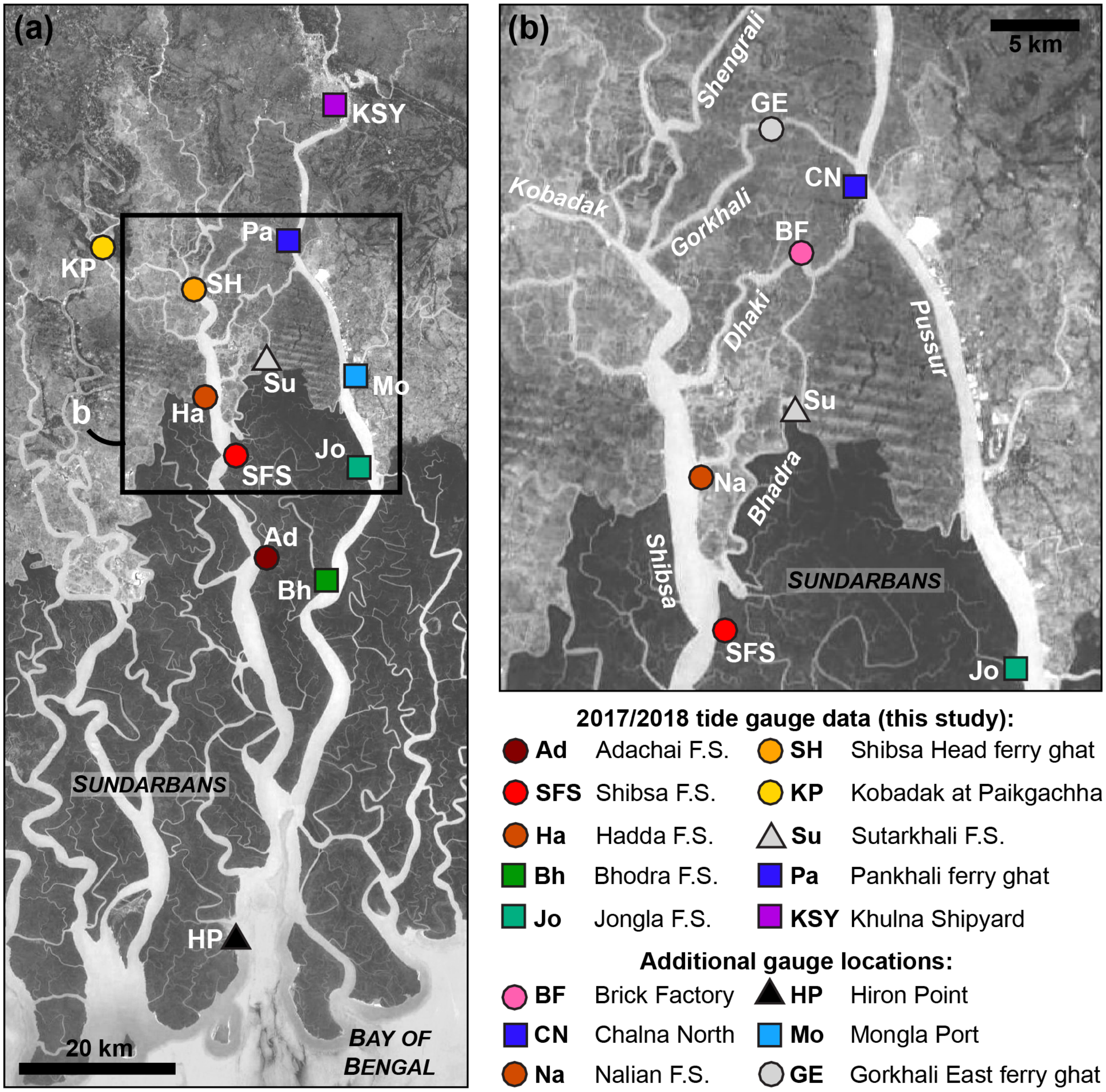

Figure 3.3: Satellite image of the study area, including instrument locations from **(a)** the 2017/2018 field study described in this chapter, and **(b)** the August/September 2015 study detailed in Hale et al. (2019a) and Bain et al. (2019). We also indicate the location of the BIWTA gauges at Hiron Point and Mongla.

we applied a spline to interpolate across these data gaps and estimate the missing values. Measured pressure was then converted to water depth using a spatially averaged but time-varying trend in measured salinity and water temperature (see Section B.1.1).

We supplement our datasets with long-term tidal records from the Bangladesh Inland Water Transport Authority (BIWTA) recording stations at Hiron Point and Mongla. These data span the years 1977 through 2010 and have a target recording interval of $\Delta t = 1$ hour. However, the data quality is variable, and both datasets have spans of missing measurements and occasional "spikes" in water level where it appears that the elevation was incorrectly recorded or transcribed. We carefully examined each dataset and deleted any corrupted values before proceeding with further analysis. Additionally, remounting or replacement of the measurement apparatus results in several abrupt datum shifts in each record (Pethick and Orford, 2013). In this chapter, we limit our analysis to the last year of data (2010) to avoid the influence of datum shifts in the long-term record.

3.3.2 DEFINITION OF VERTICAL DATUMS

All ten instruments deployed in 2017-2018 were surveyed to an absolute vertical datum via GPS and are suitable for analyzing regional water surface gradients. However, as the present study evaluates local variation in waveform shape and amplitude, we here quantify waveform shape relative to local mean water level (MWL). To compensate for the region's strongly seasonal climate and the monsoonal setup in water surface elevation, we define local MWL as a sinusoid with 1-year periodicity:

$$z_{\text{MWL}}(x,t) = \bar{z}_a(x) + A_a(x)\cos\left(\omega_a t - \phi_a(x)\right) \tag{3.3}$$

where $\bar{z}_a$ is the mean water level for a one-year averaging window, $\omega_a = {}^{360^\circ}/_{365.25\,\text{days}}$ is the angular frequency, and A_a and ϕ_a are the magnitude and phase of seasonal water level variations. The subscript a denotes that the parameters are associated with an annual periodicity to avoid confusion with the amplitude and phase of higher-frequency tidal oscillations. For each site, we determined best-fit values of the three parameters using nonlinear least-squares curve fitting in

Table 3.1: Summary of instrument locations for measuring water surface elevation.

Site	**Coordinates**	**Site description**	**Maximum exposure time**
Adachai F.S.	22.263821°N 89.494134°E	Instrument mounted on rebar in the small creek southeast of the forest station building.	—*
Bhodra F.S.	22.242186°N 89.572091°E	Mounted on rebar in the Bhodra channel 200 m north of the forest station's bamboo dock.	—
Hadda F.S.	22.455658°N 89.415041°E	Mounted with hose clamps on the concrete navigation pillar along the north bank of the mangrove creek, just west of the mainstem Shibsa.	—
Kobadak at Paikgachha	22.618353°N 89.289639°E	Mounted with hose clamps on the concrete piling under the bridge near the east bank.	5 hr
Khulna Shipyard	22.792471°N 89.581559°E	Mounted on the shipyard dock on the west bank of the mainstem Pussur River.	2.67 hr
Jongla F.S.	22.368871°N 89.615369°E	Mounted on rebar along the south bank of the mangrove creek, due south of the forest station dock.	—
Pankhali ferry ghat	22.631539°N 89.514927°E	Instrument mounted on rebar underneath the floating walkway on the north bank of the Gorkhali River.	—
Shibsa F.S.	22.384533°N 89.449678°E	Instrument mounted on rebar in the middle of the mangrove creek northeast of the forest station's bamboo dock.	—
Shibsa Head ferry ghat	22.478234°N 89.405023°E	Instrument mounted on rebar near the northeast corner of the concrete dock/walkway at the south bank of the Gorkhali channel.	4.67 hr
Sutarkhali F.S.	22.499185°N 89.489243°E	Instrument mounted on rebar near the pilings supporting the forest station pavilion on the north bank of the Bhadra River.	50 min

*Instrument was continuously submerged, but a sill at the creek mouth resulted in the instrument being cut off from the mainstem Shibsa channel at low water during low tides. We compensated for this by truncating the lowest meter of data and reconstructing it with a spline, using the same methodology as the other stations with missing data.

MATLAB. Subtracting the fitted values of $z_{\text{MWL}}(x,t)$ from the measured water surface elevation $z(x,t)$ detrends the dataset in preparation for tidal constituent analysis.

Prior research indicates a strong correlation between mean high water (MHW) and the intertidal platform elevation in the Sundarbans (Auerbach et al., 2015). Although several years of tide data would be necessary to accurately determine MHW, we here use the average high water elevation over the five-month recording period as an estimate of the local platform elevation. Deviations from MHW then approximate the local platform inundation depth Δz_{plat} for a given semidiurnal oscillation:

$$\Delta z_{\text{plat}} \approx z_{\text{HW}} - z_{\text{MHW}} \quad ; \tag{3.4}$$

notice that $\Delta z_{\text{plat}} = D^\star - \Delta z^\star_{\text{high}}$ using the terminology of the previous chapter (see Figure 2.2). The calculation of MHW is applied to the raw (non-detrended) elevation time series and includes high water values from both spring and neap tides.

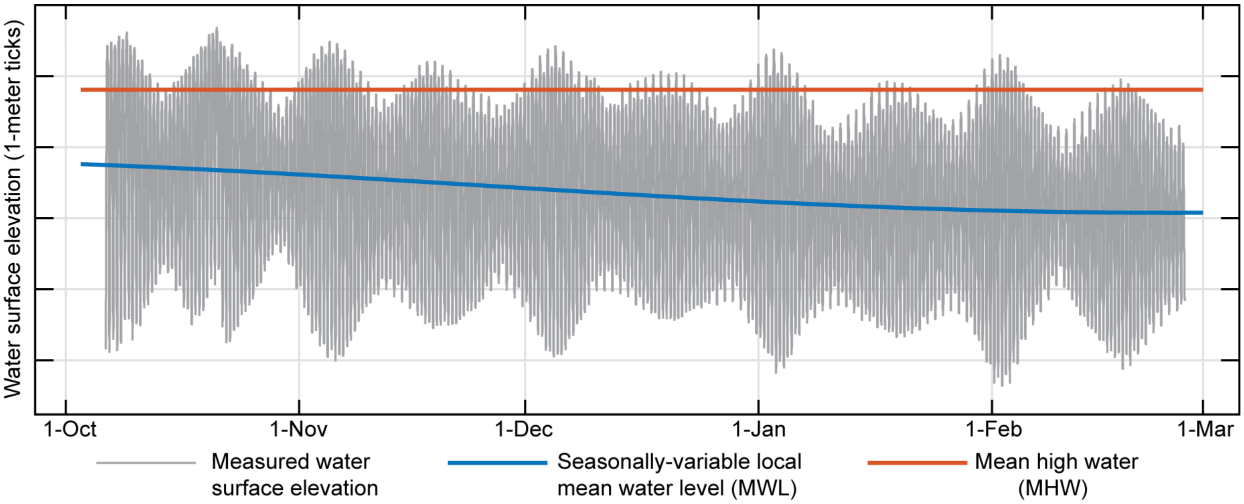

Figure 3.4: Example of MHW and seasonally-varying MWL for the 2017-2018 tidal elevation record from Hadda. MHW is a horizontal line approximating the platform inundation depth, whereas seasonal MWL is a sinusoid with one-year periodicity.

3.3.3 ANALYTICAL METHODS

3.3.3.1 Quantifying time-averaged tidal behavior

Standard methods of tidal analysis characterize a tidal signal according to the local amplitude A and phase ϕ of n unique tidal constituents, such that

$$z(x,t) - z_{\text{MWL}}(x,t) = \sum_{i=1}^{n} A_i(x) \cos\left(\omega_i t - \phi_i(x)\right) \quad , \tag{3.5}$$

where $\omega_i = {}^{360^\circ}\!/_{T_i}$ is the angular frequency of the i^{th} tidal constituent, with $\omega_i = \omega_j \iff i = j$. Unlike Fourier methods, in which the total signal is represented as a sum of mutually orthogonal sinusoids[1], tidal analysis algorithms assign the underlying frequencies based on known astronomical periods. Although theoretically n may exceed 500 (Foreman and Neufeld, 1991), in practice the Rayleigh criterion[2] limits n to a much smaller subset of this value (*e.g.*, Godin, 1972). We performed these calculations by applying the `UTide` MATLAB package (Codiga, 2011) to each detrended elevation time series, using the default settings of automated decision tree constituent selection (Foreman, 1977) and robust iteratively reweighted least squares curve fitting (Leffler and Jay, 2009).

Analytical uncertainty is minimized for long datasets because it prevents spectral leakage between constituents of similar frequency (*e.g.*, Zhang et al., 2019). However, given the strong seasonality of our study area (Hale et al., 2019a,b), we anticipate non-negligible seasonal modulation of constituent phase and amplitude (Müller et al., 2012; Gräwe et al., 2014; Müller et al., 2014). Therefore, in addition to analyzing the full five-month time series, we also applied the `UTide` analysis to 30-day windows of data. These are sufficiently long to separate the M_2 and S_2 astronomical constituents while also allowing us to quantify variable tidal behavior under monsoon and dry flow conditions. The values of A_i and ϕ_i calculated by this method represent average constituent amplitude and phase within the 30-day window, which spans two spring-neap cycles.

---

[1] That is, the angular frequencies used in the analysis are set by the total series length N and sampling interval Δt, with $\omega_m = 2m\pi(N\Delta t)^{-1}$ for $m = 1, 2, 3, \ldots, {}^{N}\!/_{2}$ assuming N is even.

[2] The Rayleigh criterion states that two tidal constituents of frequency σ_1 and σ_2 may be extracted from a time series of length N and sampling interval Δt only if $N \cdot \Delta t |\sigma_1 - \sigma_2| \geq 1$.

3.3.3.2 Analyzing high-frequency variability in waveform shape

A major goal of this study is to quantify the effects of platform inundation and multi-wave interactions on tidal waveform deformation. Whereas seasonal patterns of circulation and river discharge change slowly enough to be characterized by the method described in the previous paragraph, platform inundation depths vary between consecutive high waters due to a small yet significant diurnal signal (*e.g.*, Krien et al., 2016, report diurnal amplitudes of $A_{\mathrm{K1}} = 0.13$ meters and $A_{\mathrm{O1}} = 0.05$ meters at Hiron Point, in comparison to semidiurnal amplitudes of $A_{\mathrm{M2}} = 0.81$ meters and $A_{\mathrm{S2}} = 0.34$ meters). Moreover, visual examination of the datasets indicates that short-term meteorological events influence tidal elevations by several tens of centimeters. To isolate this type of high-frequency variability, several earlier studies propose the use of a continuous wavelet transform (CWT) for analyzing nonstationary tidal records (Flinchem and Jay, 2000; Guo et al., 2015). However, wavelet methods do not easily handle irregularly sampled datasets, which precludes CWT analysis of the 2017-2018 records from Shibsa Head, Paikgachha, and Khulna unless they are first interpolated using another method.

As a substitute for the CWT, we divided the datasets into semidiurnal windows bounded by the rising limb inflection points of the detrended time series $z - z_{\mathrm{MWL}}$ (Figure 3.5a). We then used nonlinear least squares in MATLAB to fit a curve of the form

$$z_{\text{window}} = \bar{z}_{\text{window}} + \sum_{n=2,4,6} A_n \cos\left(\frac{n\omega_2 t}{2} - \phi_n\right) \quad , \tag{3.6}$$

where ω_2 is inversely proportional to the window length ($26.7^\circ\,\mathrm{hr}^{-1} \leq \omega_2 \leq 30.9^\circ\,\mathrm{hr}^{-1}$, depending on the timespan between inflection points for any particular window). The fitted parameters A_n and ϕ_n represent the amplitudes and phases of the combined semidiurnal, quarterdiurnal, and sextadiurnal tidal *species* rather than the isolated M_2, M_4, and M_6 constituents (*c.f.* Giese and Jay, 1989; Shetye et al., 1995; Chatterjee et al., 2013; Guo et al., 2015). For example, A_2 contains energy from a band of semidiurnal frequencies including the M_2, S_2, and N_2 astronomical forcings. Results produced by this method must therefore be interpreted as the behavior of the total semidiurnal waveform, which is similar but not identical to the behavior of the M_2 constituent. Although this is not a standard method of tidal analysis, we note that Lessa (2000) used a comparable procedure to examine the influence of tidal range on the behavior of individual tidal oscillations.

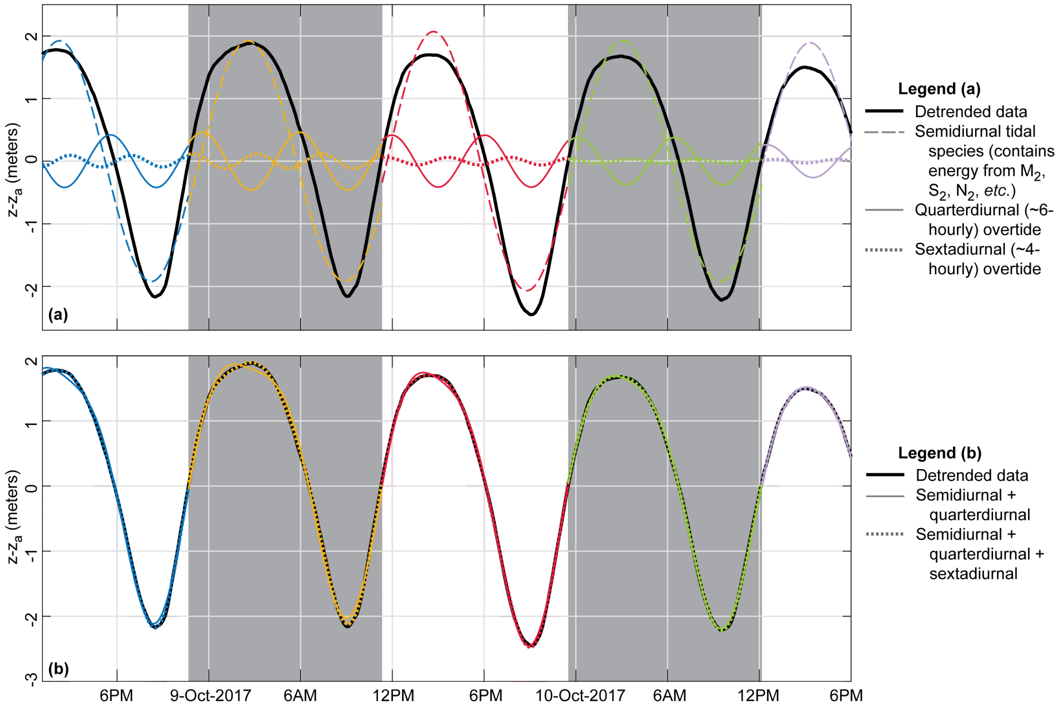

Figure 3.5: Method for analyzing the shape of individual semidiurnal waveforms. **(a)** We first separate the time series into semidiurnal windows separated by the rising limb inflection points, with the individual windows corresponding to the alternating shaded regions in the figure. We then use nonlinear least squares to fit a curve in the form of Equation 3.6, which provides the amplitude and phase of the semidiurnal, quarterdiurnal, and sextadiurnal tidal species. These approximate (but are not identical to) the M_2, M_4, and M_6 tidal constituents and are plotted respectively as dashed, solid, and dotted lines. **(b)** Example of the algorithm's ability to reconstruct the original time series by summing the colored curves from subplot (a).

3.4 Results and preliminary interpretation

3.4.1 DOMINANT TIDAL CONSTITUENTS IN THE STUDY AREA

Table 3.2 displays the amplitude and phase of major vertical tidal constituents over the five-month period from October 2017 through February 2018. For comparison, we include the corresponding Hiron Point values for calendar year 2010, after which the BIWTA dataset terminates[3].

---

[3] After the text of this chapter was written, we received additional data extending the record through 2015. Those data are included in Chapter 4.

The M_2 tide dominates the tidal signal at all sites, followed by S_2, with A_{S2}/A_{M2} ranging between 36% at Khulna and 43% at Hiron Point. Among the quarterdiurnal constituents, M_4 and MS_4 are nearly equal in amplitude; moreover, $2MS_6$ is approximately twice as large as M_6 at all sites except Hiron Point.

The results in Table 3.2 reflect the variability in the waveform shape over short (< 1 week) timescales. Geometrically, the summation of M_4 and the compound tides MS_4 produces a total quarterdiurnal signal which varies in amplitude between spring and neap tides. Similarly, summing M_6 and $2MS_6$ produces a total sextadiurnal signal with time-varying amplitude. The paper by van Rijn (2010, p. 54) attributes high-frequency compound tide generation to variations in waveform celerity as M_2 and S_2 move in and out of phase. During spring tides, the difference in celerity between crest and trough is maximized, and the waveform deformation will be greater than during neap tides. In Section 3.4.3 below, we will present additional results suggesting that intertidal platform inundation further enhances spring tide shallow water deformation and generates compound tides of such significant amplitude.

3.4.2 SEASONAL VARIABILITY OF TIDAL BEHAVIOR

Along-channel trends in propagation, amplification, and deformation vary seasonally, and there are notable differences in the wave's behavior in the Shibsa versus the Pussur. Figure 3.6(a) shows that M_2 amplifies for approximately 80 km inland from Hiron Point along the Shibsa and 100 km along the Pussur. However, the amplification magnitude is greater in the Shibsa; during the monsoon season, A_{M2} increases by 69% between Hiron Point and Shibsa Head, in comparison to a 55% increase in A_{M2} between Hiron Point and Pankhali. Although the pattern of along-channel M_2 amplification is not greatly affected by the monsoon-to-dry transition, there are seasonal changes in M_2 phase (Figure 3.6b). Monsoon season propagation rates exceed dry season propagation rates in both channels, with the Pussur displaying greater seasonal variation in celerity. This is consistent with prior observations of the Pussur's enhanced monsoon-season setup in mean water level (Shaha and Cho, 2016).

The higher-frequency overtides and compound tides also amplify with distance upchannel, often with pronounced seasonal differences. During the monsoon season, $\mathcal{R}_{2,4}$ increases at nearly the same rate in the Shibsa and the Pussur over the first ~ 45 kilometers from Hiron Point. The metrics $\mathcal{R}_{2,6}$ and $\Delta\phi_{2,6}$ display minimal variation over this reach, but $\Delta\phi_{2,4}$ increases substantially in both channels from a value of 80° at Hiron Point to 170° at Adachai and 150° at Bhodra. Upstream of Adachai/Bhodra, the Shibsa and Pussur channels have contrasting patterns of shallow water deformation. The Pussur displays a continuous increase in $\mathcal{R}_{2,4}$ and a continuous decrease in $\Delta\phi_{2,4}$, which indicates enhanced flood asymmetry with distance upstream. $\mathcal{R}_{2,6}$ and $\Delta\phi_{2,6}$ also vary monotonically in the Pussur above Bhodra. In the Shibsa, however, $\mathcal{R}_{2,4}$ and $\mathcal{R}_{2,6}$ both *decrease* slightly between Adachai and Hadda F.S., indicating a local decrease in total shallow-water deformation over this 24-kilometer reach. $\Delta\phi_{2,4}$ plateaus between these gauges, and there is also little variation in $\Delta\phi_{2,6}$.

During the dry season, these channel-specific patterns of waveform deformation persist, with the Shibsa and the Pussur displaying comparable values of $\mathcal{R}_{2,4}$ and $\Delta\phi_{2,4}$ over the first ~ 45 kilometers upstream of Hiron Point before diverging at Adachai/Bhodra. There are three primary differences between the monsoon season and the dry season deformation trends. First, the dry-season value of $\mathcal{R}_{2,4}$ is lower at all stations, which suggests that monsoon-season conditions enhance the magnitude of shallow-water deformation. Second, whereas $\Delta\phi_{2,6}$ displays little variation along the Shibsa during the monsoon season, during the dry season $\Delta\phi_{2,6}$ decreases from 130° at Hiron Point to 30° at Hadda. Geometrically, this indicates a steepening of both the rising and falling limbs as the waveform propagates inland. The final major difference between the monsoon and dry season profiles is that the dry-season value of $\Delta\phi_{2,4}^{(\mathrm{HP})}$ is $\sim 160°$ at Hiron Point, in contrast to its monsoon-season value of $\sim 80°$. The former corresponds to a flood-asymmetric tide with its crest broader than its trough, whereas the latter indicates a flood-asymmetric tide with its trough broader than its crest. However, because $\mathcal{R}_{2,4}^{(\mathrm{HP})}$ is close to zero, this seasonal phase variation has minimal impact on the total waveform shape, and we do not consider it further in this chapter.

Table 3.2: Amplitude A (in centimeters) and Greenwich phase ϕ (in degrees) of selected vertical tidal constituents. With the exception of Hiron Point, values in this table represent time-averaged values of A and ϕ over the 5-month recording period from October 2017 through March 2018. The tidal signal for the i^{th} constituent is $z_i(t) = A_i \cos(\omega_i t - \phi_i)$, where t is given in GMT and $\omega_i = {}^{360^\circ}\!/_{T_i}$ is the angular frequency.

		Tidal constituent (period T in hours)						
		K_1 (23.93)	**O_1 (25.82)**	**M_2 (12.42)**	**S_2 (12)**	**N_2 (12.66)**	**M_4 (6.21)**	**MS_4 (6.1)**
Hiron Point[*]	$A \pm 2\sigma_A$	13.4±0.1	5.4±0.1	84.9±0.5	36.3±0.5	16.8±0.5	1.6±0.1	1.6±0.1
	$\phi \pm 2\sigma_\phi$	279±1	273±1	157±1	192±1	147±2	188±4	233±4
Adachai[†]	$A \pm 2\sigma_A$	18.6±0.5	6.5±0.5	125.0±1.0	46.1±1.2	27.1±1.0	8.6±0.4	8.2±0.4
	$\phi \pm 2\sigma_\phi$	281±2	273±4	172±1	215±1	163±3	183±3	215±3
Shibsa F.S.	$A \pm 2\sigma_A$	19.2±0.6	7.0±0.6	138.5±1.0	51.7±1.4	29.8±1.3	8.8±0.4	8.7±0.4
	$\phi \pm 2\sigma_\phi$	284±2	276±6	181±1	225±1	172±2	198±3	229±3
Hadda	$A \pm 2\sigma_A$	19.4±0.5	7.0±0.6	143.2±1.5	53.6±1.3	31.0±1.3	8.9±0.4	8.8±0.5
	$\phi \pm 2\sigma_\phi$	286±2	278±5	186±1	230±1	176±2	212±3	244±3
Shibsa Head[†]	$A \pm 2\sigma_A$	19.2±0.6	7.2±0.6	149.0±3.1	55.2±2.4	31.5±1.6	10.6±1.7	10.1±1.6
	$\phi \pm 2\sigma_\phi$	291±2	282±4	196±1	241±2	185±3	256±10	288±13
Paikgachha[†]	$A \pm 2\sigma_A$	18.1±0.6	6.7±0.7	138.3±3.7	50.6±3.1	29.2±2.2	13.2±1.8	11.7±1.8
	$\phi \pm 2\sigma_\phi$	302±2	297±4	207±1	254±2	196±3	291±18	328±20
Bhodra	$A \pm 2\sigma_A$	18.2±0.5	6.1±0.4	120.2±1.0	44.3±1.2	26.1±1.3	8.8±0.3	8.3±0.3
	$\phi \pm 2\sigma_\phi$	282±2	275±5	176±1	217±2	166±2	202±3	238±3
Jongla	$A \pm 2\sigma_A$	18.4±0.5	6.4±0.5	128.6±1.3	47.1±1.1	27.6±1.3	10.7±0.5	10.0±0.5
	$\phi \pm 2\sigma_\phi$	289±1	281±4	188±1	232±1	178±2	242±3	278±3
Pankhali	$A \pm 2\sigma_A$	17.7±0.5	6.6±0.5	134.7±1.3	48.9±1.6	28.4±1.3	13.9±0.5	11.8±0.6
	$\phi \pm 2\sigma_\phi$	300±2	287±5	211±1	256±2	199±3	313±2	347±2
Khulna[†]	$A \pm 2\sigma_A$	16.4±0.3	5.8±0.4	127.0±1.5	46.2±1.3	26.2±1.3	16.6±0.5	13.4±0.5
	$\phi \pm 2\sigma_\phi$	311±1	297±5	229±1	277±2	214±3	3±2	42±2
Sutarkhali	$A \pm 2\sigma_A$	19.1±0.4	7.0±0.5	143.8±1.3	53.7±1.1	30.5±1.1	8.5±0.4	8.2±0.5
	$\phi \pm 2\sigma_\phi$	293±2	284±4	196±1	242±1	186±3	245±3	278±3

		Tidal constituent (period T in hours)					
		MN_4 (6.27)	**S_4 (6)**	**SN_4 (6.16)**	**$2MS_6$ (4.09)**	**$2MN_6$ (4.17)**	**M_6 (4.14)**
Hiron Point[*]	$A \pm 2\sigma_A$	0.6±0.1	0.7±0.1	0.5±0.1	0.6±0.1	0.9±0.1	1.45±0.1
	$\phi \pm 2\sigma_\phi$	178±10	286±10	221±10	280±9	171±5	187±4
Adachai[†]	$A \pm 2\sigma_A$	4.4±0.4	1.9±0.4	1.8±0.4	1.6±0.2	0.8±0.2	0.8±0.2
	$\phi \pm 2\sigma_\phi$	170±5	263±13	225±13	299±7	241±12	272±11
Shibsa F.S.	$A \pm 2\sigma_A$	4.6±0.5	2.4±0.4	2.2±0.4	2.1±0.2	1.2±0.2	1.1±0.2
	$\phi \pm 2\sigma_\phi$	190±5	279±10	241±10	335±5	273±8	304±10
Hadda	$A \pm 2\sigma_A$	4.7±0.4	2.7±0.4	2.3±0.4	1.9±0.2	1.3±0.2	1.0±0.2
	$\phi \pm 2\sigma_\phi$	203±6	294±10	255±9	358±6	290±8	324±13
Shibsa Head[†]	$A \pm 2\sigma_A$	5.4±1.0	3.1±0.8	2.4±0.8	3.6±2.2	1.8±0.8	2.0±1.8
	$\phi \pm 2\sigma_\phi$	243±10	330±14	298±18	32±52	321±57	353±65
Paikgachha[†]	$A \pm 2\sigma_A$	6.5±1.3	3.2±1.0	2.5±1.1	4.2±2.6	2.5±1.0	2.4±2.0
	$\phi \pm 2\sigma_\phi$	279±14	364±23	318±14	27±82	319±86	334±102
Bhodra	$A \pm 2\sigma_A$	4.4±0.4	2.0±0.4	1.7±0.4	2.4±0.2	1.2±0.2	1.5±0.2
	$\phi \pm 2\sigma_\phi$	188±5	286±10	253±13	245±5	195±9	201±9
Jongla	$A \pm 2\sigma_A$	5.4±0.4	2.6±0.5	2.4±0.5	3.0±0.3	1.7±0.2	1.8±0.2
	$\phi \pm 2\sigma_\phi$	228±5	322±10	287±12	328±4	271±9	286±7
Pankhali	$A \pm 2\sigma_A$	6.9±0.5	3.2±0.4	2.8±0.5	5.5±0.4	2.6±0.4	3.2±0.5
	$\phi \pm 2\sigma_\phi$	298±4	14±10	338±9	77±4	7±11	35±8
Khulna[†]	$A \pm 2\sigma_A$	7.9±0.5	3.1±0.5	2.5±0.5	7.4±0.6	3.8±0.5	4.6±0.5
	$\phi \pm 2\sigma_\phi$	342±3	69±9	8±10	143±4	71±7	100±6
Sutarkhali	$A \pm 2\sigma_A$	4.5±0.5	2.8±0.4	2.3±0.5	2.6±0.2	1.4±0.2	1.2±0.2
	$\phi \pm 2\sigma_\phi$	236±6	328±9	294±10	10±5	305±10	333±10

[*] BIWTA data from 1-Jan-2010 through 31-Dec-2010.

[†] At this site, all constituents' values of A, ϕ, and 2σ have been corrected to account for the effects of spline interpolation. See Section B.1.2 for details.

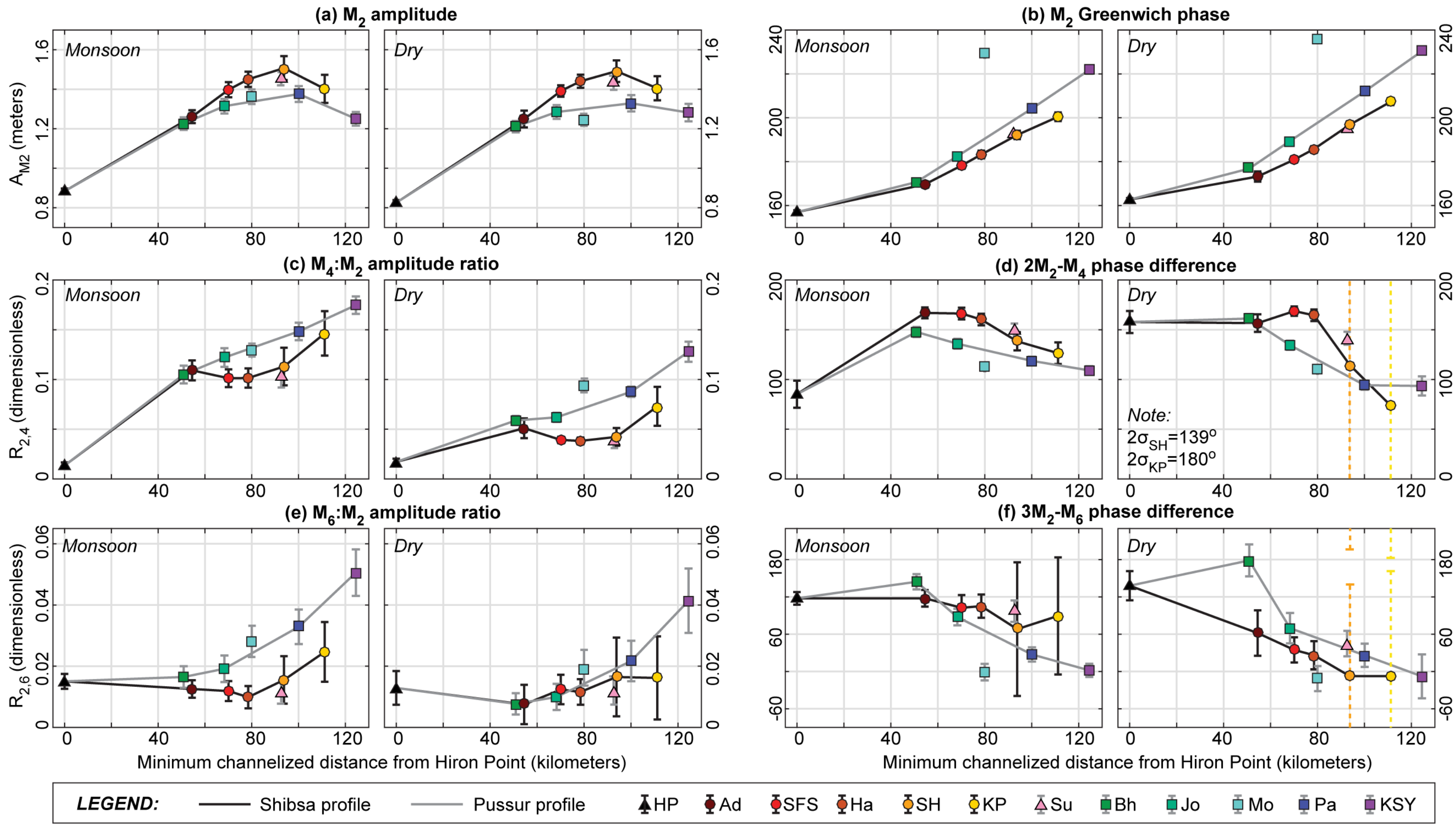

Figure 3.6: Seasonal patterns of waveform propagation, amplification, and deformation in the Shibsa and Pussur channels under monsoon (11-Oct-2017 through 10-Nov-2017) and dry season (29-Jan-2018 through 28-Feb-2018) flow conditions. For comparison, we include values for Hiron Point and Mongla calculated from the BIWTA datasets (11-Oct-2009 through 10-Nov-2009 for the monsoon season; 29-Jan-2010 through 28-Feb-2010 for the dry season). However, the Mongla values are not included in the Pussur profile line. Note that all values from Adachai (Ad), Shibsa Head (SH), Paikgachha (KP), and Khulna (KSY) have been corrected to account for systematic errors associated with spline interpolation (Section B.1.2). Profiles of additional constituents beyond M_2, M_4, and M_6 are shown in Figure B.9.

3.4.3 EFFECT OF PLATFORM INUNDATION ON WAVEFORM SHAPE

The waveform deformation patterns described in Section 3.4.2 represent average tidal behavior over 30-day periods, which encompass approximately two spring-neap cycles. However, visual examination of the time series $z(x,t)$ indicates a strong variability in the shape of the waveform between spring and neap tides. This is mathematically characterized by the large amplitudes of the MS_4 and $2MS_6$ compound tides (see Section 3.4.1). To more intuitively demonstrate the influence of platform inundation on waveform asymmetry, we characterized the shape of each individual semidiurnal oscillation using the method described in Section 3.3.3.2. It is important to note that we cannot fully separate the effect of platform inundation versus the effect of time-variable celerity on waveform deformation. This is because both the highest high waters and the lowest low waters occur during spring tides[4], so the waveforms with the greatest difference in celerity between crest and trough are also the oscillations with the greatest platform inundation depths. However, considering the relative strength of correlations between the platform inundation depth (Δz_{plat}; Equation 3.4), tidal range, and the deformation metrics provides insight into the conditions under which each physical effect dominates.

All eight sites display a strong positive correlation between Δz_{plat} and the deformation magnitude $\mathcal{R}_{2,4}$ during spring tides (*i.e.*, values of $\Delta z_{\text{plat}} > 0$ meters in Figure 3.7a). At the most extreme inundation depths, $\mathcal{R}_{2,4}$ exceeds 0.2 at all Shibsa stations and 0.3 at the northernmost Pussur stations, substantially exceeding the time-averaged values displayed in Figure 3.6. When the intertidal platform does not inundate ($\Delta z_{\text{plat}} < 0$ meters), $\mathcal{R}_{2,4}$ maintains a near-constant value regardless of Δz_{plat} at most measurement locations. The metrics $\mathcal{R}_{2,6}$ and $\Delta\phi_{2,6}$ display a similarly threshold-dependent behavior at most locations (Figures 3.7c and 3.7d), although the precise value of the threshold in Δz_{plat} is shifted rightwards relative to the graphs of $\mathcal{R}_{2,4}$. The only deformation metric lacking an obvious threshold in Δz_{plat} is $\Delta\phi_{2,4}$, with the possible exception of measurements from Bhodra and Jongla for $\Delta z_{\text{plat}} > 0.5$ meters (Figure 3.7b).

---

[4] This is not true in, *e.g.*, the Amazon mouth region, where the highest high waters occur during spring tides, but the lowest low waters occur during neap tides. See Gallo and Vinzon (2005).

In comparison, although the scatterplots in Figure 3.8 are broadly similar in shape to the plots in Figure 3.7, the correlations between tidal range and each of $\mathcal{R}_{2,4}$, $\Delta\phi_{2,4}$, $\mathcal{R}_{2,6}$, and $\Delta\phi_{2,6}$ are weaker. For example, peak values of $\mathcal{R}_{2,4}$ occur at a tidal range of approximately 3.5 meters, whereas $\mathcal{R}_{2,4}$ is approximately half of its maximum value for the largest-range oscillations. It is interesting that correlation between $\mathcal{R}_{2,4}$ and $\Delta z_{\mathrm{plat}} < 0$ is stronger than the correlation between $\mathcal{R}_{2,4}$ and tidal range even for most stations within the poldered region, which are not in direct contact with the Sundarbans. This may be a consequence of inundation-driven deformation which is generated in the Sundarbans but then propagates upchannel into the polders (*c.f.* Nidzieko and Ralston, 2012; Toublanc et al., 2015, who describe an analogous process in which shallow water overtides are generated offshore and then propagate inland). Synthesizing these observations, we interpret the results of this section as follows: although tidal range influences shallow water deformation, inundation of the intertidal platform exerts a more significant control on waveform shape, even in the poldered region. In particular, the amplitude of the quarterdiurnal and sextadiurnal tidal species are strongly a function of the platform inundation depth.

3.5 Discussion

Summarizing these results in the context of the first research question posed in Section 3.2.1, our data indicate that intertidal platform inundation exerts a strong control on tidal waveform dynamics in the study area. This is further modulated by changing seasonal conditions, as wind stresses in the Bay of Bengal (Allison and Kepple, 2001) and nonlinear interactions between opposing tidal and river discharge (see Cai et al., 2016) drive a setup in mean water level (Shaha and Cho, 2016) that increases the platform inundation depth. The seasonal influence is enhanced along the Pussur relative to the Shibsa, as evidenced by the greater monsoon-versus-dry season variability in M_2 propagation rates (Figure 3.6b). This may be due to the Pussur's conveyance of virtually all Gorai River discharge under spring tide flow conditions (Bain et al., 2019).

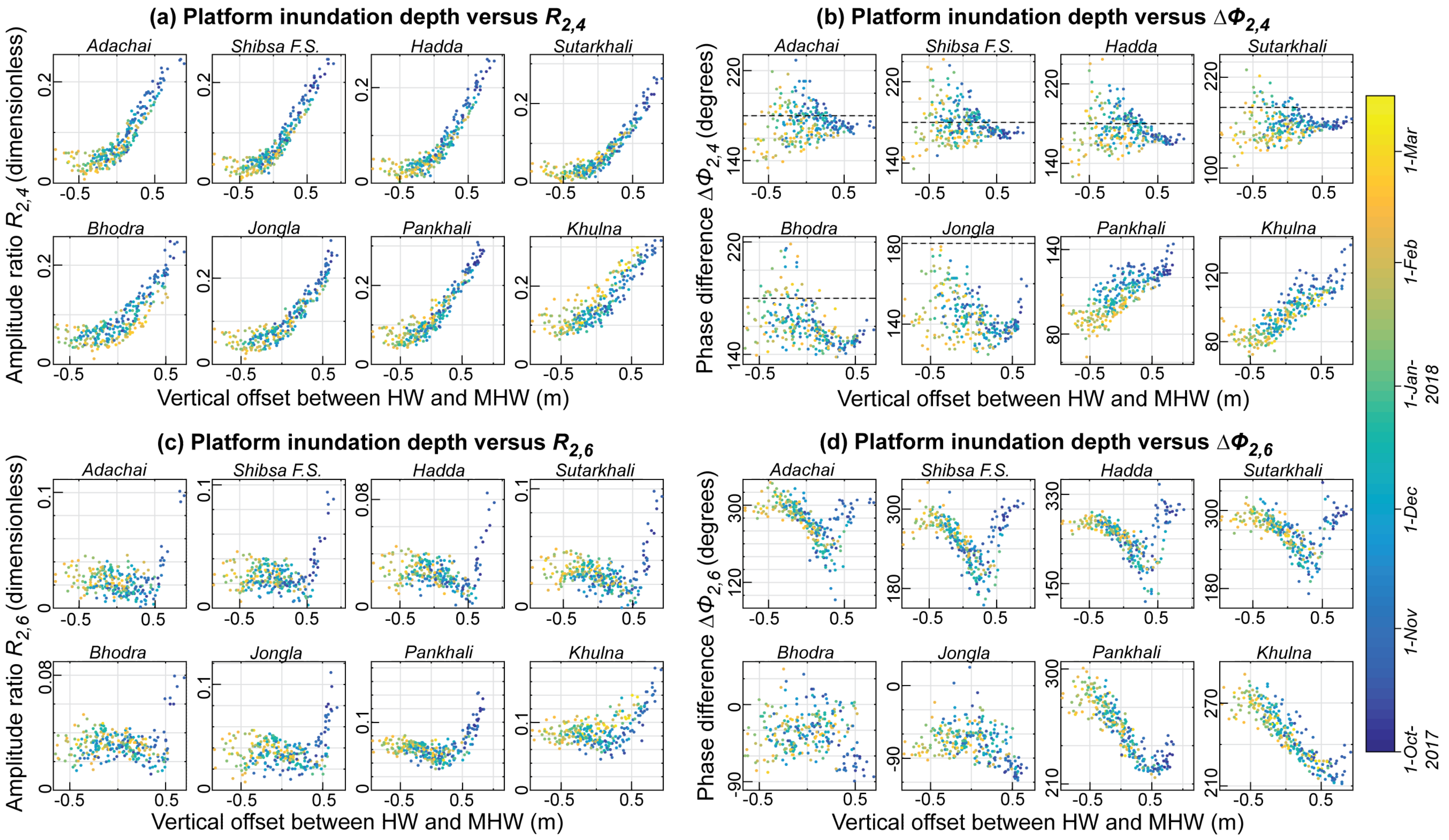

Figure 3.7: Scatterplots showing the relationship between platform inundation depth and waveform deformation. Note that we do not include results from the Shibsa Head or Paikgachha pressure sensors in this figure because we lack a robust method for estimating the deformation parameters of individual oscillations with five to six hours of missing data.

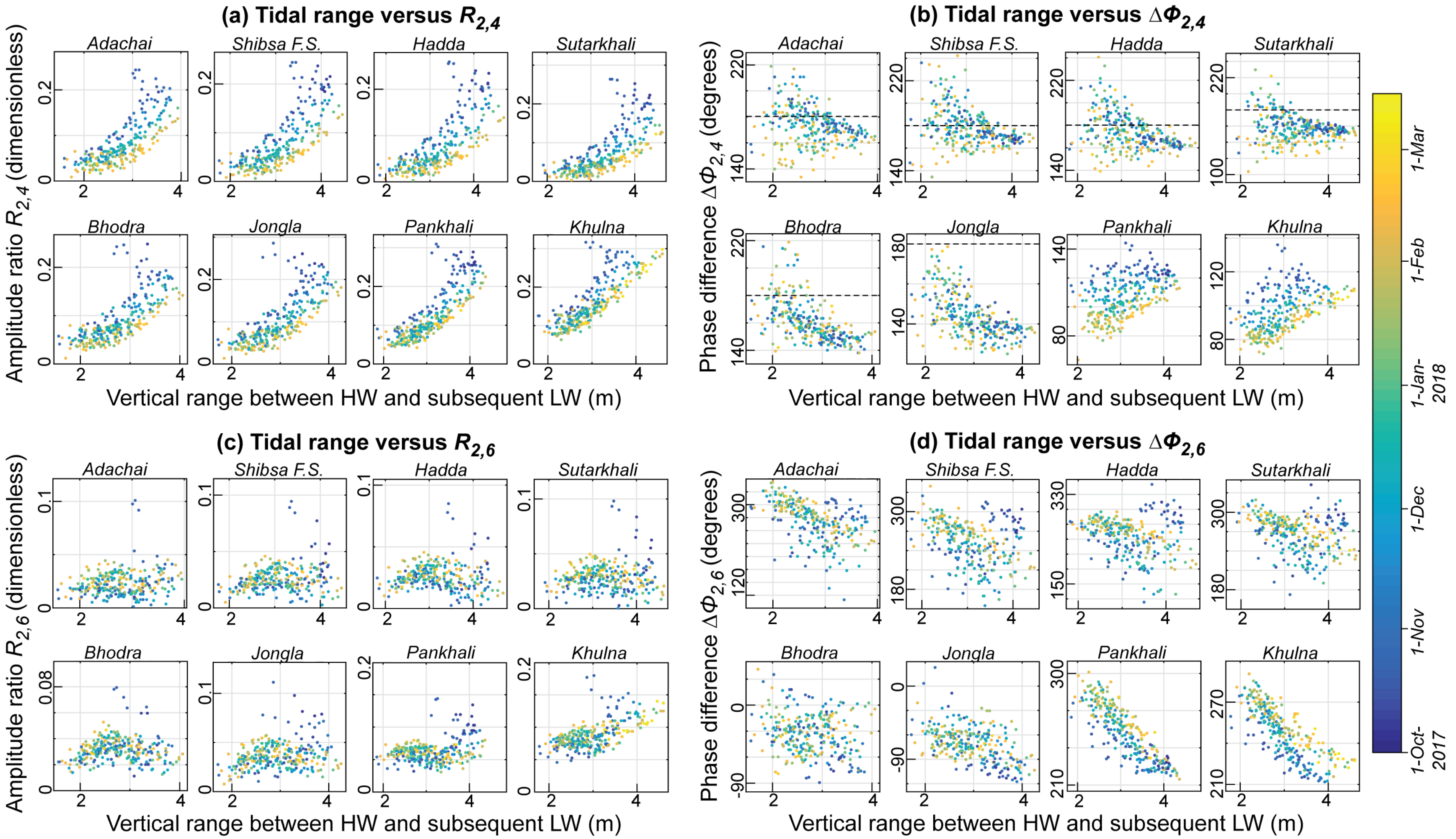

Figure 3.8: Scatterplots showing the relationship between tidal range and waveform deformation.

The dry-season reduction in $\mathcal{R}_{2,4}$ along both channels (Figure 3.6c) could theoretically be attributed to the absence of river discharge. Modeling results from Gallo and Vinzon (2005) suggest that in the absence of river discharge, $\mathcal{R}_{2,4}$ would be reduced along the entire Amazon River–by nearly a factor of 4 in some locations. However, results from the same study suggest that $\Delta\phi_{2,4}$ would maintain the same value in the Amazon Estuary even in the absence of river discharge. In contrast, our measurements indicate a non-negligible dry-season decrease in $\Delta\phi_{2,4}$ at the uppermost Pussur stations (Figure 3.6d), which is inconsistent with Gallo and Vinzon's (2005) findings. The data instead provide further support for the conclusion that shallow water deformation is strongly correlated with platform inundation depth (Figure 3.7).

3.5.1 WHAT ABOUT LOOPS?

The second question posed in Section 3.2.1 concerned the effect of waveform interactions between the two channels. The results described in Section 3.4 characterize the measured tidal signal as a sum of distinct astronomical constituents, each of which has a unique frequency. However, these analyses provide no information about waves of the *same* frequency arriving at a given pressure sensor via different routes. Taking the i^{th} constituent from Equation 3.5 as an example and assuming a simple linear superposition of the individual waves, the observed values of A_i and ϕ_i may be represented as

$$A_i(x)\cos(\omega_i t - \phi_i(x)) = \sum_{k=1}^{K} A_{i,k}(x)\cos\left(\omega_i t - \phi_{i,k}(x)\right) \quad , \tag{3.7}$$

with each index k representing a different route to the pressure sensor. If the values of $A_{i,k}$ and $\phi_{i,k}$ are known *a priori*, then calculating A_i and ϕ_i is a matter of straightforward trigonometry[5], with

$$[A_i(x)]^2 = \sum_{k=1}^{K}\sum_{j=1}^{K} A_{i,k}(x)A_{i,j}(x)\cos\left(\phi_{i,k}(x) - \phi_{i,j}(x)\right) \tag{3.8}$$

---

[5] The Wolfram Alpha website provides a good explanation of the application of trigonometric identities to sinusoid addition at `http://mathworld.wolfram.com/HarmonicAdditionTheorem.html`.

and

$$\tan\left(\phi_i(x)\right) = \frac{\sum_{k=1}^{K} A_{i,k}(x)\sin\left(\phi_{i,k}(x)\right)}{\sum_{k=1}^{K} A_{i,k}(x)\cos\left(\phi_{i,k}(x)\right)} \quad . \tag{3.9}$$

In contrast, the inverse problem of calculating values of $A_{i,k}$ and $\phi_{i,k}$ from observed values of A_i and ϕ_i is underdetermined (*i.e.*, two equations with $2K$ unknown variables) and lacks a unique solution. We here provide a kinematic description of waveform interaction to examine whether it is *possible* for our observations to be a product of interacting waves.

For the following analysis, we consider the propagation of dry season neap tides through the Shibsa-Pussur system. This eliminates the effect of Gorai River discharge on waveform deformation and greatly reduces the influence of intertidal storage, allowing us to isolate the effect of interacting waveforms on observed tidal behavior. Beginning with each non-detrended dataset z, we removed the spring tide measurements by deleting 12.5-hour windows of data centered on each peak exceeding MHW (Section 3.3.2). We then used `UTide` to recompute the apparent M_2, M_4, and M_6 phases and amplitudes from the remaining detrended measurements. The results of this analysis (Figure 3.9) indicate that although the deformation magnitude is reduced relative to the corresponding values with the spring tides included (Figure 3.6), the along-channel deformation patterns described in Sections 3.4.1 and 3.4.2 persist even when upstream river discharge and platform inundation are eliminated. In particular, the reduction in $\mathcal{R}_{2,4}$ between Adachai and Hadda is a persistent feature in both Figure 3.6 and Figure 3.9. In Sections 3.5.1.1 through 3.5.1.4, we test the hypothesis that these deformational patterns are are a consequence of interacting Shibsa and Pussur waveforms.

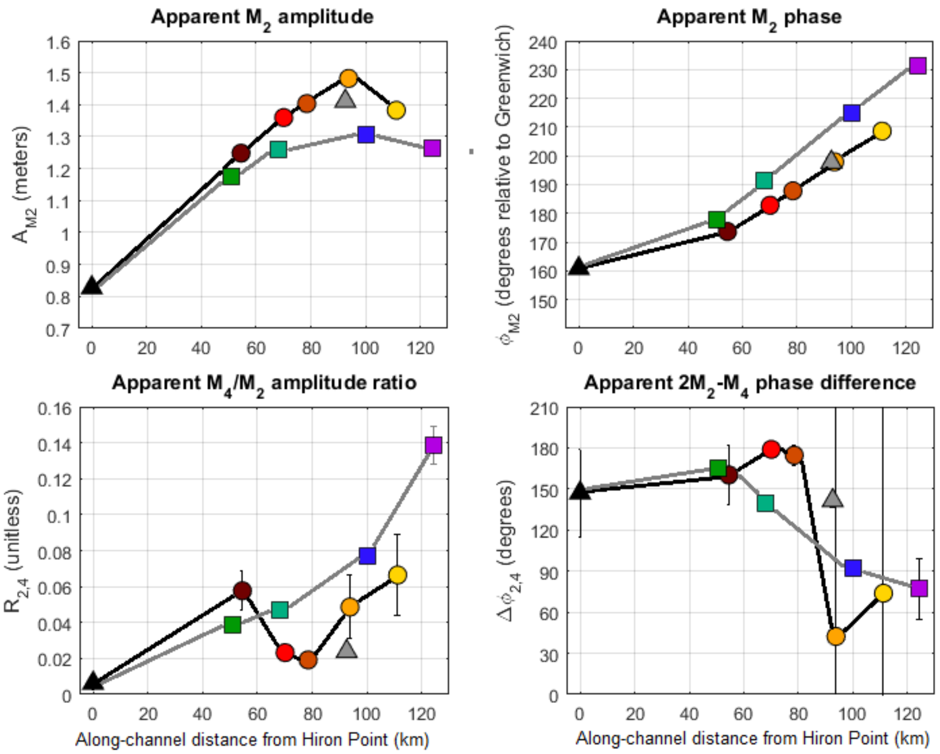

Figure 3.9: Apparent values of A_{M2}, ϕ_{M2}, $\mathcal{R}_{2,4}$, and $\Delta\phi_{2,4}$ when the `UTide` algorithm is run on the dry season neap tides only. We performed this analysis by deleting 12.5-hour windows of data centered on any peak higher than MHW, which is approximately equal to the platform elevation (see Section 3.3.2), to eliminate all spring tide data. We then recalculated the profiles from Figure 3.6 for all remaining neap measurements between 1-Dec-2017 and 1-Apr-2018.

Table 3.3: Definition of intrinsic coordinate systems for the Shibsa-Pussur channel network.

Loop description (beginning and ending at Hiron Point; x increases clockwise)	**Independent variable**	**Total loop length**
Shibsa → Dhaki → Pussur	x_d	$X_d = 200.3$ km
Shibsa → Bhadra → eastern Dhaki → Pussur	x_b	$X_b = 203.5$ km
Shibsa → Gorkhali → Pussur	x_g	$X_g = 211.0$ km
Shibsa → Shengrali → Pussur	x_s	$X_s = 242.7$ km

3.5.1.1 Conceptual model setup

To facilitate further discussion of waveform interactions in a looping channel network, we here define an intrinsic one-dimensional coordinate system for our study area. Taking the loop formed by the Shibsa, Dhaki, and Pussur Rivers, we set $x = 0$ and $x = X = 200.25$ km at Hiron Point, with the abscissa increasing clockwise. Analogous coordinate systems could be established for the Bhadra, Gorkhali, and Shengrali Rivers by substituting the values of X listed in Table 3.3.

We now consider the behavior of two waves traveling along x. A clockwise-traveling wave propagates into the system along characteristic curves satisfying

$$\frac{dx}{dt} = \sqrt{gh} \ , \tag{3.10}$$

where $h = h(x)$ is the tidally-averaged depth (as reported in Pethick, 2012). Along the characteristic originating at $(x = 0, t = \tau)$, the wave is defined by

$$z^{\circlearrowright}(x,t) = A_2^{\circlearrowright}(x) \cdot \cos\left[\omega_2 \tau - \phi_2^{\text{(HP)}}\right] + A_4^{\circlearrowright}(x) \cdot \cos\left[2\omega_2 \tau - \phi_4^{\circlearrowright}(x)\right] \ , \tag{3.11}$$

where $A_2^{\circlearrowright}$ and $A_4^{\circlearrowright}$ are functions describing the damping (or amplification) of a semidiurnal and quarterdiurnal tidal species with clockwise distance into the domain. The constant $\phi_2^{\text{(HP)}}$ is the phase of the semidiurnal species at Hiron Point, while $\phi_4^{\circlearrowright}$ is a function describing how the quarterdiurnal phase varies as the wave propagates clockwise. Similarly, a counterclockwise-traveling wave propagates along the curves satisfying

$$\frac{dx}{dt} = -\sqrt{gh} \tag{3.12}$$

with

$$z^{\circlearrowleft}(x,t) = A_2^{\circlearrowleft}(x) \cdot \cos\left[\omega_2 \tau - \phi_2^{\text{(HP)}}\right] + A_4^{\circlearrowleft}(x) \cdot \cos\left[2\omega_2 \tau - \phi_4^{\circlearrowleft}(x)\right] \tag{3.13}$$

representing the solution along the characteristic originating at $(x = X, t = \tau)$. We further require that

$$A_2^{\circlearrowright}(0) = A_2^{\circlearrowleft}(X) = A_2^{\text{(HP)}} \quad , \quad A_4^{\circlearrowright}(0) = A_4^{\circlearrowleft}(X) = A_4^{\text{(HP)}} \quad \text{, and} \quad \phi_4^{\circlearrowright}(0) = \phi_4^{\circlearrowleft}(X) = \phi_4^{\text{(HP)}} \tag{3.14}$$

since $x = 0$ and $x = X$ are in the same geographical location, and

$$A_2^{\circlearrowright}(X) = A_2^{\circlearrowleft}(0) = 0 \quad \text{and} \quad A_4^{\circlearrowright}(X) = A_4^{\circlearrowleft}(0) = 0 \tag{3.15}$$

to allow superposition of the solutions without violating Equation 3.14. The observed water surface elevation within the domain is then given by

$$z(x,t) = z^{\circlearrowright}(x,t) + z^{\circlearrowleft}(x,t) \quad . \tag{3.16}$$

3.5.1.2 Parameter estimation

In the following paragraphs, we describe our methods for approximating $A_2^{\circlearrowright}(x)$, $A_2^{\circlearrowleft}(x)$, $A_4^{\circlearrowright}(x)$, $A_4^{\circlearrowleft}(x)$, $\phi_4^{\circlearrowright}(x)$, and $\phi_4^{\circlearrowleft}(x)$. The values of $\phi_2^{\circlearrowright}(x)$ and $\phi_2^{\circlearrowleft}(x)$ are not considered here because these are calculated as a natural extension of Equations 3.10 and 3.12. All model parameters are indicated by a subscripted P, with odd subscripts corresponding to the clockwise-propagating waveform and and even subscripts corresponding to the counterclockwise waveform.

3.5.1.2.1 M_2 amplitude

In a single-channel system, the balance between convergence-driven amplification and friction-induced damping controls the along-channel variation in tidal amplitude (*e.g.,* Langbein, 1963; Dyer, 1973). Scaling analysis of the shallow water equations for a classic "funnel-shaped" estuary suggests an exponential modulation of the dominant tidal constituent's amplitude (Friedrichs and Aubrey, 1994). For channels of less idealized geometry, several studies predict along-channel

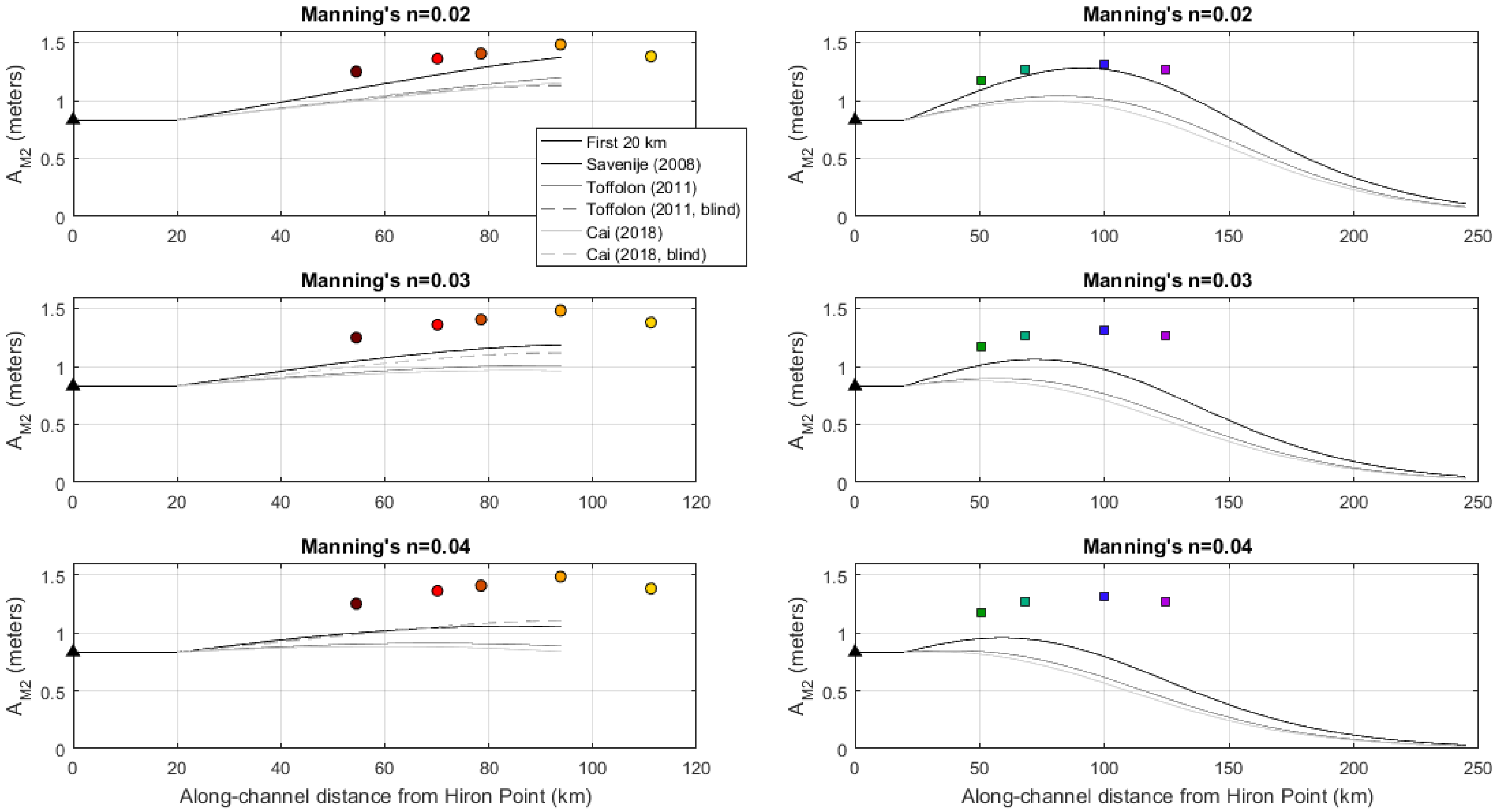

Figure 3.10: Modeled variation in along-channel M_2 amplitude in the Shibsa and Pussur channels for various values of Manning's *N*. The field data are identical to Figure 3.9. For the Shibsa channel, we include model output for an infinite-length channel as a solid line; the dashed lines indicate the results assuming a "blind" or closed channel with a full reflection at Shibsa Head. Given the Pussur's greater length, we only consider results for the infinite-length assumption. (Note that the Savenije et al. (2008) algorithm is limited to the assumption of an infinite-length channel).

amplitude variation via a set of dimensionless parameters characterizing the local dominance of convergence versus frictional dissipation (Savenije et al., 2008; Toffolon and Savenije, 2011; Cai et al., 2018). As a first approximation, we assume that the semidiurnal waves propagating northwards along the Shibsa and Pussur channels independently damp in the manner predicted for the single-channel (*i.e.*, non-looping) case, and we use the numerical algorithms from each of these three studies to estimate $A_2^{\circlearrowright}(x)$ and $A_2^{\circlearrowleft}(x)$.

To apply the methods of Savenije et al. (2008), Toffolon and Savenije (2011), and Cai et al. (2018), we used least-squares to estimate the convergence length (*i.e.*, *e*-folding length) of width, depth, and cross sectional area for the Shibsa and Pussur bathymetric profiles from Pethick (2012). The best-fit parameters are displayed in Table 3.4. Because the channel displays no clear pattern of width or depth convergence between Hiron Point and the Shibsa-Pussur bifurcation, we make the simplifying assumption that there is negligible M_2 damping or amplification over this 20-kilometer reach. We further assume that the ratio of intertidal platform width to channel width is equal to 1 everywhere in the system. Although this assumption would be grossly violated for an analysis of the full datasets, it is reasonable if we interpret our results as representative of neap-tide behavior only (*e.g.*, Figure 3.9). Finally, in the absence of suitable discharge and slope data for accurately calculating local values of the Manning friction coefficient, we produced M_2 amplification curves for a range of reasonable[6] Manning's N values between 0.02 and 0.04, with examples shown in Figure 3.10.

All three algorithms predict that convergence-driven amplification should dominate friction-driven damping of the M_2 tide between the Shibsa-Pussur bifurcation and Polder 32. Damping is predicted to begin near or slightly north of Polder 32, with the precise location of peak M_2 amplitude dependent on both the model used and the selected value of Manning's N. However,

---

[6] We are unaware of any published values of Manning's N for the Shibsa or Pussur channels. However, Simons and Sentürk (1992, p. 346) provide estimates of Manning's N for the mainstem Padma River under varying discharge conditions. At $Q = 3 \times 10^5$ CFS (8.5×10^3 m^3/s), the Padma has dune bedding, and N is approximately 0.04. As Q increases, the channel shifts to planar bedding, and N reduces to 0.03 at $Q = 6 \times 10^5$ CFS (1.7×10^4 m^3/s), $N = 0.02$ at $Q = 1.2 \times 10^6$ CFS (3.4×10^4 m^3/s), and a minimum value of $N = 0.012$ at $Q = 2.6 \times 10^6$ CFS (7.4×10^4 m^3/s). High-resolution multibeam bathymetry of our study area (Reed, 2015) suggests that the Shibsa and Pussur have fairly rough beds, and thus the range of $N = 0.02$ to 0.04 seems reasonable for this study.

Table 3.4: Best-fit geometrical parameters for the Shibsa and Pussur based on width and depth data from Pethick (2012). The "convergence length" is the *e*-folding length for an exponential relationship describing how the parameter decreases with distance upstream. A convergence length of ∞ indicates that the parameter displays no clear trend along the indicated reach.

	Hiron Point to Shibsa-Pussur bifurcation	**Shibsa River between Shibsa-Pussur bifurcation and Shibsa Head**	**Pussur River between Shibsa-Pussur bifurcation and 23.38°N**
Reach length (km)	20.0	73.8	225
Mouth* depth (m)	11.0	19.3	12.8
Depth convergence length (km)	∞	109	95
Mouth width (m)	9000	3060	3720
Width convergence length (km)	∞	88	63
Mouth area (m^2)	99,000	59,200	47,700
Area convergence length (km)	∞	49	38

*In this table, the "mouth" refers to the downstream end of the indicated channel reach.

the modeled amplitudes are persistently lower than the measured amplitude, even for the lowest tested value of $N = 0.02$. Of the three models, the algorithm from Savenije et al. (2008) produces amplitudes which are closest to matching the data, although the Cai et al. (2018) algorithm is considered to be more accurate (personal communication with H. Cai, January 2019). We therefore utilize the output of the Cai et al. (2018) algorithm to produce the results of Section 3.5.1.3.

To ensure that Equation 3.15 is satisfied, we multiply the raw M_2 amplitude profiles by a cosine-shaped tapering window. For the clockwise-traveling waveform, the window is defined by

$$W^{\circlearrowright}(x) = \begin{cases} 1 \ , & 0 \le x < P_1 \\ \frac{1}{2}\cos\left(\frac{\pi(x-P_1)}{P_3}\right) + \frac{1}{2} \ , & P_1 \le x \le P_1 + P_3 \\ 0 \ , & P_1 + P_3 < x \le X \ . \end{cases} \tag{3.17a}$$

Here, P_1 is the value of x at which tapering begins ($0 < P_1 < X$), and P_3 controls the distance past P_1 at which $A^{\circlearrowright}_{\mathrm{M2}}(x)$ is effectively zero ($0 < P_3 \le X - P_1$). Similarly, the tapering window for the counterclockwise-traveling waveform is

$$W^{\circlearrowleft}(x) = \begin{cases} 0 \ , & 0 \leq x < X - P_2 - P_4 \\ -\frac{1}{2}\cos\left(\frac{\pi(x-(X-P_2-P_4))}{P_4}\right) + \frac{1}{2} \ , & X - P_2 - P_4 \leq x \leq X - P_2 \\ 1 \ , & X - P_2 < x \leq X \ , \end{cases} \tag{3.17b}$$

with $0 < P_2 < X$ and $0 < P_4 \leq X - P_2$.

3.5.1.2.2 M_4 amplitude and phase:

Theoretical results from Speer and Aubrey (1985) suggest a systematic variability in $\mathcal{R}_{2,4}$ and $\Delta\phi_{2,4}$ as the waveform propagates upchannel. This is extended by the comprehensive field and modeling study of Friedrichs and Aubrey (1988), which predicts deformation parameter values from A_2/h and the ratio of intertidal storage volume to in-channel volume. However, the natural systems informing Friedrichs and Aubrey's (1988) conclusions are overwhelmingly short channels (<20 km in length), with the 215-km Delaware Estuary providing the only example comparable in length to the Shibsa and Pussur. The authors further note that their results are scale-dependent; for instance, the inner Delaware's $\mathcal{R}_{2,4}$-value is an order of magnitude larger than observed in the spatially short examples. To evaluate whether the broad generalizations of this study may be reasonably applied to the GBMD, we compiled published tidal deformation measurements from the Western Scheldt (Bolle et al., 2010), Guadalquivir (Díez-Minguito et al., 2012), Hooghly (Jena et al., 2018), and Guadiana (Cai et al., 2018) estuaries. These were selected because they are long (> 50 kilometer) channels with dominantly semidiurnal tides and a relatively low river input compared to the tidal discharge. Although these systems display a proportionally small intertidal area when compared to the southwestern GBMD, limiting the focus of our conceptual model to neap conditions allows us to draw analogies between these better-studied channels and the Shibsa/Pussur region.

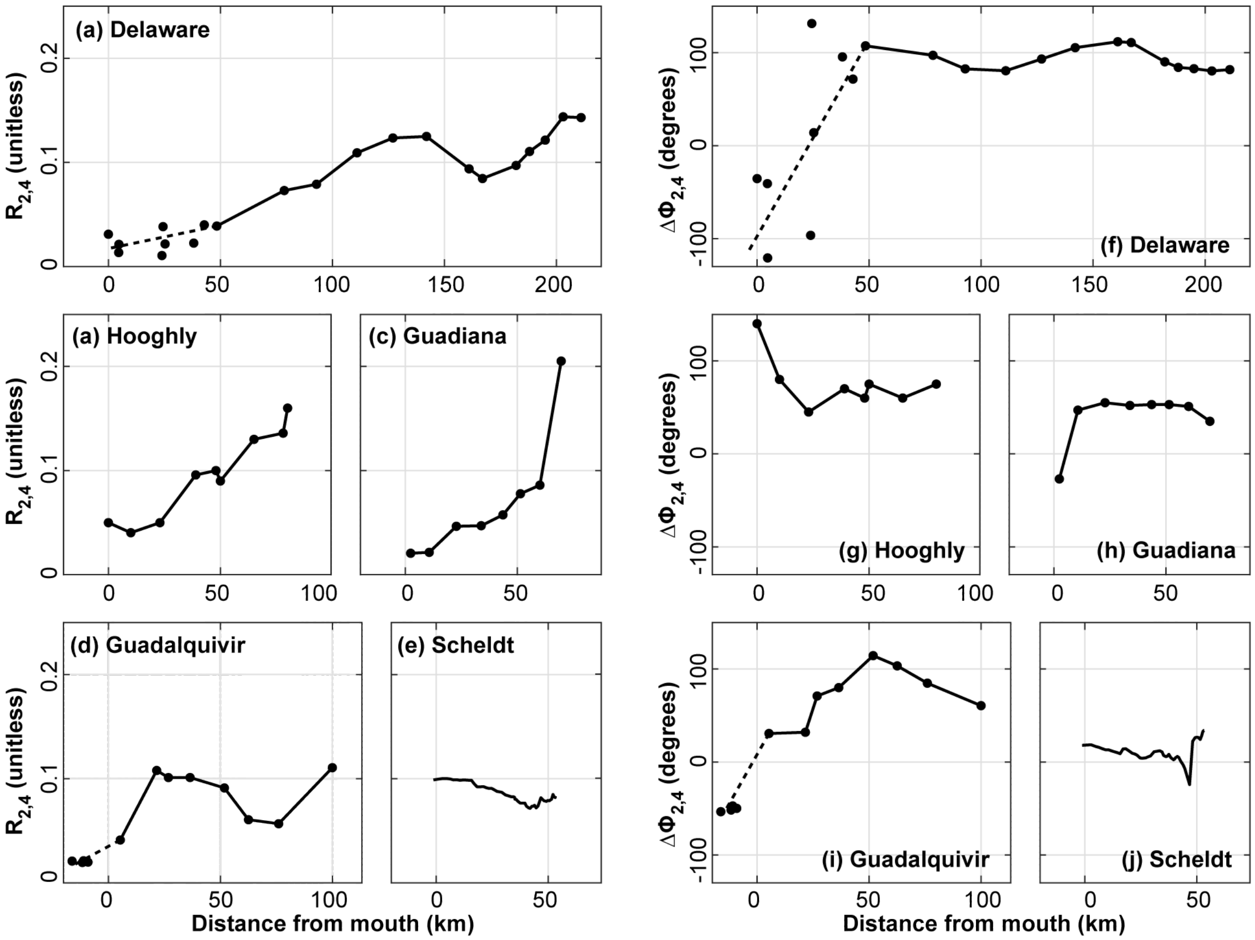

Figure 3.11: Along-channel profiles of $\mathcal{R}_{2,4}$ and $\Delta\phi_{2,4}$ for the Delaware (data from Parker, 1984), Hooghly (Jena et al., 2018), Guadiana (Cai et al., 2018), Guadalquivir (Díez-Minguito et al., 2012), and Western Scheldt (Bolle et al., 2010) estuaries. The Western Scheldt profiles are based on modeled flow conditions for the 1983 bathymetry; all other plots display field measurements. Negative values on the horizontal axis indicate that the measurement station is offshore from the estuary mouth.

Figure 3.11 displays the along-channel variation in $\mathcal{R}_{2,4}$ and $\Delta\phi_{2,4}$ for each of these large-scale systems. Although we observe some local variability, on average $\mathcal{R}_{2,4}$ increases with distance inland, achieving a maximum value above 0.1 in each system. This agrees with the results of Speer and Aubrey (1985) and Friedrichs and Aubrey (1988), who found that waveform asymmetry should be enhanced with distance traveled due to the cumulative effect of the crest propagating faster than the trough. The exception to this pattern is the Western Scheldt (Figure 3.11e), where $\mathcal{R}_{2,4}$ decreases from 0.1 to 0.08 over a distance of 50 km. Based on Figure 3.11 and the generalizations of Friedrichs and Aubrey (1988), we assume a linear increase in $\mathcal{R}_{2,4}$ for both the clockwise and counterclockwise-traveling waves, such that

$$A_4^{\circlearrowright}(x) = A_2^{\circlearrowright}(x) \cdot \left(P_5 x + \mathcal{R}_{2,4}^{(\mathrm{HP})}\right) \tag{3.18a}$$

and

$$A_4^{\circlearrowleft}(x) = A_2^{\circlearrowleft}(x) \cdot \left(P_6 X - P_6 x + \mathcal{R}_{2,4}^{(\mathrm{HP})}\right) \quad , \tag{3.18b}$$

where P_5 and P_6 are parameters on the order of 10^{-6} m^{-1} representing the rate at which $\mathcal{R}_{2,4}$ increases with distance inland.

The Delaware, Hooghly, and Guadiana channels each display a rapid adjustment in $\Delta\phi_{2,4}$ from its value at the mouth towards a fairly stable flood-asymmetric value in the inner estuary (Figure 3.11f-h). The Scheldt lacks an abrupt change in $\Delta\phi_{2,4}$ near the mouth, but it is similar in that $\Delta\phi_{2,4}$ displays minimal variation over the first 45 kilometers from the mouth. These observations are consistent with Friedrichs and Aubrey's (1988) suggestion that $\Delta\phi_{2,4}$ should be less dependent on along-channel travel distance compared to $\mathcal{R}_{2,4}$. Additionally, the results of Speer and Aubrey (1985) support the possibility of a near-mouth adjustment in relative M_2 and M_4 phase. The largest exception to this pattern is the Guadalquivir Estuary, in which $\Delta\phi_{2,4}$ increases from approximately 0° at the mouth ($x = 0$ km) to $\Delta\phi_{2,4} = 110^\circ$ at $x = 50$ km, inland of which $\Delta\phi_{2,4}$ decreases continuously. This may be a consequence of the dam 110 km upstream of the Guadalquivir mouth, which produces a strong reflection of the tidal waveform (Díez-Minguito et al., 2012). In our conceptual model, we assume that $\Delta\phi_{2,4}$ approaches a constant value as the wave propagates upstream, but we allow for the possibility of a near-mouth adjustment in $\Delta\phi_{2,4}$ by defining the M_4 phase as

$$\phi_4^{\circlearrowright}(x) = 2\phi_2^{\circlearrowright}(x) - \left(\Delta\phi_{2,4}^{(\mathrm{HP})} - P_7\right) \exp\left[\frac{-x}{P_9}\right] - P_7 \tag{3.19a}$$

and

$$\phi_4^{\circlearrowleft}(x) = 2\phi_2^{\circlearrowleft}(x) - \left(\Delta\phi_{2,4}^{(\mathrm{HP})} - P_8\right) \exp\left[\frac{-(X-x)}{P_{10}}\right] - P_8 \ . \tag{3.19b}$$

Here, P_7 and P_8 are the assumed values of $\Delta\phi_{2,4}$ far upstream, while P_9 and P_{10} are parameters controlling the rate of near-mouth phase adjustment.

We emphasize that there is no theoretical basis for the form of Equations 3.19a and 3.19b. In other words, the exponential decay equation for $\Delta\phi_{2,4}$ was not derived from the underlying physics, but rather was selected as a matter of convenience. Representing the along-channel variation in ϕ_4 using a straightforward mathematical expression facilitates systematic variation of the parameters in order to evaluate their influence on the modeled system's behavior. We discuss these influences in the following section.

3.5.1.3 Conceptual model results and interpretation

Figure 3.12 displays an example of model output[7] for A_{M2} profiles produced by the Cai et al. (2018) algorithm with Manning's $N = 0.03$. Given the Shibsa's greater depth relative to the Pussur, we assumed that the Pussur displays a faster rate of increase in $\mathcal{R}_{2,4}$ and a lower asymptotic value of $\Delta\phi_{2,4}$. We make three key observations concerning these model results. First, the M_2 amplitude of the superimposed waveform is enhanced in the center of the domain (Figure 3.12b), which we interpret as a possible explanation for the published algorithms' systematic underprediction of the measured M_2 amplitude in the Polder 32 region (Figure 3.11). The modeled M_2 amplitudes in Figure 3.12b are still lower than the measured values. However, this simple conceptual model does

---

[7] The specific parameters used to produce Figure 3.12 are $P_1 = 84.6$ km (*i.e.*, the Shibsa-Dhaki confluence), $P_2 = 104$ km (the Dhaki-Pussur confluence), $P_3 = 115.65$ km, $P_4 = 104$ km, $P_5 = 1 \times 10^{-6}$ m^{-1}, $P_6 = 1.5 \times 10^{-6}$ m^{-1}, $P_7 = 90°$, $P_8 = 70°$, $P_9 = 30$ km, $P_{10} = 80$ km, $A_{\mathrm{M2}}^{(\mathrm{HP})} = 0.83$ meters, $\mathcal{R}_{2,4}^{(\mathrm{HP})} = 0.01$, and $\Delta\phi_{2,4}^{(\mathrm{HP})} = 147.1°$.

not consider the additional effect of waveforms arriving via the Bhadra, Gorkhali, and Shengrali channels, and it is plausible that adding these signals would allow us to more accurately reproduce the M_2 amplitude profile suggested by the data. Reducing Manning's N in the Cai et al. (2018) amplification algorithm and/or substituting amplitude predictions from Savenije et al. (2008) or Toffolon and Savenije (2011) could likewise reduce the error in the superimposed M_2 amplitude.

Second, Figure 3.12(c) demonstrates that superimposing two waveforms with monotonically-increasing $\mathcal{R}_{2,4}$ values is able to produce regions of locally-decreasing $\mathcal{R}_{2,4}$ due to the summation of out-of-phase M_4 signals. In the example, these occur around $x \approx 65$ kilometers and $x \approx 145$ kilometers, which are respectively located in the Shibsa and Pussur channels south of Polder 32. The modeled local minimum in the Shibsa occurs 15 kilometers left (*i.e.*, south) of the measured minimum value at Hadda, but the magnitude of the $\mathcal{R}_{2,4}$ reduction shows good agreement with the data from both channels. This error in position could again result from neglecting the effect of the remaining three waveforms. Alternatively, several of the model parameters influence the position of the local minima.

The final key observation relates to the effect of waveform superposition on the total signal's asymmetry. Figure 3.12d shows the example of two waveforms that individually increase in flood asymmetry (*i.e.*, decreasing values of $\Delta\phi_{2,4}$) with distance into the domain, as expected for a shallow-water wave with negligible intertidal volume. However, summing these waveforms produces regions in which the flood asymmetry locally decreases; in the example of Figure 3.12d, $\Delta\phi_{2,4}$ has local maxima at $x = 55$ kilometers and $x = 152$ kilometers. Immediately inland of these peaks, the flood asymmetry is locally enhanced relative to the single-wave case. In this particular example, the Shibsa's modeled peak in $\Delta\phi_{2,4}$ is shifted left relative to the measured maximum at Shibsa F.S., and the modeled extrema in both the Shibsa and the Pussur are lower in magnitude than the data.

To quantify the model's sensitivity to varying parameters, we performed a Monte Carlo analysis with 250,000 model realizations. For each realization, Manning's N and the parameters P_1 through P_{10} were randomly sampled from probability distributions encompassing their range of physically

Table 3.5: Parameter distributions for our Monte Carlo sensitivity test of the conceptual model.

Parameter	**Description**	**Sampling distribution**	**Notes**
Manning's N	Roughness coefficient	Uniform over $[0.02, 0.04]$.	See Footnote 6.
P_1, P_2	Values of x at which $A_{\mathrm{M2}}^{\circlearrowleft}$ and $A_{\mathrm{M2}}^{\circlearrowright}$ respectively begin tapering towards zero.	Offset value $\mathcal{O}$ drawn from uniform distribution over $[-50\,\mathrm{km}, 60\,\mathrm{km}]$, then $P_1 = 84.6\,\mathrm{km} + \mathcal{O}$ and $P_2 = 104\,\mathrm{km} - \mathcal{O}$.	Shibsa-Dhaki confluence is at $x =$ 84.6 km. Pussur-Dhaki confluence is at $x = 104.0$ km. For each Monte Carlo realization, the same value of $\mathcal{O}$ is used to set P_1 and P_2.
P_3	Distance between P_1 and the point at which $A_{\mathrm{M2}}^{\circlearrowleft}$ becomes effectively zero.	Uniform over $[50\,\mathrm{km}, X - P_1]$.	P_3 and P_4 are sampled independently of each other, but the upper limits of their respective distributions are both conditional on $\mathcal{O}$.
P_4	Distance between P_2 and the point at which $A_{\mathrm{M2}}^{\circlearrowright}$ becomes effectively zero.	Uniform over $[50\,\mathrm{km}, X - P_2]$.	
P_5	Linear growth rate of $\mathcal{R}_{2,4}^{\circlearrowleft}$.	Truncated normal distribution with $\mu = 0.8 \times 10^{-6}\ \mathrm{m}^{-1}$ and $\sigma = 0.99 \times 10^{-6}\ \mathrm{m}^{-1}$; must be positive.	The value of P_6 is conditional on the value of P_5 based on the assumption that the shallower channel with display a greater magnitude of deformation. The values of μ and σ characterize the distribution of trendline slopes in Figure 3.11.
P_6	Linear growth rate of $\mathcal{R}_{2,4}^{\circlearrowright}$.	Truncated normal distribution with $\mu = 0.8 \times 10^{-6}\ \mathrm{m}^{-1}$ and $\sigma = 0.99 \times 10^{-6}\ \mathrm{m}^{-1}$. Must be greater than P_5.	
P_7	Asymptotic value of $\Delta\phi_{2,4}^{\circlearrowleft}$.	Uniform over $[50°, 179°]$.	We assume that both waveforms independently display flood-asymmetric values of $\Delta\phi_{2,4}$ due to the absence of intertidal flooding during neap tides, but we require $P_8 < P_7$ due to the depth disparity.
P_8	Asymptotic value of $\Delta\phi_{2,4}^{\circlearrowright}$.	Uniform over $[10°, P_7]$.	
P_9, P_{10}	e-folding lengths for $\Delta\phi_{2,4}^{\circlearrowleft}$ and $\Delta\phi_{2,4}^{\circlearrowright}$, respectively.	Uniform over $[1\,\mathrm{km}, 100\,\mathrm{km}]$.	Bounds of uniform distribution are based on the wide variability in near-mouth phase adjustment in Figure 3.11. P_9 and P_{10} are sampled independently.

reasonable values; this is summarized in Table 3.5. The values of $A_{\mathrm{M2}}^{(\mathrm{HP})} = 0.83$ meters, $\mathcal{R}_{2,4}^{(\mathrm{HP})} =$ 0.01, and $\Delta\phi_{2,4}^{(\mathrm{HP})} = 147.1°$, along with the time-averaged depth profile $h(x)$ (see Figure 3.12a), were treated as constants for all iterations.

Due to the large uncertainty in how the individual M_2 waveforms damp after exiting the main-stem channels, the shape of the superimposed waveforms' M_2 amplitude profiles is strongly variable. 81% of all Monte Carlo realizations produce A_{M2} profiles that descend below $A_{\mathrm{M2}}^{(\mathrm{HP})}$. Although our data do not categorically rule out this behavior, we also have no evidence to suggest that the total M_2 signal damps in the Dhaki channel, and we therefore limit our analysis to the remaining 19% of the samples (*i.e.*, 47,234 model realizations).

Out of the 47,234 model realizations with A_{M2} everywhere greater than $A_{\mathrm{M2}}^{(\mathrm{HP})}$, over 96% of the profiles display at least one local minimum in $\mathcal{R}_{2,4}$ somewhere within the domain interior (*i.e.*, not at $x = 0$ or $x = X$). As shown in Figure 3.13, the vast majority of these profiles have exactly one or two local minima in $\mathcal{R}_{2,4}$. These local minima display a strong tendency to occur slightly south of the Shibsa-Dhaki confluence at $x = 84.6$ km. Specifically, the reach between $x = 66.8$ and $x = 91.0$ km contains 80% of the local minima for profiles with with exactly one $\mathcal{R}_{2,4}$-minimum (Figure 3.14a). For profiles with exactly two $\mathcal{R}_{2,4}$ minima, the central 80% of the leftmost minimum values fall between between $x = 59.8$ and $x = 78.9$ km (Figure 3.14c). Meanwhile, the rightmost minima show a strong tendency to occur near $x = 146.0$ km, which is in the Pussur channel between the Jongla and Bhodra instruments. We also observe that it is extremely common for a local maximum in $\Delta\phi_{2,4}$ to occur in close proximity to a minimum in $\mathcal{R}_{2,4}$; ##% of all minima in the one-minimum case and ##% of all minima (left and right together) in the two-minima case have a $\Delta\phi_{2,4}$ maximum within 20 km (Figures 3.14b and 3.14d).

To summarize the implications of the parameter sensitivity test, we find that although the precise location and magnitude of local minima in $\mathcal{R}_{2,4}$ and $\Delta\phi_{2,4}$ varies depending on the combination of parameters, the *existence* of such features is largely insensitive to parameter variation. Indeed, fewer than 4% of all Monte Carlo realizations with reasonable A_{M2} profiles display zero local extrema in the deformation metrics. Second, these features tend to occur over a geographically-limited range of x-coordinates for the majority of parameter combinations. The most likely location for a local minimum in $\mathcal{R}_{2,4}$ to occur is in the Shibsa channel just south of Polder 32. When a second minimum value of $\mathcal{R}_{2,4}$ exists, it is most likely to occur in the Pussur channel near the Bhodra-Jongla reach.

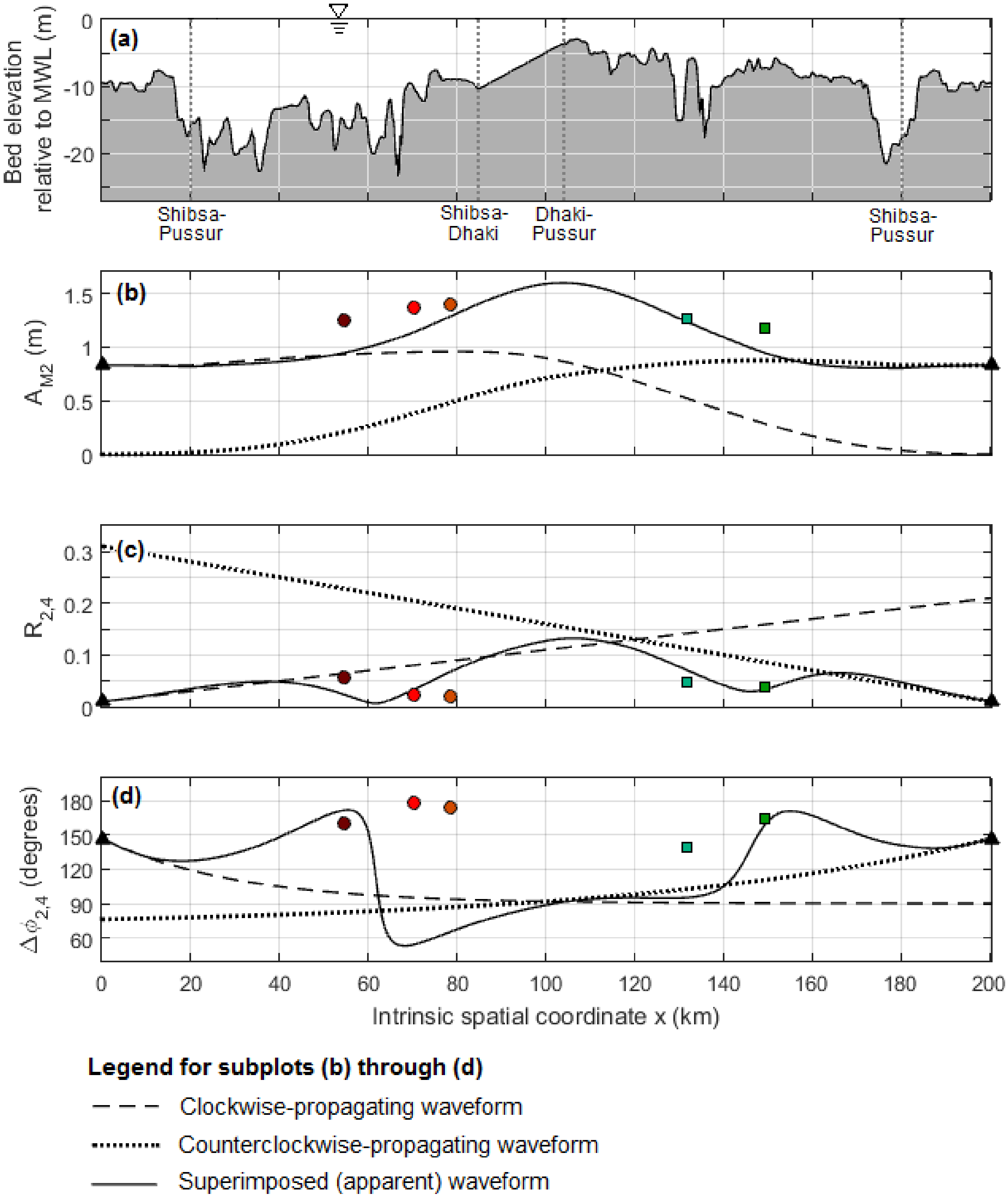

Figure 3.12: Example of conceptual model results. Here, the M_2 amplitude is based on the Cai et al. (2018) algorithm with Manning's $N = 0.03$ (Figure 3.10c and 3.10d, using the case of an infinite channel for the Shibsa). We assume that $\mathcal{R}_{2,4}$ increases more rapidly in the Pussur than in the Shibsa due to the Shibsa's greater depth. By the same reasoning, we assume that $\Delta\phi_{2,4}$ approaches 70° in the Pussur and 90° in the Shibsa. The plotted field measurements, which are based exclusively on neap-tide data, are identical to those displayed in Figure 3.9.

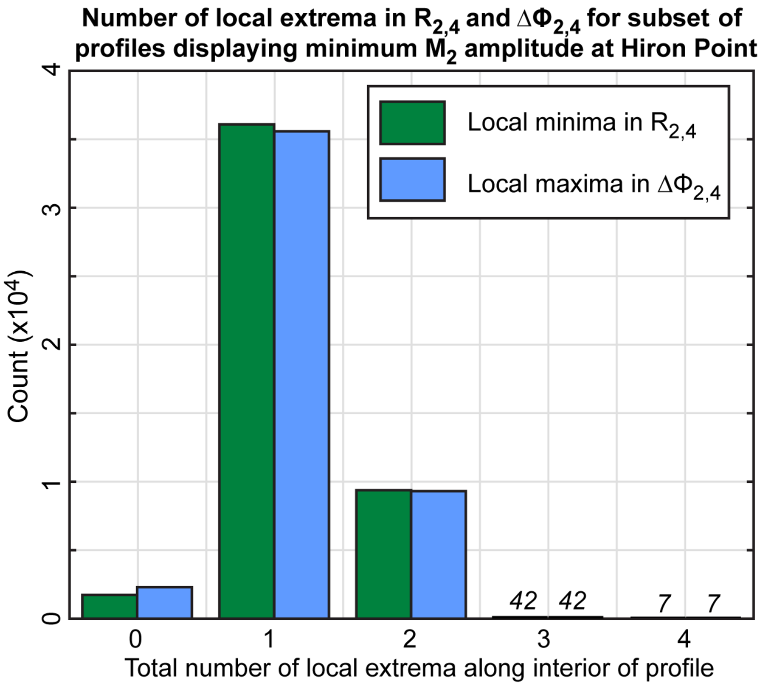

Figure 3.13: Histogram indicating the frequency of a profile displaying a given number of local minimum values of $\mathcal{R}_{2,4}$ (green) or local maximum values of $\Delta\phi_{2,4}$ (blue) along the interior of the domain. The counts do not include local minima occurring at $x = 0$ or $x = X$. Italicized numbers indicate the height of bars which are too small to be seen on the graph. The histogram counts only consider profiles for which the superimposed profile $A_{\text{M2}}(x) \geq A_{\text{M2}}^{(\text{HP})}\ \ \forall x \in [0, X]$. This reduces the sample size to 47,234 of the original 250,000 Monte Carlo realizations.

Figure 3.14: *(Continued on following page.)* **(a,c)** Distribution of the position of interior local minima in $\mathcal{R}_{2,4}$ for profiles containing exactly one (36,084 runs) and exactly two (9,371 runs) local minimum values. In subplot (c), we display separate histograms for the leftmost and rightmost minima in each $\mathcal{R}_{2,4}$ profile. **(b,d)** Distribution of the distances between each local minimum in $\mathcal{R}_{2,4}$ and the nearest local maximum in $\Delta\phi_{2,4}$. Positive distances indicate that the local minimum in $\mathcal{R}_{2,4}$ occurs to the right of the corresponding local maximum in $\Delta\phi_{2,4}$; negative distances indicate that the local minimum in $\mathcal{R}_{2,4}$ occurs to the left. Note that 506 of the runs from subplot (a) did not contain any interior local maxima in $\Delta\phi_{2,4}$ and therefore are not represented in subplot (b). Similarly, 65 of the runs from subplot (c) did not contain any interior local maxima in $\Delta\phi_{2,4}$, so these runs are not represented in subplot (d).

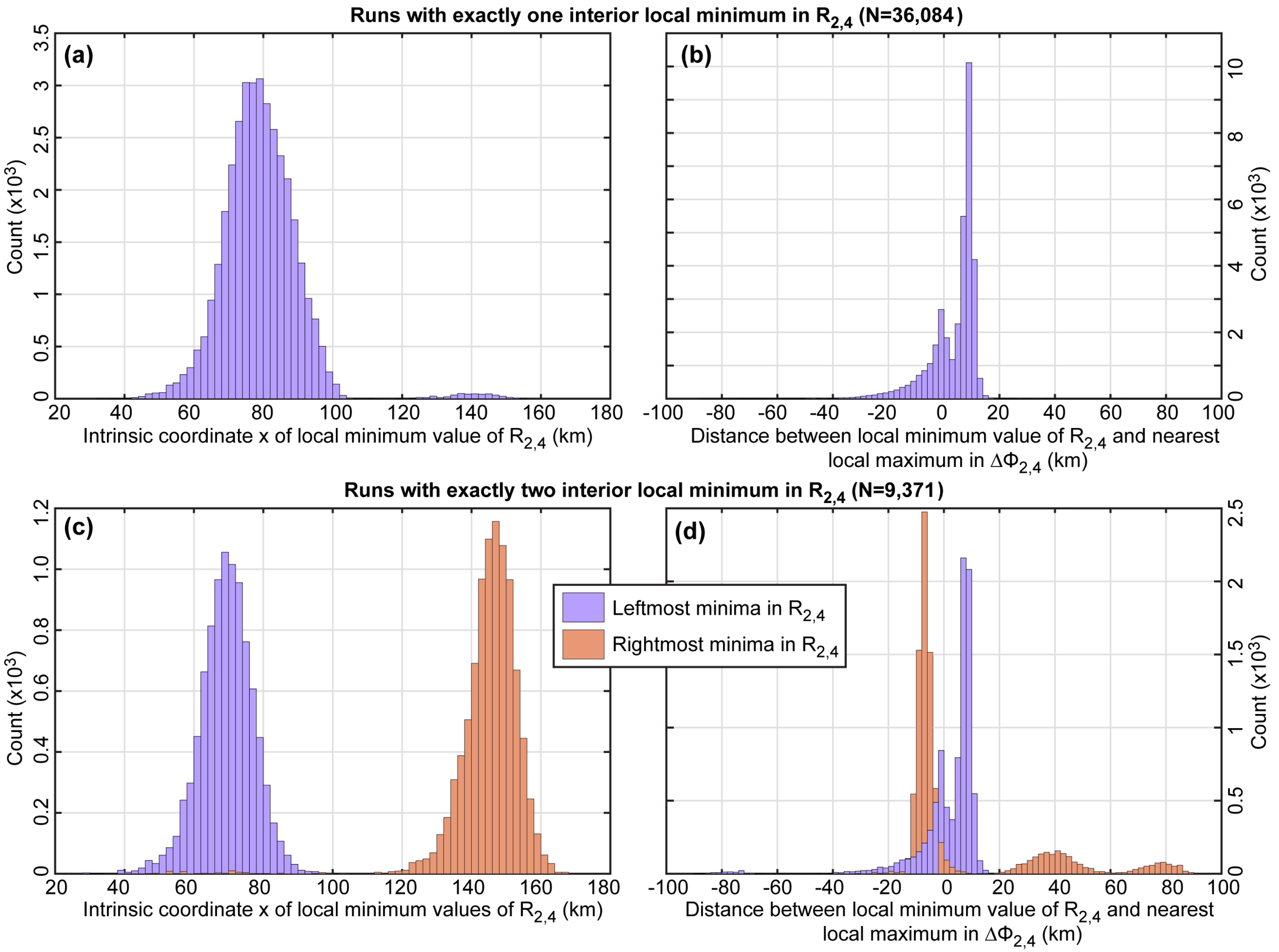

Figure 3.14: *(Continued from previous page)*

3.5.1.4 Model limitations

The conceptual model described in the preceding sections is a highly simplified representation of the natural system's behavior and should not be over-interpreted. Due to the presence of multiple loops in the tidal channel network, the measured tidal signal at Polder 32 represents the combined influence of no fewer than five waveforms (*i.e.*, one waveform propagating directly to the measurement station via either the Shibsa or the Pussur, and four additional waveforms traveling in the opposite direction via the Bhadra, Dhaki, Gorkhali, and Shengrali channels). Additionally, we have not considered partial reflections of the waveform due to irregular bathymetry and width convergence (*e.g.*, Giese and Jay, 1989; Jay, 1991; Garel and Cai, 2018). It is reasonable to anticipate that the measured signal will be dominated by energy from the first and second waves, since the remaining waves generally propagate over longer distances and should be more greatly influenced by frictional damping. Nevertheless, including additional waveforms in the total solution may shift the local extrema in $\mathcal{R}_{2,4}$ and $\Delta\phi_{2,4}$ and/or produce more complex profiles than displayed in Figure 3.12.

The assumption of simple monotonic variation in the individual waveforms' values of $\mathcal{R}_{2,4}$ and $\Delta\phi_{2,4}$ (*i.e.*, Equations 3.18a, 3.18b, 3.19a, and 3.19b) may not be strictly true for a natural tidal system. Although most of the single-channel systems in Figure 3.11 display increasing values of $\mathcal{R}_{2,4}$ and near-constant inland values of $\Delta\phi_{2,4}$ on average, there are also local deviations from the broader regional trends. The Scheldt Estuary model results from Bolle et al. (2010) illustrate the extreme case in which the $\mathcal{R}_{2,4}$ deformation magnitude *decreases* with distance inland, which is opposite our assumption. Based on the generalizations of Friedrichs and Aubrey (1988) and data from the other four systems in Figure 3.11, we believe that our assumptions about the along-channel variation in M_4 magnitude and phase are reasonable to first order. However, we cannot eliminate the possibility that the irregularities in the Shibsa's waveform deformation are generated by some mechanism internal to the Shibsa channel and would therefore occur even if the Shibsa were isolated from the Pussur waveform.

Finally, our conceptual model assumes linear superposition of the Shibsa and Pussur waveforms. Although we have represented the influence of nonlinear flow effects by including spatially-variable M_4 deformation for each individual waveform, we have not considered the possibility of nonlinear interactions between the two waveforms. Quantifying these nonlinear interactions would require a full numerical solution of the shallow water equations, which is outside the scope of this chapter. Nevertheless, these results illustrate the *possibility* that waveform superposition may contribute to the patterns of waveform deformation displayed in Figures 3.6 and 3.9, and this behavior merits a more robust analysis in future studies.

3.5.2 IMPLICATIONS FOR INTERPRETING LONG-TERM MORPHODYNAMIC TRENDS

As indicated in Section 3.2.2, asymmetries in the vertical tide are a useful predictor of sediment transport and long-term morphodynamic stability of single-inlet, non-looping tidal channel systems. Under this simple geometric scenario, an unequal duration of the rising and falling limbs will necessarily generate higher flow velocities during the shorter tidal limb in order to conserve the mass of water transported in and out of the system. Assuming that asymmetries in flow velocity govern the net sediment transport over a tidal cycle, *flood dominant* horizontal tides (and the associated flood asymmetric vertical tidal signals) characterize systems with a net import of sediment, which are susceptible to siltation and abandonment. In contrast, *ebb dominant* systems tend to be morphodynamically stable and will remain open in the long term.

To test whether this association between vertical asymmetry and horizontal current speeds holds for the Polder 32 region's looping channel network (where there is no requirement of zero net water transport over a tidal cycle; see Bain et al., 2019), we used the discharge, tide gauge, and bathymetric datasets of Hale et al. (2019a) and Bain et al. (2019) to calculate time series of cross-sectionally averaged flow velocity for a total of 14 semidiurnal ADCP surveys in the Shibsa, Pussur, Dhaki, Bhadra, and Gorkhali channels. We then compared the velocity asymmetry with the vertical tidal asymmetry recorded at the nearest pressure sensor on the same date as the ADCP survey.

Having observed that summing the semidiurnal and quarterdiurnal tidal species is often inadequate for reproducing the shape of a single waveform (*e.g.*, Figure 3.5b), we here consider the statistical skewness of the time derivative $\partial z/\partial t$ as an alternative metric for the tidal asymmetry (Nidzieko, 2010). This allows us to examine the asymmetry of the total waveform including the contributions of higher order harmonics, rather than just the asymmetry introduced by the quarterdiurnal tidal species. For a time series containing n samples of $z'(t) = \partial z/\partial t$ with mean value $\overline{z'}$, we define the skewness as[8]

$$\gamma = \frac{\frac{1}{n-1}\sum_{i=1}^{n}\left(z'(t_i) - \overline{z'}\right)^3}{\left[\frac{1}{n-1}\sum_{i=1}^{n}\left(z'(t_i) - \overline{z'}\right)^2\right]^{3/2}} \ . \tag{3.20}$$

The skewness metric γ is positive when the waveform is flood asymmetric and negative when ebb asymmetric.

Figure 3.15a shows the relationship between the vertical tidal asymmetry and the horizontally tidal dominance, which we here quantify as the difference in magnitude between the peak flood and peak ebb current speeds. Although all 14 ADCP surveys correspond to a flood asymmetric vertical tidal signal, 10 of the sites display ebb dominant cross-sectionally averaged flow velocities. This is the opposite of what would occur in a single-channel system where the volume of water entering and exiting the system is the same over a semidiurnal tidal oscillation. Although the remaining four survey sites display both flood asymmetric vertical tides and flood dominant horizontal tides, the overall absence of a systematic relationship between the vertical and horizontal tidal signals suggests that vertical tidal records alone are insufficient to predict net sediment transport in the Shibsa-Pussur network. It is worth noting that three of the four measurements which are both flood asymmetric and flood dominant were collected during the dry season. Several studies (Gallo and Vinzon, 2005; Losada et al., 2017) recognized that river discharge of sufficient magnitude

---

[8] This equation is a variant on the skewness metric of Nidzieko (2010), who defined γ as the third moment of the n samples, normalized by the cubed standard deviation of the *full dataset* (including measurements of $z'(t)$ that fall outside the analysis window). Nidzieko's definition allows γ to retain information about spring-neap variability in tidal amplitude. However, because we do not have an extended time series of the flow velocity, we cannot perform an analogous normalization for the asymmetry of v. Therefore, we confine our asymmetry calculations to the window of discharge data collection.

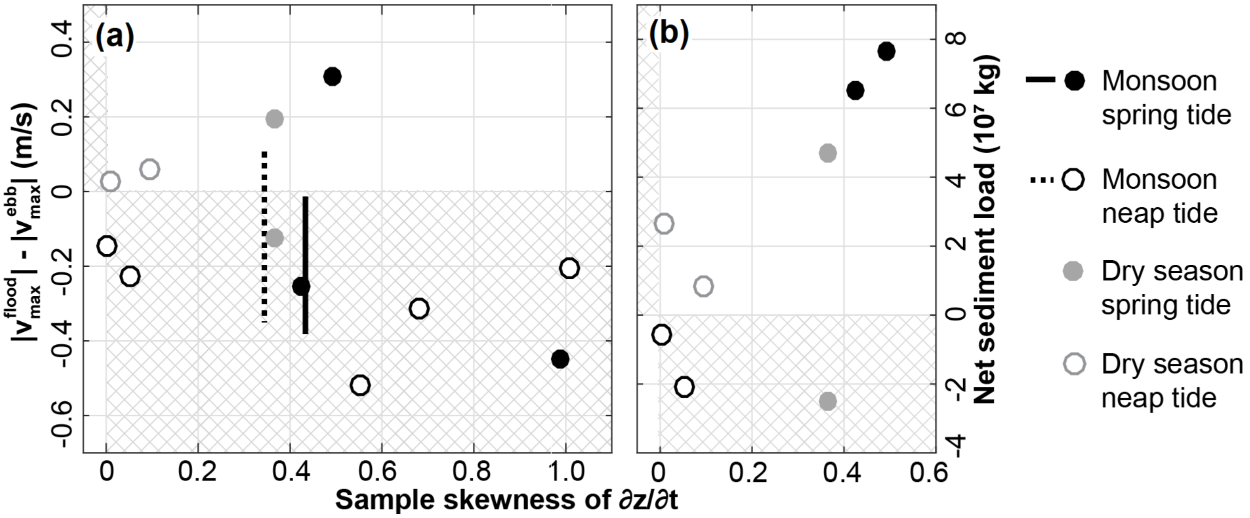

Figure 3.15: **(a)** Compilation of data from Hale et al. (2019a) and Bain et al. (2019) demonstrating the absence of a relationship between vertical and horizontal tidal asymmetry in the study area. The horizontal axis displays the statistical skewness γ of $^{dz}/_{dt}$ at the nearest pressure sensor during the ADCP survey. Positive values of γ indicate flood asymmetry (rising limb duration < falling limb duration). The vertical axis displays the difference between maximum flood and maximum ebb flow speeds, with positive values indicating flood dominance (maximum value of $|v|_{\text{flood}} >$ maximum value of $|v|_{\text{ebb}}$). The two sites which plot as error bars are from Bhadra South and Dhaki West, where we did not directly measure either peak ebb or peak flood velocity. (The length of the error bars corresponds to the lower and upper bounds of the uncertainty envelopes in Figure 2.3 in the previous chapter.) In a single-inlet, non-looping channel system, conservation of mass dictates that a flood asymmetric vertical tide will generate a flood dominant horizontal tide and vice versa. The cross-hatched regions of the graph indicate that the site displays an incoherent relationship between the vertical and horizontal tidal asymmetry. **(b)** Net sediment load data from Shibsa North and Shibsa South (Hale et al., 2019a) plotted against the local vertical tidal asymmetry. Sediment transport is here defined as positive when directed towards the north.

can force ebb dominance, regardless of the waveform shape. However, the remaining dry season measurement (which corresponds to the Shibsa North survey site from Hale et al., 2019a) is flood asymmetric but ebb dominant. This illustrates that nonzero net water transport in interconnected tidal systems (Bain et al., 2019) also allows for incoherencies between tidal asymmetry and tidal dominance.

Despite the absence of relationship between vertical and horizontal asymmetry in Figure 3.15a, suspended sediment transport measurements from Hale et al. (2019a) suggest a correlation between tidal asymmetry and sediment transport in the Shibsa River (Figure 3.15b). The observed relationship between γ and net sediment load is partly due to sampling bias; out of the five measurements that display coherent asymmetry and transport in Figure 3.15b, four also plot as flood-dominant in Figure 3.15a. Although we do not have suspended sediment transport data from any non-Shibsa locations, it is reasonable to suspect that including data from these sites in Figure 3.15b would substantially weaken the apparent correlation. However, it is interesting that one site which plots as flood asymmetric but ebb dominant in Figure 3.15a has net flood-directed sediment transport (the solid black point at $\gamma = 0.41$, which corresponds to the Shibsa South survey site during monsoon-season spring tides). This may be related to the time-variability in suspended sediment concentrations (SSC), as many sites in this region display higher SSC during flood compared to ebb (Hale et al., 2019a,b). During monsoon-season spring tides at Shibsa South, the slower northwards transport of high-SSC water appears to compensate for the faster southwards transport of low-SSC water. Of course, this then raises the question of *why* the faster ebb-directed currents are not entraining more sediment at this location; possible explanations include (1) dilution of high-SSC tidal water by low-SSC Gorai water during ebb, or (2) settling lag, in which the faster ebb currents suspend a large concentration of sediment which has not yet settled when flood begins. A more spatially-comprehensive SSC dataset would be necessary to test the validity of these hypothesized mechanisms; however, both explanations again illustrate the complexities of mass transport in a large-scale, interconnected tidal channel system.

The observation of a general incoherence between vertical tidal asymmetry and the dominant current direction implies that vertical tidal records are insufficient for predicting how the Shibsa-Pussur channel network will continue to evolve. Although the observed tides are predominantly flood asymmetric, which under a simpler geometric configuration would make them susceptible to sedimentation (*e.g.*, Friedrichs and Aubrey, 1988; Pethick, 1994; Mazda et al., 1995), the complicating effects of river discharge and net water exchange between the Shibsa and Pussur channels generate ebb dominant currents in many locations throughout the study area. However, one should note that many of the blind channels upstream of the study area (including the Kobadak and relict Shibsa, along with several unnamed *khasland* channels in Figure 2.1) do not form loops. In the absence of upstream water storage, the volume of water flooding into these channels must equal the volume of water ebbing out, and it is thus likely that these channels are both flood asymmetric and flood dominant. Assuming that net sediment transport is in the same direction as the dominant current velocity, an enhancement in flood asymmetry after polder construction disconnected the channels from the intertidal platform may explain the rapid and spatially-extensive extensive siltation in the upstream reaches of the study area (Wilson et al., 2017).

3.6 Conclusion

In shallow water environments, the tidal waveform distorts relative to a pure sinusoid due to the presence of nonlinear terms in the equations representing conservation of mass and conservation of momentum. Vertical tidal asymmetry is addressed extensively in the literature for two reasons. First, the tidal asymmetry records how the tide is interacting with the basin bathymetry; long, shallow channels with limited intertidal exchange tend to have flood asymmetric tides, whereas tidal basins with a substantial intertidal volume develop ebb asymmetric waveforms. Quantifying the tidal asymmetry thus provides information about the relative influence of the intertidal platform on the flow behavior. Second, in channel networks of sufficiently simple geometry, the asymmetry of the vertical tide is closely related to asymmetries in the horizontal tide. Flood asymmetric waveforms tend to produce flood dominant currents, whereas ebb asymmetric waveforms produce ebb dominant currents. Since the vertical signal is less costly to measure and thus more readily available than long-term, high-frequency records of current velocity, it is common to evaluate asymmetries in the vertical tide as a predictor of net sediment transport and long-term system stability.

Considering the value of tidal asymmetry research in other natural systems, we sought to quantify spatial variability in tidal asymmetry for a system of interconnected channels in the tidally-dominated southwestern region of the Ganges-Brahmaputra-Meghna Delta. We are aware of only one other study to date specifically addressing shallow-water tide deformation in this region (the paper by Chatterjee et al., 2013, whose data span only three days at 1-hour sampling), so our goals for the project were (1) to quantify the along-channel variability in the M_2 tide and its higher-frequency overtides as the waveform propagates into the system; (2) to use these data to evaluate how intertidal platform inundation and waveform interactions between the two channels influence the shape of the measured signal; (3) to evaluate whether vertical tidal asymmetry is a reasonable predictor of horizontal tidal dominance in a looping channel system, where the ebb and flood tidal prisms conveyed by a given transect are not necessarily equal in magnitude; and (4) contingent on the outcome of the third objective, to use our data to interpret long-term morphodynamic changes to the system and predict its future behavior. Our primary findings are as follows:

- Tidal deformation increases, on average, with distance into the system. In the Shibsa channel, the ratio of M_4 to M_2 amplitude increases from 0.02 at Hiron Point to 0.10 in the Kobadak River near Paikgachha when calculated over the full five-month recording period. The rate of relative M_4 growth is even higher in the Pussur channel, with the M_4:M_2 amplitude ratio achieving a value of 0.13 at Khulna.

- Inundation of the intertidal platform during spring tides significantly increases the deformation amplitude. This is characterized mathematically by the comparatively large magnitude of the compound tides MS_4 and $2MS_6$, which at many locations are as large or larger than M_4 and M_6. However, analysis of individual semidiurnal windows of data indicates that the waveform remains flood asymmetric even during peak platform inundation events, which suggests that flooding the Sundarbans does not significantly retard propagation of the wave crest.

- In the Shibsa River south of Polder 32, we observe a local deviation from the regional trends of increasing M_4:M_2 amplitude ratio and decreasing $2M_2$-M_4 phase difference. A simple conceptual model of superimposed waves arriving via multiple routes through the channel network illustrates the possibility that this could be a consequence of Shibsa-Pussur waveform interactions, although further analysis would be necessary to fully address the nonlinear behavior of converging waves in looping channel systems.

- We observe no straightforward relationship between vertical tidal asymmetry and horizontal current dominance in the study area, which suggests that knowledge of vertical tide behavior is insufficient to predict the of net sediment transport in looping tidal channel networks. The lack of relationship is further confounded by the addition of Gorai discharge from upstream, which necessitates an increase in ebb velocity to transport the excess water out of the system during the ebbing limb of the tide.

In summary, although we have been able to quantify the shape of the tide as it propagates through the system and identify several of the physical controls on its behavior, we cannot use this information to predict how the system will change in the future due to the absence of a relationship between waveform asymmetry and velocity dominance. In the following chapter, we will examine the relationship between water surface gradient and velocity as an alternative predictor of flow behavior.

Chapter 4

Quantifying the relationship between velocity and surface gradients in the Shibsa-Pussur channel network

4.1 Abstract

As the tide enters a long river channel, it creates a water surface gradient which must be balanced (in the absence of complicating factors) by a reversal in flow velocity. Understanding the relationship between water surface gradient and flow may therefore be useful for predicting preferential flow routes through a tidal channel network, and we examine this idea in the following chapter. From October 2017 through mid-March 2018, we collected high-frequency vertical tide data at nine locations in the Shibsa-Pussur channel network in southwest Bangladesh. All stations were referenced to an absolute vertical datum using high-precision, RTX™-corrected GPS measurements, allowing us to calculate instantaneous surface gradients along the mainstem channel profiles, as well as in three "transverse" channels connecting the Shibsa to the Pussur. Maximum instantaneous gradients magnitudes are as large as 5 cm/km, with typical values of mean surface gradient ranging between -1 and +2 cm/km when calculated over a 7-day averaging window. A momentum balance of surface gradient and velocity time records collected during a prior visit to the field area indicates that local accelerations are the same order of magnitude as the quadratic friction term, which implies that momentum effects are significant for controlling flow within the channels. Consequently, velocities may be against an adverse surface gradient for up to three hours before the flow reverses. In addition, the relationship between time-averaged velocity and time-averaged surface gradient is weak, and there are local deviations from the predicted behavior. We conclude that water surface gradient measurements provide insufficient information for predicting flow routes through an interconnected tidal system like the southwestern Ganges-Brahmaputra-Meghna Delta.

4.2 Introduction

In Chapter 2, we described an ongoing tidal basin capture event between the Shibsa and Pussur channels, two of the major north-south-oriented conduits for delivering water and sediment to the southwestern Ganges-Brahmaputra-Meghna Delta (GBMD). Although we find it likely that the observed flow reorganization resulted from anthropogenic modification of delta (see Section 1.3), we do not fully understand the underlying physical mechanism that drove the Shibsa channel to expand into the Pussur's former tidal basin. Chapter 3 reported the results of a study evaluating whether vertical tidal asymmetry may be used as a predictor of net sediment transport pathways, which would have utility for evaluating the system's future stability. Unfortunately, we determined that there is little to no correlation between vertical tidal asymmetry and the dominant current direction in the study area, and our tidal asymmetry analysis has few morphodynamic implications.

This chapter continues our analysis of tidal behavior in the Shibsa-Pussur region by examining water surface gradients and their role in establishing preferential flow routes through the network. At the end of Chapter 2, we hypothesized that polder-induced tidal amplification reduced the Pussur's gradient advantage in the vicinity of the transverse channel bifurcations, thereby forcing a larger percentage of upstream Gorai discharge into the Shibsa. Here, we consider a two-step approach to testing this hypothesis. We first perform a momentum balance on the present-day velocity and surface gradient data, which quantifies the relative importance of surface gradients for driving flow through the channels. We then consider a multi-decadal record of tidal elevations along the Pussur channel to examine whether the long-term trends in surface gradient are consistent with the proposed mechanism.

The analysis in this chapter is centered on the expression for conservation of momentum in an open channel flow. Neglecting the influence of bed slope (which is typically reasonable in alluvial estuaries; see Savenije, 2005) and assuming a constant water density everywhere in the system, momentum conservation may be expressed as

$$\frac{\partial v}{\partial t} + v\frac{\partial v}{\partial x} = -g\frac{\partial z}{\partial x} - gN^2\frac{v|v|}{R^{4/3}} \ , \tag{4.1}$$

where t is time, x is position in space, v is the cross-sectionally averaged flow velocity, z is the water surface elevation relative to a datum, R is the hydraulic radius, N represents Manning's friction coefficient, and g is the magnitude of gravitational acceleration. Numerous authors present detailed analyses of 4.1, with objectives ranging from the derivation of an analytical solution for the tidal motion (*e.g.*, Dronkers, 1964; Friedrichs and Aubrey, 1994; Jay, 1991), quantifying the nonlinear mechanisms which contribute to tidal asymmetry (Parker, 1984; Le Provost, 1991), or explaining the behavior of a specific tidal environment (Warner et al., 2003; Mariotti and Fagherazzi, 2011; Orescanin et al., 2016). Our analysis stems from the observation that if the friction coefficient N is sufficiently large, then the quadratic friction term will dominate over the acceleration terms on the left-hand side of Equation 4.1, and the relationship reduces to

$$\frac{\partial z}{\partial x} = -N^2 \frac{v|v|}{R^{4/3}} \quad . \tag{4.2}$$

Equation 4.2 implies that the reversals in flow should coincide with reversals in surface gradient (*i.e.*, $\partial z/\partial x = 0 \implies v = 0$). Moreover, for two channels with comparable friction coefficients and hydraulic geometry, the channel with the greater surface gradient should also display the greater velocity magnitude. In this paper, we evaluate whether Equation 4.2 reasonably characterizes the behavior of the Shibsa-Pussur system and therefore represents a simplified method for predicting the dominant flow paths within the network.

We note that Equation 4.1 is generally coupled with the equation for conservation of mass:

$$b\frac{\partial z}{\partial t} + \frac{\partial}{\partial x}(A \cdot v) = 0 \quad , \tag{4.3}$$

where A and b represent the cross-sectional area and width of the channel, respectively. We do not consider Equation 4.3 further, except in a qualitative sense, but we list it here for completeness.

4.3 Methods

4.3.1 FIELD DATA COLLECTION

As described in Chapter 3, we deployed 10 pressure sensors in the Polder 32 region of southwest Bangladesh to collect high-frequency vertical tide data. Table 4.1 describes each measurement site, with the instrument positions are shown on the map in Figure 3.3. The instruments were installed in early October 2017 and recorded at a sampling interval of $\Delta t = 10$ minutes until retrieval in mid-March 2018, producing datasets which span the transition from late monsoon to fully dry-season conditions.

To reference the elevation time series to an absolute vertical datum, we used an RTX™-enabled[9] Trimble NetR9 GPS rover to establish an elevation benchmark near each pressure sensor. At each site, an immobile antenna collected elevation readings while receiving satellite-broadcast RTX™corrections[10]. The rover recorded between 45 minutes and 3 hours of continuous measurements until the elevation time series converged to a stable, trend-free value. After obtaining a minimum of 30 minutes of stable elevation data, we recorded the mean of the trend-free segment as the benchmark elevation. Finally, we manually surveyed from the benchmark to the tip of the pressure sensor housing using a theodolite and 5-meter stadia rod.

4.3.2 POST-PROCESSING AND UNCERTAINTY QUANTIFICATION

4.3.2.1 Drift correction and datum shifts

Slight pressure sensor miscalibrations prevent two proximal instruments from recording identical pressure values, and the relative error may drift through time. To ensure consistency between the datasets, we fit a site-specific drift correction curve to the relative error between the instru-

---

[9] RTX™refers to Trimble's proprietary, real-time, satellite-broadcast GPS correction signal. The technology is analogous to real-time kinematic (RTK) GPS surveying, in which corrections for satellite clock errors, orbital errors, and ionospheric/tropospheric delays are broadcast from an immobile base station via radio. This allows the rover's signal to be corrected in real time and significantly improves survey accuracy relative to differential GPS (DGPS). In contrast to better-known RTK methods, Trimble sends the real-time corrections to the rover via satellite instead of radio.

[10] Note that we could not establish line-of-site to the RTX™satellite at Sutarkhali Forest Station, and consequently this particular GPS dataset is uncorrected. Although we intended to post-process the Sutarkhali GPS data using a base station recording from the Gonari schoolhouse, the base station suffered an electronic failure over its two week deployment, and its measurements were unrecoverable.

Table 4.1: Summary of instrument locations used for this study. The table continues on the following page.

Site	Coordinates	Site description	Raw sensor elevation (WGS84)*	Max. error associated with theodolite	Maximum exposure time
Adachai F.S.	22.263821°N 89.494134°E	Instrument mounted on rebar in the small creek southeast of the forest station building. Instrument was — at low water, but a sill at the creek mouth cut off the instrument from the mainstem Shibsa channel during spring tide low waters.	$\mu_z = -57.468$ m $\sigma_z = 0.004$ m	$b_z = 0.20$ m	—[§]
Bhodra F.S.	22.242186°N 89.572091°E	Instrument mounted on rebar in the Bhodra channel 100 m north of the forest station's bamboo dock.	$\mu_z = -57.745$ m $\sigma_z = 0.006$ m	$b_z = 0.50$ m	—
Hadda F.S.	22.455658°N 89.415041°E	Instrument mounted with hose clamps on the concrete navigation pillar along the north bank of the mangrove creek connecting the mainstem Shibsa River to the forest station dock.	$\mu_z = -58.881$ m $\sigma_z = 0.017$ m	$b_z = 0.05$ m	—
Kobadak at Paikgachha	22.618353°N 89.289639°E	Instrument mounted with hose clamps on the concrete piling under the bridge near the west bank. Poor working conditions during deployment prevented us from installing the instrument farther out from the bank, so instrument was exposed during all low waters (spring and neap).	$\mu_z = -55.264$ m $\sigma_z = 0.024$ m	$b_z = 0.20$ m	5 hr
Khulna Shipyard	22.792471°N 89.581559°E	Instrument mounted on the green and blue shipyard dock on the west bank of the mainstem Pussur River. We could not place it farther out from the bank without introducing a navigational hazard, so the instrument was subaerially exposed during dry season spring tides.	$\mu_z = -56.366$ m $\sigma_z = 0.024$ m	$b_z = 0.02$ m	2.67 hr
Jongla F.S.	22.368871°N 89.615369°E	Instrument mounted on rebar along the south bank of the mangrove creek, due south of the forest station dock.	$\mu_z = -58.541$ m $\sigma_z = 0.017$ m	$b_z = 0.20$ m	—
Pankhali ferry ghat	22.631539°N 89.514927°E	Instrument mounted on rebar underneath the floating walkway leading to the ferry boarding platform, on the north bank of the Gorkhali River.	$\mu_z = -58.098$ m $\sigma_z = 0.035$ m	$b_z = 0.05$ m	—
Shibsa F.S.	22.384533°N 89.449678°E	Instrument mounted on rebar in the middle of the mangrove creek northeast of the forest station's bamboo dock.	$\mu_z = -57.843$ m $\sigma_z = 0.032$ m	$b_z = 0.50$ m	—

(Continued on following page.)

(Continued from previous page.)

Site	**Coordinates**	**Site description**	**Raw sensor elevation (WGS84)***	**Max. error associated with theodolite**	**Maximum exposure time**
Shibsa Head ferry ghat	22.478234°N 89.405023°E	Instrument mounted on rebar near the northeast corner of the concrete dock/walkway at the south bank of the Gorkhali channel. We could not place the instrument farther out into the channel without introducing a navigational hazard, so instrument was exposed during almost all low waters (spring and neap).	$\mu_z = -56.277$ m $\sigma_z = 0.002$ m	$b_z = 0.01$ m	4.67 hr
Sutarkhali F.S.	22.499185°N 89.489243°E	Instrument mounted on rebar near the pilings supporting the forest station pavilion on the north bank of the Bhadra River. Instrument was exposed during a handful of dry season spring tide lows, but the record is very nearly complete.	$\mu_z = -56.816$ m $\sigma_z = 1.060$ m[‡]	$b_z = 0.20$m	50 min

---

[*] The reported values of μ_z and σ_z refer to the mean and standard deviation of the trend-free segment of the GPS elevation time series, which contained at least 30 minutes of continuous data. The raw value of σ_z does not include the uncertainty associated with variable GPS convergence, theodolite surveying, and out-of-water interpolation (if applicable).

[‡] We could not obtain line-of-sight to the RTX™satellite at Sutarkhali Forest Station and therefore could not obtain real-time elevation corrections. Although we intended to post-process the Sutarkhali GPS time series using base station data from the Gonari schoolhouse, electronic failure of the Gonari instrument later rendered the base station data unrecoverable. As such, we are unable to reduce the size of this value.

[§] Although the Adachai Forest Station instrument remained continuously submerged for 5 months, a sill at the creek mouth resulted in the instrument being cut off from the mainstem Shibsa channel for ∼3 hours during spring tide lows. We corrected for this by deleting the lowest meter of data and treating the missing values as "out of water" measurements for data reconstruction purposes.

ment's atmospheric data and barometric data from the Gonari meteorological monitoring station. At the four sites which were exposed at low water (Shibsa Head, Paikgachha, Khulna, and Sutarkhali), we included all subaerial measurements when determining the best-fit drift correction curve. At the remaining locations, we collected atmospheric pressure data before deployment and after retrieval to compare with the Gonari dataset; in this case the drift correction curve takes the form of a trendline fitted to the two clusters of measurements. Subtracting each site's drift correction curve from its raw measurements eliminates the error introduced by internal instrument drift. Section B.1.3 in Appendix B shows examples of the drift correction procedure.

In addition to internal drift, the ubiquity of bank instability and slumping in the study area (Reed, 2015) introduces the possibility that instruments mounted near the channel bank may shift in absolute elevation over a five month period. Although this does not affect the shape of the high-frequency signal and should therefore have minimal influence on the results of the previous chapter, unidentified datum shifts could have serious ramifications for analysis of absolute water surface elevations. We examined the datasets for datum shifts by subtracting proximal instruments' time series and looking for abrupt changes in the relative pressure difference between the sites. An example is shown in Figure B.6 of the Supporting Information. This analysis suggests that the Hadda instrument was influenced by a bank slump in mid-February, and the Bhodra instrument experienced two separate slump events in early January and early February. We deleted all measurements from Hadda after 8-Feb-2018 and all measurements from Bhodra after 1-Jan-2018 before proceeding with further analysis.

4.3.2.2 Conversion to elevation

After applying the drift correction, we converted raw pressure to depth of water column h using a spatially-averaged but time-variable conversion factor based on measured values of salinity and water temperature (see Figure B.3 in Appendix B). The local absolute water surface elevation is then given by[11]

$$z(x,t) = \mu_z(x) + h(x,t) \ , \tag{4.4}$$

where μ_z is the absolute elevation of the pressure sensor recorded in Table 4.1.

Throughout this chapter, we perform all calculations and report all values relative to the EGM-2008 geoid. For deep ocean basins, where there is minimal waveform distortion, this model of the gravitational equipotential surface coincides closely with mean sea level as calculated from tidal records. In contrast, nonlinear processes in shallow embayments deform the tidal waveform and cause the measured mean water level to sit well above the "mean sea level" zero-elevation suggested by the geoid (Le Provost, 1990). Nevertheless, calculating water surface gradients in EGM2008 allows us to understand how the water surface is aligned relative to the gravitational restoring force of the tidal waveform (*e.g.*, Giese and Jay, 1989).

4.3.2.3 Out-of-water interpolation

Five of the instruments (Shibsa F.S., Hadda, Bhodra, Jongla, and Pankhali) were continuously submerged over the entire recording period, whereas the remaining instruments were truncated at low water. The instruments at Sutarkhali, Shibsa Head, Paikgachha, and Khulna were subaerially exposed for durations ranging from 50 minutes to 5 hours. The Adachai instrument remained submerged for the full five months, but a sill at the channel mouth caused it to be cut off from the mainstem Shibsa channel at low water. We applied a cubic spline interpolant to reconstruct the unmeasured values after observing that this method outperformed several standard tidal analysis algorithms (including `T_TIDE` from Pawlowicz et al., 2002, and `UTide` from Codiga, 2011) for reconstructing the low water elevations (Bain et al., 2019).

---

[11] The independent variable x is formally a vector containing two spatial coordinates. However, since the system is quasi-one-dimensional except near channel junctions, it is not particularly critical to perform the calculations in multiple spatial dimensions. The important point to remember is that the tidal signal z is a function of both space and time.

4.3.2.4 Error analysis

There are three potentially-significant sources of uncertainty in our absolute water surface elevation measurements. First, the RTX™-corrected GPS signal does not converge to the same value of μ_z each time the instrument is powered on. Although the standard deviation of the convergence value tends to be small during any given 30-minute period (frequently on the order of 10^{-3} meters; Table 4.1), testing the instrument at a fixed position over 14 consecutive days produced an actual measurement uncertainty of $\sigma_z = 2.35$ cm. We describe the details of the testing procedure in Appendix B. This value is substantially smaller than the uncertainty of $\sigma_z = 5$ cm reported by Mondal et al. (2018), who used the same instrument to quantify paleoseismic uplift in southeastern Bangladesh. However, given the good reproducibility of our GPS measurements under several testing scenarios, we believe the lower value of $\sigma_z = 2.35$ cm is reasonable for this analysis (see Section B.2).

The second source of error is the measurement uncertainty from the theodolite surveys. Given the manual nature of these measurements, we estimated the uncertainty in the theodolite measurements based on the horizontal measurement distance, the repeatability of the measurements by multiple researchers, and a general assessment of the working conditions. For example, the uncertainty associated with the theodolite is only $b_z = 1$ cm at Shibsa Head, where the GPS antenna was positioned on a dock immediately above the pressure sensor, allowing us to measure the vertical distance between the antenna and the instrument using just a tape measure. The other extreme is Bhodra ($b_z = 50$ cm), where the antenna and the pressure sensor were separated by 100 m, visibility was poor due to a tropical depression in the Bay of Bengal, and navigational conditions prevented us from having several people take independent theodolite readings. When assigning these uncertainty values, we were cautious to select a number that almost certainly exceeded the actual error, and we are confident that the error introduced by the theodolite is no larger than the respective values listed in Table 4.1.

The third source of uncertainty is the error introduced by cubic spline interpolation for the instruments that were subaerially exposed. To determine how reconstruction of missing measurements influences our data, we truncated the datasets from Bhodra, Jongla, Pankhali, Shibsa F.S., Hadda, and Sutarkhali (which is only missing 4 low waters from the entire 5-month period) at 5-cm increments moving upwards from lowest low water. For each truncation increment, we reconstructed the truncated values with the cubic spline algorithm and compared the known and reconstructed elevation values. This allowed us to determine empirical relationships between (1) the percentage of measurements p missing from the 7-day averaging window and the error in calculated mean elevation, (2) the duration of individual gaps ΔT in the dataset and the error in low water elevation, and (3) the duration of ΔT and the error in low water timing (Figure 4.1).

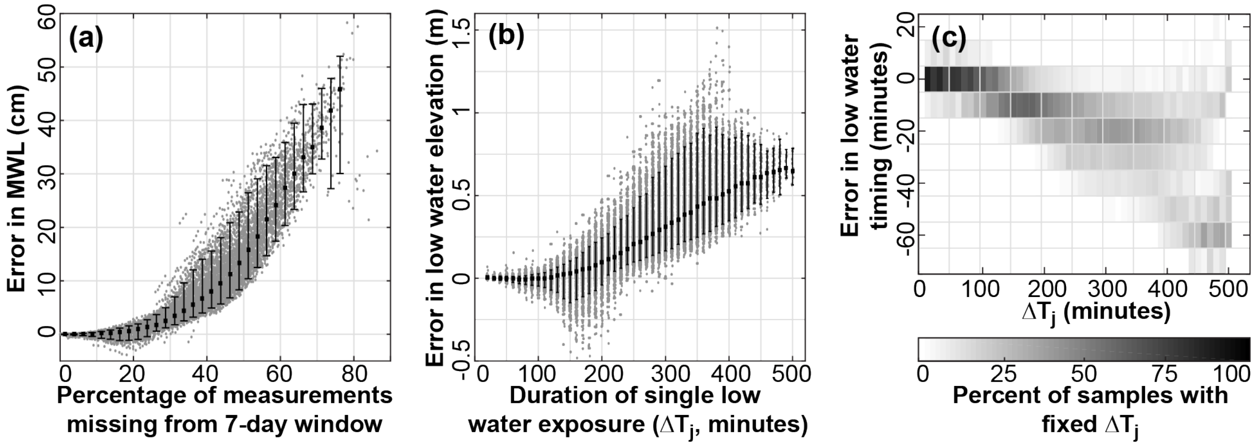

Figure 4.1: Results of truncation testing for the six complete datasets. **(a)** Empirical relationship between the percentage of data missing from a 7-day averaging window and the error in calculated mean elevation for that window. Positive error values indicate that the calculated mean elevation is higher than the known mean elevation. Black squares with error bars indicate the 5th, 50th, and 95th percentiles of the data after dividing the points into horizontal bins which are 2.5 percentage points wide. **(b)** Empirical relationship between the duration of a single gap in the dataset and the error in reconstructed low water elevation. Positive error values indicate that the reconstructed low water elevation is higher than the known low water elevation. Due to the 10-minute sampling interval, all points' horizontal coordinates fall on discrete values (integer multiples of 10 minutes). **(c)** Empirical relationship between the duration of a single gap in the dataset and the error in low water timing. Positive error values indicate that the reconstructed low water occurs *after* the timestamp of the known low water, whereas negative error values indicate that the reconstructed value occurs too early. The horizontal and vertical coordinates are both discrete multiples of 10 minutes, and all data thus are binned into 10-minute by 10-minute boxes. Each column of the graph, which corresponds to a discrete value of ΔT_j, has been normalized by the total number of samples in that column such that the shading of each column sums to 100%.

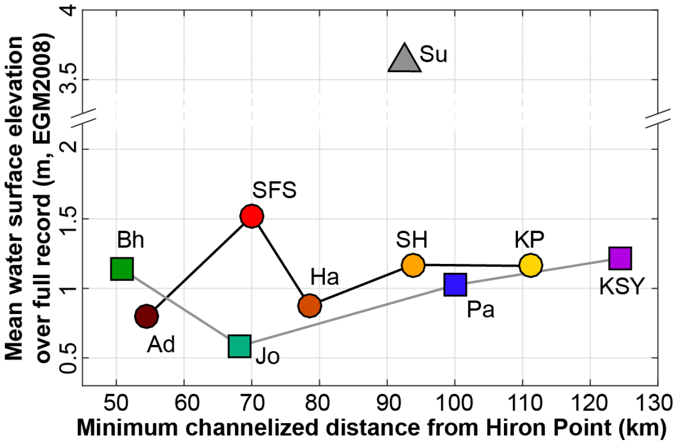

Figure 4.2: Raw values of mean water surface elevation at the ten measurement sites over the full ∼5-month recording period. Periods of subaerial exposure were reconstructed with a spline interpolant prior to calculating the mean value, but no additional corrections are included in this figure. Note the break in vertical scale between 2 and 3.5 meters elevation.

4.3.2.4.1 Initial data quality test

As an initial data quality test, we plotted the long-term average of the raw elevation time series (Equation 4.4) against the minimum distance from Hiron Point along either the Shibsa or Pussur channels. Although we do not expect a perfectly linear increase in the channels' mean elevation profiles, published results from other systems (*e.g.* Hoitink and Jay, 2016) suggest that there should be a systematic trend in mean water level with distance inland from the coast.

Figure 4.2 shows that when averaged over the five-month recording period, water surface elevations tend to increase with distance from the coast along both channels. However, three stations display a substantial deviation from this overall trend. The measured mean water level at Shibsa F.S. is over 50 cm higher than the stations immediately upstream and downstream (Adachai and Hadda, respectively). The mean water level at Bhodra is also 50 cm higher than the most proximal upstream station (Jongla) and 10 cm higher than Pankhali, nearly which is 50 km upstream. These unlikely results can most likely be attributed to theodolite measurement errors. Additionally, the measured mean at Sutarkhali is over 3 meters higher than any of the other stations. Bomer et al. (2019) report a long-term mean water level of +1.0 m EGM96 at the same site based on earlier GPS surveys[12] by Auerbach et al. (2015), which grossly contradicts our value of +3.63 m EGM2008 even after adjusting for the change in datum. The large measurement error at Sutarkhali is most likely a consequence of dense tree cover, which prevented us from obtaining line-of-sight to the RTX™satellite. The electronic failure of our Gonari base station also prevented us from post-processing the Sutarkhali elevation dataset to reduce σ_z.

In consideration of these apparent measurement errors, we discarded the datasets from Bhodra, Shibsa F.S., and Sutarkhali from all calculations requiring an absolute elevation. With the exception of the datum shifts due to bank slumping at Bhodra (Section 4.3.2.1), these three datasets appear to be internally consistent and are still useful for waveform asymmetry and phase analysis, as in Chapter 3. However, we limit our attention to the remaining seven datasets (Adachai, Hadda, Shibsa Head, Paikgachha, Jongla, Pankhali, and Khulna) for the remainder of Chapter 4.

4.3.2.4.2 *Monte Carlo analysis of subtidal water surface gradients*

To determine the cumulative influence of the three error sources on subtidal (time-averaged) water surface gradients, we performed a Monte Carlo-style analysis of the elevation data. Letting n index the 10,000 Monte Carlo iterations, we set

$$Z_n(x,t) = z(x,t) + \varepsilon_n(x) + \delta_n(x) \quad , \tag{4.5}$$

where $z(x,t)$ is the measured absolute water surface elevation given by Equation 4.4. The value ε_n is a random error associated with GPS convergence, which is drawn from a normal distribution with $\mu_\varepsilon = 0$ meters and $\sigma_\varepsilon = \max\left[0.0235\,\mathrm{m}\,,\,\sigma_z(x)\right]$, where $\sigma_z(x)$ is the standard deviation of the GPS elevation time series listed in Table 4.1 and 2.35 cm is the GPS convergence error produced across 14 days of testing. The random error associated with the theodolite survey is represented by $\delta_n(x)$, which is drawn from a uniform distribution spanning $[-b_z(x)\,,\,b_z(x)]$. Then, dividing

---

[12] Bomer et al. (2019) referenced the Sutarkhali sensor to EGM96 by assuming that MWL at Sutarkhali was equal to MWL at Sorbothkhali Forest Station (personal communication with C. Wilson, August 2019), which Auerbach et al. (2015) measured with GPS in 2014. Since Sutarkhali is 8 km farther upstream than Sorbothkhali, it is likely that its actual MWL is somewhat higher than the Sorbothkhali value; however, a 3.6-meter increase in MWL over an 8-km distance is physically implausible.

the data into 7-day averaging windows indexed by k, we calculated the local mean water surface elevation as

$$\overline{Z}_{n,k}(x) = \overline{Z_n(x,t_k)} - \xi_{n,k}\Big|p(x,t_k) \quad . \tag{4.6}$$

Here, t_k refers to the subset of t falling within the k^{th} window, and $p(x,t_k)$ is the percentage of measurements missing from this window for the pressure sensor at location x. The random value $\xi_{n,k}$ is the error in mean water level associated with spline reconstruction, which is drawn from the truncation test results in Figure 4.1(a) conditional on the known value of p.

Having produced values of $\overline{Z}_{n,k}(x)$ for each individual pressure sensor, the local subtidal water surface gradient between adjacent instruments for the n^{th} Monte Carlo iteration and the k^{th} averaging window is simply[13]

$$\overline{S}_{n,k}(x) = \frac{\overline{Z}_{n,k}(x_{i+1}) - \overline{Z}_{n,k}(x_i)}{L} \quad , \tag{4.7}$$

where $\overline{S}$ indicates a time-averaged spatial slope and L is the along-channel distance between the instruments located at x_i and x_{i+1}. We define x as increasing upstream such that S is positive when the water surface is sloping towards the Bay of Bengal and negative when sloping inland (Figure 4.3). Additionally, we used linear regression to fit regional subtidal gradients along the Shibsa River (Adachai, Hadda, Shibsa Head, and Paikgachha instruments) and the Pussur River (Jongla, Pankhali, and Khulna instruments).

4.3.2.4.3 *Monte Carlo analysis of instantaneous water surface gradients*

We performed a second Monte Carlo analysis to estimate confidence intervals for the instantaneous water surface gradients between adjacent measurement stations. For the n^{th} Monte Carlo iteration, we first determined $Z_n(x,t)$ using the method described in the previous section (Equation

---

[13] Straightforward algebra demonstrates that time-averaging the individual sites' elevations and then calculating the spatial slope is the same as calculating a time series of instantaneous spatial slopes and then taking a time average. I chose the former because the computational demands for the Monte Carlo were lower. My computer does not have enough RAM to simultaneously store 70,000 time series (7 sites times 10,000 Monte Carlo iterations) which each contain over 20,000 instantaneous values.

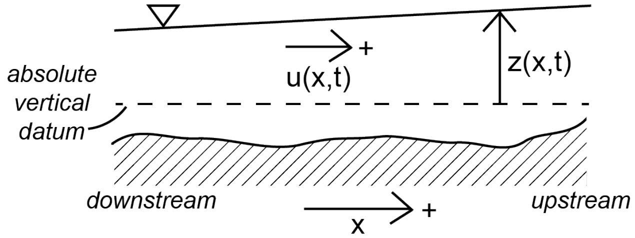

Figure 4.3: Sign convention for variables discussed in this chapter. We define the spatial coordinate x as increasing upstream in order to produce positive values of $S = {}^{\Delta z}/_{L}$ when the water surface is sloping towards the Bay of Bengal. In this coordinate system, positive flow velocities are then directed upstream in the direction of increasing x.

4.5). Then, letting j index the individual gaps in the dataset caused by subaerial exposure at low water, we calculated adjusted values of the low water time and elevation as

$$\hat{z}_{n,j}^{(\mathrm{LW})} = z_{n,j}^{(\mathrm{LW})} - \zeta_{n,j}\Big|\Delta T_j \tag{4.8}$$

and

$$\hat{t}_{n,j}^{(\mathrm{LW})} = t_j^{(\mathrm{LW})} - \tau_{n,j}\Big|\Delta T_j \ , \tag{4.9}$$

where $t_j^{(\mathrm{LW})}$ and $z_{n,j}^{(\mathrm{LW})}$ are the time and elevation of low water in the j^{th} gap in the dataset as predicted by the spline interpolant. Note that the spline itself does not change shape between Monte Carlo iterations, but $z_{n,j}^{(\mathrm{LW})}$ is dependent on n due to the vertical shifting of the time series datum in Equation 4.5. The low water elevation correction $\zeta_{n,j}$ is drawn from the empirical distribution in Figure 4.1(b) conditional on the known duration of the gap in the dataset, ΔT_j. The low water timing correction $\tau_{n,j}$ is similarly conditional on ΔT_j and is drawn from the empirical distribution in Figure 4.1(c). Finally, we applied a piecewise linear scaling of the spline interpolant to shift $(t_j^{(\mathrm{LW})}, z_{n,j}^{(\mathrm{LW})})$ to its corrected position $(\hat{t}_{n,j}^{(\mathrm{LW})}, \hat{z}_{n,j}^{(\mathrm{LW})})$. An example is shown in Figure 4.4.

The outcome of this algorithm is a corrected elevation time series $\hat{Z}_n(x,t)$, which is identical to $Z_n(x,t)$ at all times t when the instrument was submerged. A time series of instantaneous water surface gradients between adjacent instruments is then calculated as

$$S_n(x,t) = \frac{\hat{Z}_n(x_{i+1},t) - \hat{Z}_n(x_i,t)}{L} \quad . \tag{4.10}$$

As shown in Figure 4.3, we define positive S as sloping towards the Bay of Bengal.

4.3.3 LONG-TERM DATASETS

To put our data in the broader context of decadal changes in the system's behavior, we examined water surface elevation records collected by Bangladesh Water Development Board (BWDB),

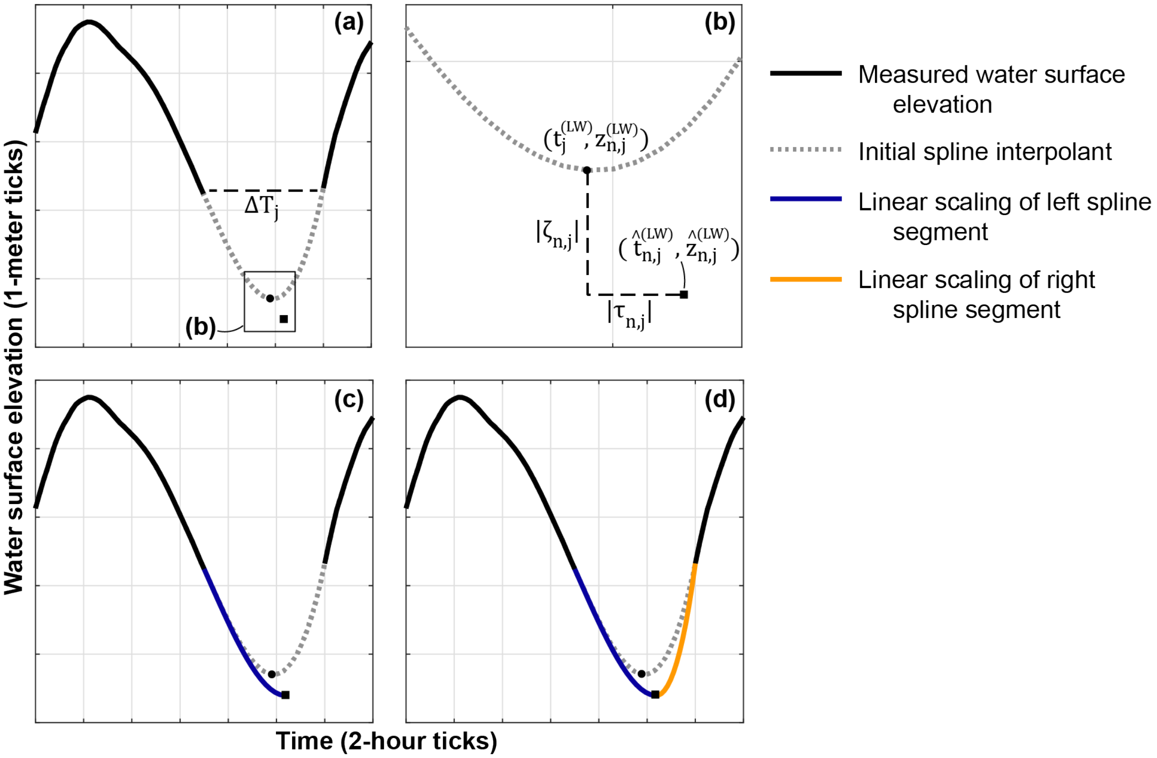

Figure 4.4: Method for correcting the spline interpolant during Monte Carlo analysis. **(a)** The j^{th} gap in the dataset, which has duration ΔT_j, is reconstructed using a cubic smoothing spline. **(b)** During the n^{th} Monte Carlo iteration, the spline-reconstructed low water coordinates $(t_j^{(LW)}, z_{n,j}^{(LW)})$ are randomly shifted to new coordinates $(\hat{t}_{n,j}^{(LW)}, \hat{z}_{n,j}^{(LW)})$ by drawing random values of $\zeta_{n,j}$ and $\tau_{n,j}$ from the empirical distributions in Figures 4.4(b) and 4.4(c), respectively. **(c)** We linearly scale the spline segment left of $t_j^{(LW)}$ such that low water falls at its corrected coordinates. **(d)** A second linear scaling is applied to the spline segment right of $t_j^{(LW)}$.

Bangladesh Inland Water Transport Authority (BIWTA), and the Mongla Port Authority (MPA). Records of varying quality exist for six locations along the Shibsa and Pussur channels; these are summarized in Table 4.2. After visually examining each dataset to determine whether the records were internally consistent, we discarded the data from Sundarikota, Chalna, and Nalian due to the large spans of missing data, erroneous water level spikes of up to 7 meters which do not coincide with any major atmospheric event (*i.e.*, cyclone-driven storm surge), and/or apparent inconsistencies in vertical datum which could not be easily corrected. Figure 4.5 displays an example of typical data quality. The remaining sites (Hiron Point, Mongla, and Khulna) displayed better overall quality, and we opted to retain these records after deleting several periods of questionable data from each site. For the Mongla record, which was comprised of two overlapping datasets with their timestamps offset by one hour, we retained the timestamp of the second dataset and shifted the first dataset one hour earlier in time to align the two records. This correction is supported by the M_2 phase plot in Figure 3.6 from the previous chapter, which shows that the first Mongla dataset may have been timestamped one hour too late given the overall regional trend in tidal propagation.

The BWDB, BIWTA, and MPA datasets are reported relative to the Public Works Datum (PWD), which is defined on the BWDB website as

> *...a horizontal datum believed originally to have zero at a determined Mean Sea Level (MSL) at Calcutta [Kolkata]. PWD is located approx. 1.5 ft below the MSL established in India under the British Rule and brought to Bangladesh during the Great Trigonometric Survey.*[14]

The ambiguity of this definition does not inspire confidence in the absolute vertical referencing of the data; in particular, it is unclear how a “horizontal” datum would be useful over long (order of 10^2 km) distances on a curved planet[15]. To compensate for this uncertainty, we discarded the original vertical referencing and instead aligned the long-term datasets with the better-defined

---

[14] From `www.ffwc.gov.bd/index.php/definitions`; retrieved 8-Oct-2019.

[15] I suspect that the term “horizontal” actually refers to a smooth reference surface similar to the WGS84 ellipsoid. Given the mention of MSL, it also seems likely that this reference surface intersects the geoid (gravitational equipotential surface) at Kolkata. However, I have no independent support of this interpretation.

Table 4.2: Summary of long-term water surface elevation datasets provided by BWDB, BIWTA, and MPA, with notes on data quality.

Site name	**Coordinates**	**Dates recorded**	**Notes**
Hiron Point	21.8146°N, 89.4653°E	January 1977 to December 2010	As reported in Pethick and Orford (2013).
Sundarikota	22.1292°N, 89.5815°E	January 1977 to December 1991	Station is along the Pussur River about halfway between Hiron Point and Mongla. Missing significant portions of 1978, 1979, and 1983; abrupt datum shift at the end of December 1985.
Mongla Port	22.4718°N, 89.6003°E	January 1977 to November 2015	Composed of two datasets: first is from January 1977 to December 2011 (as reported in Pethick and Orford, 2013); second is from January 2000 to November 2015. During the overlap period, the second dataset is timestamped one hour *earlier* than the first dataset. Considering that the first dataset, which was used to produce Figure 3.6 in the previous chapter, generates an M_2 phase which is about 40° (≈80 minutes) later than predicted by the regional trend, we assume that the timestamp on the second dataset is more accurate. We therefore shifted the first dataset one hour earlier in time when splicing the two time series together.
Chalna	22.6016°N, 89.5279°E	January 1996 to March 2016	Missing data from May 2004 through August 2008. Data quality is extremely bad, with several abrupt datum shifts, non-negligible changes in tidal amplitude between consecutive spring-neap cycles, and regular 7-meter spikes in tidal range in 2015 and 2016 which do not appear in the remainder of the record (see Figure ## for examples). The data were also collected manually (presumably via tide staff; see Chatterjee et al., 2013, for method description), so measurements were taken only during daylight hours.
Khulna*	22.8130°N, 89.5641°E	April 1990 to March 2016	Composed of two datasets: first is from April 1990 to November 2008; second is from January 1996 to March 2016. The timestamps on the two datasets agree during the overlap period. There are several datum shifts, but they are obvious enough to be recognized and deleted from the dataset. The final year of the record contains frequent spikes suggesting a 7-meter tidal range, which is inconsistent with our knowledge of the system; we deleted this segment of the record before proceeding with further analysis. Manual data collection at this sites limits the measurements to daylight hours only.
Nalian†	22.4650°N, 89.4349°E	April 1990 to March 2016	Station is located along the Shibsa River near Polder 32. Missing data from March 1995 to December 1995 and March 2001 to September 2008. Data quality is extremely bad, and the record does not appear to follow any consistent vertical datum.

*The metadata do not indicate where the measurements were taken in the Khulna region. We here provide general coordinates of the city center.

†Shaha and Cho (2016) alternately refer to this station as 'Nalianala'.

absolute vertical datum given by the 2017/2018 measurements. Our specific assumptions for each location are as follows:

- At Hiron Point, we assume minimal waveform amplification or deformation relative to the Bay of Bengal. This is consistent with our assumption in Section 3.5.1.2.1 of Chapter 3. Then, assuming that mean sea level in the Bay of Bengal coincides with the zero elevation in the EGM2008 geoid, we assign the long-term mean water level at Hiron Point (averaged over the full record, from 1977 to 2010) an absolute elevation of 0 m EGM2008.
- Mongla is positioned along the Pussur channel between Jongla and Pankhali, which are two sites with relatively low elevation uncertainty (see Table 4.1). Limiting our consideration to the 50^{th} percentile of instantaneous Monte Carlo elevations, the highest high water elevations recorded in October 2017 were 2.54 m EGM2008 at Jongla and 3.31 m EGM2008 at Pankhali. Meanwhile, the highest high water elevations at Mongla were 4.70 m PWD in October 2014 and 4.68 m PWD in October 2015. Under the assumption of a monotonic increase in high water level along the Pussur channel, we aligned the long-term data with the modern datasets by subtracting 1.76 meters (*i.e.*, $\frac{4.70\,\text{m}+4.68\,\text{m}}{2} - \frac{2.54\,\text{m}+3.31\,\text{m}}{2}$) from the original BWDB water surface elevations.
- After deleting the 7-meter spikes from the BWDB Khulna dataset, the remainder of the 2016 record appears visually well-aligned with the 50^{th} percentile of instantaneous Monte Carlo elevations collected at Khulna in 2017/2018. We therefore make no corrections to the vertical datum for the long-term Khulna record.

After applying the indicated corrections to the long-term datasets, we calculated long-term series of instantaneous gradients, $S = {}^{\Delta z(t)}/_{L}$ (see Equation 4.10), for the reaches from Hiron Point to Mongla and from Mongla to Khulna.

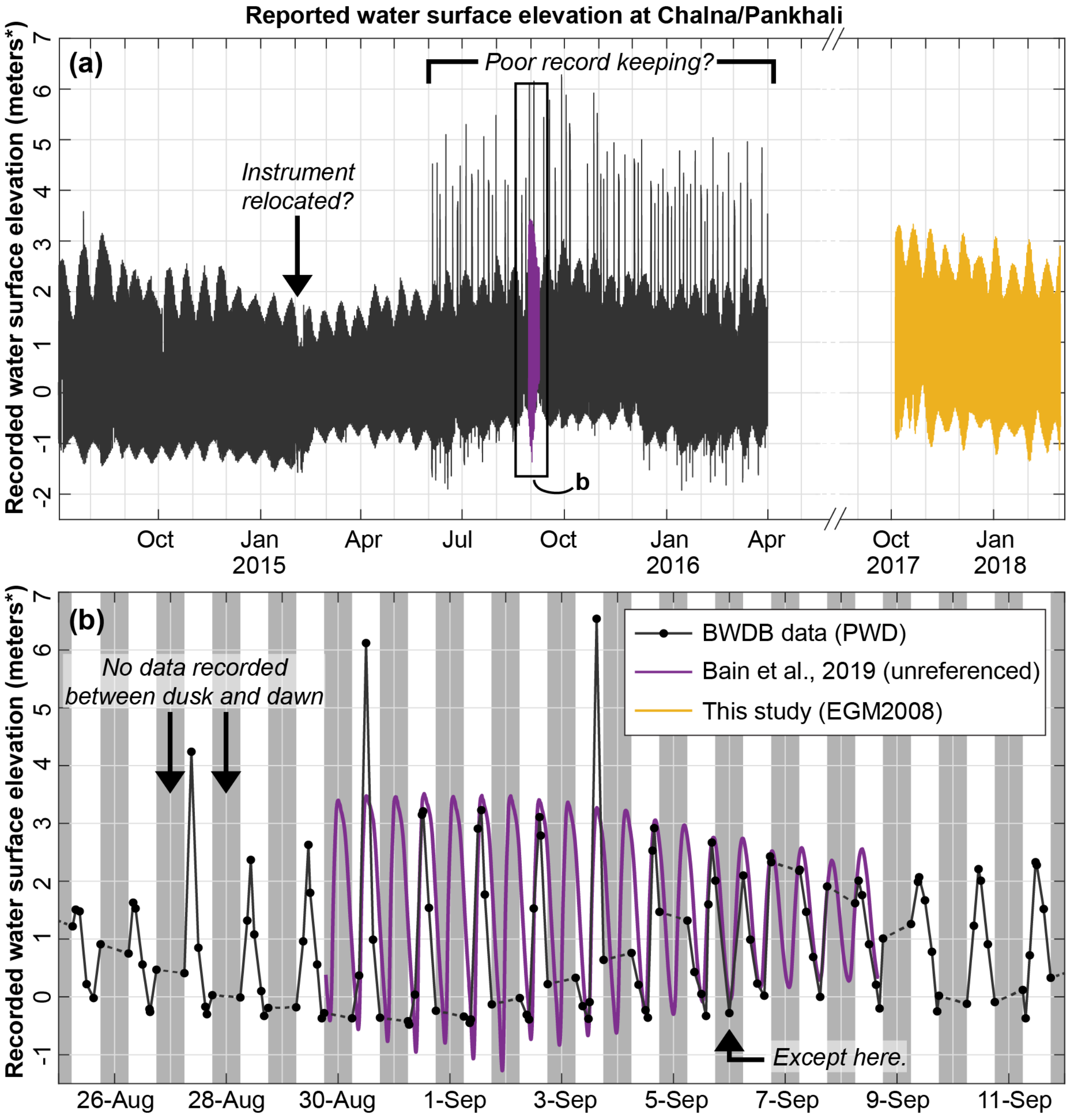

Figure 4.5: Example of data quality issues for the long-term BWDB tidal record from Chalna North. **(a)** When viewing the data collected during a 21-month period, we observe a sudden decrease in spring tide range (in February 2015), which suggests that the instrument was relocated to a new location where the tide is more strongly damped. However, there are no metadata available to confirm this. Additionally, from June 2015 to April 2016, the record is corrupted by arbitrary "spikes" which suggest a $\sim$ 7 meter tidal range, but this is inconsistent with the known behavior of the system. For comparison, we overlay our data from the same location in August/September 2015 and a second dataset from the Pankhali ferry ghat (less than two river kilometers away from Chalna North) collected in 2017/2018. **(b)** Viewing the data over a two-week window illustrates the manual nature of data collection. Measurements are recorded by hand based on a tide staff planted in the channel bed, and no readings are taken between sunset and sunrise. Although this is generally sufficient to produce an estimate of tidal range and semidiurnal phase, the detailed shape of the time series is not captured at this sampling frequency.

4.4 Results

4.4.1 SUBTIDAL WATER SURFACE GRADIENTS

Figure 4.6 displays time series of regionally- and temporally-averaged water surface gradients along the Shibsa and Pussur channels. As described in Section 4.3.2.4.2, these spatial gradients are defined as the slope of the regression line through the time-averaged water surface elevation values $\overline{Z(x,t_k)}$ for all sites x along a given channel, with the subscript k referring to a seven-day averaging window. Although the uncertainty is large, we are able to make two significant observations concerning water surface gradients in the Shibsa and the Pussur. First, both time series in Figure 4.6 display a persistent oscillatory behavior that corresponds with the spring-neap cycles of the tide. The peaks in subtidal surface gradient align with peak spring tide conditions. Second, we observe that the Pussur channel is more responsive to monsoon-season flow conditions. The 50^{th} percentile of subtidal water surface gradients in the Pussur decreases by ~ 0.3 cm/km between early October and early December, corresponding to the monsoon-to-dry transition. During the remainder of the dry season, the Pussur's spring-neap variations in water surface gradient oscillate about an approximately constant value of 1.05 cm/km. In contrast, the 50^{th} percentile of subtidal water surface gradients in the Shibsa oscillates about ~ 0.6 cm/km over the entire duration of the dataset, with no obvious response to changing seasonal conditions.

Separating the datasets into reach-specific subtidal gradients (Equation 4.7) elucidates the local variability in time-averaged tidal behavior, which is shown in Figure 4.7. Although the uncertainty on individual gradient measurements is large, it does not preclude the following observations. First, along the Shibsa channel, it is probable that maximum subtidal slopes occur along the 15-kilometer reach between Hadda and Shibsa Head (sites Ha and SH, respectively, in Figure 4.7d). The 50^{th} percentile of all Monte Carlo iterations for this reach remains near 1.5 cm/km over the full duration of the record. In contrast, the northernmost Shibsa reach between Shibsa Head and Paikgachha (KP) likely displays a lower subtidal gradient, with the 50^{th} percentile near 0 cm/km and the 95^{th} percentile not exceeding 1.5 cm/km. Our second observation is that the monsoon-to-dry variation in the Pussur's regional surface gradient (Figure 4.6) is a persistent feature in both

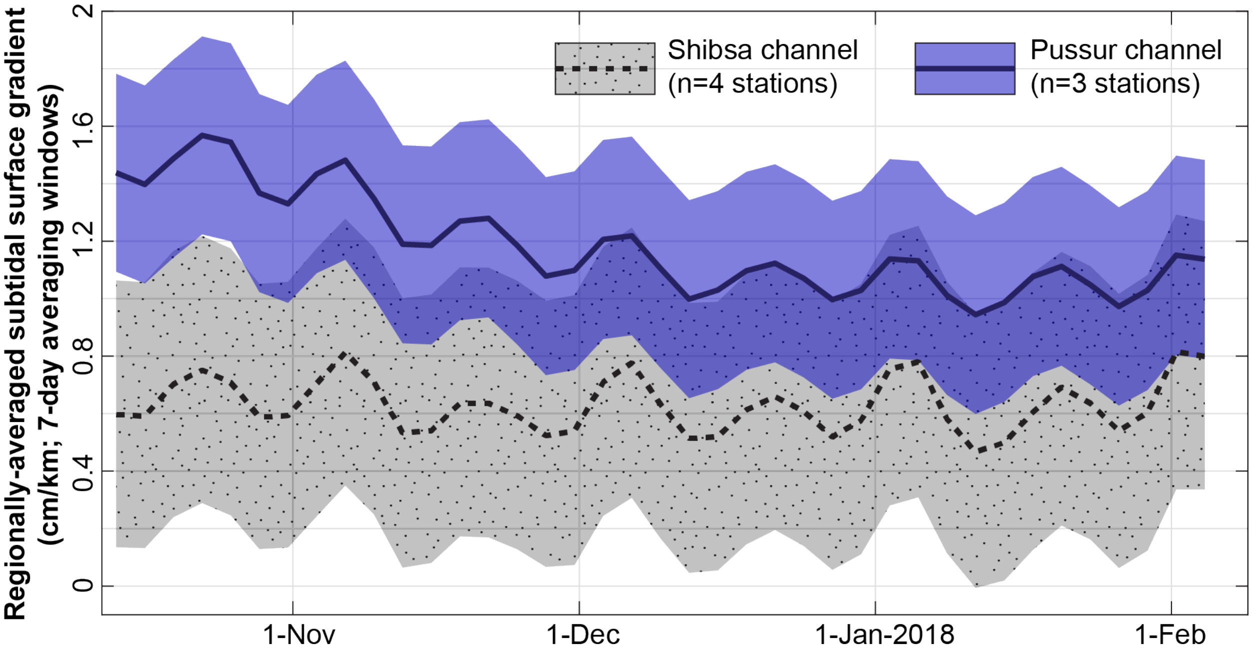

Figure 4.6: Time series of regionally averaged, subtidal surface gradients for 7-day averaging windows. These gradients are defined as the spatial slope of the regression line through the time-averaged measurements for a given channel (*i.e.*, Adachai, Hadda, Shibsa Head, and Paikgachha for the Shibsa River; Jongla, Pankhali, and Khulna for the Pussur River). Positive gradients slope towards the south or southwest, which favors ebb-directed flow. Dark lines indicate the 50th percentile of 10,000 Monte Carlo iterations, while the shaded regions bound the 5th through 95th percentiles.

local Pussur reaches displayed in Figure 4.7(b). Moreover, this seasonally-variable behavior is largely absent from the Shibsa reaches, with the possible exception of a slight dry season decrease in gradient for the channel segment between Hadda and Shibsa Head (Figure 4.7a).

Third, Figure 4.7(c) indicates a strong likelihood of a negative (*i.e.*, northeastwards-directed) subtidal gradient along the Gorkhali channel between Shibsa Head and Pankhali. This is unusual because it indicates that the water surface on average slopes inland, away from the Bay of Bengal. In contrast, the Dhaki and Shengrali channels (sites Ha to Pa and SH to KSY, respectively) most likely have positive or southeastwards-directed subtidal gradients, which is consistent with the expected direction for a deltaic distributary network. We revisit the influence of these mean surface slopes in Section 4.5.3.

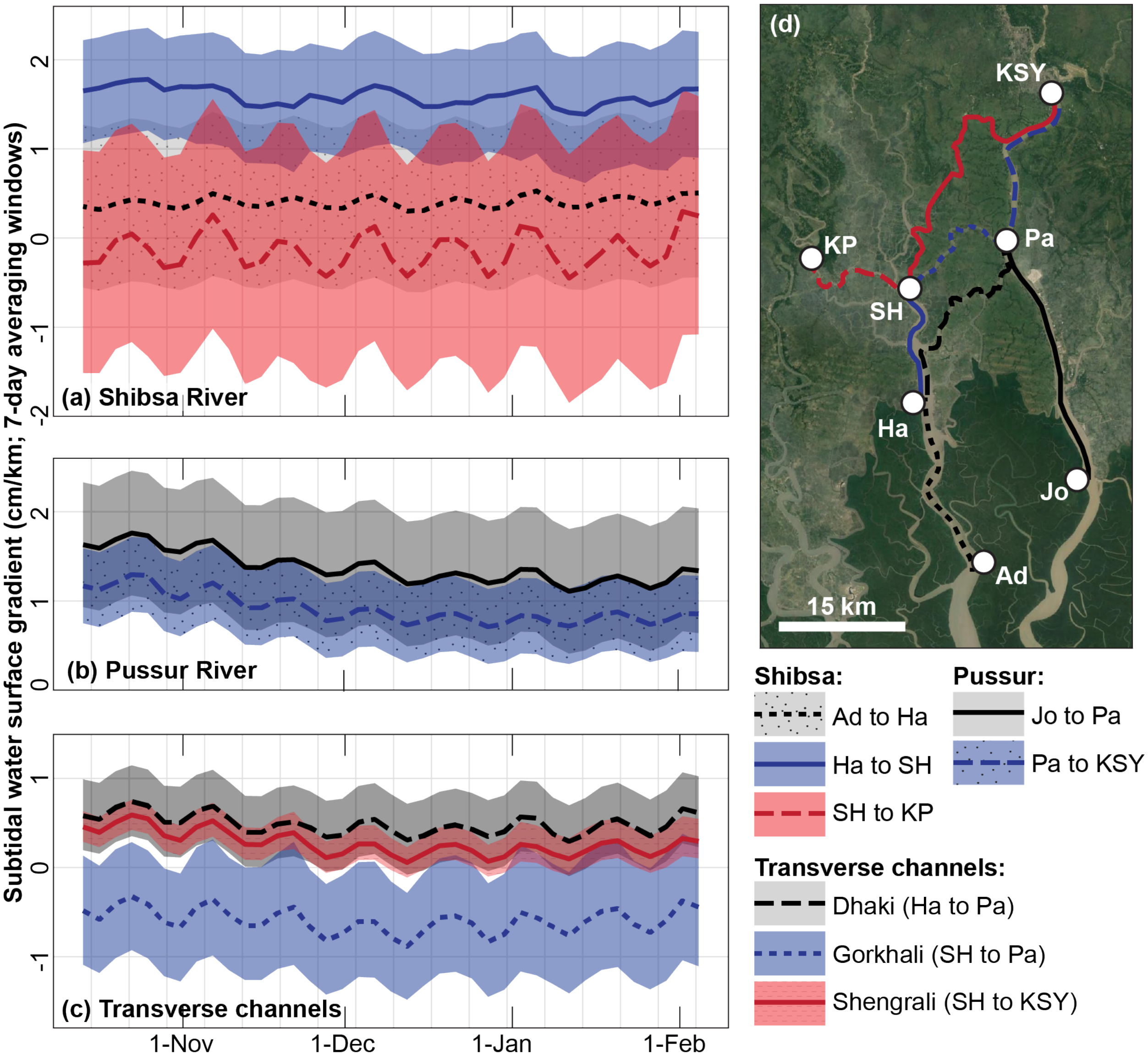

Figure 4.7: Time series of spatially localized subtidal surface gradients for 7-day averaging windows. Positive gradients slope towards the south or southwest, favoring ebb-directed flow, whereas negative gradients slope towards the north or northeast. Note that the vertical scale is the same in each of subplots (a), (b), and (c). Dark lines indicate the 50th percentile of 10,000 Monte Carlo iterations, while the shaded regions bound the 5th through 95th percentiles. Subplot (d) displays the location of all measurement stations used in these calculations.

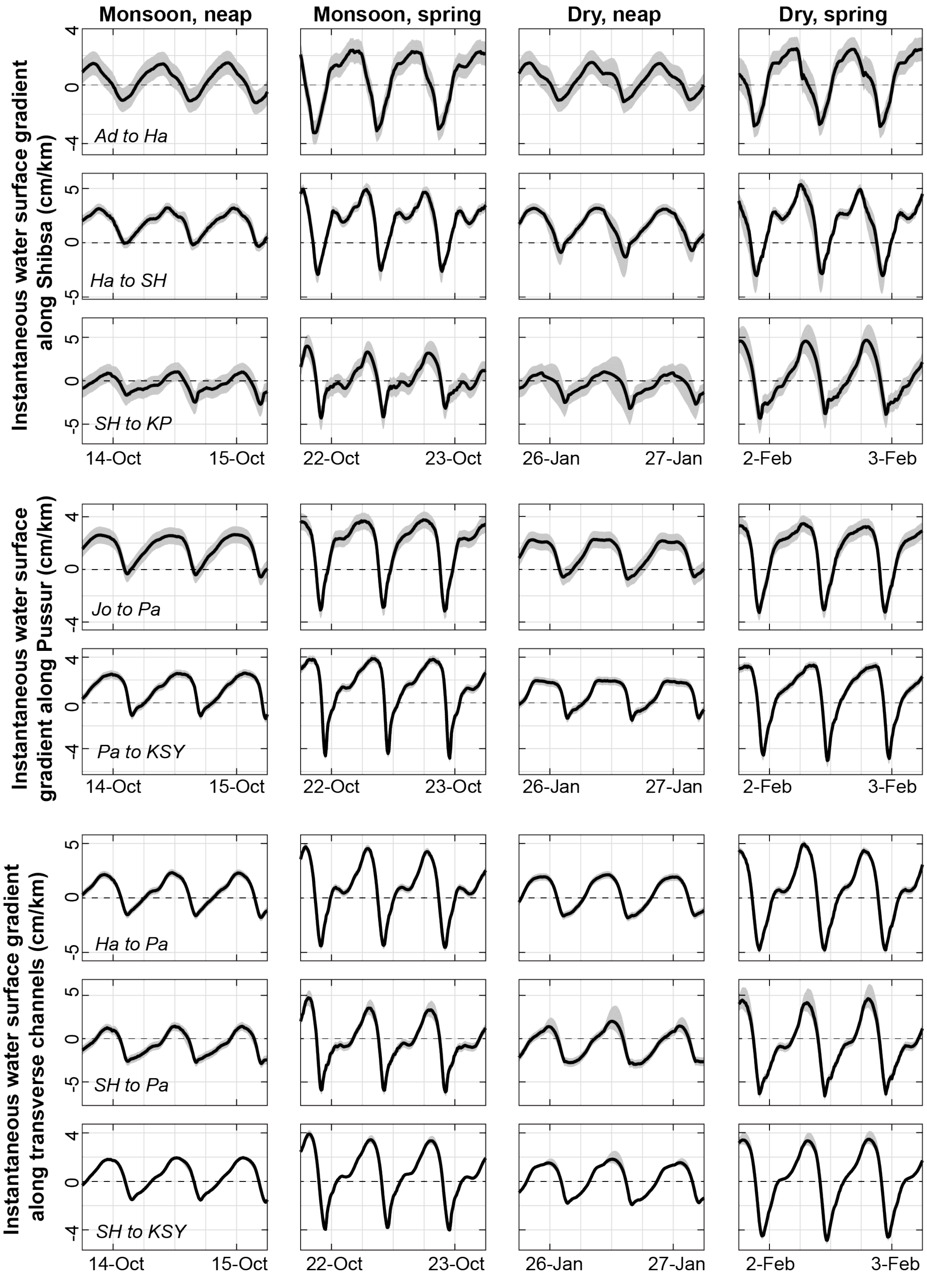

Figure 4.8: Local, instantaneous water surface gradients under various flow conditions in October 2017 and January/February 2018. Each row corresponds to the channel reach labeled in the first column; see Figure 4.7(d) for a map of reach locations. The black line indicates the 50th percentile of 10,000 Monte Carlo iterations, while the gray shaded regions bound the 5th through 95th percentiles.

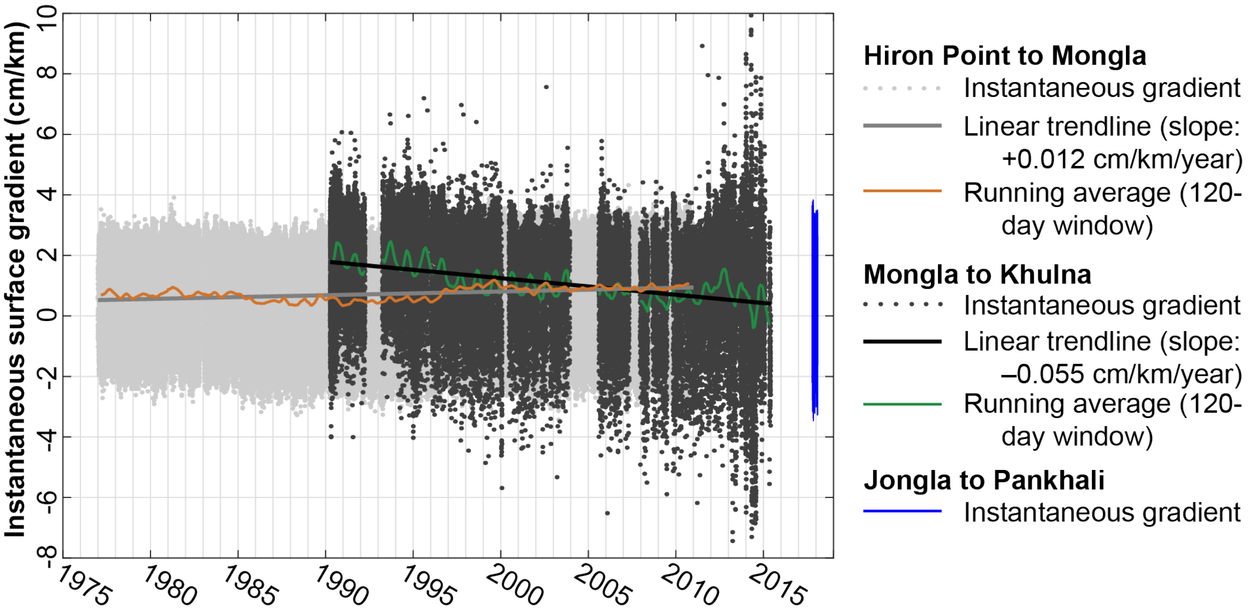

Figure 4.9: Instantaneous water surface gradients along the Pussur channel between Hiron Point and Mongla and between Mongla and Khulna based on long-term records from BWDB, BIWTA, and MPA. For comparison, we include the 50th percentile of the Monte-Carlo generated instantaneous surface gradients for the Pussur reach between Jongla and Pankhali in 2017/2018. The solid black and gray lines are best-fit trends for all data calculated via linear regression, whereas the green and orange lines are running averages with a 120-day window. Due to irregular sampling (*e.g.*, missing months of data, no nighttime measurements from Khulna, *etc.*), the number of samples in any given 120-day window is not constant.

4.4.2 INSTANTANEOUS GRADIENTS

Figure 4.8 displays time series of instantaneous water surface gradients under contrasting flow conditions for the same channel reaches shown in Figure 4.7(d). During spring tides, the water surface gradient reverses sign at all sites, with peak gradient magnitudes of $|S| \approx 4$ to 5 cm/km. At most locations and under most flow conditions, the duration of $S > 0$ equals or exceeds the duration of $S < 0$, indicating the expected tendency for the water surface to slope towards the Bay of Bengal. Three extreme cases are the Shibsa River between Hadda and Shibsa Head (labeled as "Ha to SH" in Figure 4.8), the Pussur between Jongla and Pankhali (Jo to Pa), and the Pussur between Pankhali and Khulna (Pa to KSY), where the water surface gradient is continuously positive or reverses sign only briefly. However, there are two significant exceptions to this behavior. The Gorkhali River (SH to Pa) displays the opposite pattern in which the duration of $S < 0$ exceeds the duration of $S > 0$ during both spring and neap tides and under both monsoon and dry flow conditions. The northernmost Shibsa reach (SH to KP) also slopes northwards for a larger-than-expected portion of the tidal cycle, with the exception of dry season spring tides when the anomalous behavior disappears.

4.4.3 LONG-TERM GRADIENTS ALONG THE PUSSUR

As shown in Figure 4.9, instantaneous surface gradients along the Pussur channel have a nonzero trend through time. Along the southernmost reach between Hiron Point and Mongla, the amplitude of the slope oscillations displays minimal long-term variability, although the time-averaged surface gradient has increased by approximately 0.01 cm/km/year over the 34-year record. However, the running average plots above the trendline from 1977 to 1985, below the trendline from 1985 to 1997, and above the trendline for the remainder of the time series; these abrupt transitions in mean surface gradient may indicate datum shifts due to instrument remounting (Pethick and Orford, 2013) which we did not successfully remove from the original record. Consequently, it is not clear whether the long-term increase in mean surface gradient is an actual signal or a consequence of inconsistent data collection. In the northern Pussur reach between Mongla and Khulna, the long-term trend is much stronger, with the linear trendline indicating a best-fit change in surface gradient of -0.055 cm/km/year between 1990 and mid-2015. The range of instantaneous gradient values also increases from approximately 10 cm/km in 1990 to 17 cm/km in 2015. Visual examination of the datasets provides no obvious indication that this increase in range is a consequence of poor recordkeeping or an inconsistency in vertical datum. However, considering that the range of values calculated for the overlapping Jongla-to-Pankhali reach in 2017/2018 is comparable to the earlier segment of the Mongla-to-Khulna time series, and given the overall low quality of the long-term datasets, we cannot eliminate the possibility that the increase in instantaneous gradient range around 2015 is a product of poor data quality rather than a real signal.

4.5 Discussion

4.5.1 INITIAL INTERPRETATION OF THE DATA

The results presented in Section 4.4 provide insight into how the channel network geometry and the boundary conditions influence water surface elevations along the Shibsa and Pussur channels. In the following subsections, we describe several features of the system which likely contribute to the observed tidal behavior.

4.5.1.1 Influence of platform inundation on water surface gradients

As shown in Figures 4.6 and 4.7, time-averaged or "subtidal" water surface gradients are more positive during spring tides compared to neap tides. A variety of mechanisms may underlie this phenomenon, including enhanced river-tide interactions during spring tides (*e.g.* Cai et al., 2016), time-variable discharge routing (Hale et al., 2019a; Bain et al., 2019), and inundation of the Sundarbans. We here consider the latter because it has received comparatively little attention in the literature and may have significant implications for interpreting the system's long-term behavior. Platform inundation influences the tide in terms of both waveform amplitude and waveform shape. The paper by Pethick and Orford (2013) documents significant tidal amplification in this region since the 1970s, with the tidal range at Khulna more than doubling between 1972 and 2017 (see also Bain et al., 2019). The authors attribute this amplification to the embankment-induced constriction of the channels; since the tidal prism can no longer be stored horizontally on the platform, the vertical range must increase to accommodate the volume of water entering the system. By the same reasoning, we would expect regionally-averaged subtidal surface gradients (Figure 4.6) to be greater during spring tides because platform inundation limits tidal amplification in the southernmost channel segments.

However, when we consider the local subtidal gradients (Figure 4.7), embankment-generated waveform amplification cannot entirely explain the spring-versus-neap gradient variations. If horizontal-versus-vertical volume storage were the exclusive cause of spring tide slope enhancement, then we would expect the greatest spring-versus-neap variation in slope to occur in channel reaches spanning the boundary between the Sundarbans and the polders. The data do not support this; for example, the largest oscillations in time-averaged gradient magnitude occur in the northernmost Shibsa reach (SH to KP), whereas the southernmost Shibsa reach (Ad to Ha) displays comparatively lower variation in gradient between spring and neap tides. Additionally, the southern and northern Pussur reaches (Jo to Pa and Pa to KSY, respectively) display approximately equal-amplitude variations in gradient. It rather appears that enhanced waveform deformation during spring tides (see Figures 3.7 and 3.8 in the previous chapter) is largely responsible for the observed increase in subtidal gradient. This effect is best illustrated by examining Figure 4.8, which shows that the increase in time-averaged slope during spring tides is not generally a result of $|S_{\max}| \gg |S_{\min}|$, but rather is driven by the extended duration of $S > 0$.

4.5.1.2 Influence of Gorai discharge

Figures 4.6 and 4.7 also indicate a greater seasonality in water surface gradients along the Pussur channel. One possible explanation for this behavior is the river-tide interaction between the tidal waveform and the Gorai River discharge entering the system from the north, which produces a monsoon-season setup in mean water level. This observation supports our analysis in Section 3.5 of the previous chapter, where we proposed that the Pussur's greater seasonal variation in M_2 celerity results from river-tide interactions in the Pussur channel. The primary significance of these results is to illustrate that although the Shibsa channel is the dominant conduit for tidal discharge within the study area (Pethick, 2012; Hale et al., 2019a; Bain et al., 2019), the Gorai River nevertheless exerts a stronger control on tidal propagation in the Pussur channel.

In Chapter 2, we proposed two alternative hypotheses to explain the ongoing basin-capture event in which a large volume of Pussur basin is now filled and drained by the Shibsa channel. Specifically, we suggested that:

- **Alternative hypothesis #1:** Polder construction drove tidal amplification (Pethick and Orford, 2013), which then generated an enhanced tidal setup (Cai et al., 2016) in the Pussur channel. This had the effect of *reducing* the Pussur's water surface gradient at a critical position in the network (*i.e.*, the Pussur reach containing the transverse channel bifurcations), which minimized the Pussur's gradient advantage and increased the proportion of Gorai discharge allocated to the Shibsa (*c.f.* Sassi et al., 2011).

- **Alternative hypothesis #2:** Under pre-1960s flow conditions, the large influx of freshwater Gorai discharge (Winterwerp and Giardino, 2012) behaved as a "barrier" to Shibsa tidal discharge entering the transverse channels. The subsequent upstream infilling and decline of Gorai flow rates enabled the Shibsa's flood prism to propagate into the Pussur via the transverse channels, leading to the basin capture event described in Chapter 1.

Although the data in this chapter are insufficient to test Hypothesis 2, we are able to revisit the validity of Hypothesis 1. A necessary implication of the first hypothesis is that although the water surface gradient along the *entire* Pussur (*i.e.*, from Hiron Point to an arbitrary location above the tidal limit) should be greater than the water surface gradient along the Shibsa, there must be a *local* decrease in the Pussur's water surface gradient in the vicinity of the transverse channel bifurcations. Figure 4.9 supports the idea of a long-term decrease in time-averaged water surface gradient for the Pussur reach containing the transverse channels (Mongla to Khulna). However, in the absence of data prior to the 1990s, we cannot determine whether the onset of this slope decrease coincided with polder construction in the 1960s and 1970s. If the possible long-term increase in mean surface gradient between Hiron Point and Mongla is a real signal and not a consequence of uncorrected datum shifts in one or both datasets, this would also support our first hypothesis, but the poor data quality hinders a more accurate result. In other words, the data are not inconsistent with Hypothesis #1, but they are also insufficient to draw a strong conclusion about its validity. Obtaining longer and/or higher quality tidal records from would enhance our ability to evaluate the hypotheses from Chapter 2.

4.5.1.3 Influence of channel head bathymetry

The results presented in Section 4.4 also suggest that the geometry of the northernmost channel reaches exerts a significant control on water surface gradient. Although the Pussur's monsoon-season gradient enhancement may be partly explained by the influx of Gorai discharge from the north, Figure 5 also indicates the possibility that the Pussur's regional surface gradient is greater than the Shibsa's even during the dry season, when Gorai flow rates are effectively zero (Winterwerp and Giardino, 2012). Varying bed profiles in the Shibsa and Pussur are one explanation for this difference in dry season gradients. It is typically reasonable to assume a negligible bed slope in estuarine settings (*e.g.* Savenije, 2005); however, bathymetric profiles from Pethick (2012) indicate Khulna is far enough inland for the bed slope to influence waveform behavior. Since the tidal range remains nearly constant between Mongla and Khulna (Bain et al., 2019), the effect of a nonzero bed slope must be to force the entire waveform higher in absolute elevation as it travels upstream, thereby increasing the time-averaged water surface gradient along the Pussur channel.

In contrast, the channel geometry near Shibsa Head may generate a different tidal behavior in the Shibsa River. Published discharge data from Shibsa South and Shibsa North (Hale et al., 2019a) and an unpublished ADCP dataset collected at Shibsa Head during the same study indicate a systematic variation in phase lag between the vertical and horizontal tide with distance northwards along the Shibsa channel. Figure 4.10 shows that there is a 130-minute delay between low water and low water slack at Shibsa South; this reduces to 70 minutes at Shibsa North and only 30 minutes at Shibsa Head, indicating that the waveform behaves increasingly like standing a wave as it approaches the upper reaches of the channel. One explanation for this change in behavior is the abrupt decrease in channel depth at Shibsa Head (see bathymetry in Figure A.1), which may produce a substantial reflection in waveform energy that generates a standing wave in this region. It is well established that fully closed channels (*e.g.*, due to damming; Díez-Minguito et al., 2012) will develop a standing wave at the channel head due to full reflection of the waveform energy, and observations from the Taiwan Strait indicate that partial waveform reflections at a bathymetric step can produce a similar transition towards standing wave behavior (Jan et al., 2004). Such a reflection would also drive a local increase in water surface elevation (*e.g.*, Garel and Cai, 2018). This is consistent with our observation that the time-averaged water surface elevation at Shibsa Head is likely several centimeters higher than the average water surface elevation at both Paikgachha and Pankhali (sites KP and Pa, respectively; see Figures 4.2) and explains the near-zero or negative subtidal surface gradients between Shibsa Head and these two locations (Figure 4.7).

Alternatively, theoretical analyses (Hunt, 1964; Wright et al., 1973; Jay, 1991; Friedrichs and Aubrey, 1994) indicate that strongly convergent, frictional channels will generate a tide that behaves like a standing wave in the sense that the horizontal and vertical signals are exactly 90° out-of-phase, although no reflected wave is present. If this is a more accurate description of the Shibsa channel, then perhaps the transition from a wide, deep channel with large *e*-folding lengths for both width and depth (see Table 3.4 in the previous chapter) to funnel-shaped khasland channels (Wilson et al., 2017) is responsible for the unusual tidal behavior near Shibsa Head. Nevertheless, the data presented in Figure 4.10 support the idea that some aspect of channel geometry exerts a strong control on tidal behavior in the northern Shibsa channel.

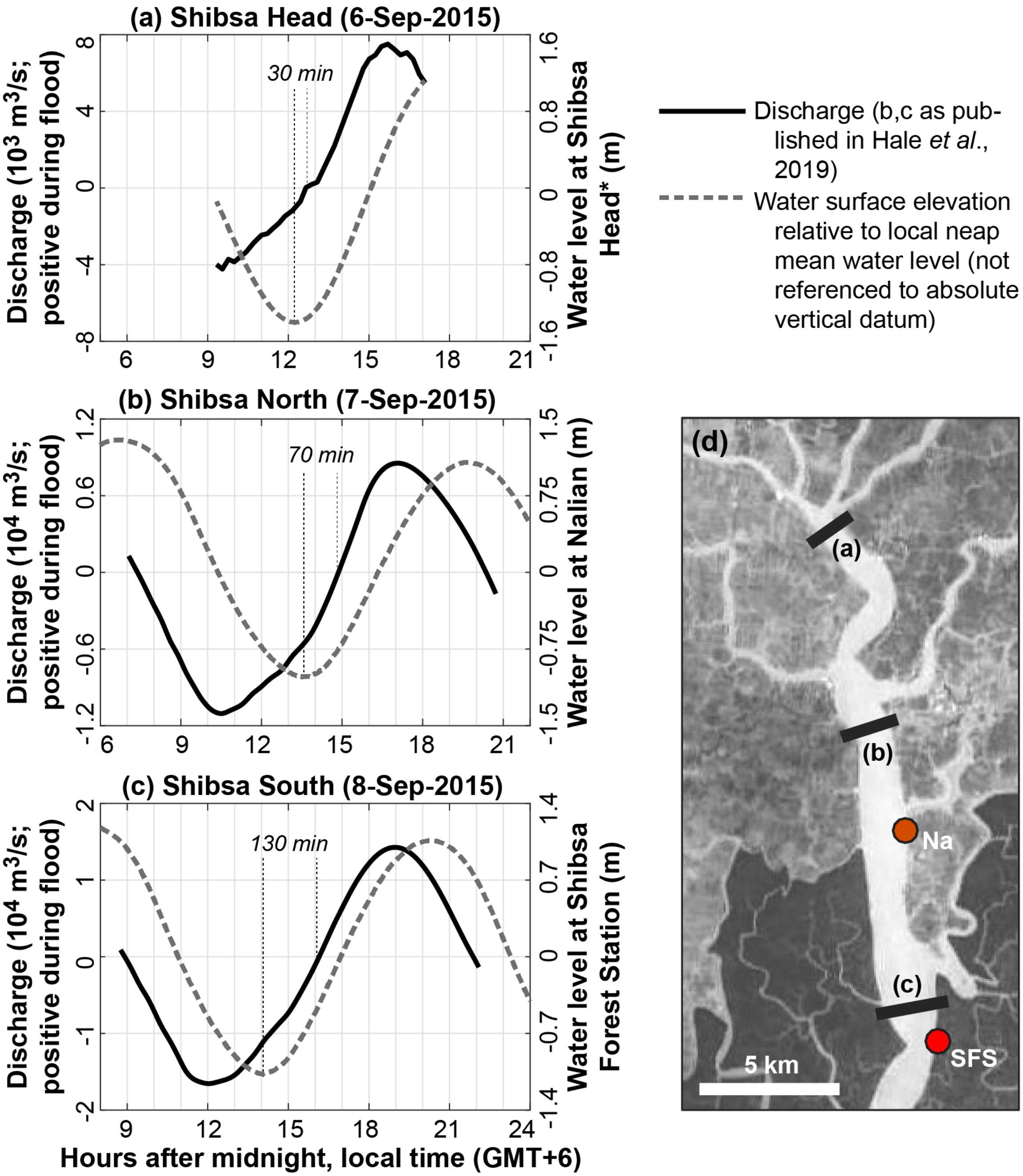

Figure 4.10: Plots of neap tide discharge and water surface elevation at three locations along the Shibsa River: **(a)** unpublished data from Shibsa Head, **(b,c)** the Shibsa North and Shibsa South transects from Hale et al. (2019a). The Shibsa Head ADCP data were collected using the method described by Hale et al. (2019a) andBain et al. (2019). Notice that the wave acquires an increasingly "standing" character (*i.e.*, the lag between low water and low water slack approaches zero) with distance northwards along the channel. *Due to the failure of the Shibsa Head pressure sensor in September 2015, we reconstructed the vertical tidal record at this site from the ADCP's vertical beam bathymetry by extracting a time series of depth each time the boat crossed a discrete point in space.

4.5.2 RELATIONSHIP BETWEEN INSTANTANEOUS SLOPE AND DISCHARGE

Prior studies of the Shibsa-Pussur channel network have quantified discharge under a variety of flow conditions (Hale et al., 2019a; Bain et al., 2019). The authors observed that net water transport over a semidiurnal tidal cycle may reverse direction under spring versus neap flow conditions, and the transport patterns are further influenced by the system's strong seasonality. However, the tide gauge data supplementing these projects were not referenced to an absolute vertical datum, and it was not possible to determine whether the observed discharge patterns were a response to seasonal or high-frequency variations in water surface gradient. We here reexamine the discharge datasets in the context of our vertically-referenced water surface elevation data with the goal of quantifying the slope-discharge relationship. For the following analysis, we define flood (*i.e.*, inland-directed) discharge as positive and ebb discharge as negative to be consistent with the coordinate system defined in Figure 4.3; note that this is opposite the sign convention adopted in Chapter 2.

As a first step, we observe that the slope between two vertically-unreferenced pressure sensors can be expressed as

$$S(x,t) = \frac{h(x_{i+1},t) - h(x_i,t)}{L} + \overline{S}(x) = \frac{\Delta h}{L} + \overline{S}(x) \ , \tag{4.11}$$

with h as defined in Equation 4.4 and $\overline{S}$ representing the yet-unknown mean water surface gradient between the two measurement sites during the period of interest. In other words, the magnitude of the oscillations in slope is independent of the sites' absolute elevations. We calculated the first term on the right-hand side of Equation 4.11 for three reaches that were instrumented in August/September 2015: the Shibsa reach between Shibsa Forest Station and Nalian, the Pussur reach between Jongla and Chalna, and the Dhaki River between Nalian and Chalna[16]. Then, to estimate appropriate values of $\overline{S}$ for the 2015 field campaign, we used nonlinear least squares to fit

---

[16] Although Hale et al. (2019a) also report Shibsa River discharge measurements from March 2015, the spatial distribution of pressure sensors (three instruments total, located at Sutarkhali, Nalian, and the Brick Factory) prevents us from calculating water surface gradients along the Shibsa River during this time period. We therefore focus our analysis on the August/September 2015 discharge datasets, which were supplemented by seven pressure sensors that provide more comprehensive spatial coverage.

a curve of the form

$$S_a(t) = \overline{S}_a + A_a \cos\left(\frac{360t}{365.25\,\mathrm{days}} - \phi_a\right) \tag{4.12}$$

to the 50th Monte Carlo percentile of each 2017/2018 surface gradient time series. Notice that Equation 4.12 is a sinusoid with 1-year periodicity to account for possible monsoon-versus-dry season changes in the local mean surface gradient; the subscript a indicates that the parameters are associated with annual variability[17]. We then estimated $\overline{S}$ (Equation 4.11) by minimizing the squared residual between $S_a(t)$ and the unreferenced values of ${}^{\Delta h}/_{L}$ from 2015. The outcome of this procedure is shown in Figure 4.11.

Comparing the time series of instantaneous surface gradients with the discharge data indicates that flow is against an adverse gradient for a large portion of the tidal cycle. For a frictionally-dominated flow, in which the quadratic friction term of the momentum equation is substantially larger than the momentum term (*e.g.* Parker, 1984), we would expect $S = 0$ and slack water (flow velocity $v = 0$ m/s) to occur nearly simultaneously. However, the velocity-slope phase plots in Figure 4.12 document a significant phase shift between S and v in the channels surrounding Polder 32. The duration of flow against an adverse gradient ranges from 50 minutes (at Shibsa South during spring tides and at Dhaki West during neap tides, in both cases leading up to the ebb-to-flood flow reversal) to over three hours (*e.g.*, at Chalna South during neap tides, leading up to the flood-to-ebb flow reversal). The only instance in which the phase plots approach the origin occurs during the extended spring tide high-water slack, although the slope never actually reverses from positive to negative during this period of zero or near-zero flow velocities.

The extended periods of flow against an adverse surface gradient suggest that momentum effects are important for driving tidal propagation through the Shibsa-Pussur channel network. To quantify the relative magnitude of friction and momentum effects in the study area, we first consider a scaling analysis of the momentum equation. Following the work of Parker (1984), we define

---

[17] An analogous approach was used in Chapter 3 for detrending the individual water surface elevation datasets; see Equation 3.3.

the following characteristic values of the system:

$\mathcal{D}$,	a representative channel depth
$\mathcal{N}$,	a representative amplitude of the vertical tide
$\mathcal{U}$,	a representative flow velocity
$\mathcal{T}$,	the tidal period
$\mathcal{L}$,	the tidal wavelength $(\approx \mathcal{T}\sqrt{g\mathcal{D}})$
ℓ,	the e-folding length of channel width .

Letting $\hat{\ell} = \min(\ell, \mathcal{L})$, and defining the dimensionless variables

$$\widetilde{h} = \frac{h}{\mathcal{D}} \ , \ \widetilde{z} = \frac{z}{\mathcal{N}} \ , \ \widetilde{v} = \frac{v}{\mathcal{U}} \ , \ \widetilde{t} = \frac{t}{\mathcal{T}} \ , \text{and} \ \widetilde{x} = \frac{x}{\mathcal{L}} \ ,$$

the momentum equation (Equation 4.1) scales as

$$\left[\frac{\hat{\ell}\mathcal{L}}{g\mathcal{D}\mathcal{T}^2}\right]\frac{\partial \widetilde{v}}{\partial \widetilde{t}} + \left[\frac{\mathcal{N}\hat{\ell}^2}{g\mathcal{D}^2\mathcal{T}^2}\right]\widetilde{v}\frac{\partial \widetilde{v}}{\partial \widetilde{x}} = -\frac{\partial \widetilde{z}}{\partial \widetilde{x}} - \left[\frac{8N^2\mathcal{N}\hat{\ell}^2\mathcal{L}}{\mathcal{D}^{10/3}\mathcal{T}^2}\right]\left(\widetilde{h} + \frac{\mathcal{N}}{\mathcal{D}}\widetilde{z}\right)^{-4/3}\widetilde{v}|\widetilde{v}| \tag{4.14}$$

(see Parker, 1984, for details). In Equation 4.14, the expressions in brackets scale the dimensionless term that follows, with the nondimensional water surface gradient $\partial\widetilde{z}/\partial\widetilde{x}$ having order of magnitude 10^0. We determined reasonable values of $\mathcal{D}$, $\mathcal{L}$, ℓ, $\mathcal{N}$, $\mathcal{T}$, and $\mathcal{U}$ using the bathymetric profiles from Pethick (2012) and Winterwerp and Giardino (2012), the discharge data of Hale et al. (2019a) and Bain et al. (2019), and the tidal elevation data described in Section 4.4; these are summarized in Table 4.3. In both the Shibsa and Pussur channels, we obtain scales on the order of 10^{-1} for the temporal acceleration term and 10^{-3} for convective acceleration. The friction term in the Shibsa is on the order of 10^{-1} to 10^0 for Manning's N ranging between 0.01 and 0.03, whereas in the Pussur this term is between 10^0 and 10^1 for the same range of Manning's N.

This analysis suggests that for the Shibsa-Pussur system, the momentum equation should be dominated by the temporal acceleration $\partial v/\partial t$, the surface gradient $\partial z/\partial x$, and the quadratic friction

Table 4.3: Parameters from the Shibsa and Pussur channels used to scale the momentum equation.

Variable	**Shibsa River**	**Pussur River**	**Notes**
$\mathcal{D}$	15 m	7 m	Based on bathymetric profiles from Pethick (2012) and Winterwerp and Giardino (2012).
$\mathcal{L}$	542 km	371 km	Calculated as $\mathcal{T}(g\mathcal{D})^{1/2}$.
ℓ	88 km	63 km	Fitted to bathymetric profiles from Pethick (2012) and Winterwerp and Giardino (2012).
$\mathcal{N}$	1.4 m	1.3 m	Typical M_2 amplitude in Polder 32 region; see Figure 3.6 in Chapter 3.
$\mathcal{T}$	44,712 s	44,712 s	=12.42 hours, *i.e.*, the M_2 period.
$\mathcal{U}$	1 m/s	1 m/s	Based on data from Hale et al. (2019a) and Bain et al.. (2019).

term. Although the balance between acceleration and friction varies between the two channels, the convective acceleration term $v\,{\partial v}/{\partial x}$ is persistently several orders of magnitude smaller than the other terms. This allows us to simplify Equation 4.1 to

$$\underbrace{\frac{\partial v}{\partial t} + gN^2\frac{v|v|}{R^{4/3}}}_{\text{LHS}} = \underbrace{-g\frac{\partial z}{\partial x}}_{\text{RHS}} . \tag{4.15}$$

Because we can determine the hydraulic radius $R(t)$ from the ADCP's vertical beam bathymetry (see Bain et al., 2019, for details), Manning's N is the only remaining unknown in Equation 4.15. We can therefore estimate the local balance between acceleration and friction by determining the value of N that produces the best fit between the left (LHS) and right-hand (RHS) sides of this equation.

Figure 4.13 displays time series of the individual terms in Equation 4.15 for the best-fitting local value of N, which ranges between 0.01 and 0.02. The agreement between the two sides of the equation is reasonable at most locations, although there are several exceptions. For example, at Shibsa South during spring tides, the LHS and RHS deviate substantially between 16:00 and 18:00 on 30-Aug-2015. This occurs during a period of time when the velocity was not measured directly (see Hale et al., 2019a), so the misfit most likely represents discharge extrapolation error. The largest error occurs for the Chalna South (Pussur) transect, where the entire LHS is shifted upwards by approximately 2×10^{-4} m/s^2 relative to the RHS. With the exception of this rigid vertical shift, the two curves are visually similar in shape; this suggests that the misfit could be generated by an error in referencing the 2015 slope dataset to the 2017/2018 data. However, it is also possible that irregular bathymetry or flow convergence at the nearby Pussur-Dhaki channel junction locally increases the convective acceleration term above the magnitude predicted by the scaling analysis.

The relative magnitude of the acceleration ($^{\partial v}/_{\partial t}$) and quadratic friction (containing $v|v|$) terms provides information about the role of frictional dissipation in generating the observed tidal behavior. In each subplot of Figure 4.13, we observe that maximum positive values of the friction term are substantially smaller than the maximum positive value of local acceleration. This suggests that when the tidal waveform enters the system from the Bay of Bengal and generates a north- or northeastwards-directed water surface gradient (which appears as positive values of the dashed blue line in Figure 4.13 due to the presence of $-g$ on the RHS of Equation 4.15), frictional dissipation is insufficient to balance this gradient, and the system's response is a large positive flow acceleration to balance Equation 4.15. In contrast, south- or southwestwards-directed water surface gradients (which plot as negative in Figure 4.13) are balanced by a frictional dissipation term which is as large or larger in magnitude than the acceleration term. This is true at all sites considered in Figure 4.13 but is particularly pronounced along the Dhaki channel, where the extreme negative values of the friction term are two to three times larger than the corresponding extrema in $^{\partial v}/_{\partial t}$. Based on these observations, we arrive at the following conclusions related to using water surface gradients as a predictor of flow:

1. For the Dhaki channel, the peak ebb flow velocity (*i.e.*, the extreme negative value of v) may be predicted, at first order, by the maximum southwestwards-directed water surface gradient between the Shibsa and Pussur. This relationship is especially strong under neap flow conditions. Due to the absence of suitable surface slope measurements to compare with discharge data from the Bhadra and Gorkhali channels (as reported in Bain et al., 2019), it is not clear whether this relationship holds for *all* transverse channels or whether it is specific to the Dhaki.

2. At all examined locations in the Shibsa and Dhaki channels, the maximum north- or northwest-directed water surface gradient is a reasonable first-order predictor of the maximum value of $\frac{\partial v}{\partial t}$. Unfortunately, an estimate of $(\frac{\partial v}{\partial t})_{\max}$ is insufficient to predict $v_{\max}$ in the absence of additional information.

3. Assuming that the systematic offset between the LHS and RHS for the Chalna South transect (Figure 4.13d) is a consequence of errors in vertical referencing rather than the product of a non-negligible convective acceleration term, Conclusions 1 and 2 also hold for the Pussur channel.

More generally, the reasonable agreement between the LHS and RHS in Figure 4.13 suggests that suitable bathymetry and absolute water surface elevation data, along with a reasonable value of Manning's N, may be sufficient information to obtain a first-order estimate of the velocity time series $v(t)$. Rewriting Equation 4.15 as

$$v'(t) + P(v,t)v(t) = Q(t) \ , \tag{4.16}$$

where

$$v'(t) = \left.\frac{\partial v}{\partial t}\right|_{x=x_i} \quad , \quad P(t) = gN^2\left[R(t)\right]^{-4/3}|v(t)| \quad \text{, and} \quad Q(t) = -g\left(\frac{z_{i+1}(t)-z_i(t)}{L}\right) \ ,$$

emphasizes that the equation is a first order, nonhomogeneous, nonlinear ordinary differential equation which could be solved numerically under the assumption of a suitable initial condition.

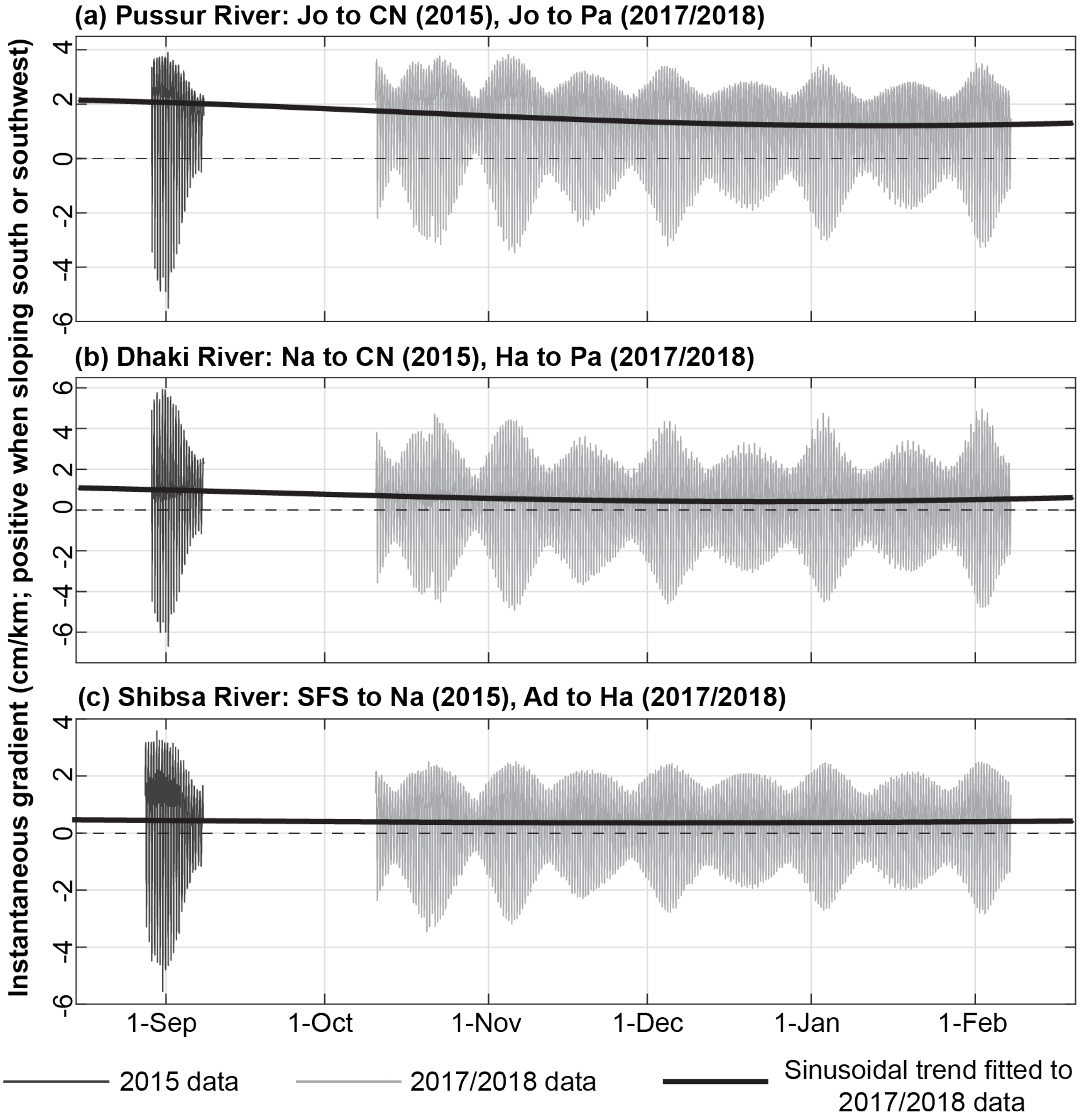

Figure 4.11: Method for estimating the absolute elevation difference between vertically-unreferenced tide gauge data from August/September 2015. After fitting a sinusoidal trend to the 2017/2018 water surface slope data, we minimize the squared residual between the trend and the differenced 2015 datasets to determine their absolute position on the *S* axis. Because the waveform is strongly deformed in our study area (see Chapter 2), the peaks of the slope time series are much broader than the troughs. This causes the sinusoidal trend to appear vertically "uncentered" on the data when plotted at this scale.

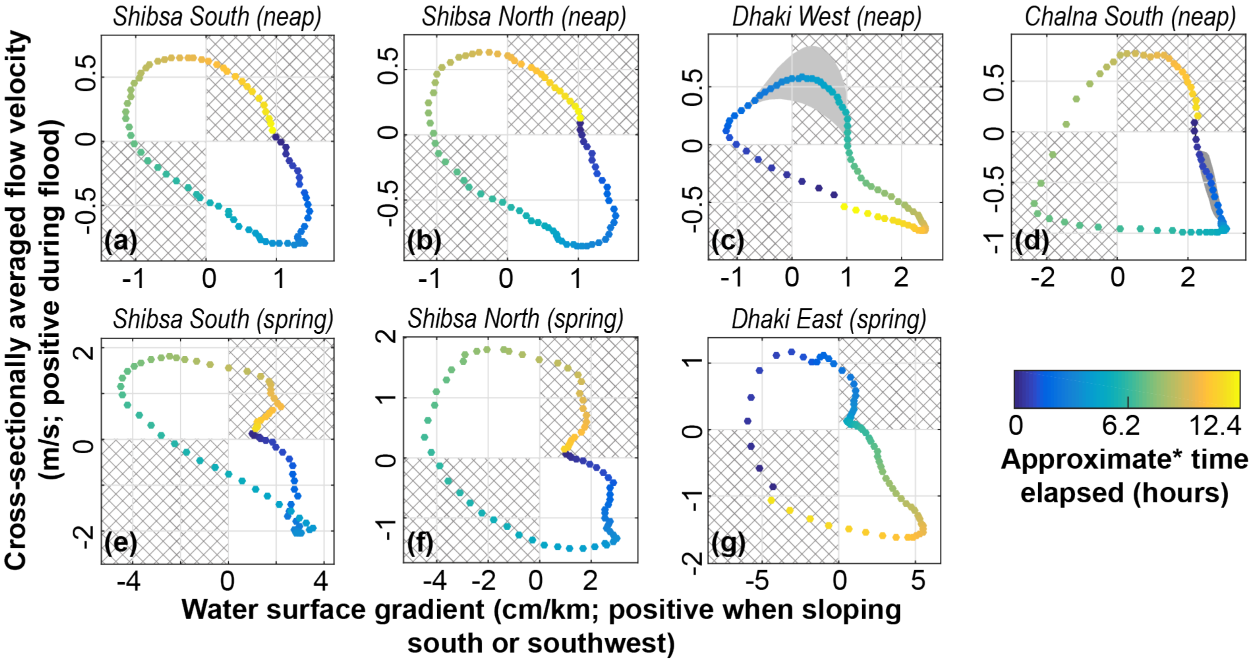

Figure 4.12: Relationship between water surface gradient and cross-sectionally averaged flow velocity during the August/September 2015 monsoon season for the Shibsa, Dhaki, and Pussur channels. Consecutive points are separated by a 10-minute sampling interval, and cross-hatched regions show times at which the flow is against an adverse surface gradient. The shaded regions in subplots (c) and (d) correspond to the discharge extrapolation envelopes in Figure 2.3. *Due to the presence of a small but non-negligible diurnal signal, the duration of any given oscillation varies between 12 and 13 hours (Hale et al., 2019a). The long-term average oscillation duration is the M_2 period of 12.42 hours.

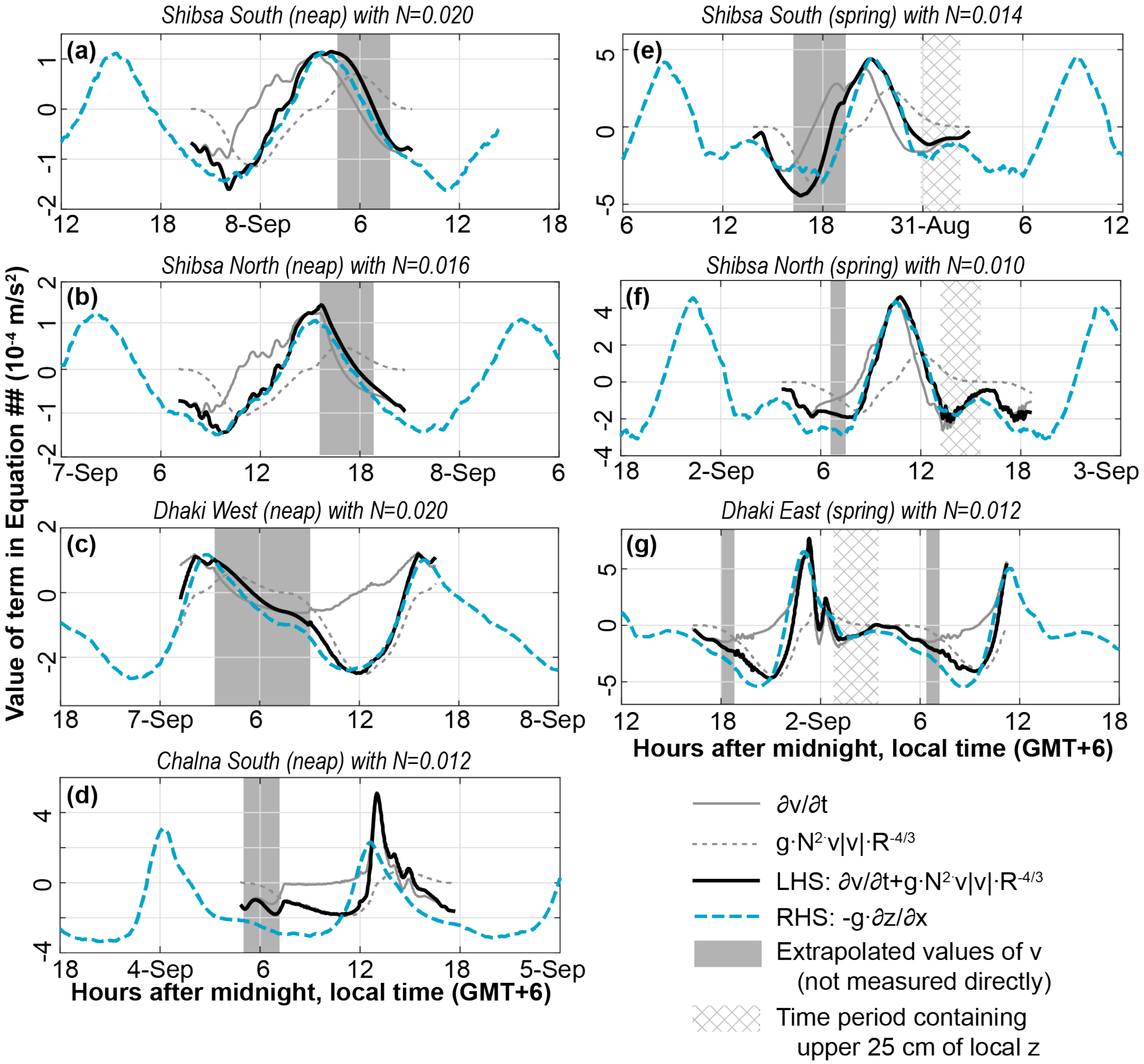

Figure 4.13: Time series of the individual terms in Equation 4.15 after selecting Manning's *N* to minimize the squared residual between the left- and right-hand sides ("LHS" and "RHS", respectively). The best-fit value of *N* is listed in the subfigure title. Periods of time containing extrapolated velocity values are indicated by gray shading. At Dhaki West, we utilize the lower bound of the velocity uncertainty envelope (corresponding to the interior of the phase ellipse in Figure 4.12c or the upper perimeter of the envelope in Figure 2.3f) because larger values of *v* produced a visually poor fit between the LHS and RHS. At Chalna South, we use the center of the velocity uncertainty envelope because there is no visual improvement in the fitted curves when we substitute higher or lower velocities. Note that the velocity dataset from Shibsa South during neap tides (subplot a) has been plotted one semidiurnal period earlier than the actual ADCP survey because the Nalian water surface elevation dataset terminates at midday on 8-Sep-2015.

4.5.3 RELATIONSHIP BETWEEN SUBTIDAL SLOPE AND DISCHARGE

The results of the previous section indicate that the local acceleration term $\partial v / \partial t$ is the same order of magnitude as the quadratic friction term in the momentum balance equation, and consequently we do not observe a one-to-one relationship between the water surface gradient $\partial z / \partial x$ and $v|v|$ in an instantaneous sense. However, several studies suggest that even for cases of non-negligible $\partial v / \partial t$, the subtidal (time averaged) momentum balance should be between the surface gradient and the friction term (*e.g.*, LeBlond, 1979; Liu and Aubrey, 1993; Gallo and Vinzon, 2005; Buschman et al., 2009). To examine whether this is true in the Shibsa-Pussur channel network, we approximate time-averaged flow velocity as the net tidal prism over one semidiurnal period, normalized by the mean cross-sectional area and the M_2 period of 12.42 hours. This definition allows us to include several transects from Bain et al. (2019) at which the net tidal prism was calculated by systemwide mass balance, but we lack a time series of $v(t)$ to average directly.

Plotting the time-averaged flow velocity against the mean water surface gradient (Figure 4.14a) suggests the possibility of a relationship between slope and discharge, especially when we consider that the predicted relationship is quadratic rather than linear. However, due to the large uncertainty in $\overline{\partial z / \partial x}$ (indicated by the horizontal extent of the rectangles in Figure 4.14) and the small sample size, we cannot draw a strong conclusion about whether our data support the hypothesis that $\overline{\partial z / \partial x} \propto -\overline{v|v|}$.

Even if such a relationship between $\overline{\partial z / \partial x}$ and $\overline{v|v|}$ exists in general, we observe several local deviations from the overall pattern. For example, at both Shibsa South and Shibsa North during monsoon season spring tides, the time-averaged flow velocity is towards the north, yet it is probable that the time-averaged water surface gradient is towards the south. The Gorkhali West ADCP transect reported in Bain et al. (2019) is also a likely exception to the proposed relationship. Due to the failure of the Shibsa Head pressure sensor in September 2015, we are unable to calculate water surface gradients along the Gorkhali River corresponding to the ADCP survey and consequently do not include Gorkhali West in Figure 4.14. However, assuming that the October 2017 water surface gradients depicted in Figure 4.7 are comparable in *direction* (if not magnitude) to those

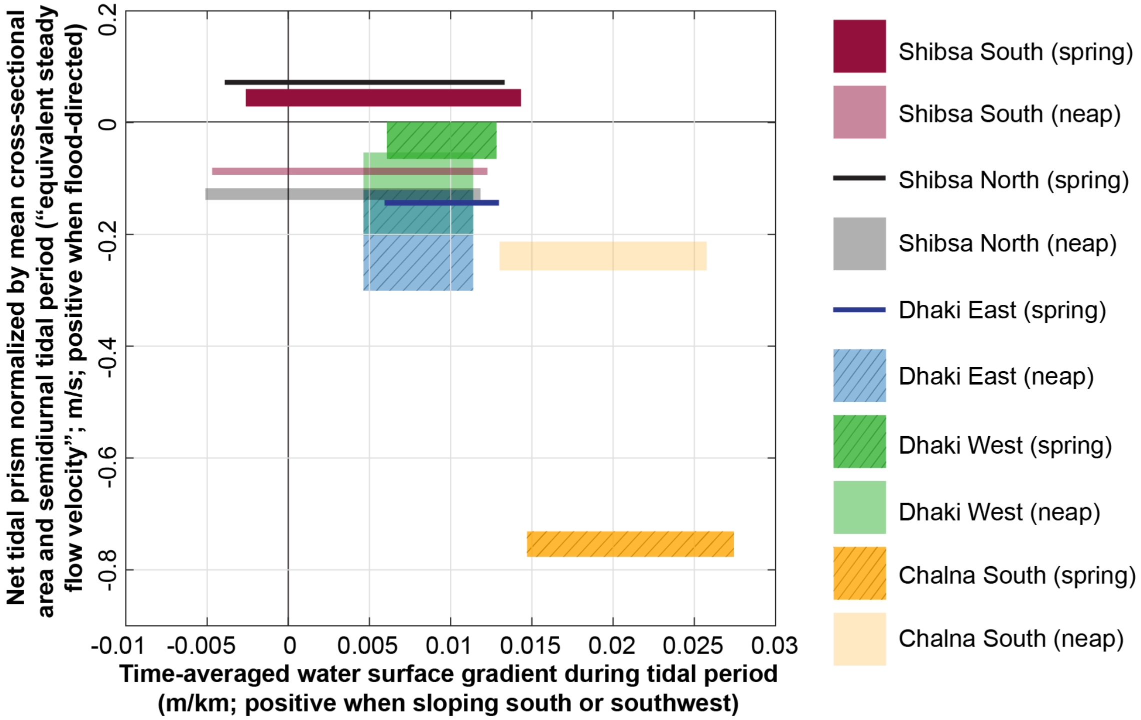

Figure 4.14: Plot of time-averaged water surface gradient versus the net tidal prism, normalized by mean cross sectional area and tidal period to approximate the mean cross-sectionally averaged flow velocity. Each rectangle is horizontally bounded by the 5th and 95th percentiles of the Monte-Carlo generated values, and vertically bounded by the tidal prism error bars reported by Hale et al. (2019a) and Bain et al. (2019). Recall that positive water surface gradients are directed to the south or southwest, while positive flow is directed north or northeast. All survey data are from the 2015 monsoon season, with the solid shading indicating a measurement that was collected directly by ADCP and diagonal lines indicating the the value was calculated by mass balance. See Figure 2.1 for a map of survey locations.

in September 2015, then the mean slope along the Gorkhali would have been towards the east, and the Gorkhali West transect would plot in the lower left quadrant of Figure 4.14. These three examples demonstrate that mean surface gradient alone is insufficient to determine the direction of time-averaged velocity in the Shibsa-Pussur network.

4.5.4 IMPLICATIONS FOR INTERPRETING THE CHANNEL-PLATFORM RELATIONSHIP IN LARGE-SCALE TIDAL DELTA PLAIN SYSTEMS

Tidal delta plain systems are characterized by a spatially extensive intertidal region which inundates during spring tides. Large-scale embankment construction on the GBMD in the 1960s and 1970s precipitated a several unintended consequences, including tidal amplification (Pethick and Orford, 2013), widespread channel abandonment (Wilson et al., 2017), accelerated compaction and subsidence on the embanked landscape (Auerbach et al., 2015), and bank retreat and collapse (Reed, 2015) due to flow reorganization within the interconnected channels (Bain et al., 2019). These issues illustrate the importance of understanding how tidally-driven flow within the channels interacts with the intertidal platform in order to inform sustainable long-term management of the engineered system. In this section, we synthesize observations from this chapter and Chapter 3 to determine the most accurate conceptualization of channel-platform interactions in the southwestern GBMD.

Mangroves are often cited as a major contributor to frictional effects on flow in a variety of contexts, including short-period wave attenuation (*e.g.*, Quartel et al., 2007; Horstman et al., 2014), tidal current dissipation (Chen et al., 2016; Mullarney et al., 2017), and mitigation of catastrophic inundation events including tsunamis and storm surge (Paul, 2009; Teh et al., 2009; Yanagisawa et al., 2009; Zhang et al., 2012; Chatterjee et al., 2013; Maza et al., 2015; Sakib et al., 2015). Although certain authors caution against overstating mangroves' efficacy for reducing the impact of extreme events (Baird et al., 2009; Feagin et al., 2010), the broad tendency is to equate mangrove systems with frictionally-dominated hydrodynamic behavior. It is therefore remarkable that, despite extending over 100 km through the largest mangrove forest on earth, we observe a relatively low frictional resistance to flow in the Shibsa and Pussur channels. For example, at Shibsa South (which is fully within the Sundarbans), the best-fit spring tide value of Manning's N is 0.014, and the local flow accelerations necessary to balance the slope term are the same order of magnitude as the friction term (Figure 4.13e). This Manning's N value is comparable to that obtained for the other survey sites in Figure 4.13, even though these sites are located in the poldered area and are not in direct contact with the Sundarbans[18].

---

[18] Except in localities experiencing rapid bank retreat, there is typically a stretch of intertidal platform (order of 10^1 meters wide, but occasionally exceeding 100 meters) outside of the embankments, so platform inundation effects are not fully absent even in the poldered region. See examples in Figure 4.15.

The observation of relatively low frictional dissipation in the channels has significant implications for interpreting how the channels interact with the intertidal platform in large-spatial-scale tidal delta plain systems like the GBMD. The literature presents two contrasting perspectives on how cross-platform flow influences tidal hydrodynamics within the channels. First, several studies suggest that the intertidal platform essentially behaves as an extension of the channel for conveying flow through the system (*e.g.*, Pethick, 1994; Fortunato and Oliveira, 2005; Brown and Davies, 2010). Taking the conceptual model of Pethick (1994) as an example, a large intertidal zone generates a geometry in which the cross-sectionally averaged depth at high water is *less* than the cross-sectionally averaged depth at low water. We provide the following quotation for illustrative purposes:

> *In such a channel the crest of the tidal wave tends to drag relative to the trough and an ebb-tide* [*asymmetry*][19] *is set up.* (Pethick, 1994, p. 81)

In other words, since $(gh_{\text{LW}})^{1/2} > (gh_{\text{HW}})^{1/2}$, the trough propagates at a faster rate than the crest and generates an ebb-asymmetric tidal waveform. If this conceptual model accurately represented the behavior of the Shibsa-Pussur channel system, then we would expect a large frictional influence on flow behavior, particularly during periods of platform inundation (*i.e.*, the cross-hatched regions of Figure 4.13e through 4.13g). Our data do not support this interpretation.

The alternative conceptualization of channel-platform interactions, which we believe is more consistent with our observations of the Shibsa-Pussur system, is that frictional dissipation within the channels is effectively independent of frictional dissipation on the platform. **This** idea follows from the work of Speer and Aubrey (1985), Giese and Jay (1989), Friedrichs and Aubrey (1994), Savenije (2005), and Savenije et al. (2008), each of whom treated the intertidal platform as an independent storage volume which does not convey flow in a direction parallel to the channel axis. We do not wish to imply that inundation of the Sundarbans has *no influence whatsoever* on tidal behavior in the Shibsa and Pussur channels. To the contrary, Equation 4.3 requires that volume exchange between the channel and the platform will locally change the water surface elevation within the

---

[19] We have substituted the word "asymmetry" for "dominance" to be consistent with the terminology of Chapter 3.

channel. Assuming a spatially variable rate of channel-platform exchange, this local variation in z will then increase or decrease $\frac{\partial z}{\partial x}$ along the channel axis, and this change in water surface gradient must be balanced an acceleration in v. Several authors have additionally introduced a source term into Equation 4.1 to quantify the channels' response to platform draining during ebb (Dronkers, 1964; Speer, 1984; Mariotti and Fagherazzi, 2011). The basic idea is that the water surface gradient must increase in order to accelerate the newly-added water draining from the intertidal platform, which initially has no momentum in the direction of the channel axis. It is outside the scope of this chapter to address whether it is more appropriate to modify Equation 4.3 or Equation 4.1 to best represent channel-platform interactions in the Sundarbans region. However, the key point is that drag on the intertidal platform does not directly increase flow dissipation within the channels themselves.

In Chapter 3, we examined the shape of the tidal waveform as a means of elucidating the dominant physical controls on tidal propagation through the system. Preliminary visual examination of the time series in Figure 3.1 suggests an that spring tides at Shibsa Forest Station are ebb asymmetric. This is consistent with the well-established idea that intertidal platform inundation will generate an ebb-asymmetric waveform by slowing crest advection, which influences the wave's second harmonic (*e.g.*, Parker, 1984; Friedrichs and Aubrey, 1988; Pethick, 1994; Fortunato and Oliveira, 2005; Brown and Davies, 2010). However, the $\Delta\phi_{2,4}$ profiles in Figure 3.6(d) indicate that $\Delta\phi_{2,4}$ never exceeds 170° along the Shibsa channel; this value indicates that the sum of M_2+M_4 is flood asymmetric. The observed values of $\Delta\phi_{2,4} < 180^\circ$ could conceivably result from averaging ebb-asymmetric spring tides and flood-asymmetric neap tides over 30-day analysis windows, but our analysis of high-frequency waveform shape confirms that the summed semidiurnal and quarterdiurnal species never produce an ebb asymmetric waveform when the platform inundates (corresponding to values of $\Delta z_{\text{plat}} \gtrapprox 0$ m in Figure 3.7b). This phenomenon is illustrated geometrically in Figure 3.5(b); notice that reconstructing a spring-tide signal using only the semidiurnal and quarterdiurnal species generates a flood asymmetric waveform. The reconstructed waveform does not become ebb asymmetric in appearance until the sextadiurnal tidal species are included in the sum.

Considering our prior observation that frictional dissipation does not translate into higher drag within the channel, the observed enhancement in M_6 deformation during platform inundation lacks a straightforward physical interpretation. As described in Section 3.2.2, the M_6 overtide is often associated with the product $v|v|$ in the quadratic friction term, and an increase in the drag coefficient has been correlated with enhanced M_6 amplitude in other systems (*e.g.*, Orescanin et al., 2016). However, if flow velocities on the platform are effectively zero as the data from the present chapter suggest, then the the quadratic friction term must also take a value of zero on the Sundarbans platform. Therefore, it is unlikely that enhanced frictional drag due to cross-platform flow is the generating mechanism for enhanced M_6 overtide production during spring tides in the GBMD system. Instead, M_6 generation in the Shibsa-Pussur system appears to be associated with the large-scale storage of water in the Sundarbans. Developing a theoretical explanation for third harmonic generation via volume loss effects is outside the scope of this paper, but we find this to be an interesting problem that merits attention in future studies.

The study by Aucan and Ridd (2000) may provide insight into this unexpected channel-platform dynamic in the Sundarbans region. These authors found that the ground surface slope of the intertidal region strongly influences the system's ability to produce ebb asymmetric tides. If the swamp slope is too low (order of 10^{-4} m/m), a large volume of water becomes perched on the platform during ebb which cannot drain efficiently into the main channel. This volume must instead ebb via a network of small, high-friction creeks, and its return to the main channel is sufficiently gradual that an ebb-asymmetric waveform geometry does not develop. An order-of-magnitude increase in the ground surface slope allows the intertidal platform to more efficiently drain into the main channel as sheetflow, and this rapid delivery of water from platform to channel generates an ebb asymmetry. Although we lack the necessary microtopographic data for quantifying surface slopes in the Sundarbans, qualitative observations suggest that natural levees on the channel banks may cause water to pond in the center of the platform and become disconnected from the main channels early during ebb. Evaluating the two-dimensional velocity field in the Sundarbans would therefore be a valuable tool for elucidating how the channel-platform interaction influences total waveform shape.

4.6 Conclusion

This chapter quantified instantaneous and subtidal water surface gradients with to evaluate whether tide gauge records can be used as a predictor of flow in the interconnected Shibsa and Pussur channels in southwest Bangladesh. We observe both spatial and seasonal variations in surface gradient between the two channels, including a systemwide increase in time-averaged surface gradient during spring tides and a monsoon-season steepening of the Pussur's surface gradient. Among the smaller "transverse" channels connecting the Pussur to the Shibsa, two have a west-directed (towards the Shibsa) time-averaged slope, while a third channel's time-averaged slope is towards the east. However, when the surface gradient data are examined in conjunction with flow velocity data collected during an earlier field campaign (Hale et al., 2019a; Bain et al., 2019), we observe that flow accelerations are the same order of magnitude as frictional dissipation, and the velocity may be directed against an adverse surface gradient for up to three hours before reversing. Predicting instantaneous flow velocities from a record of water surface gradients could conceivably be accomplished to first order by solving the momentum equation for a reasonable value of Manning's N and bathymetric data describing the hydraulic radius R as a function of the local tidal elevation, but there is not a straightforward one-to-one relationship between surface gradient and flow velocity.

When the data are averaged over a tidal cycle, we observe a weak relationship between the tidally-averaged water surface gradient and the tidally-averaged flow velocity. However, several locations deviate from the predicted behavior; these include two transects along the Shibsa River during monsoon-season spring tides, when the mean surface gradient is towards the south but the time-averaged flow velocity is towards the north, and the western Gorkhali River, where the mean surface gradient is towards the east but the mean velocity is towards the west. These examples illustrate the complex behavior of a large-scale, looping channel network with relatively low frictional dissipation to overcome the momentum of the flow.

An unanticipated outcome of this project is its implications for interpreting channel-platform interactions in tidal delta plain systems like the GBMD. Our data from Chapter 3 indicate a substantial increase in M_6 amplitude when the platform inundates; based on the often-cited association between the M_6 overtide and friction, one might interpret our results as a consequence of high frictional dissipation as the waveform travels through the Sundarbans mangrove forest. However, the results of this chapter indicate that frictional effects are overall low in the Shibsa-Pussur channel network, including at a site fully within the Sundarbans (the Shibsa South transect from Hale et al., 2019a). M_6 generation during platform inundation must therefore be a consequence of volume storage effects on the intertidal platform. We are unaware of any prior studies which identify an association between channel-platform volume exchange and the M_6 overtide, and further evaluation of this relationship may improve our understanding of flow patterns and mass exchange within the Sundarbans region.

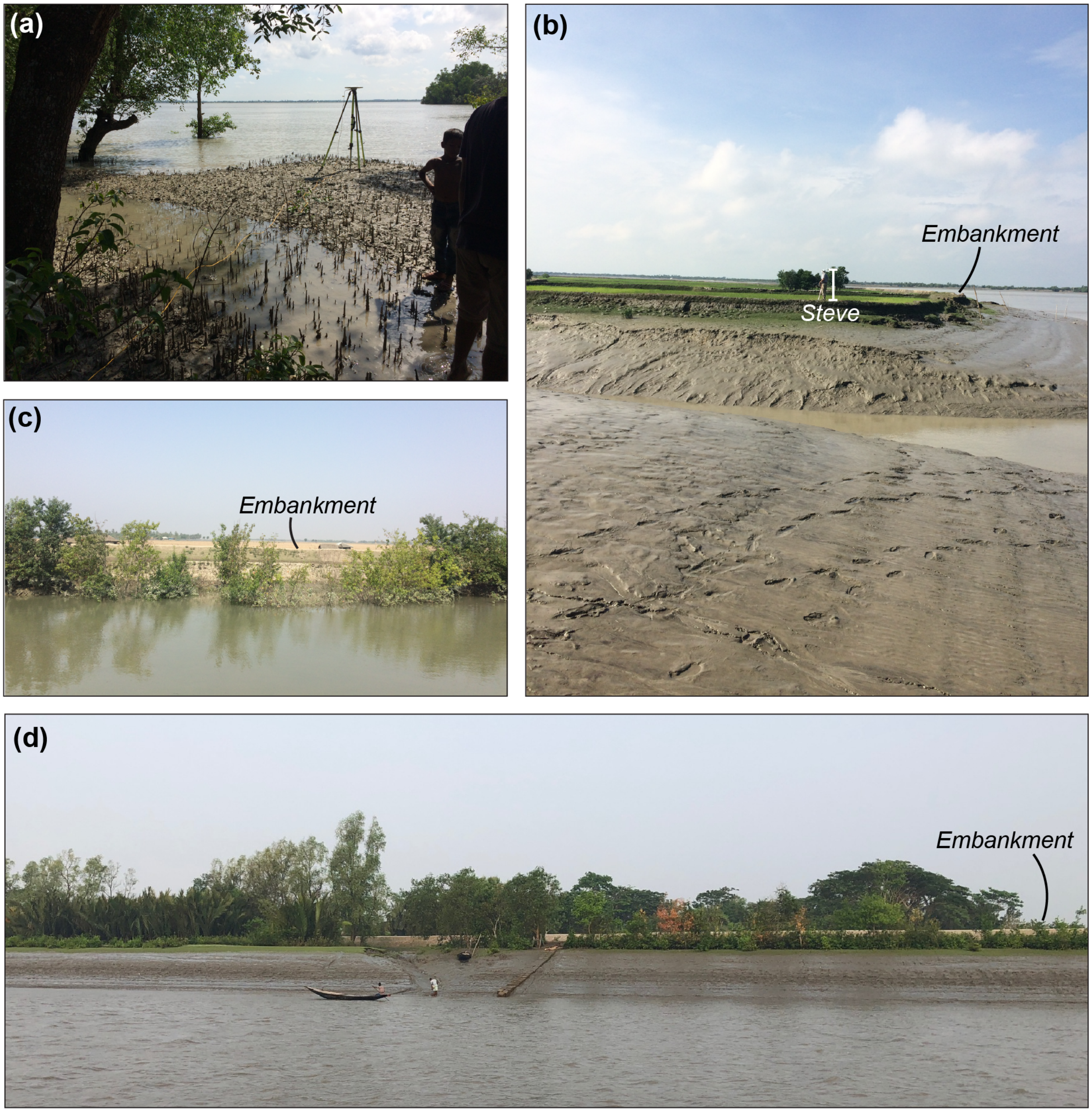

Figure 4.15: Examples of intertidal platform area outside of the embankments. **(a)** Outside of the Polder 10/12 embankment near Hadda Forest Station, looking southeast towards the Shibsa River; note 1.5-meter tripod for scale. The embankment is ∼100 meters to the left of the camera. Photo was taken approximately one hour before high water on 4-Oct-2017; the region around the tripod was inundated shortly afterwards. **(b)** Intertidal region at Shibsa Head, looking west towards the Shibsa River. Steve is standing on the embankment for scale. Photo was taken at mid-water on 5-Oct-2017. **(c)** Along the southern Bhadra River, looking north-northeast towards Polder 32. Notice the partly-inundated mangroves outside of the embankment. Photo was taken near high water on 26-Feb-2018. **(d)** Embankment near Polder 32 in May 2019, with adult men in the water for scale. Photo was taken around low water; notice that the bank slopes up to a level, vegetated intertidal platform area outside of the embankment. Copyright for (a) through (c) belongs to the author; image (d) ©2019 Matt Dietrich.

Chapter 5

Conclusion

5.1 Summary of key findings

The research presented in this dissertation illustrates the complexities of tidal hydrodynamics in an anthropogenically-modified, interconnected tidal channel system. The construction of embankments or "polders" in the 1960s and 1970s generated a variety of unintended consequences, including widespread and rapid abandonment of formerly-navigable channels (Wilson et al., 2017). However, several smaller "transverse" channels in the Shibsa-Pussur subnetwork of the channel system responded to polder construction by widening and straightening, which suggests a local increase in discharge. In Chapter 2, we combined field measurements with GIS analysis to quantify the channels' relative basin sizes before and after embankment construction; this analysis suggests that the Shibsa River maintained its pre-polder tidal prism by expanding its tidal basin eastward into the former Pussur basin via the transverse channels. The primary conclusion of this research is that looping tidal channel systems may respond unpredictably to anthropogenic perturbation because the flow is able to reorganize, in contrast to single-channel systems where the "tidal prism-inlet area" relationship (*e.g.*, O'Brien, 1969) requires that a reduction in basin volume will lead to shoaling.

In Chapters 3 and 4, we evaluated the utility of two methods for better understanding the channel network's past behavior and predicting its future morphological stability. Chapter 3 focused on quantifying asymmetries in the vertical tidal signal as a possible predictor of the dominant current direction and net sediment transport, both of which are challenging to measure directly. During this project, we quantified the dominant physical mechanisms which generate vertical tidal asymmetries in the study area; in particular, there is a strong correlation between intertidal platform inundation depth and waveform asymmetry magnitude. This is true even in the poldered region, which may be a consequence of tidal asymmetries developing in the Sundarbans and then propagating northwards. However, we observe no relationship between vertical tidal asymmetry and the dominant current direction, which likely results from (1) non-negligible Gorai River discharge during the monsoon season, which must be conveyed into the Bay of Bengal during ebb tides and therefore necessitates an increase in ebb flow velocity, and (2) the looping geometry of the channel network, which allows for a nonzero net tidal prism through individual channel transects. The most important conclusion from this analysis is that vertical tidal records alone are insufficient for predicting net sediment transport pathways through the channel network and cannot be used to predict future loci of erosion and deposition in the study area.

After determining the tidal asymmetry is not a good tool for evaluating sediment transport in the Shibsa-Pussur channel network, in Chapter 4 we considered the relationship between water surface gradients and flow velocity in the Shibsa-Pussur region. Our underlying goal for this analysis was to test whether steepening a channel's surface gradient enhances its favorability as a flow route for the tidal discharge. A momentum balance of the surface gradient and velocity time series indicates that acceleration and quadratic friction are the same order of magnitude in the study area, leading to up to three-hour periods of flow against an adverse surface gradient. Additionally, the correlation between time-averaged surface gradient and time-averaged velocity is weak, and there are several locations where the subtidal gradient is in the opposite direction of mean flow. We therefore conclude that water surface gradients provide minimal information about flow velocities in the channel system unless one can independently account for the influence of momentum.

5.2 Practical advice for future research in the study area

The negative results of Chapters 3 and 4 highlight an important practical consideration for future hydrodynamic research in southwest Bangladesh. Specifically, these projects demonstrate the necessity of collecting direct measurements of discharge and sediment transport, rather than attempting to predict these variables from the vertical tide data. This is particularly critical for studies which will be used to inform delta management policy decisions and hazard mitigation strategies. Many hydrodynamic models of the study area have been validated against vertical tidal records collected by various Bangladeshi government agencies; however, it is clear from our data that the horizontal tide does not behave as one might intuit from vertical tidal records. We here emphasize the absolute necessity of validating numerical models against both vertical and horizontal tide data to ensure that such models accurately capture the system's complex behavior.

5.3 Directions for future study

First, it would be valuable to examine seasonal variations in the results from each of Chapters 2 through 4. For example, the net circulation patterns reported in Figure 2.4 strictly represent the tidal behavior under monsoon-season conditions. Considering that one of the primary results of this chapter was the Pussur's role in conveying a significant fraction (up to 100% during spring tides) of Gorai-contributed water volume, reexamining routes of Shibsa-Pussur exchange during the dry season would enhance our understanding of how interconnected channels interact under purely tidal conditions. Similarly, with the exception of four dry season discharge datasets from the Shibsa River (as reported in Hale et al., 2019a), our observation of incoherent vertical and horizontal tidal asymmetry in Chapter 3 is based on monsoon-season discharge data, when the confounding influence of Gorai discharge necessitates enhanced ebb velocities to transport the excess volume of water out of the system. Augmenting the dry season discharge dataset would provide information about the extent to which our observations are related to loops within the channel network.

Channel-platform interactions are a second possible area of focus for future projects in the southwestern GBMD. Our results from Chapter 3 suggest that the $2M_2 - M_4$ phase difference does not exceed 180° anywhere in the study area, including at stations that are fully within the Sundarbans. This characterizes a flood asymmetric tide, which is inconsistent with general knowledge of waveform deformation in systems with a large intertidal volume. Additionally, the combined results of Chapters 3 and 4 indicate that although the M_6 tidal amplitude is enhanced during platform inundation events, this deformation cannot be a product of the quadratic friction term, as the literature tends to emphasize. In Section 4.5.4, we suggested that our observations may be related to the findings of Aucan and Ridd (2000), who found that intertidal regions with a low topographic slope (order of 10^{-4} m/m) may become disconnected from the channel during ebb. This forces the water perched on the platform to drain off the platform via a network of smaller mangrove creeks and prevents an ebb asymmetry from developing in the mainstem channels. However, Aucan and Ridd's study area in northeastern Australia is one to two orders of magnitude smaller than the Shibsa-Pussur channel system. From the perspective of tidal hydrodynamic theory, it would be interesting to see of those results are also applicable to a large-scale tidal delta plain system. In terms of practical implications, such a project may elucidate net transport pathways and spatial trends in sediment deposition within the Sundarbans region.

Finally, shortly before the completion of this dissertation (and several months after Chapter 2 had been published as Bain et al., 2019), we encountered the conference proceedings by Collins et al. (1987). This interpretation of tidal channel interactions is based on data from a small marsh system; however, it may provide a new framework for conceptualizing the large-scale tidal basin capture described in Chapter 2. Collins et al. (1987) made two key observations which are possibly related to tidal dynamics in the Shibsa-Pussur channel network. First, the authors consider the idea of marsh channel "retrogression", in which vegetation encroachment near the channel head enhances silt deposition and causes a relatively rapid reduction in channel length. However, rather than reducing its tidal prism due to the loss of basin volume near the head, the channel maintains its original tidal prism by headcutting in a nearby branch of the dendritic network.

If we consider the rapid, polder-induced siltation upstream of Shibsa Head (Wilson et al., 2017) to be analogous to Collins et al.'s vegetation-generated channel head retrogression, then perhaps the enhanced discharge exchange through the transverse channels was caused by rerouting the Shibsa's tidal prism to the west. While this may appear to be a restatement of the second basin capture hypothesis from Section 2.3.3, the underlying mechanism is fundamentally different. Specifically, the hypothesized sequence of events in Chapter 2 is:

1. Polder construction caused rapid siltation upstream of Shibsa Head.

2. In the absence of other complicating factors, the mainstem Shibsa River should have responded to this reduction in upstream basin volume by shoaling.

3. However, the contemporaneous reduction in Gorai River discharge removed the freshwater "barrier" that was formerly preventing significant Shibsa tidal intrusion into the transverse channels.

4. The higher celerity Shibsa waveform captured the entirety of the transverse channels, and the mainstem Shibsa was consequently able to maintain (or re-obtain) its pre-polder prism.

In other words, *the loss of Gorai River discharge drove the Shibsa River to capture the Pussur's former basin*. Drawing an analogy with the observations of Collins et al. (1987) instead, the sequence of events becomes:

1. Polder construction caused rapid siltation upstream of Shibsa Head.

2. The mainstem Shibsa did not reduce its tidal prism in response to the loss of upstream basin volume. Rather, the tidal prism in the mainstem Shibsa remained constant through time because Shibsa began "head-cutting" into the transverse channels (which were not formerly conveying a significant net volume of water).

Under the Collins et al. (1987) model, the key idea is that *a reduction in upstream basin volume does not guarantee a tidal prism decrease in the downstream channel reaches*. The mainstem channel may instead maintain its original tidal prism by expanding into a different location, and such expansion is independent of a coincidental decrease in upstream river discharge.

A second idea described by Collins et al. (1987) and revisited by Warner et al. (2003) is the idea of tidal "convergence zones" as regions of enhanced sediment accumulation in interconnected tidal marsh systems. Both sets of authors consider that in tidal channel systems with multiple entrances, there must be one or more sites where the convergence of currents from opposite directions produces a local zone of zero flow velocity and low bed shear during flood tide. Such locations will experience enhanced deposition and, in the extreme case, will develop emergent topography that divides the loop into separate single-channel systems. Although our velocity datasets have insufficient spatial coverage to examine this idea further, it is worth noting that the travel-time minimization algorithm applied in Chapter 2 predicts that the pre-polder Shibsa and Pussur waveforms would have converged in the transverse channels approximately halfway between the two mainstem channels (Figure 2.5). Satellite imagery indicates that this was also the narrowest portion of the pre-polder channel network, supporting the idea of a region of enhanced sediment accumulation. For the modern system, travel-time minimization predicts the two waveforms converging in the Pussur channel south of the Dhaki-Pussur bifurcation (Figure A.8). This is within the Pussur reach that has been experiencing major siltation issues and navigation disruption (*e.g.* Rahman, 2017). It therefore may be worth exploring whether the idea of salt marsh convergence zones is relevant at larger scales like the GBMD as a tool for predicting where deposition will occur.

We again emphasize that the results of Collins et al. (1987) were developed using data from a small marsh system and may be scale-dependent. Any project applying these ideas to the GBMD would first need to establish that the underlying physical mechanisms operate in systems with spatial dimensions spanning several orders of magnitude. Nevertheless, if such a scale-invariance could be established, these marsh-system processes may provide new insight into the dynamics of interconnected tidal channels on the GBMD.

Appendix A

Supporting Information for Chapter 2

This appendix contains the supporting information for

> Bain, R.L., Hale, R.P., and Goodbred, S.L. (2019), Flow reorganization in an anthropogenically modified tidal channel network: An example from the Southwestern Ganges-Brahmaputra-Meghna Delta: *Journal of Geophysical Research–Earth Surface*, v. 124, pp. 1–19, DOI:10.1029/2018JF004996.

The text that follows is identical to the text of the published manuscript's supporting information, with the exception of figure, table, and section numbering.

A.1 Introduction

This document provides additional data supporting the conclusions of Chapter 2, including bathymetric maps, tidal range estimates upstream of the study area, and a compilation of width:depth ratios for tidal channels around the globe. We also include a detailed explanation of our methods for tide gauge interpolation, discharge interpolation, upstream storage volume calculation, and waveform travel-time minimization.

A.2 Bathymetric data

Figure A.1 shows examples of bathymetry from the Shibsa, Dhaki, Gorkhali, and Shengrali channels. The data were collected in October 2014, March 2015, or August/ September 2015 using either a single-beam SonarMite echosounder or the ADCP's vertical beam. The raw depth readings were corrected against water surface elevations from the nearest pressure sensor to give depth at the highest high water recorded during a given field campaign. Finally, we generated the maps in Figure A.1 by kriging the depth data in Surfer (version 11.6.1159, ©2013 Golden Software, Inc.). The results indicate scouring up to 20 meters deep in the Dhaki and up to 55 meters deep in the

Shibsa; this is consistent with an increase in discharge at these locations. Additional bathymetric data from the study area are available in Auerbach et al. (2015) and Reed (2015).

A.3 Tide gauge interpolation

Placement of the Brick Factory, Chalna North, Gorkhali East, Jongla, Nalian, and Shibsa Forest Station pressure sensors above the spring-tide low water elevation resulted in gaps of up to 2.9 hours in the time series. To determine the optimal method for reconstructing the missing values, we truncated the lowest meter of the long-term Sutarkhali dataset corresponding to the deployment dates of the six short-term instruments. We then attempted to reconstruct the known low water elevation at Sutarkhali using the MATLAB algorithms `T_TIDE` (Pawlowicz et al., 2002), `TIDALFIT` (unpublished code by A. Grinstead), `UTide` (Codiga, 2011), and the standard cubic smoothing spline function `csaps` with smoothing parameter $p = 0.999\,999\,99$. The results of this test indicate that the cubic smoothing spline outperforms the three constituent-based algorithms, with a maximum low water error magnitude of 0.13 meters (compared to 0.81 meters for `UTide`, 0.83 meters for `T_TIDE`, and 0.88 meters for `TIDALFIT`; Figures A.2 and A.3).

The poor performance of the constituent-based algorithms is partially a consequence of short time series duration. Rayleigh's criterion (see, *e.g*, Godin, 1972) states that two frequencies σ_1 and σ_2 can be separated only if

$$n \cdot \Delta t |\sigma_1 - \sigma_2| \geq 1 \quad , \tag{A.1}$$

where n is the number of samples and Δt is the sampling interval. Evaluating this expression for the lunar and solar semidiurnal frequencies ($\sigma_{\mathrm{M2}} = 0.0805114006$ hours^{-1}; $\sigma_{\mathrm{S2}} = 0.08\bar{3}$ hours^{-1}) and the Sutarkhali sampling interval of $\Delta t = 1/6$ hour reveals that a minimum record length of $n = 2127$ (just over 14 days, 18 hours of data at 10-minute sampling) is necessary to resolve the M_2 and S_2 constituents. Consequently, algorithms that apply Rayleigh's criterion for frequency selection (`T_TIDE` and `UTide`) will not, by default, reproduce a spring-neap pattern from only 13 days of data. `TIDALFIT` differs from the other two algorithms by attempting to fit all constituents with

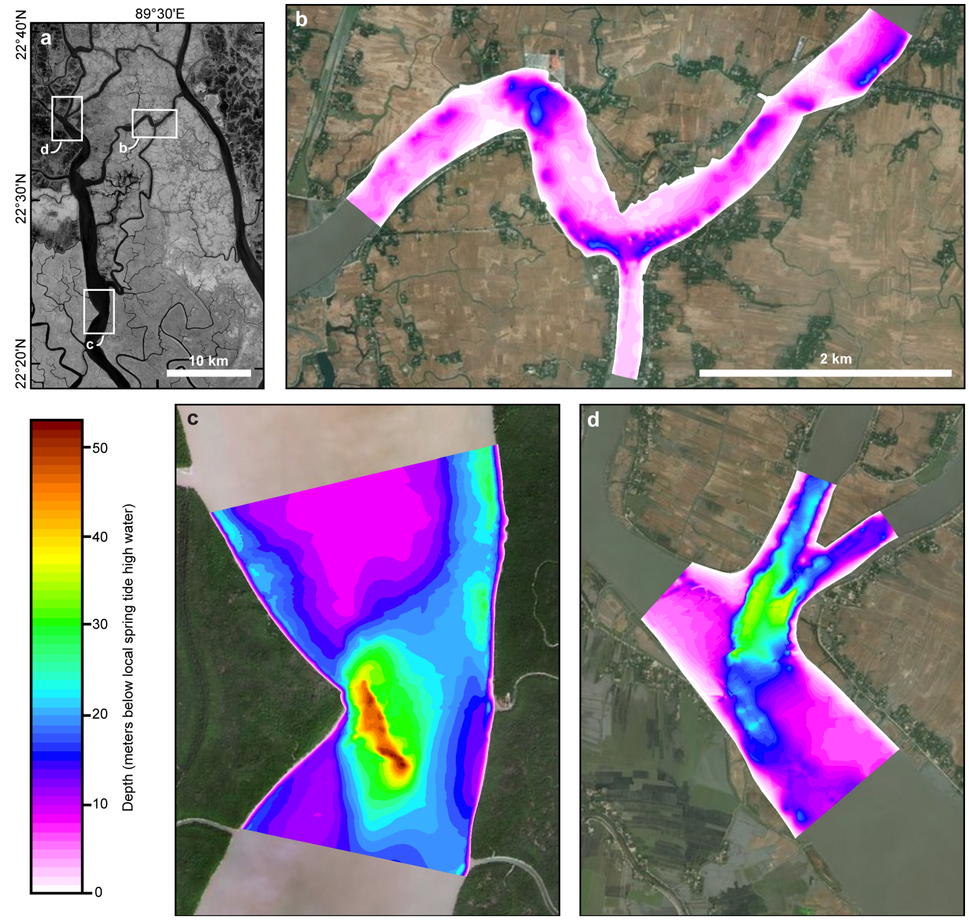

Figure A.1: Bathymetry from the study area showing scouring of the Shibsa, Dhaki, and the Gorkhali-Shengrali confluence at Shibsa Head. The vertical datum is the maximum high water elevation recorded during the field campaign corresponding to data collection. (a) Index map showing the location of the remaining subplots. (b) Dhaki River near its confluence with the Bhadra, collected in October 2014 and September 2015. (c) Shibsa River south of its confluence with the Bhadra, collected on 12-Mar-2015. (d) Shibsa Head region, including portions of the Gorkhali and Shengrali channels, collected on 5-Sep and 6-Sep-2015. Background: (a) mosaic of Landsat 8 (Band 5–NIR) imagery collected on 9-Feb-2017 and 18-Feb-2017; (b) undated TerraColor imagery, ©2018 Earthstar Geographics, obtained through ESRI/ArcMap. *Note: This figure was published by the American Geophysical Union in Bain et al. (2019) and is reprinted here under AGU's "Rights Granted to Authors" policy. AGU retains copyright of this figure.*

frequency $\sigma > {}^{4}\!/\!{}_{(n \cdot \Delta t)}$ regardless of whether Rayleigh's criterion is satisfied[20]. As shown in Figure A.2b, this allows for a spring-neap amplitude variation; however, the accuracy of the reconstructed elevations is poor.

The nonstationary character of the shallow water constituents likely also limits the algorithms' ability to reconstruct our data. A short-term (*i.e.*, windowed) harmonic analysis (Jay and Flinchem, 1999) of the Sutarkhali dataset indicates that the shallow water distortion of the tidal waveform is strongly dependent on whether the intertidal platform inundates. We observe that the M_4/M_2 amplitude ratio, which characterizes the strength of the shallow water distortion (Friedrichs and Aubrey, 1988, 1994; Guo et al., 2014), is up to three times greater during spring tides compared to neap tides (Figure A.4). Additionally, the $2M_2 - M_4$ phase difference is $\sim 145^\circ$ during neap tides but approaches 180° during spring tides, indicating that the relative duration of the rising and falling limbs depends on platform inundation. Since the standard tidal analysis algorithms represent the time series with the average magnitude and phase of each constituent over the full recording period, these algorithms cannot accurately reconstruct the 13-day time series.

A.4 Discharge interpolation

We collected the discharge data using two boat-mounted Sontek M9 acoustic Doppler current profilers (ADCPs) with autonomous GPS positioning. Challenging local working conditions prevented us from collecting discharge data for a full semidiurnal period at any of the survey sites. We applied a variant of the extrapolation procedure from Hale et al. (2019a), which is detailed in this section, to estimate the missing discharge values. The primary assumption of this method is that the discharge magnitude does not vary appreciably between consecutive oscillations, which allows us to shift the measurements forward or backward by one semidiurnal period to constrain the curve's behavior beyond the bounds of the data collection window. Since the duration of any given semidiurnal oscillation varies between 11.9 and 13.1 hours (Hale et al., 2019a), we first convert the abscissa from time to phase using the following algorithm:

---

[20] See the `TIDALFIT` documentation at `www.mathworks.com/matlabcentral/fileexchange/19099-tidal-fitting-toolbox`.

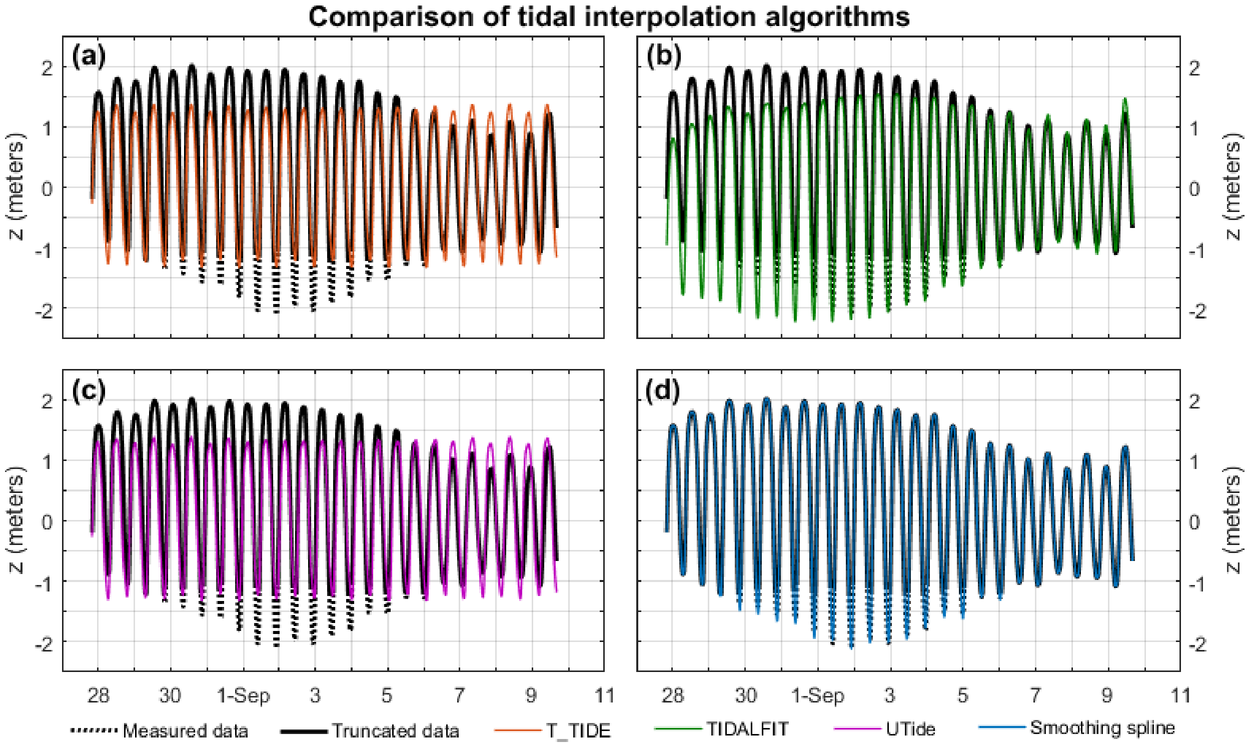

Figure A.2: Comparison of algorithms for reconstructing the truncated August-September 2015 dataset from Sutarkhali Forest Station: (a) `T_TIDE`, (b) `TIDALFIT`, (c) `UTide`, and (d) the standard MATLAB cubic smoothing spline algorithm `csaps` with smoothing parameter $p = 0.99999999$. *Note: This figure was published by the American Geophysical Union in Bain et al. (2019) and is reprinted here under AGU's "Rights Granted to Authors" policy. AGU retains copyright of this figure.*

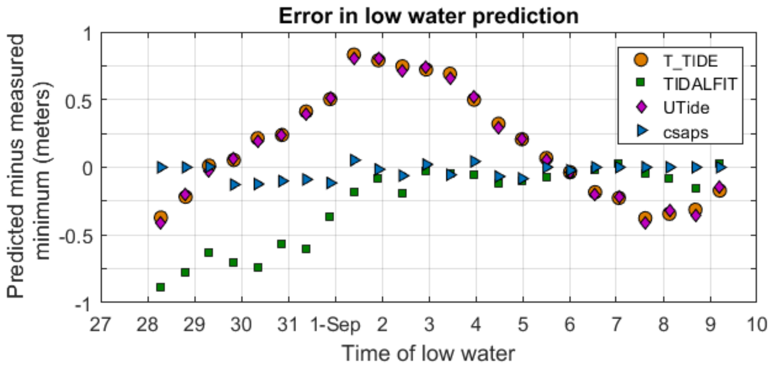

Figure A.3: Error in the reconstructed low water elevation for the August-September 2015 Sutarkhali dataset displayed in Figure A.2. Positive error values indicate that the predicted low water elevation is too high, and negative error values indicate that the predicted low water elevation is too low. Our results indicate that using the cubic smoothing spline (`csaps` in MATLAB) instead of a constituent-based method reduces the error in low water elevation by nearly an order of magnitude. *Note: This figure was published by the American Geophysical Union in Bain et al. (2019) and is reprinted here under AGU's "Rights Granted to Authors" policy. AGU retains copyright of this figure.*

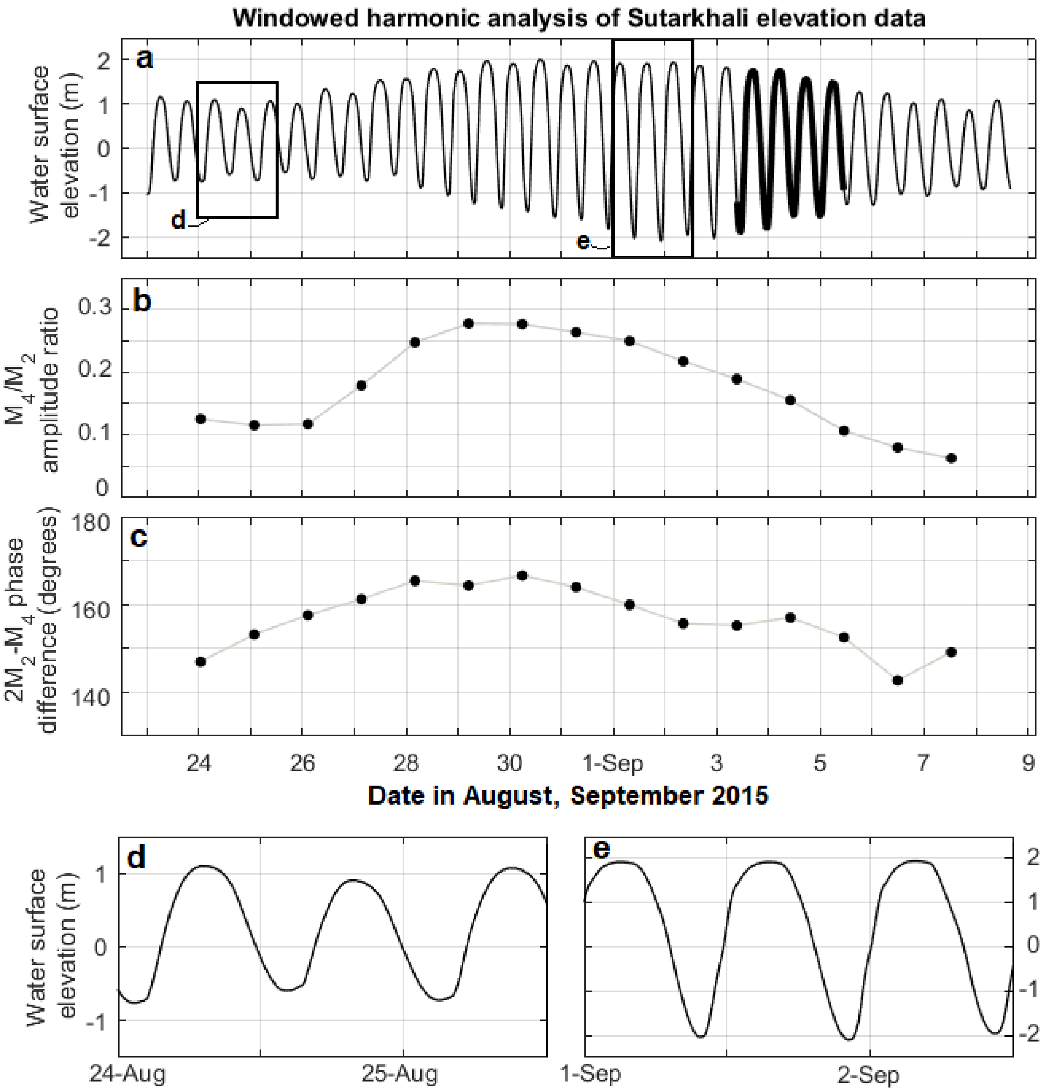

Figure A.4: Example of windowed harmonic analysis (or "short-term harmonic analysis"; Jay and Flinchem, 1999) of the Sutarkhali tide gauge data. In this example, the window length is 49.68 hours (four M_2 periods) and the sampling interval Δt is 10 minutes. (a) Time series of water surface elevation at Sutarkhali in August and September 2015. The bold segment of the curve shows the duration of one 49.68-hour window. (b) The M_4/M_2 amplitude ratio for each window, plotted at the center of the window. This parameter characterizes the strength of the shallow water distortion. (c) The $2M_2 - M_4$ phase difference for each window, plotted at the center of the window. This parameter characterizes the asymmetry of the tidal waveform, with a value of $2M_2 - M_4 = 180°$ corresponding to symmetrical rising and falling limbs. Values between 0° and 180° indicate the flood duration is shorter than the ebb duration, whereas values between 180° and 360° indicate a shorter ebb duration relative to flood. (d) Time series showing 36 hours of neap data; note that the breadth of the peaks and the troughs is similar (relatively low M_4/M_2 ratio), but the rising limb is much shorter than the falling limb ($2M_2 - M_4 \ll 180°$). (e) Time series showing 36 hours of spring tide data. The peaks are much wider than the troughs (comparatively high M_4/M_2 ratio), but the rising and falling limbs are more uniform in duration ($2M_2 - M_4$ close to 180°). *Note: This figure was published by the American Geophysical Union in Bain et al. (2019) and is reprinted here under AGU's "Rights Granted to Authors" policy. AGU retains copyright of this figure.*

1. Determine the times of low water $t_{\mathrm{L}_1}, t_{\mathrm{L}_2}, \ldots, t_{\mathrm{L}_N}$ at Sutarkhali Forest Station from the pressure sensor data. We use low water as a reference point because the absence of low water slack ensures unambiguous identification of t_{L}. In contrast, monsoon-season spring tides have a prolonged high water slack up to two hours in duration that may include multiple peaks, making it difficult to isolate any single point in time as "high water".

2. Convert $t_{\mathrm{L}_1}, t_{\mathrm{L}_2}, \ldots, t_{\mathrm{L}_N}$ to phase $\theta_{\mathrm{L}_1}, \theta_{\mathrm{L}_2}, \ldots, \theta_{\mathrm{L}_N}$ by mapping the time of low water onto consecutive multiples of 2π; that is, $t_{\mathrm{L}_j} \mapsto 2(j-1)\pi$.

3. Assume that phase varies linearly with time over any interval $\left[t_{\mathrm{L}_j}, t_{\mathrm{L}_{j+1}}\right]$, and use piecewise-linear interpolation to obtain the phase value associated with each discharge measurement. In MATLAB syntax, the command is

   ```
   theta_meas=interp1(t_L,theta_L,t_meas,‘linear’)  ,
   ```

   where `t_L` is the $N \times 1$ vector containing $t_{\mathrm{L}_1}, t_{\mathrm{L}_2}, \ldots, t_{\mathrm{L}_N}$, `theta_L` is the $N \times 1$ vector containing $\theta_{\mathrm{L}_1}, \theta_{\mathrm{L}_2}, \ldots, \theta_{\mathrm{L}_N}$, and `t_meas` is a $M \times 1$ vector containing the measurement times of the transect's M corrected discharge values.

4. Shift the discharge measurements forward or backward in phase by adding multiples of 2π to the measured phase values.

5. Reverse the piecewise-linear interpolation to convert the shifted phase values back to time. For example:

   ```
   t_shift=interp1(theta_L,t_L,theta_meas+2*pi,‘linear’).
   ```

After using the above algorithm to "tile" the data, the interpolation itself depends on the duration of the gap and which features of the curve (zero crossings or turning points) are missing. In the following sections, we describe the specific procedure and the underlying assumptions for each survey site.

A.4.1 DHAKI EAST AND BHADRA NORTH

The Bhadra North ADCP survey produced over 10 hours of data, with a 1-hour gap during flood and a second 1-hour gap during ebb. At Dhaki East, we collected data over two consecutive days, with 8 hours of data on the first day and 4 hours of data on the second day. We overlay the two datasets by shifting the second day's data back in time by two tidal periods to produce a nearly complete record, with the exception of a 1-hour gap during ebb. Given the short gap durations, we estimate the missing values using a cubic smoothing spline to produce the discharge curves shown in Figures 2.3b and 2.3c.

A.4.2 BHADRA SOUTH, CHALNA SOUTH, AND GORKHALI WEST

At the Bhadra South, Chalna South (Pussur), and Gorkhali West survey sites, our datasets include peak flood discharge and both zero crossings, but we did not definitively record peak ebb discharge. In place of the cubic smoothing spline, we interpolate using a fourth-degree polynomial constrained by the spline-based values of Q and ${}^{dQ}/_{dt}$ at both sides of the gap and and a predetermined value for the area under the interpolant, Ω_{gap}. As we have insufficient information to select Ω_{gap} *a priori*, we generate a suite of possible interpolants and report the range of reasonable values. This is accomplished by first defining a transect's *normalized net prism*:

$$\hat{\Omega}_{\text{net}} = \frac{|\Omega_{\text{ebb}}| - |\Omega_{\text{flood}}|}{|\Omega_{\text{ebb}}| + |\Omega_{\text{flood}}|} \quad . \tag{A.2}$$

In the specific case where the missing data occur entirely during ebb, as is true for the Bhadra South, Chalna South, and Gorkhali West datasets, Equation A.2 rearranges to

$$\Omega_{\text{gap}} = -\Omega_{\text{ebb}}^{\text{partial}} + \Omega_{\text{flood}} \cdot \frac{\hat{\Omega}_{\text{net}} + 1}{\hat{\Omega}_{\text{net}} - 1} \quad , \quad -1 < \hat{\Omega}_{\text{net}} < 1 \quad , \tag{A.3}$$

where $\Omega_{\text{ebb}}^{\text{partial}}$ refers to the integral of the incomplete ebb discharge curve, such that $\Omega_{\text{ebb}} = \Omega_{\text{ebb}}^{\text{partial}} + \Omega_{\text{gap}}$. Note that we have dropped the absolute value signs since, by definition, Ω_{ebb} is always positive and Ω_{flood} is always negative. By systematically varying $\hat{\Omega}_{\text{net}}$ in Equation A.3, we obtain a set of values for Ω_{gap} which serve as the fifth constraint on the quartic interpolants. The range of tidal prism values reported in Table 2.1, along with the perimeters of the gray error envelopes in Figure 2.3a, 2.3d, and 2.3e, correspond to $+0.34 \leq \hat{\Omega}_{\text{net}} \leq +0.39$ at Chalna South, $+0.1 \leq \hat{\Omega}_{\text{net}} \leq +0.2$ at Bhadra South, and $+0.40 \leq \hat{\Omega}_{\text{net}} \leq +0.48$ at Gorkhali West.

As addressed in Chapter 2, a primary focus of this study involves determining the relative magnitudes of each site's ebb and flood prisms. It is therefore relevant to note that although the range of reasonable tidal prisms is often large (see Table 2.1), we are confident that we have accurately determined the *net* flux direction at each ADCP transect. Specifically, balancing the ebb and flood prisms at Bhadra South, Chalna South, or Gorkhali West results in unreasonably-shaped discharge curves. Thus, although the uncertainty envelopes are large, they do not invalidate the conclusions of this study.

A.4.3 DHAKI WEST

The gap in the Dhaki West dataset exceeds five hours, and we did not record peak flood discharge or the flood-to-ebb flow reversal. Splitting Ω_{gap} between ebb and flood introduces the additional complication of not being able to systematically vary $\hat{\Omega}_{\text{net}}$ in Equation A.3 to set the fifth constraint on the quartic interpolant. Instead, we fix the time of the discharge zero-crossing (along with the measured values of Q and ${}^{dQ}/_{dt}$ at both endpoints of the gap) when fitting the polynomial, which has the effect of decreasing or increasing $\hat{\Omega}_{\text{net}}$ depending on whether we force $Q = 0$ to occur, respectively, earlier or later in time.

The extended duration of missing data introduces considerable uncertainty in the value of $\hat{\Omega}_{\text{net}}$. Fixing the discharge zero-crossing at 8:23 PM results in $\hat{\Omega}_{\text{net}} = +0.5$, with $\Omega_{\text{ebb}} = 4.07 \times 10^7$ m^3 and $\Omega_{\text{flood}} = -1.36 \times 10^7$ m^3, whereas shifting the discharge zero-crossing to 8:59 PM produces $\hat{\Omega}_{\text{net}} = +0.1$, with $\Omega_{\text{ebb}} = 3.96 \times 10^7$ m^3 and $\Omega_{\text{flood}} = -3.24 \times 10^7$ m^3. The interpolant acquires a peculiar shape if $\hat{\Omega}_{\text{net}} \gg +0.5$, and allowing $\hat{\Omega}_{\text{net}} < +0.1$ produces a peak neap flood discharge exceeding the peak spring flood discharge at the nearby Dhaki East survey site, which is unlikely. We thus report $+0.1 \leq \hat{\Omega}_{\text{net}} \leq +0.5$ as the reasonable range of values at Dhaki West on 7-Sep-

2015. Again, we emphasize that although this uncertainty envelope is large, we are confident that we have accurately determined the net prism direction at this site.

A.5 Storage volume calculations

In this section, we address the assumptions and auxiliary calculations that support the storage volume calculations. In Section 2.1.3, we indicated that we visited a variety of sites and spoke with local fishermen to estimate the modern tidal damping rate upstream of the study area, which was not instrumented. Section A.5.1 summarizes these "anecdotal" tide range data and describes our method for fitting damping trends along each channel. Then, Section A.5.2 describes our compilation of tidal channel aspect ratio data from the literature, which we later use to estimate local channel depths at sites for which bathymetric data were not available. Section A.5.3 details our methods for estimating the tidal range under pre-polder flow conditions. Finally, Section A.5.4 summarizes the entire storage volume calculation method which is presented in Chapter 2 and expanded herein.

A.5.1 MODERN TIDAL DAMPING UPSTREAM OF THE STUDY AREA

Within the immediate study area, we can obtain a reasonable estimate of the vertical storage parameters by linearly interpolating along channel between pressure sensors. The absence of instruments farther upstream necessitates the use of a best-fit tidal damping model to estimate $\Delta z^{\star}_{\text{max}}$. Between October 2017 and July 2018, we estimated the maximum tidal range at nine additional sites along the Kobadak, relict Shibsa, and Pussur/Gorai channels by speaking to local fishermen, measuring the distance between the low and high water lines (if our visit coincided with low water), and/or extrapolating backwards from an October 2017 instrument redeployment. The results are summarized in Table A.1.

We used least-squares to approximate the damping rate as a function of distance along each channel (Figure A.5). The Pussur/Gorai channel maintains an approximately constant peak tidal range of ~ 4 meters over the 56-kilometer reach between Jongla Forest Station and Khulna before

Table A.1: Estimated modern spring tide ranges upstream of the study area for calculating the tidal damping rate.

Kobadak River

Site description	Latitude	Longitude	Along-channel distance from Shibsa Head (km)	Anecdotal or estimated modern spring tide range (m)
Shibsa Head*	22.576076°N	89.398647°E	0	4.5 – 4.7
Bridge near Paikgachha*	22.618358°N	89.289504°E	17.4	4.0 – 4.5
Beel site south of Tala†	22.671038°N	89.259979°E	31.3	2.0 – 3.0
Highway north of Kumira†	22.805118°N	89.178158°E	75.3	0.5 – 1.0

Relict Shibsa channel

Site description	Latitude	Longitude	Along-channel distance from Shibsa Head (km)	Anecdotal or estimated modern spring tide range (m)
Shibsa Head*	22.576076°N	89.398647°E	0	4.5 – 4.7
Bridge east of Chuknagar†‡	22.823118°N	89.350599°E	35.6	3

Pussur/Gorai River

Site description	Latitude	Longitude	Along-channel distance from Hiron Point (km)	Anecdotal or estimated modern spring tide range (m)
Jongla Forest Station§	22.370202°N	89.615085°E	68.5	3.9 – 4.1
Chalna North§	22.612880°N	89.521563°E	97	4.2 – 4.4
Pankhali ferry ghat*	22.631629°N	89.515192°E	100	4.1 – 4.3
Khulna*	22.792071°N	89.581584°E	124.5	4.0 – 4.2
Fukra village‡	23.154954°N	89.749182°E	189.6	1
Gorai ferry ghat†	23.194271°N	89.689556°E	202.6	0.5

[*] Peak tidal range based on October 2017 instrument redeployment.

[†] Estimated using the distance between low water level and the visible high water line.

[‡] Anecdotal tidal range based on conversations with local fishermen.

[§] See Chapter 2.

beginning to decrease linearly with a best-fit slope of -4.7 cm/km. The slope between the two relict Shibsa sites is similar at -4.5 cm/km. We used these trendlines to approximate $\Delta z^{\star}_{\text{max}}$ in all channels upstream of the instrumented region, with the exception of the Kobadak River. Visual examination of the Kobadak tidal range data suggests that an exponential trend with a best-fit *e*-folding length of 33 km is a more appropriate representation of the damping in this channel.

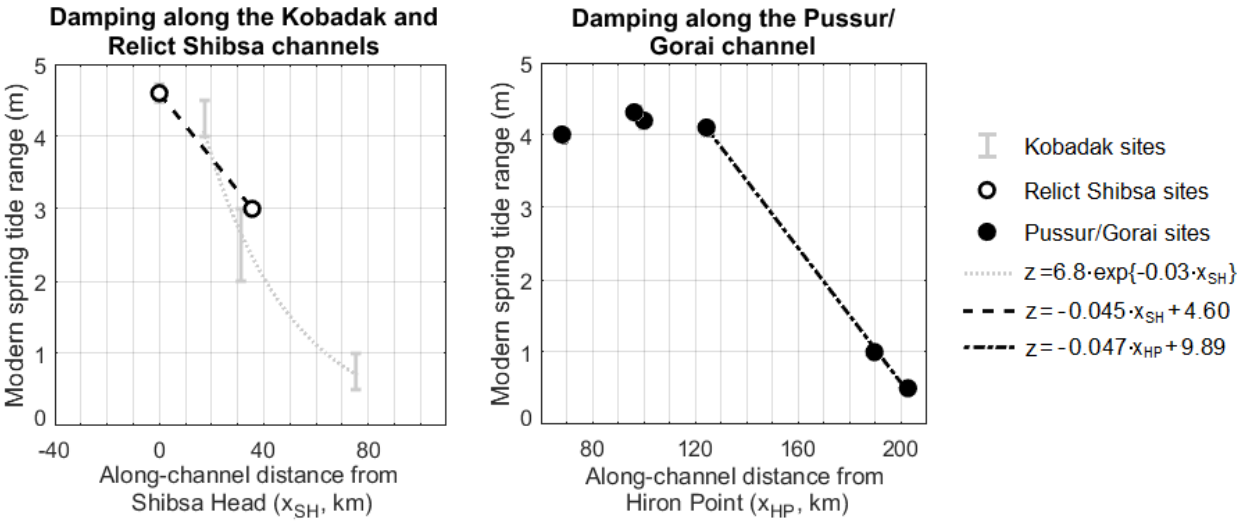

Figure A.5: Damping trends fitted to estimated spring tidal range values along the Kobadak, relict Shibsa, and Pussur/Gorai channels upstream of Polder 32. *Note: This figure was published by the American Geophysical Union in Bain et al. (2019) and is reprinted here under AGU's "Rights Granted to Authors" policy. AGU retains copyright of this figure.*

Calculating the storage volume in a channel segment for a particular date of interest (for example, corresponding to one of the ADCP surveys) also requires a method for determining $\Delta z^{\star}_{\text{low}}$ and $\Delta z^{\star}_{\text{high}}$ upstream of the instrumented region. In the absence of direct measurements, we assume that

$$\frac{\Delta z^{\star}_{\text{low}}}{\Delta z^{*}_{\text{max}}} = \frac{\Delta z^{\text{Nalian}}_{\text{low}}}{\Delta z^{\text{Nalian}}_{\text{max}}} \quad \text{and} \quad \frac{\Delta z^{\star}_{\text{high}}}{\Delta z^{*}_{\text{max}}} = \frac{\Delta z^{\text{Nalian}}_{\text{high}}}{\Delta z^{\text{Nalian}}_{\text{max}}} \tag{A.4}$$

in the Kobadak and relict Shibsa channels, and

$$\frac{\Delta z^{\star}_{\text{low}}}{\Delta z^{*}_{\text{max}}} = \frac{\Delta z^{\text{ChalnaN}}_{\text{low}}}{\Delta z^{\text{ChalnaN}}_{\text{max}}} \quad \text{and} \quad \frac{\Delta z^{\star}_{\text{high}}}{\Delta z^{*}_{\text{max}}} = \frac{\Delta z^{\text{ChalnaN}}_{\text{high}}}{\Delta z^{\text{ChalnaN}}_{\text{max}}} \tag{A.5}$$

in the Pussur upstream of the Chalna North pressure sensor. Assigning $\Delta z^{\star}_{\text{low}}$ and $\Delta z^{\star}_{\text{high}}$ as a fraction of the maximum tidal range ensures that the local tidal range on any given date, $\Delta z^{\star}_{\text{max}} - \Delta z^{\star}_{\text{low}} - \Delta z^{\star}_{\text{high}}$, will always be greater than zero.

A.5.2 ESTIMATING CHANNEL WIDTH:DEPTH RATIOS

In Section 2.1.4, we described our use of a best-fit power law relationship to estimate unknown channel depths based the local channel width. To determine this relationship, we compiled tidal channel aspect ratio data from a variety of published sources (Langbein, 1963; Myrick and Leopold, 1963; Dury, 1971; Wright et al., 1973; Zeff, 1988, 1999; Schulz et al., 2015; Hale et al., 2019a), in addition to aspect ratios determined from our ADCPs' single beam bathymetry (Figure A.1). The final dataset is shown in Figure A.6. With the exception of bathymetric transects collected near a channel mouth, the data's tendency to follow a straight line in log-log space suggests the existence of a power-law relationship between depth and width, which holds over several orders of magnitude. We applied linear least squares to the log-transformed, non-mouth data to calculate Equation 2.1 in Chapter 2.

A.5.3 ESTIMATION OF PRE-POLDER TIDAL RANGE

We are unaware of any direct measurements of the tidal range before polder construction. Pethick and Orford (2013) provide best-fit trends in monthly high and low water data from Hiron Point (1990-2011), Mongla (1998-2010), and Khulna (1968-2000). Projecting these trends back in time to the year 1960 provides an approximation of the spring tide amplitude at each location (Table A.2). Evaluating Pethick and Orford's trendlines for the year 2015 suggests a maximum spring tide range of 2.22 m at Hiron Point, 3.03 m at Mongla, and 2.80 m at Khulna. However, our data (Figure A.5; Table A.1) indicate that the spring tide range is substantially larger than predicted at Mongla and Khulna, with both sites displaying maximum tidal ranges of ~ 4.1 meters. Dividing the 1960 tidal range by the 2015 tidal range, we observe an approximately linear trend in the amplitude ratio with distance along the Pussur/Gorai channel (Figure A.7). Applying linear

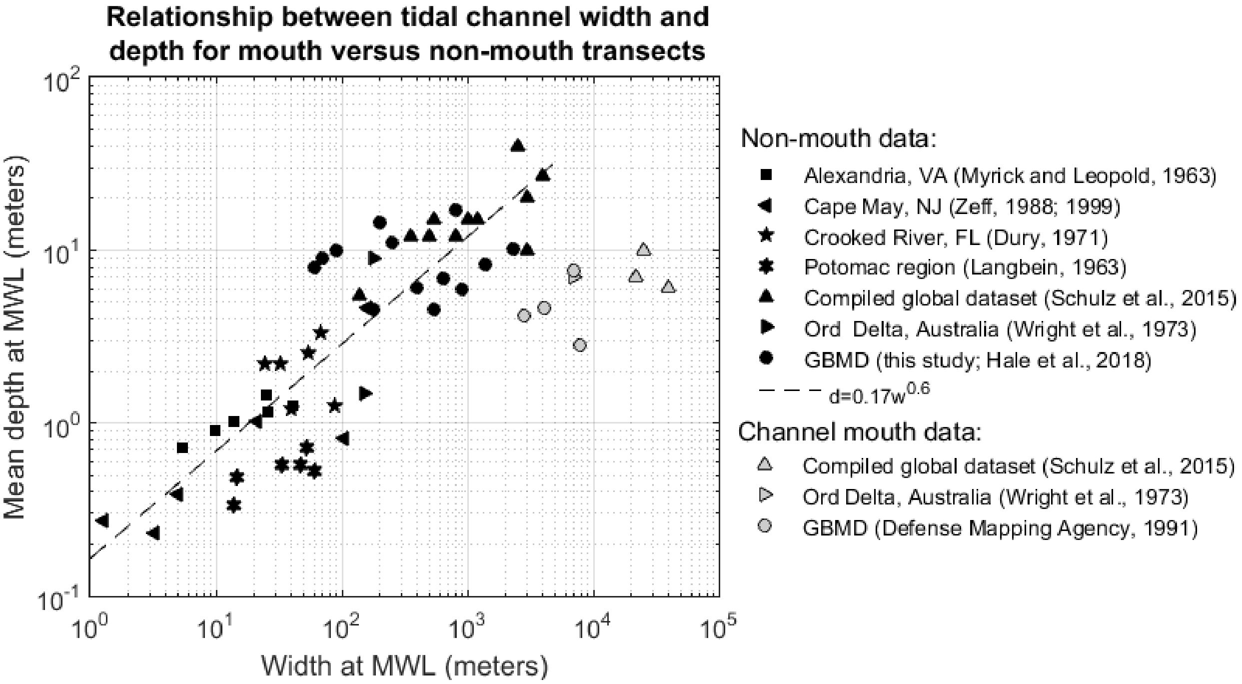

Figure A.6: The relationship between tidal channel width and depth based on values compiled from the literature and from this study. The abbreviation *MWL* refers to mean water level, and *GBMD* refers to the Ganges-Brahmaputra-Meghna Delta. *Note: This figure was published by the American Geophysical Union in Bain et al. (2019) and is reprinted here under AGU's "Rights Granted to Authors" policy. AGU retains copyright of this figure.*

regression, we obtain

$$(\Delta z^{\star}_{\max})_{1960} = (-0.005x_{\mathrm{HP}} + 0.863) \cdot (\Delta z^{\star}_{\max})_{2015} \quad , \tag{A.6}$$

where x_{HP} is along-channel distance from Hiron Point in kilometers, as the best-fit equation relating the modern tidal range to the pre-polder tidal range.

Table A.2: Tidal amplification since 1960

Site	Distance from Hiron Point (km)	Amplification rate (mm/yr)*	Projected tidal range in 1960 (m)	Tidal range in 2015 (m)	Ratio (1960 range: 2015 range)
Hiron Point	0	5.6 (1990-2011)	1.91	2.22†	0.86
Mongla	78.2	16.5 (1998-2010)	2.13	4.1‡	0.52
Khulna	124.5	28.8 (1968-2000)	1.22	4.1‡	0.30

*Calculated by subtracting the high water and low water trendlines in Figure 4 of Pethick and Orford (2013). The time range in parentheses indicates the timespan of data used for Pethick and Orford's regression analysis.
†Calculated based on the trendlines in Pethick and Orford (2013).
‡Based on our field data as shown in Figure A.5.

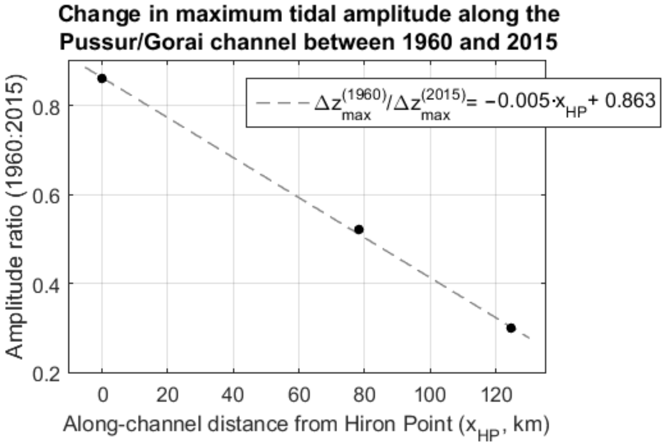

Figure A.7: Ratio of the the maximum tidal amplitude $\Delta z_{\max}$ in 1960 and 2015 as a function of distance along the Pussur channel. The 1960 amplitudes at Hiron Point ($x_{\mathrm{HP}} = 0$ km), Mongla ($x_{\mathrm{HP}} = 78.2$ km) and Khulna ($x_{\mathrm{HP}} = 124.5$ km), along with the 2015 amplitude at Hiron Point, are based on trendlines from Pethick and Orford (2013). The 2015 amplitudes at Mongla and Khulna are based on our data, as shown in Figure A.5 and Table A.1. *Note: This figure was published by the American Geophysical Union in Bain et al. (2019) and is reprinted here under AGU's "Rights Granted to Authors" policy. AGU retains copyright of this figure.*

For channel segments in the pre-polder network that still exist in the present (and therefore have a preassigned value of $(\Delta z^{\star}_{\max})_{2015}$ produced by the algorithm in Section A.5.1), calculating

$(\Delta z^\star_{\text{max}})_{1960}$ requires the simple application of Equation A.6. We automated these calculations in ArcGIS to take advantage of the software's inbuilt along-network distance calculation algorithm for determining values of x_{HP}. However, many of the channels in the pre-polder network lack a modern counterpart as a result of polder construction and subsequent channel abandonment (Wilson et al., 2017). For these channels, one of two cases applies. If the channel segment of interest is connected at both ends to a channel existing in the 2015 network, we apply linear interpolation between the known values of $(\Delta z^\star_{\text{max}})_{1960}$ at its endpoints. If the upstream end of the channel is "blind" (*i.e.*, the channel terminates without intersecting another channel), we assume a linear decrease in tidal range of 2 cm/km from the known value of $(\Delta z^\star_{\text{max}})_{1960}$ at the downstream endpoint; this damping rate was selected to match the 1960 rate of amplitude decrease in the Pussur/Gorai channel between Mongla and Khulna (Table A.2).

A.5.4 SUMMARY OF STORAGE VOLUME CALCULATIONS

Having determined $\Delta z^\star_{\text{max}}$, $\Delta z^\star_{\text{low}}$, $\Delta z^\star_{\text{high}}$, $A^\star_{\text{LL}}$, $A^\star_{\text{OB}}$, $A^\star_{\text{HH}}$, and $D^\star$ for all channel segments using the methods described above (summarized in Table A.3), we calculate the volume of water stored within a given channel segment as

$$V^\star = \begin{cases} \left[\frac{1}{2} \cdot \frac{A^\star_{\text{OB}} - A^\star_{\text{LL}}}{\Delta z^\star_{\text{max}} - D^\star} \cdot \left(\Delta z^\star_{\text{max}} + \Delta z^\star_{\text{low}} - \Delta z^\star_{\text{high}}\right) + A^\star_{\text{LL}}\right] & \\ \qquad \cdot \left[\Delta z^\star_{\text{max}} - \Delta z^\star_{\text{high}} - \Delta z^\star_{\text{low}}\right] \;, & \Delta z^\star_{\text{high}} > D^\star \\ & \\ \frac{1}{2} \cdot \left[\left(\frac{A^\star_{\text{OB}} - A^\star_{\text{LL}}}{\Delta z^\star_{\text{max}} - D^\star}\right) \cdot \Delta z^\star_{\text{low}} + A^\star_{\text{LL}} + A^\star_{\text{OB}}\right] & \\ \qquad \cdot \left[\Delta z^\star_{\text{max}} - D^\star - \Delta z^\star_{\text{low}}\right] & \\ \qquad + A^\star_{\text{HH}} \cdot \left[D^\star - \Delta z^\star_{\text{high}}\right] \;, & \Delta z^\star_{\text{high}} \leq D^\star \;. \end{cases} \tag{A.7}$$

This equation follows directly from the geometry in Figure 2.2, along with the assumption of a linear change in $A^\star(z)$ between $z^\star_{\text{LL}}$ and $z^\star_{\text{OB}}$ (see Section 2.1.3). In both cases, the first bracketed term gives the mean planform area within the channel on the date of interest, and the second bracketed term gives the vertical elevation change below the platform elevation. The second case includes an additional term giving the extra volume entering the platform (for channels adjacent to the Sundarbans) or trapped between the embankments (in the poldered region).

A.6 Justification and limitations of using travel-time minimization as a discharge proxy

Tidal propagation through a channel network is represented by the shallow water equations, which quantify conservation of mass and conservation of momentum under system-specific geometry and flow parameters. For a large-scale system like the southwestern GBMD, solving the flow equations is computationally-intensive, and the relevance of the output is strongly dependent on the quality of bathymetric data and the modeler's ability to quantify bed friction. Prior studies of tidal propagation in the GBMD required supercomputing resources (Angamuthu et al., 2018) or alternatively reduced the computational demands by making the simplifying assumption that the intertidal platform does not flood at high water (Bricheno et al., 2016). Considering that a primary goal of our study is to understand how the elimination of platform flooding has influenced tidal behavior, we cannot reasonably remove all platform inundation from our calculations. Moreover, even if we were to solve the full flow equations with platform flooding included, the complete absence of accurate pre-polder bathymetry (and the paucity of publicly-available modern bathymetry) would almost certainly influence the accuracy of our solution.

Our goal was to find a computationally simple method for estimating the Shibsa and Pussur basin boundaries without solving the full flow equations. The availability of a channel network shapefile from Passalacqua et al. (2013) and the existence of inbuilt network analysis algorithms in ArcMap made waveform travel-time minimization an attractive solution to basin boundary approximation. However, given the complexity of the GBMD tidal channel network, the relationship between waveform travel distances and the discharge basin boundaries is not immediately obvious. The spatially-variable distortion of the discharge curves relative to the local water surface elevations (Figure 2.3) suggests that flow interactions between the Shibsa and Pussur waveforms, rather than simply the earliest wave arrival, drive the local discharge direction and magnitude. More

Table A.3: Summary of variables used in the storage volume calculations. See Figure 2.2 in for a schematic.

Variable in Figure 2.2 (Ch. 2)	**Source of modern values**	**Source of pre-polder values**
Local peak tidal range, $\Delta z^{\star}_{\text{max}}$	*Within the instrumented region:* linear interpolation with along-channel distance between the two nearest instruments. *North of the instrumented region:* extrapolation using trendlines fitted to the anecdotal tidal ranges in Table A.1.	*For channels that still exist in 2015:* Calculated from $(\Delta z^{\star}_{\text{max}})_{2015}$ using Equation A.6. *For channels that existed before polder construction but are now fully infilled:* Linear interpolation if the channel segment is connected to a modern channel at both ends; linear decrease of 2 cm/km if channel segment is blind.
Local offset between daily high water and peak high water, $\Delta z^{*}_{\text{high}}$, and local offset between daily low water and peak low water, $\Delta z^{*}_{\text{low}}$	*Within the instrumented region:* linear interpolation with along-channel distance between the two nearest instruments. *North of the instrumented region:* assume the ratios $\Delta z^{\star}_{\text{low}}/\Delta z^{\star}_{\text{max}}$ and $\Delta z^{\star}_{\text{high}}/\Delta z^{\star}_{\text{max}}$ remain constant upstream of Nalian or Chalna, as applicable (Equations A.4 and A.5).	Not applicable; we only consider peak spring tide conditions (*i.e.*, $\Delta z^{\star}_{\text{high}} = 0$ and $\Delta z^{\star}_{\text{low}} = 0$).
Planform area of the water surface at lowest low water, $A^{\star}_{\text{LL}}$	Manually outlined using the lowest low water visible in 1 m/px Google Earth imagery.	$A^{\star}_{\text{LL}} = 0.8 A^{\star}_{\text{OB}}$
Planform area of the water surface at the overbank elevation, $A^{\star}_{\text{OB}}$	Manually outlined using the embankment position from the Google Earth image nearest in time to September 2015, corresponding to the ADCP data.	Original embankment position as digitized by Wilson et al. [2017].
Planform area of the water surface at highest high water, $A^{\star}_{\text{HH}}$	*Within the poldered region:* $A^{\star}_{\text{HH}} = A^{\star}_{\text{OB}}$ *Adjacent to the Sundarbans:* Manually-delimited tidal basin boundaries based on the quasi-dendritic mangrove creeks visible in Google Earth imagery.	All non-channelized area was assigned to the nearest channel segment by generating Voronoi polygons for a set of points spaced at ~ 1 km increments along the channels.
Local peak platform inundation depth, $D^{\star}$	*In the Sundarbans:* 0.25 meters based on field observations *Upstream of the Sundarbans:* Smoothly decays to $D^{\star} = 0$ m at the limit of historical tidal inundation.	Same as modern values of $D^{\star}$ since platform sedimentation has kept pace with tidal amplification [Auerbach et al., 2015].

specifically, the waveform travel-time minimization algorithm does not allow for discharge mixing at channel confluences. The basin boundary is set according to whichever waveform arrives at a given location first, whereas in reality a convergence of discharge from the Shibsa, Pussur, and Gorai will together determine the direction and magnitude of discharge at that site. Additionally, the algorithm ignores the role of momentum and spatially-variable subtidal water surface gradients in determining flow routes through the network.

Given these limitations, we tested the validity of the method by performing the travel time calculations on the modern network configuration and comparing the results to the known, ADCP-based basin boundaries. When performing these calculations, we used the best available data for the modern channel depths (including Defense Mapping Agency, 1991; Bricheno et al., 2016, and the bathymetry obtained in conjunction with our ADCP surveys) or Equation 2.1 for locations at which no data were available. The results of the modern travel time minimization are shown in Figure A.8. Comparing the algorithm output to Figure 2.5a, we observe a reasonable correspondence between the Shibsa basin boundaries produced by the two methods. In particular, the southeastern boundary between the Shibsa and Pussur basins is closely aligned in both figures (with the error labeled as "excess volume" in Figure A.8). The primary issue in Figure A.8 involves identifying the entire Pussur/Gorai channel north of Polder 32 as belonging to the Shibsa basin, whereas the ADCP data indicate that this region is filled by mixing of water sourced from the Shibsa, Pussur, and Gorai channels. However, we anticipate that this would be less of an issue for determining the pre-polder boundary between the Shibsa and the Pussur, when (based on the width of the secondary channels) the magnitude of east-west exchange was smaller. Moreover, historical records of Gorai discharge (Winterwerp and Giardino, 2012) allow us to correct for the volume of water contributed by the Gorai, which further reduces the uncertainty in the positioning of the pre-polder Shibsa-Pussur boundary.

As described in Section 2.2.3, the issue of quantifying mixing is likewise a concern for determining the pre-polder Shibsa-Arpangasia basin boundary. Although we cannot apply waveform travel-time minimization to determine the relative contributions of the Shibsa and Arpangasia to

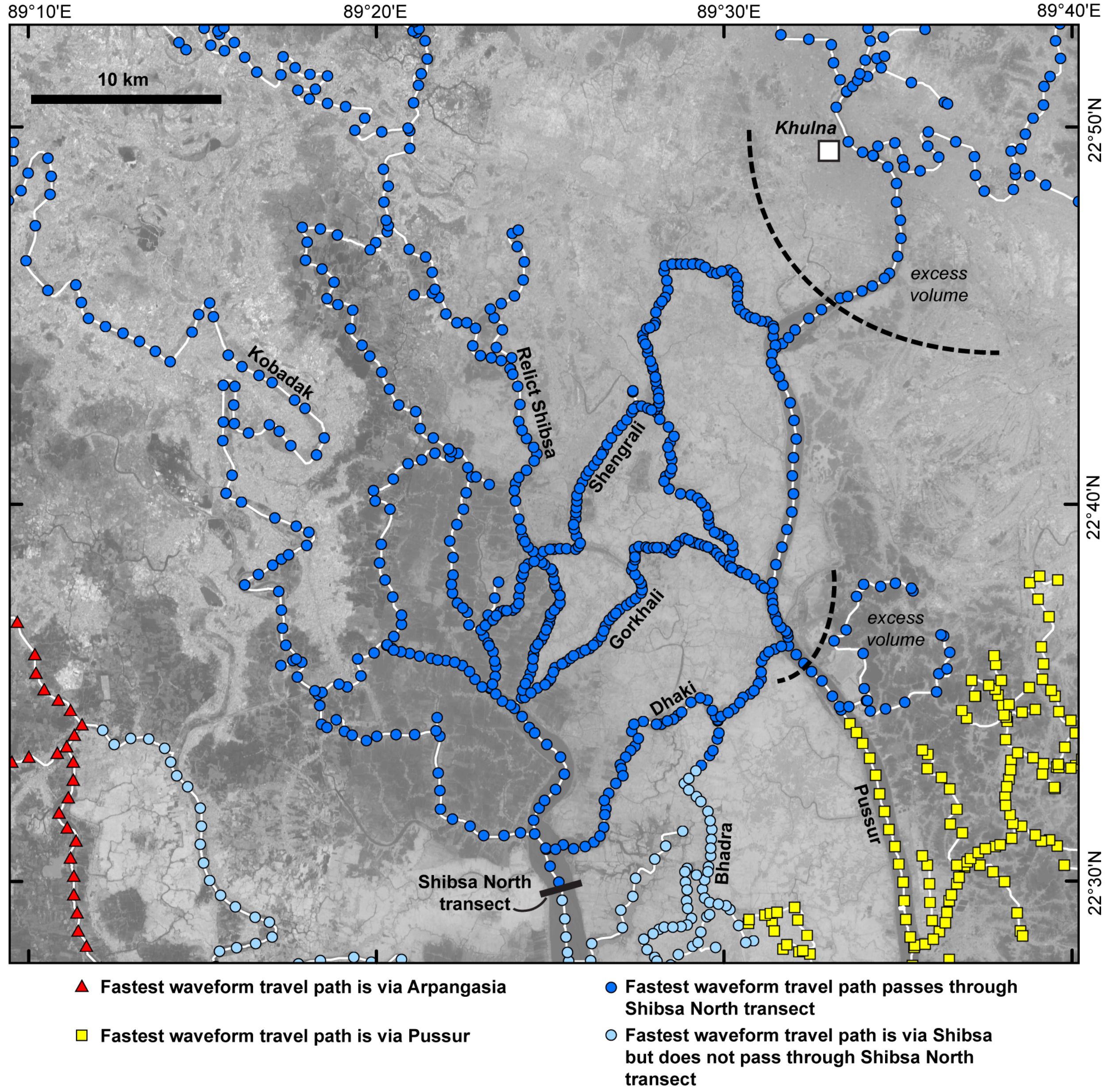

Figure A.8: Output of the travel time minimization algorithm using the network geometry and channel depths from 2015. The white line along the center of each channel is the network from Passalacqua et al. (2013), updated to represent the 2015 system configuration. For each point on the channel network, we performed a "closest facility" analysis in ArcMap to determine the fastest along-channel travel time to the 80° M_2 cotidal line in the Bay of Bengal. In the figure, the Pussur River is the fastest route to each of the yellow squares, whereas the Shibsa River is the fastest route to each of the blue circles. We have further classified the blue circles according to whether the fastest route passes through the Shibsa North ADCP transect. The two regions labeled "excess volume" are regions of the channel network that we know (based on ADCP data; see Figure 2.5a) are not part of the Shibsa North discharge basin. Background: mosaic of Landsat 8 (Band 5–NIR) imagery collected on 9-Feb-2017 and 18-Feb-2017. *Note: This figure was published by the American Geophysical Union in Bain et al. (2019) and is reprinted here under AGU's "Rights Granted to Authors" policy. AGU retains copyright of this figure.*

the upper Arpangasia basin (Figure 2.5b), this uncertainty does not change our qualitative assessment of poldering's relative influence in the Shibsa and Pussur basins: the Shibsa lost a greater percentage of its total basin volume and should have been more susceptible to abandonment than the Pussur (Table 2.3). Considering that our results are not dependent on knowing the precise position of the basin boundaries, we thus find that travel time minimization produces an acceptable first-order estimate of the channels' respective tidal basins in the absence of discharge data.

A.7 Gorai River discharge data

Figure A.9 displays discharge data from the government-run gauging station at Gorai Railway Bridge (22.885931°N, 89.180615°E; 11 km downstream of the Ganges-Gorai bifurcation) from June 2015 through December 2015. There are no major tributaries entering the Gorai between this location and the study area. Although the ungauged Gorai-Madhumati bifurcation is positioned between the Gorai Railway Bridge and Khulna, the channels' width ratio ($>$700 meters for the Gorai versus $<$150 meters for the Madhumati near the bifurcation at 23.094861°N, 89.688835°E) and a bifurcation angle which favors the Gorai suggests that the volume of water lost to the Madhumati should not be significant. Based on this time series, we assume a volume of 3000 m^3/s entering the study area from upstream. Note that these data are available by request from the Bangladesh Water Development Board website[21]; we include them here for convenience.

---

[21] `www.hydrology.bwdb.gov.bd/`

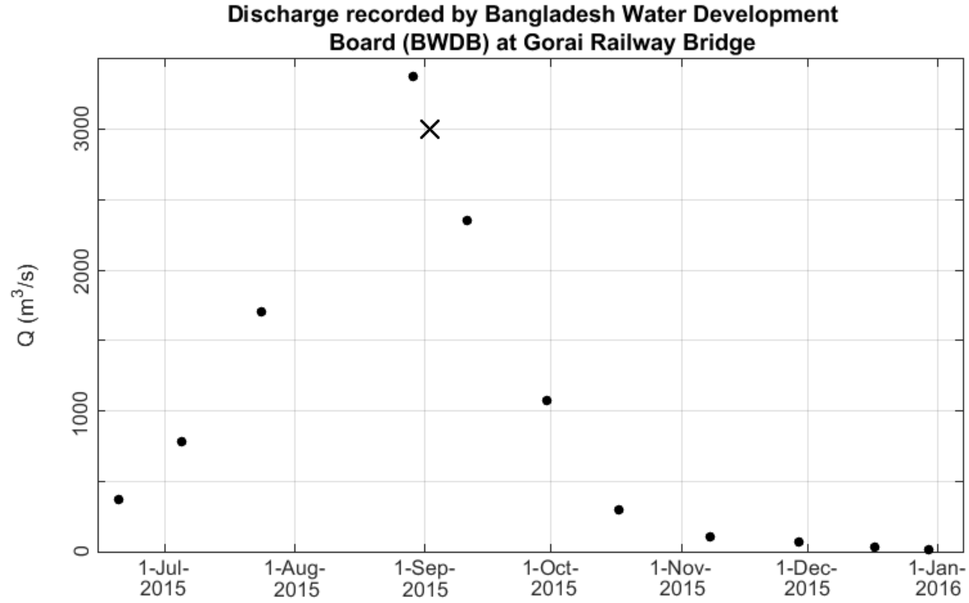

Figure A.9: Discharge data from the government gauging station at Gorai Railway Bridge, which is upstream of the limit of tidal oscillations. The measurements indicate a volume of $\sim$3000 m^3/s entering the study area from upstream during the ADCP surveys, indicated by the X symbol. These data were requested through the Bangladesh Water Development Board website; no value was provided for early August 2015. *Note: This figure was published by the American Geophysical Union in Bain et al. (2019) and is reprinted here under AGU's "Rights Granted to Authors" policy. AGU retains copyright of this figure.*

Appendix B

Supporting Information for Chapters 3 and 4

B.1 Pressure sensor post-processing

From October 2017 to March 2018, we performed a longer-term deployment at five sites along the Shibsa River and four sites along the Pussur River (Figure 3.3). We again supplemented these measurements with data from the multi-year record at Sutarkhali Forest Station. The following sections describe our methods for post-processing the data to produce the results in Chapters 3 and 4.

B.1.1 CONVERSION TO DEPTH

A long-term weather station at the Gonari schoolhouse on Polder 32 (Figure 2.1) recorded barometric pressure over the entire duration of instrument deployment, which we subtract from the raw pressure sensor measurements before converting from pressure to depth. Unlike our earlier study in 2015 (Chapter 2), which was only two weeks in duration, the regional water temperature and conductivity cannot reasonably be represented as time-constant over the spring-to-neap transition. Due to the inland advection of saltwater from Bay of Bengal during this period (Shaha and Cho, 2016), we must apply a time-varying conversion factor to obtain water depth from the pressure data. Unfortunately, out of the six available CTD-Divers, the Kobadak-Paikgachha and Khulna Shipyard instruments were regularly exposed during the lowest low tides. Since the conductivity readings tend to spike immediately after resubmersion, we discard these two datasets. The salinity sensor from the Pankhali ferry ghat also appears to have failed, with most of the record showing a conductivity of 0 mS/cm with arbitrarily-spaced spikes of 120 mS/cm. We thus limit our analysis to the three remaining datasets from Bhodra, Hadda, and Sutarkhali Forest Stations. After converting from conductivity to salinity using the algorithm[22] from Fofonoff and Millard (1983), we observe

---

[22] An unpublished calculator using Fofonoff and Millard's algorithms is provided by J. Douglass at http://jamesgdouglass.blogspot.com/ (retrieved March 2018).

that these three datasets display the anticipated increase in salinity for the first three to four months of the record before dropping off to much lower salinity values in early winter (Figure B.1). This behavior is inconsistent with published salinity records for the same region (Shaha and Cho, 2016) and also contradicts a short-term dataset collected at Sorbothkhali Forest Station in early March 2018. We interpret the abrupt drop in salinity as biological obscuration of the sensor, as shown in the lower frame of Figure B.1 (see also Hale et al., 2019b). Consequently, we truncate the records at the time of sensor failure and fit a smooth trendline to the remaining data; this trendline serves as the salinity term for determining the pressure-to-depth conversion factor.

We have no reason to suspect instrument failure for any of the ten instruments' temperature sensors between October 2017 and March 2018. However, a pre-deployment "bucket test" in August 2017 revealed a systematic offset of up to 0.2°C between the instruments (Figure B.2), which is likely a consequence of internal thermometer miscalibration. Unlike the conductivity sensors, the temperature sensors are less prone to artificial spikes after resubmersion, so we use data from all ten long-term instruments to generate the regionally-generalized temperature trend. At each measurement time ($\Delta t = 10$ minutes), we averaged the temperature from the subset of instruments that were submerged at that moment to produce a time series of spatially-averaged water temperature. We then smoothed the temperature curve using a boxcar filter with window length = 299 measurements (*i.e.*, four M_2 periods) to produce the thick black line displayed in the lower frame of Figure B.2. This smoothed record serves as the temperature term for calculating the pressure-to-depth conversion factor.

Finally, we translated the regional salinity and temperature curves into water density using the `sw_dens0` function from the MATLAB SEAWATER package (unpublished code[23] by P. Morgan), as shown in Figure B.3. This allowed us to convert measure water pressure into the depth of the water column above each pressure sensor. The depth was later tied to an absolute elevation datum using the procedure described in Section B.2.

---

[23] Archived versions of this code are available at http://www.cmar.csiro.au/datacentre/ext_docs/seawater.htm.

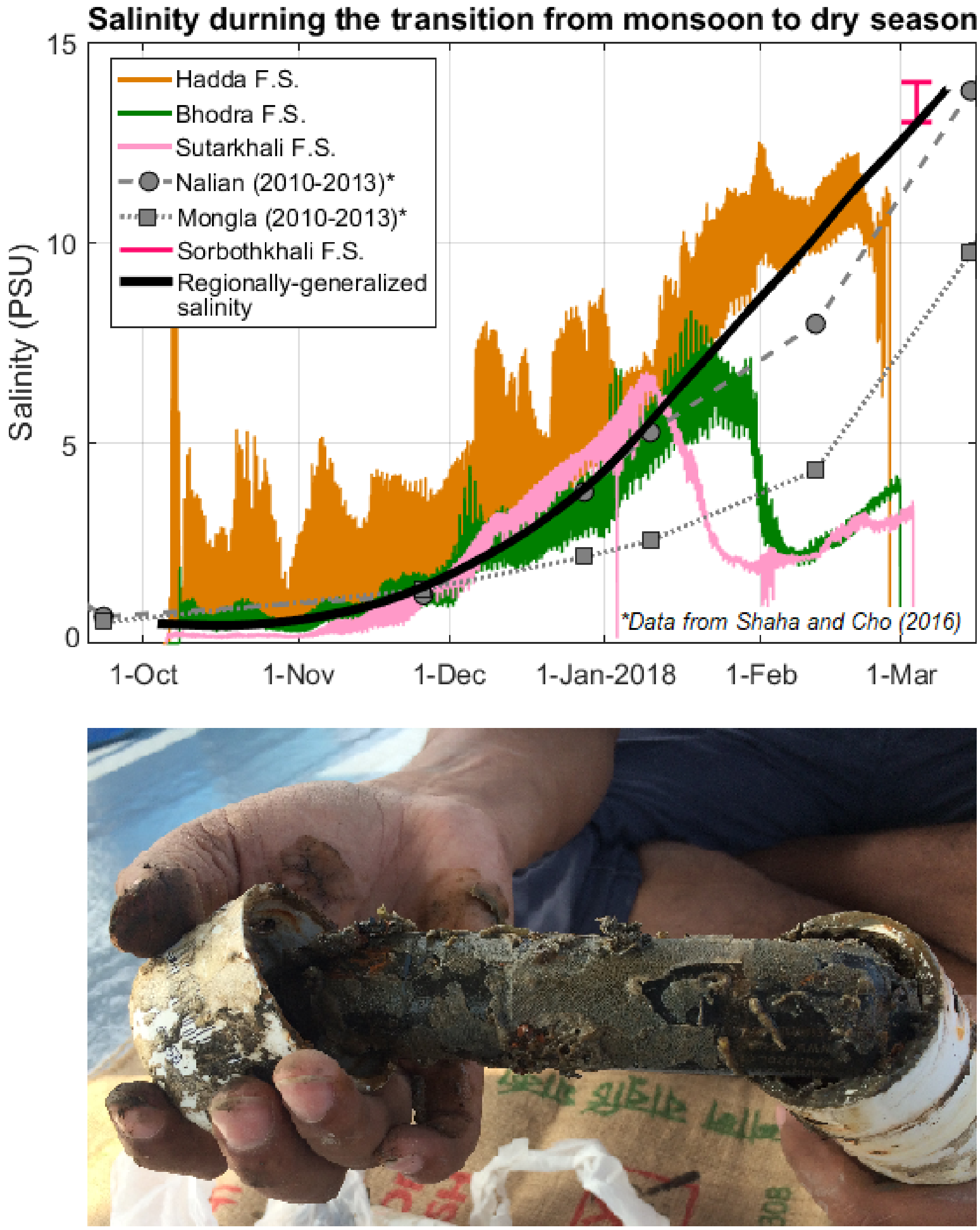

Figure B.1: *(upper)* Time series of salinity from the CTD-Divers at Bhodra, Hadda, and Sutarkhali F.S. overlain with published salinity data from the same region. Note the abrupt drop in salinity in early January at Sutarkhali, early February at Bhodra, and late February at Hadda. We interpret this as a consequence of instrument biofouling rather than an actual salinity signal, especially considering that a clean instrument recorded salinity values between 13 and 14 PSU at Sorbothkhali F.S. in early March (pers. com. with R. Hale, April 2018). The thick black line, which is based on the smooth trend of all data prior to sensor failure, shows the salinity used in the pressure-to-depth conversion at all recording sites. *(lower)* Example of biofilm on an instrument after five months of continuous deployment. We attribute the drop in recorded salinity to this growth obscuring the conductivity sensor.

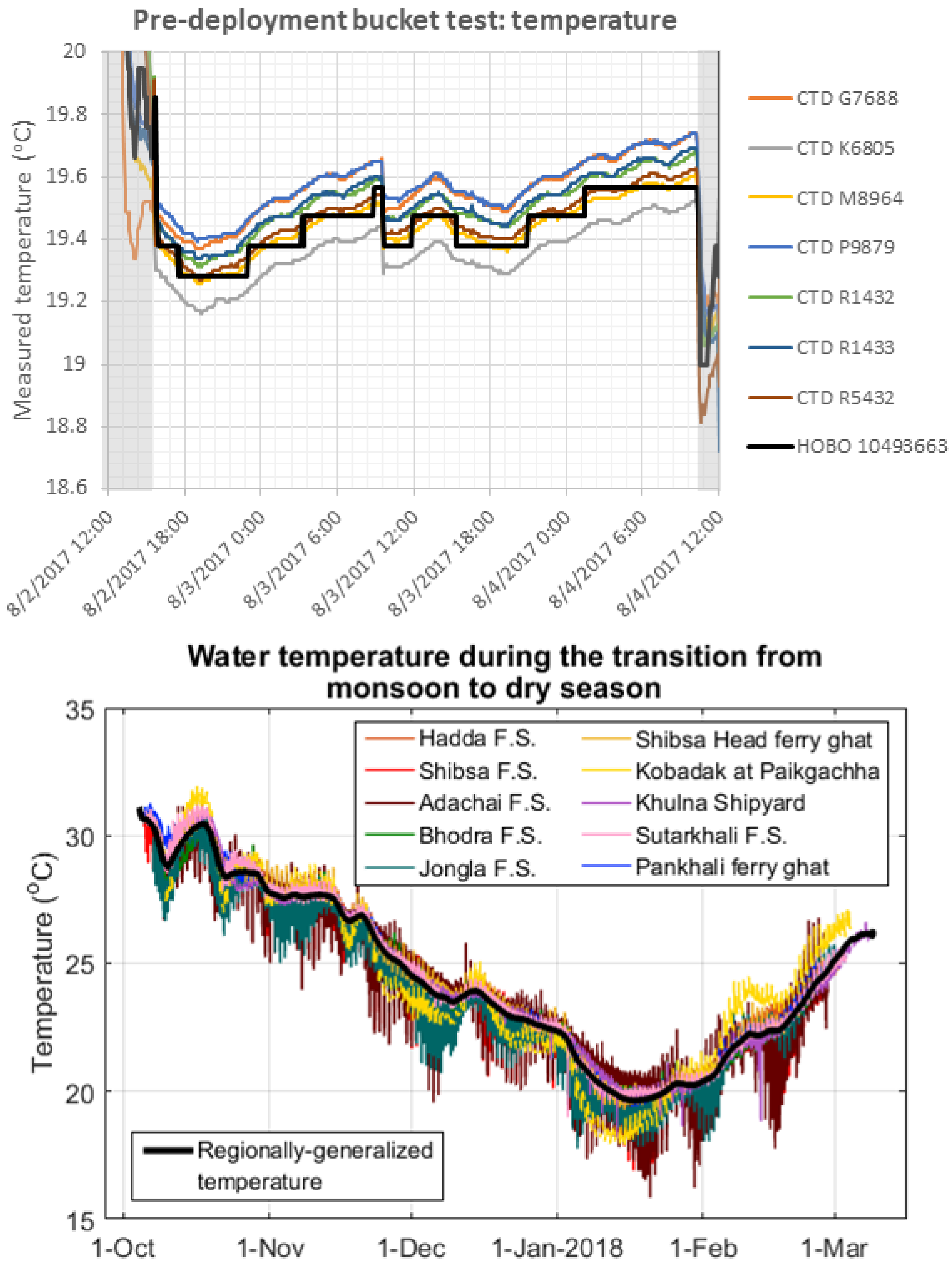

Figure B.2: *(upper)* Results of bucket test for several of the instruments prior to deployment. Note the systematic temperature offset of up to 0.2°C among pairs of instruments. The gray shaded regions on both sides of the graph indicate times when the instruments were out of the water. *(lower)* Water temperature data from all ten long-term instruments; the black line is the smoothed average temperature used in the pressure-to-depth conversion.

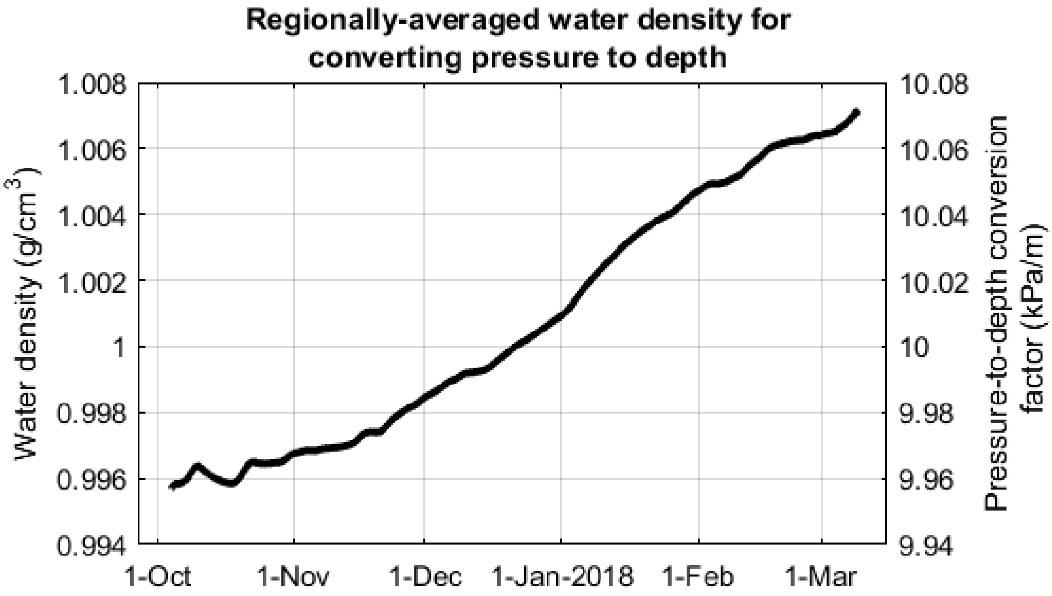

Figure B.3: Time series of calculated regional water density based on the salinity data in Figure B.1 and the temperature data in Figure B.2.

B.1.2 CORRECTING INTERPOLATION-GENERATED ERRORS IN CONSTITUENT PHASE AND AMPLITUDE

Instrument safety considerations required us to deploy certain pressure sensors in sub-optimal locations above the spring-tide low water elevation. From October 2017 to March 2018, we were able to eliminate the issue of low water exposure at several locations by mounting the instruments on 15-foot (4.57 m) lengths of 0.75-inch (1.91 cm) rebar pounded into the bed below the low water line. Unfortunately, dangerous working conditions at the Kobadak site and the risk of introducing a navigational hazard at the Khulna and Shibsa Head locations prevented us from effectively implementing this deployment method. The HOBO at Adachai Forest Station remained continuously submerged, but the placement of the instrument in a mangrove creek with a sill near the mouth influenced the readings for $\sim$ 3 hours during spring tide lows. The Sutarkhali instrument was briefly exposed for several periods up to 50-minutes in February 2018, but the record is almost entirely complete. In Section A.3, we observed that a cubic spline was the optimal method for reconstructing the missing 2015 data, so we applied the same method to reconstruct all unmeasured values for the 2017/2018 field campaign. This included truncating the lowest meter of water at Adachai and reconstructing those values to compensate for the bathymetric influence on the tide at this location.

In Chapter 2 of this dissertation, our primary focus was the total tidal *range* on any given day. This allowed us to estimate the total volume of water filling the channels upstream of each ADCP transect. As demonstrated in Section A.3, a smoothing spline algorithm performs better than several standard tidal analysis methods for reconstructing the low water elevation. In Chapters 3 and 4, however, we focus on the shape and absolute elevation of the tidal waveform. The following methods describe our method for ensuring that the inclusion of spline-interpolated elevation data does not interfere with the calculation of the individual constituents' phase and amplitude.

In the following, let $i = 1, \ldots, 6$ index the six 2017-2018 instruments that were not subaerially exposed (Shibsa F.S., Hadda F.S., Sutarkhali F.S., Bhodra F.S., Jongla F.S., and the Pankhali ferry ghat). Values of $j = 1, \ldots, 4$ refer to the four incomplete datasets (Adachai F.S., the Shibsa Head ferry ghat, Kobadak at Paikgachha, and the Khulna Shipyard), and $k = 1, ..., N$ refers to N distinct astronomical tidal constituents. Beginning from the six complete datasets, we detrended the measurements by subtracting the seasonally-varying mean water level (see Equation 3.3 in Chapter 3). We then calculated known values of constituent phase $\phi_{i,k}^{(\text{known})}$ and amplitude $A_{i,k}^{(\text{known})}$ using the `UTide` algorithm (Codiga, 2011). Next, we truncated the non-detrended elevation datasets at a water level mimicking the truncation elevation of the four incomplete datasets. Specifically:

- **To mimic the truncation at Shibsa Head:** we truncated all measurements below the elevation of the midday low water on 29-Oct-2017. This was the only low water that was not exposed at Shibsa Head.

- **To mimic the truncation at Adachai:** we truncated all measurements below the elevation of the evening low water on 18-Nov-2017. This appears to be the lowest elevation that was not affected by the sill at the Adachai creek mouth.

- **To mimic the truncation at Khulna:** we truncated all measurements below the elevation of the evening low water on 3-Nov-2017. This was the lowest low water that was not exposed at Khulna.

- **To mimic the truncation at Paikgachha:** we truncated the data at the elevation required to make the early-morning peak on 3-Jan-2018 twice as tall as the mid-morning peak on 12-Jan-2018, based on the observation that this is true for the Paikgachha instrument.

After truncating the original data, we reconstructed the missing values using a spline interpolant and then re-calculated the apparent seasonally-varying water level trend for the reconstructed dataset. We detrended the reconstructed elevations by subtracting this seasonal trend and then re-calculated the phase and amplitude of each constituent. This produced values $\phi_{i,k}^{(j)}$ and $A_{i,k}^{(j)}$; *i.e.*, the apparent phase and amplitude of the k^{th} tidal constituent when the i^{th} dataset is truncated at an elevation mimicking the truncation elevation of the j^{th} dataset and then reconstructed with a spline interpolant. We then calculated correction values C_A and C_ϕ for each tidal constituent from each incomplete dataset as:

$$(C_A)_{j,k} = \frac{\sum_{i=1}^{6}(A_{i,k}^{(\text{known})} - A_{i,k}^{(j)})}{6} \quad \text{and} \quad (C_\phi)_{j,k} = \frac{\sum_{i=1}^{6}(\phi_{i,k}^{(\text{known})} - \phi_{i,k}^{(j)})}{6} \quad , \tag{B.1}$$

which are the mean error in the k^{th} constituent's amplitude and phase calculated from a complete dataset truncated to mimic the truncation of the j^{th} dataset.

Finally, we reconstructed the four incomplete datasets using the spline interpolant, detrended using a seasonally-varying mean water level, and used `UTide` to calculate apparent values of amplitude and phase $A_{k,j}^{(\text{apparent})}$ and $\phi_{k,j}^{(\text{apparent})}$. The final, reported amplitude and phase values are then:

$$A_{j,k}^{(\text{corrected})} = A_{j,k}^{(\text{apparent})} + (C_A)_{j,k} \quad \text{and} \quad \phi_{i,k}^{(\text{corrected})} = \phi_{j,k}^{(\text{apparent})} + (C_\phi)_{j,k} \ . \tag{B.2}$$

`UTide` also automatically returns uncertainty bounds $(2\sigma_A)_{j,k}^{(\text{apparent})}$ and $(2\sigma_\phi)_{j,k}^{(\text{apparent})}$ for each tidal constituent. However, because the algorithm does not "know" that the data have been interpolated prior to analysis, we increase the uncertainty to

$$(2\sigma_A)_{j,k}^{(\text{corrected})} = \left\{ \left[(2\sigma_A)_{j,k}^{(\text{apparent})} \right]^2 + \left[(2\sigma_A)_{j,k}^{(\text{spline})} \right]^2 \right\}^{1/2} \tag{B.3}$$

and

$$(2\sigma_\phi)_{j,k}^{(\text{corrected})} = \left\{ \left[(2\sigma_\phi)_{j,k}^{(\text{apparent})} \right]^2 + \left[(2\sigma_\phi)_{j,k}^{(\text{spline})} \right]^2 \right\}^{1/2} \quad , \tag{B.4}$$

where

$$(2\sigma_A)_{j,k}^{(\text{spline})} = 2 \left\{ \frac{\sum_{i=1}^{6} \left[A_{i,k}^{(\text{known})} - A_{i,k}^{(j)} - (C_A)_{j,k} \right]^2}{5} \right\}^{1/2} \tag{B.5}$$

and

$$(2\sigma_\phi)_{j,k}^{(\text{spline})} = 2 \left\{ \frac{\sum_{i=1}^{6} \left[\phi_{i,k}^{(\text{known})} - \phi_{i,k}^{(j)} - (C_\phi)_{j,k} \right]^2}{5} \right\}^{1/2} \quad . \tag{B.6}$$

It is important to note that the correction values $(C_A)_{j,k}$ and $(C_\phi)_{j,k}$, along with the added spline uncertainty $(2\sigma_A)_{j,k}^{(\text{spline})}$ and $(2\sigma_\phi)_{j,k}^{(\text{spline})}$, are specific to a given analysis window. We repeated this procedure multiple times to produce the corrected values displayed in Figures 3.6 and B.9.

B.1.3 INTERNAL DRIFT CORRECTION

Our pre-deployment bucket test in August 2017 revealed a systematic offset in the various sensors' pressure measurements (Figure B.4), likely due to slight miscalibration of the pressure sensors during manufacturing. Our original strategy for correcting this issue was to select one instrument's measurements as the "correct" values (*i.e.*, assume perfect calibration) and then add or subtract a site-specific but temporally-constant correction C_p to the other sensors' datasets. We chose the Gonari barometer as the reference instrument due to its centralized location (see Figure 1.1) and programmed the other pressure sensors to record atmospheric pressure for at least 30 minutes prior to submersion and after retrieval. The local value of C_p then should have been given by the mean error between the local atmospheric measurements and the atmospheric data from Gonari.

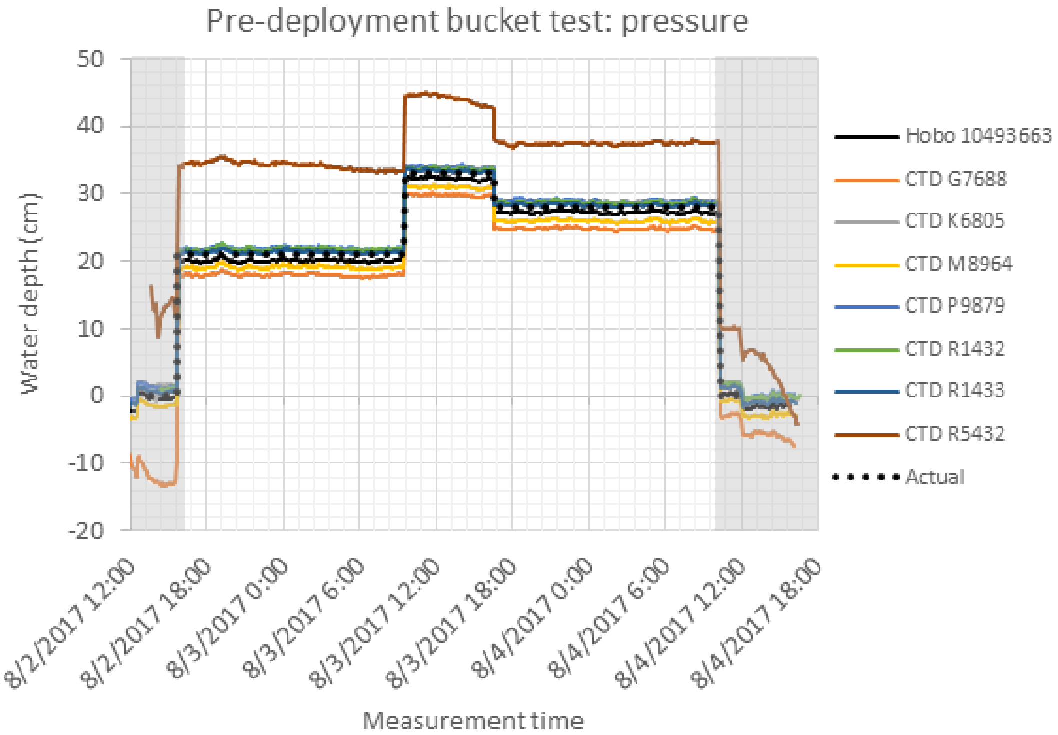

Figure B.4: Results of a pre-deployment bucket test showing miscalibration of the instruments' pressure sensors. We performed this test by submerging the instruments in a bucket of deionized water for two days and occasionally changing the depth of the water in the bucket (measured with a ruler and displayed in the figure as the "Actual" depth). We subtracted the atmospheric pressure recorded by the National Weather Service barometer at Nashville International Airport (data available at www.wrh.noaa.gov/mesowest/timeseries.php?sid=KBNA&wfo=ohx) before converting measured pressure to depth. The gray regions at either side of the graph indicate times when the instruments were not submerged in water; as an example of instrument sensitivity, observe the drop in pressure during a six-story elevator ride at 12:00 PM on 4-Aug-2017. Due to the outcome of this test, we decided not to use CTD R5432 to record pressure data in the field.

However, deployment of the Khulna Shipyard, Shibsa Head, and Kobadak-Paikgachha instruments above the lowest low water elevation produced additional atmospheric data revealing non-negligible drift in the error relative to Gonari. The drift appears to be site-specific and is likely internal to the individual instruments. For the three regularly-exposed locations, we visually identified segments of the error time series where the drift followed a linear trend and then fit a piecewise-linear trendline estimating the local, time-dependent value of $C_p(t)$. For the Shibsa Head and Kobadak instruments, the trendline is based on all available atmospheric data. At Khulna, we ignore the atmospheric data from late January through mid-February, when there is a temporary fivefold increase in the error values' standard deviation; we instead fit the trendline to the error values before and after this period.

At Sutarkhali Forest Station, instrument exposure during five extreme low tides in early February produced enough mid-deployment atmospheric data to suggest an upwards drift. Consequently, $C_p(t)$ at Sutarkhali is given by a single linear trendline fitted to three "clusters" of atmospheric data: pre-deployment, early February, and post-retrieval. At all other sites (Adachai, Bhodra, Hadda, Jongla, Pankhali, and Shibsa), we have only two "clusters" of atmospheric error data at the beginning and end of the time series. Mathematically speaking, we could fit a linear trendline estimating $C_p(t)$ at these sites. However, considering the total lack of data to constrain drift behavior for the intervening five months, we cannot justify representing the error with a linear model and instead treat $C_p(t) \equiv K$; *i.e.*, a time-constant value calculated as the mean error relative to Gonari during the brief periods of exposure. Assuming that the drift at these sites is no larger in magnitude than observed at Khulna, Shibsa Head, or Kobadak-Paikgachha, the elevation error associated with using a time-constant value of C_p should be no greater than 3 cm.

Figure B.5: *(Continued on following page.)* Method for drift correction at Khulna, Paikgachha, Shibsa Head, and Sutarkhali, using the atmospheric data recorded during periods of subaerial exposure. There are three subfigures for each location; the upper is the raw pressure time series from the site listed in the title overlaid with the atmospheric pressure data from Sutarkhali. The middle figure for each site shows the difference between the sensor's atmopsheric pressure reading and the Gonari pressure reading at any time when the instrument was subaerially exposed. The black line is a piecewise-linear trend used for error correction. The third figure for each site shows the error between that site and Gonari after subtracting the error trendline from the raw data.

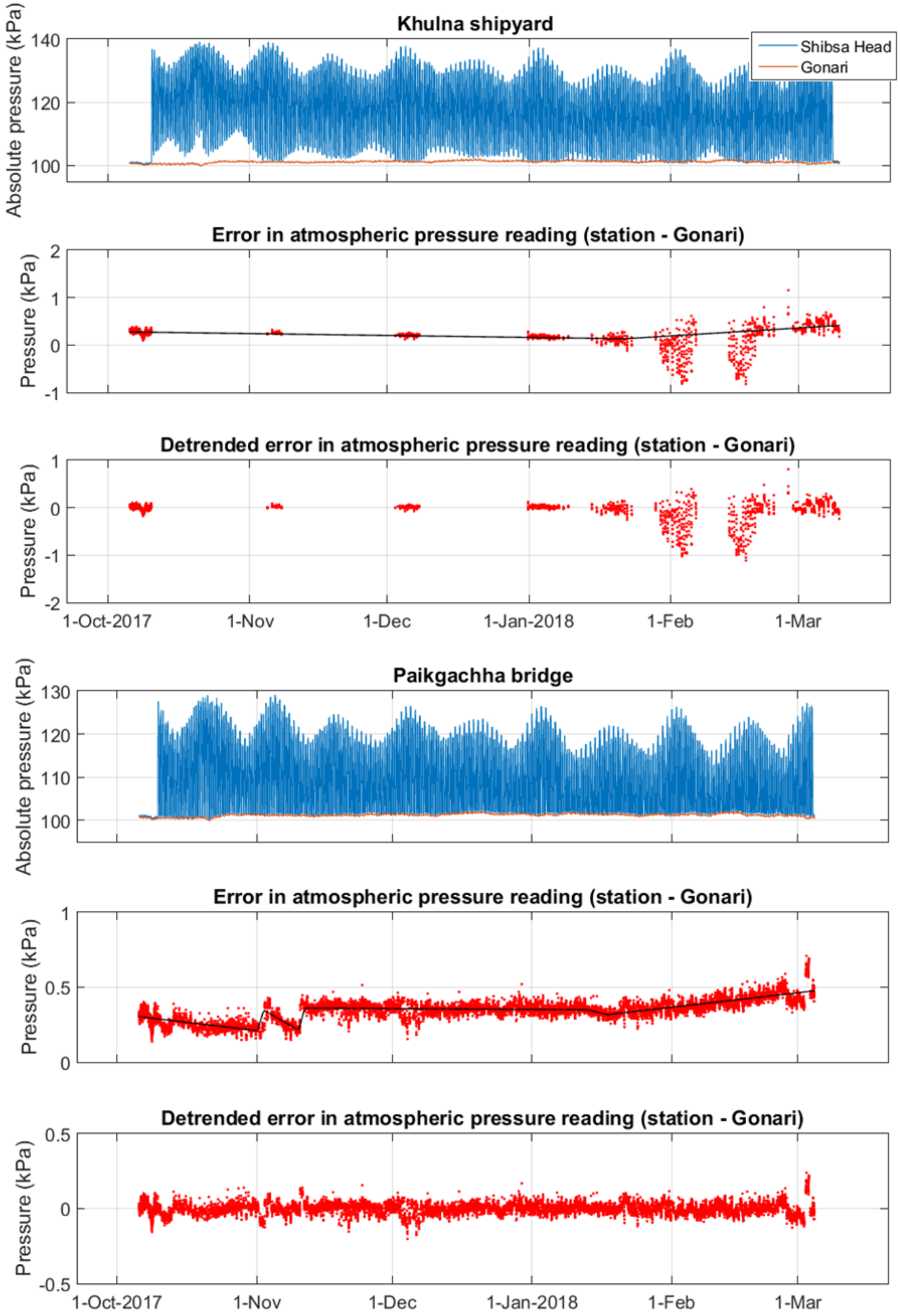

Figure B.5: *(Continued from previous page.)*

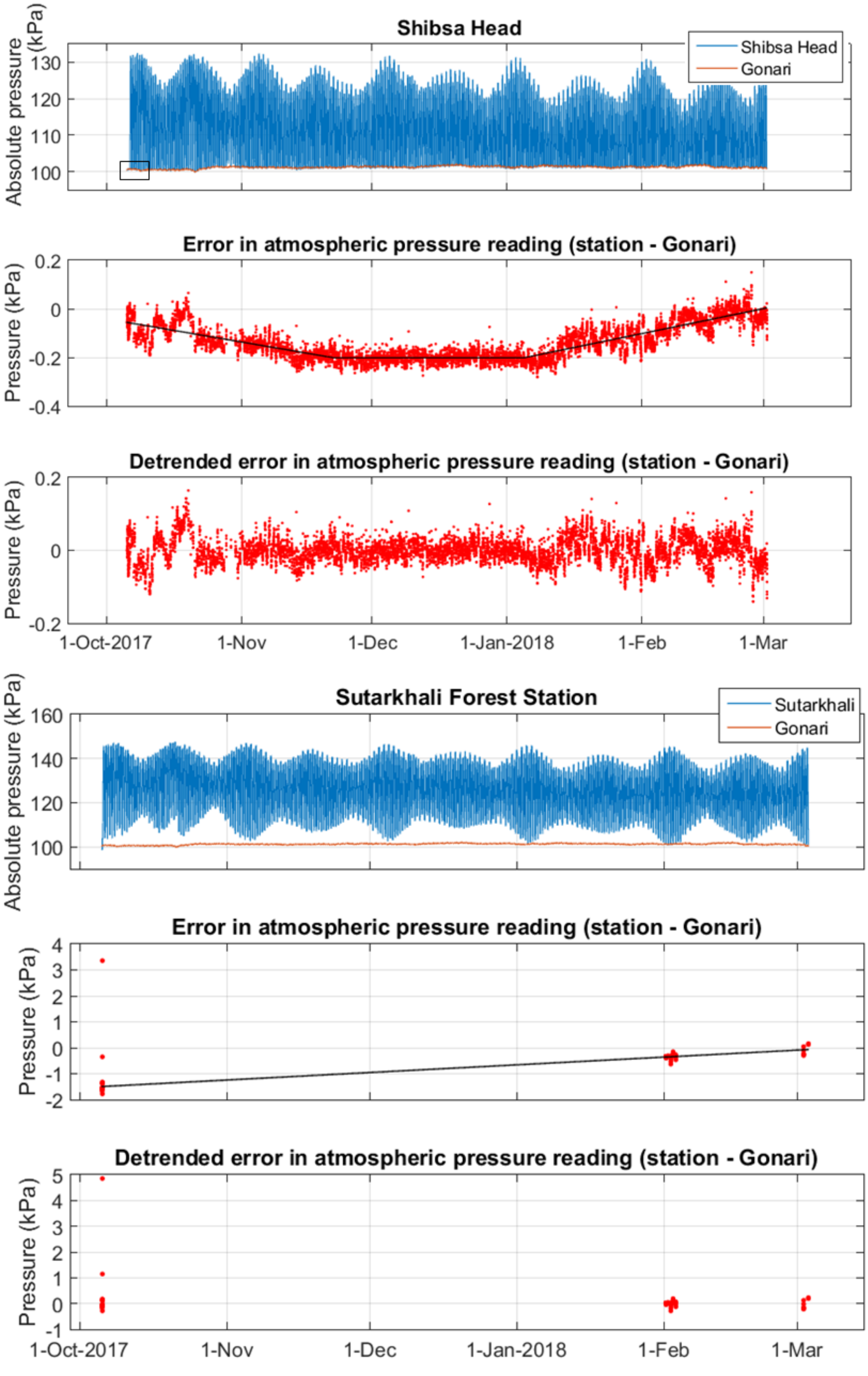

Figure B.5: *(Continued from previous page.)*

B.1.4 BANK SLUMPING

To ensure that none of the instruments had shifted in absolute vertical elevation over the 5-month recording period, we examined time series of the elevation difference between proximal sites for abrupt changes in relative elevation. The majority of the paired instruments display either no long-term trend in elevation difference or a low-frequency trend that we interpret as seasonal variation in the sites' tidal behavior. The two exceptions are the Hadda-Shibsa F.S. elevation difference, which changes abruptly in mid-February 2018, and the Jongla-Bhodra elevation difference, which displays two sudden changes in relative elevation in early January and early February 2018 (Figure B.6). However, the Shibsa F.S.-Jongla time series does not display any abrupt changes in relative elevation, indicating that the datum shifts occured at Hadda and Bhodra. The most likely cause of these datum shifts behavior is bank slumping, which is common in the study area (Reed, 2015). Bank slumping should have minimal influence on the shape of the high-frequency waveform, so we continue to use these datasets for Chapter 3. However, we discarded all data from Hadda and Bhodra after early January for the calculations in Chapter 4.

B.2 Elevation survey methods and post-processing

In October 2017, we used GPS technology to perform a high-precision elevation survey at the pressure sensor deployment sites. A Trimble R7 GPS unit was deployed on the roof of the Gonari schoolhouse to collect base-station data for post-processing. The rover was a Trimble NetR9 GPS unit receiving RTX™corrections. Unfortunately, the base station suffered an electronic failure that prevented it from recording the necessary data for post-processing. We were consequently limited to the RTX™-corrected values for the remainder of the study.

After using the rover to set an elevation benchmark on the channel bank or a nearby permanent structure, we used a theodolite and a 5-meter stadia rod marked at 1-centimeter increments to determine the relative elevation change between the benchmark and the permanent (or semi-permanent, in the case of the 15-foot pieces of rebar) structure on which the instrument was mounted. We then used a tape measure with 1-millimeter increments to measure the vertical drop from the base of

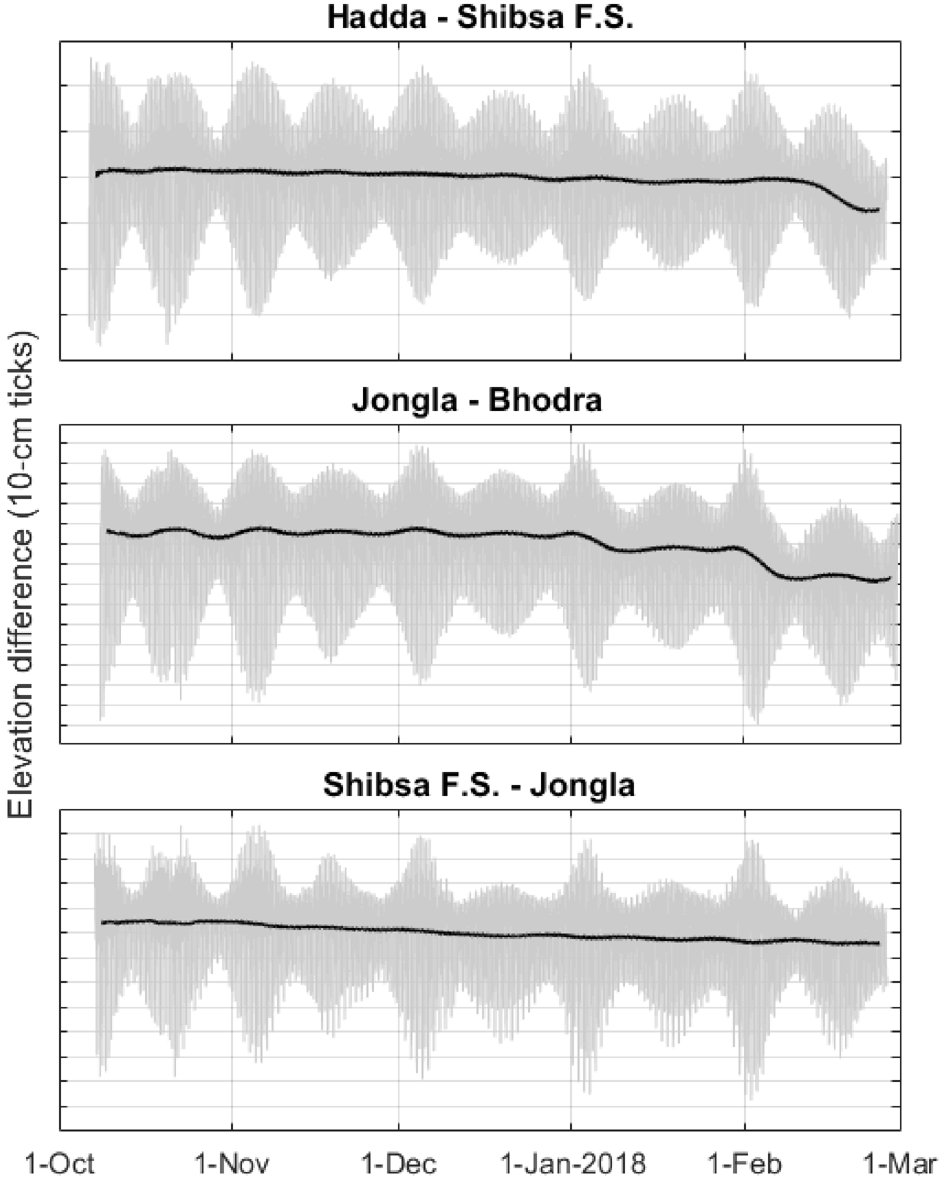

Figure B.6: Examples of our method for identifying datum shifts caused by bank slumping. Each figure shows a time series of the relative elevation difference between the two instruments listed in the title in gray; the black curve is a 7-day running average. Notice the abrupt change in relative elevation (best seen from the running average) in mid-February for the Hadda-minus-Shibsa F.S. time series. Similarly, there are two sudden changes in relative elevation, one in early January and one in early February, for the Jongla-minus-Bhodra time series. We interpret these as bank slump events. For comparison, although there is a long-term trend in the relative elevation difference between Shibsa F.S. and Jongla, there are no sudden changes that would indicate a datum shift.

the stadia rod to the nose of the instrument. To ensure accuracy, two or three team members took independent readings with the theodolite which were then compared for consistency; if the values did not agree, we measured again until converging on a repeatable value.

To determine the error associated with the RTX™-corrected GPS data, especially considering that failure of the base station unit prevents post-processing, we performed several tests evaluating measurement reproducibility. The results of these tests are summarized in the following sections.

B.2.1 ABILITY TO REPRODUCE NATIONAL GEODETIC SURVEY BENCHMARK ELEVATIONS

In late October 2017, we used the NetR9 with RTX™corrections to measure the elevation of seven National Geodetic Survey (NGS) benchmarks in central Tennessee, as described in Table B.1. We positioned the antenna directly above the benchmark and then allowed the receiver to collect elevation data until converging to a horizontal line. After obtaining at least 30 minutes of trend-free elevation measurements, we recorded the mean and standard deviation of the horizontal segment as the site's elevation parameters. After converting the measurements to a common vertical datum, we compared our measurements to the reported elevation at each site. The mean error magnitude for the seven data is 3.1 cm, with a maximum of 7.8 cm at the Love Circle benchmark. However, it is worth noting that the NGS' reported elevation at Love Circle is based on a model and was never, to our knowledge, measured with a GPS. The Love Circle elevation reported by the NGS may therefore be less accurate than at the other sites. If we limit our analysis to the six locations where the NGS data were obtained by GPS (Franklin, Montgomery Bell State Park, Murfreesboro, Reservoir Park, Spring Hill, and Walter Hill), the mean error magnitude reduces to 2.3 cm, and the maximum error magnitude is likewise reduced to 4.2 cm.

B.2.2 EVALUATING MEASUREMENT DRIFT FOR A SINGLE SITE

We also performed a two-week drift test with the NetR9 unit to examine the possibility of systematic measurement drift influencing the field data. On each day of the test, we set up the antenna at a precise location on the Vanderbilt University campus and allowed the receiver to converge to a horizontal line while receiving RTX™corrections. After obtaining a minimum of 30 minutes of trend-free elevation data, we took the mean and standard deviation of the horizontal

Table B.1: National Geodetic Survey benchmarks used for GPS error testing. The six-digit code behind the site name is the NGS permanent identifier (PID); additional information about each site is available by searching for the PID at www.ngs.noaa.gov/NGSDataExplorer/.

Site	Coordinates	NGS reported elevation (m, NAD1983 ellipsoid)	Measured elevation (m, ITRF2008 and NAD1983 ellipsoid*)	Error (m; measured minus reported)	Notes
Franklin (FD1646)	35.965775°N, 86.805072°W	195.354	193.769 (ITRF2008) 195.396 (NAD1983)	+0.042	NGS elevation measured by GPS; last updated 2012.
Lebanon (GC0267)	36.189414°N, 86.272213°W	146.034	—	—	Benchmark not found despite an hour-long search of the vicinity.
Love Circle (GC0454)	36.138184°N, 86.815483°W	198.090	196.725 (ITRF2008) 198.012 (NAD1983)	−0.078	NGS elevation is based on a gravitational model and was never measured by GPS.
Montgomery Bell State Park (DG7709)	36.113387°N, 87.267560°W	216.777	215.192 (ITRF2008) 216.774 (NAD1983)	−0.003	NGS elevation measured by GPS; last updated 2012.
Murfreesboro (DG7704)	35.784926°N, 86.415004°W	163.311	162.061 (ITRF2008) 163.344 (NAD1983)	+0.033	NGS elevation measured by GPS; last updated 2012.
Reservoir Park (GC1967)	36.137662°N, 86.779117°W	143.976	142.705 (ITRF2008) 143.970 (NAD1983)	−0.006	NGS elevation measured by GPS; last updated 2016.
Spring Hill (FD0496)	35.778161°N, 86.929132°W	212.770	211.456 (ITRF2008) 212.733 (NAD1983)	−0.037	NGS elevation measured by GPS; last updated 2016.
Walter Hill (GC2723)	36.011672°N, 86.364079°W	149.364	148.068 (ITRF2008) 149.345 (NAD1983)	−0.019	NGS elevation measured by GPS; last updated 2012.

*To perform the conversion from the default GPS output of ITRF2008 and the NGS reporting datum of NAD1983, we used the NGS *Horizontal Time-Dependent Positioning* conversion worksheet at www.ngs.noaa.gov/cgi-in/HTDP/htdp.prl?f1=4&f2=1.

segment of the time series. The receiver was then powered off and disconnected from the antenna until the following day's test, analogous to its usage in the field. On the last day of testing, we collected two back-to-back elevation measurements (each corresponding to thirty minutes of trend-free data), with the receiver powered off for several minutes between the two collection periods.

The results of this test are shown in Figure B.7, from which we make two important observations about the GPS unit's performance. First, the data do not display any obvious trend in low-frequency drift. This does not guarantee that our measurements from Bangladesh were not influenced by low-frequency instrument drift; however, it does increase our confidence that any drift over the seven days of field data collection was small. The second key observation is that even if the elevation time series for a given measurement period has a very small variance, the uncertainty on the site's absolute elevation is still substantially larger. As seen in Figure B.7, the receiver converges to a slightly different, albeit very precise, value every time it is powered off; the standard deviation of the fifteen mean values is $\sigma_z = 2.35$ cm. If we assume that the mean of the fifteen elevation measurements, $\mu_z = 139.90$ m, is the "true" elevation, attempting to capture this value with a single datum produces a maximum error of slightly less than 5 cm.

B.2.3 REPEATED MEASUREMENTS IN THE FIELD

Finally, a serendipitous duplicate measurement in Bangladesh allows us to test the accuracy of our field data directly. During our first day in the field, the team members were not in agreement about the most reasonable parameters for programming the NetR9 unit, and we were unsure if the resulting GPS data were reasonable. After consulting with experts in the United States, we returned to the same location (Hadda Forest Station) two days later and repeated the GPS measurements and the theodolite survey. Despite the confusion, the results from the two independent elevation surveys are agree within 5 cm, which is only slightly larger than the 2σ value of 4.7 cm obtained when testing the instrument in the United States. A field sketch comparing the results of the two surveys is shown in Figure B.8.

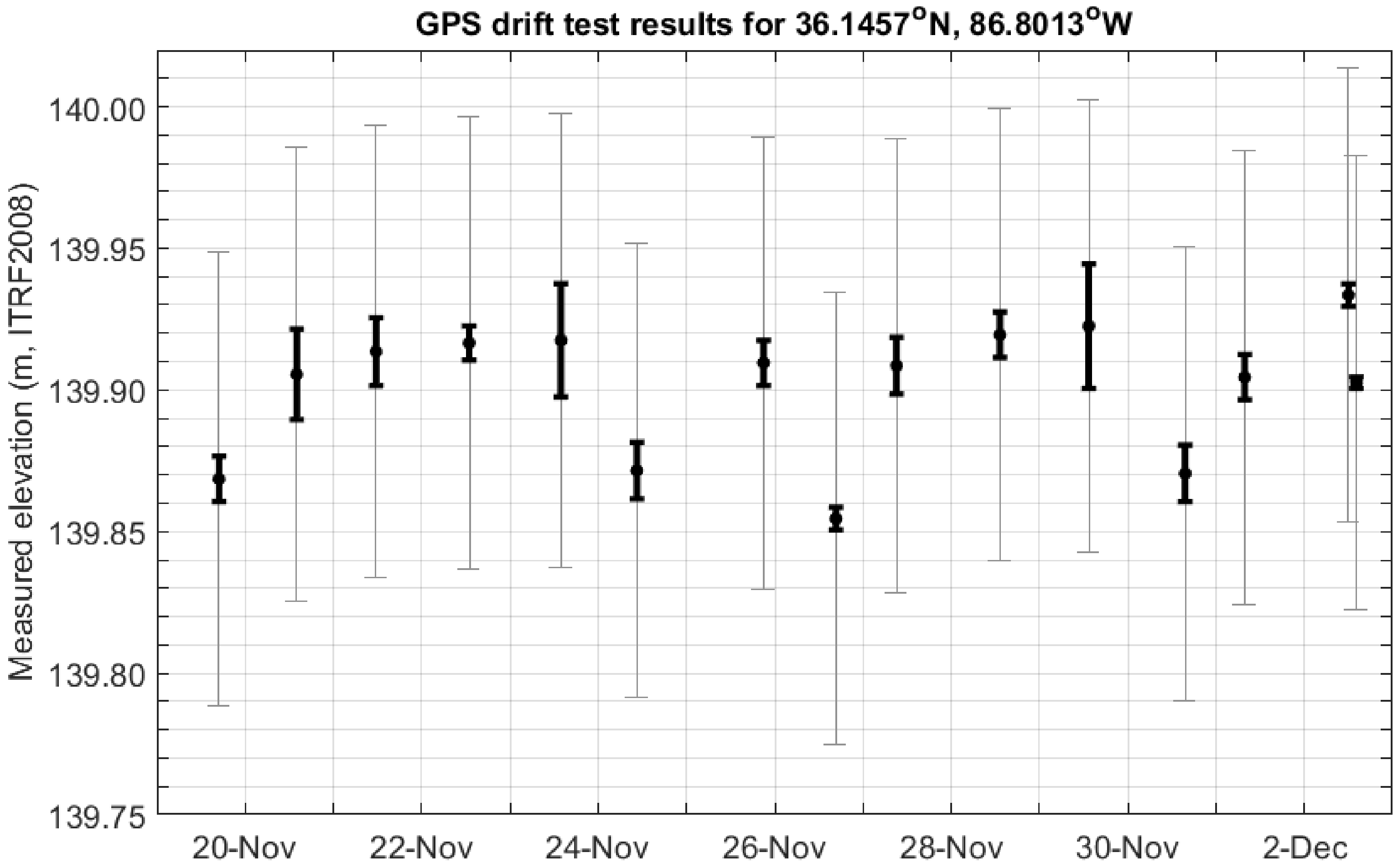

Figure B.7: Results of a two-week test of the Trimble NetR9 GPS unit at a single location on the Vanderbilt University campus in November and December 2017. The dark black lines indicate the actual 2σ uncertainty of the time series during the recording period. The thin gray lines represent $2\sigma = 8$ cm, which is similar in magnitude to the standard deviations of the elevation time series collected in the field. Notice that we collected two back-to-back measurements on the final day of testing, with the GPS receiver powered off for several minutes in between.

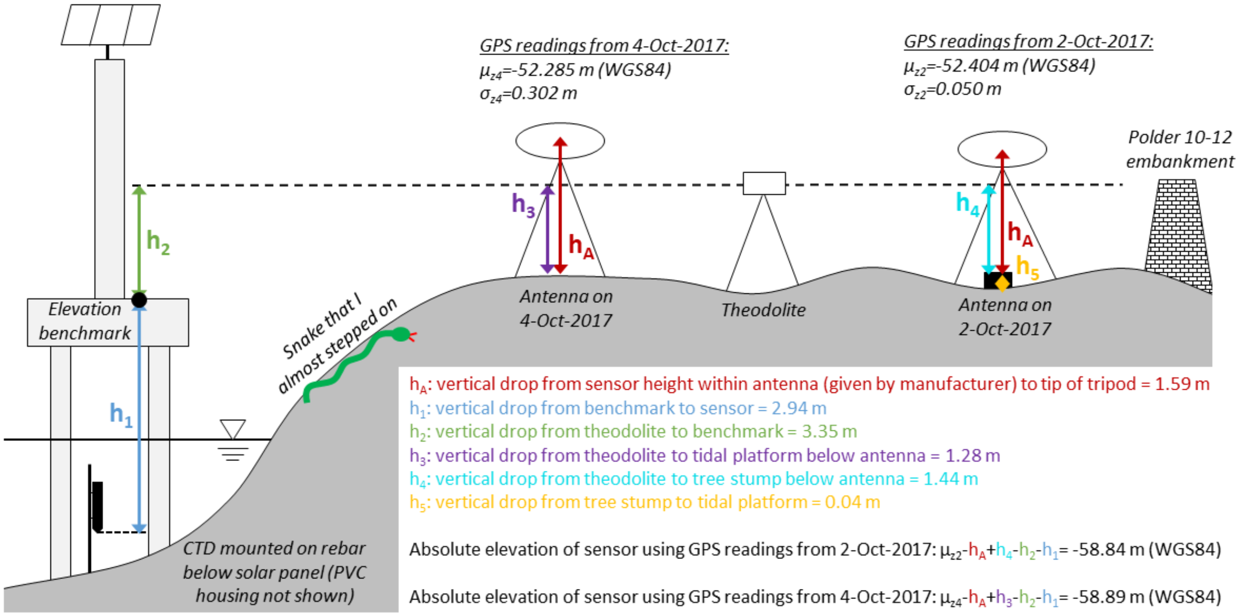

Figure B.8: Field sketch comparing the GPS survey data from 2-Oct and 4-Oct-2017 north of Hadda Forest Station. Independent readings taken on these two days agree within 5 cm.

B.3 Supplemental Results

Figure B.9 displays along-channel profiles of the smaller-amplitude tidal constituents which were not included in the main text of Chapter 3. We do not consider these results directly, but we include them here for completeness.

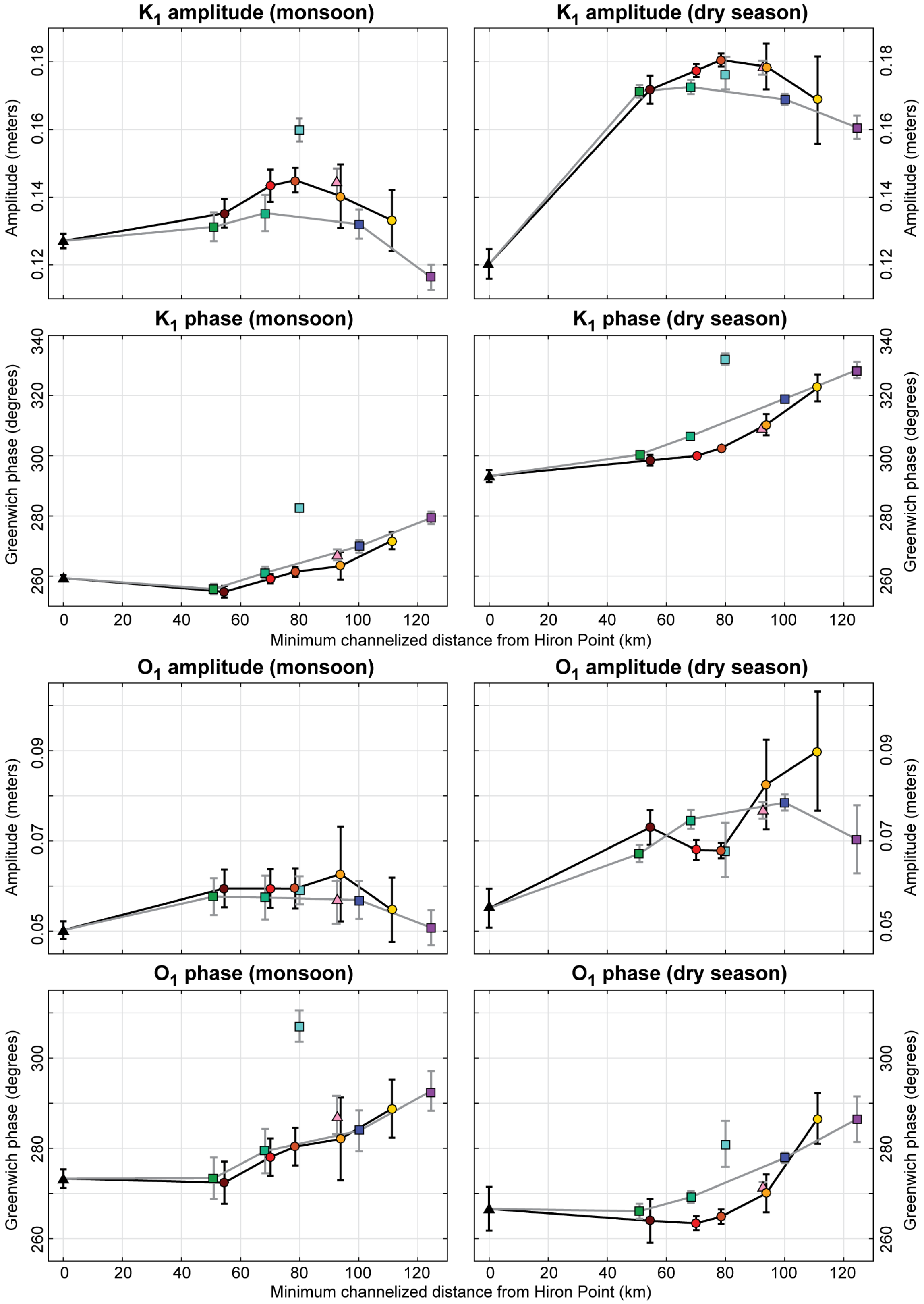

Figure B.9: *(Continued on following page.)*

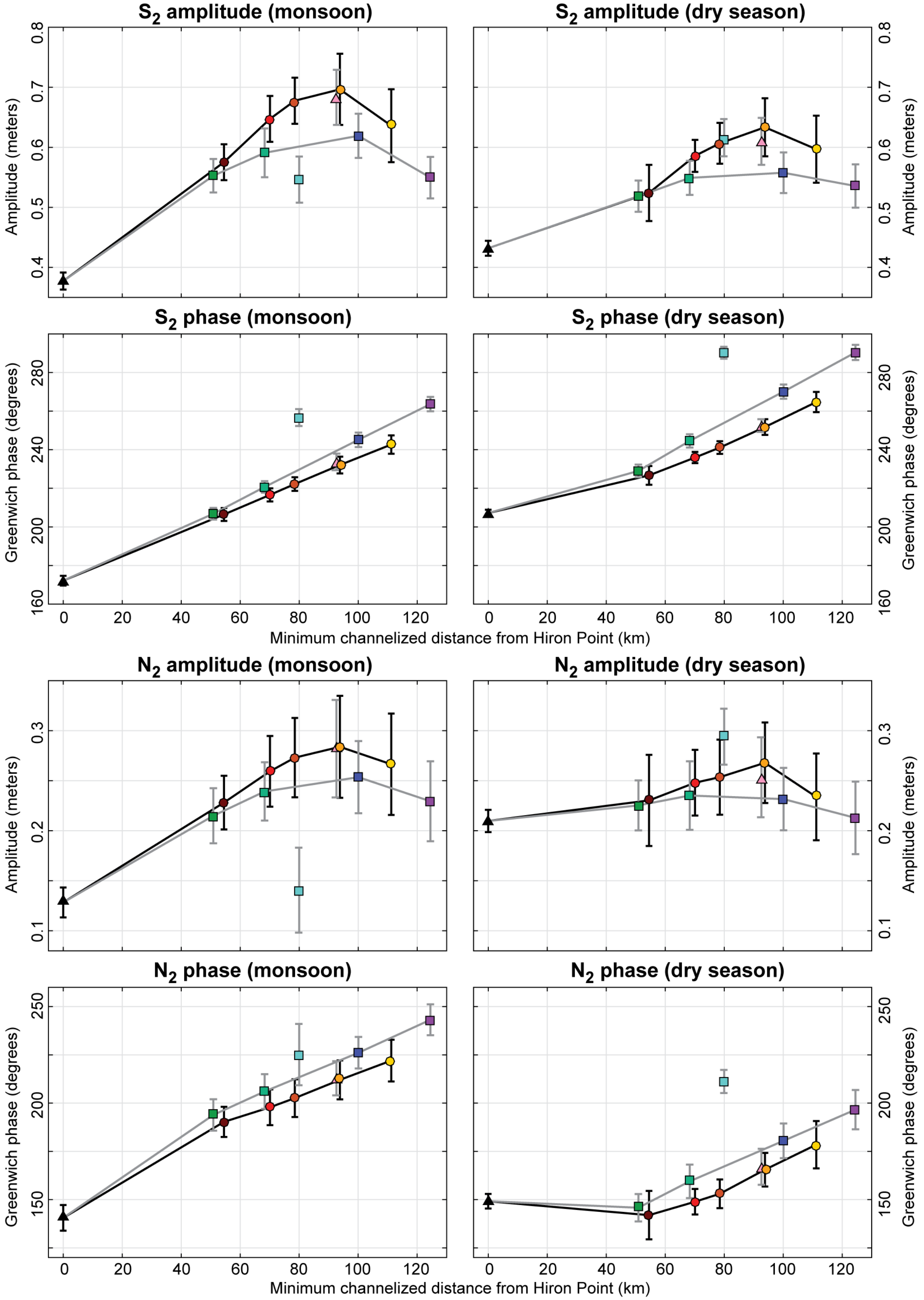

Figure B.9: *(Continued on following page.)*

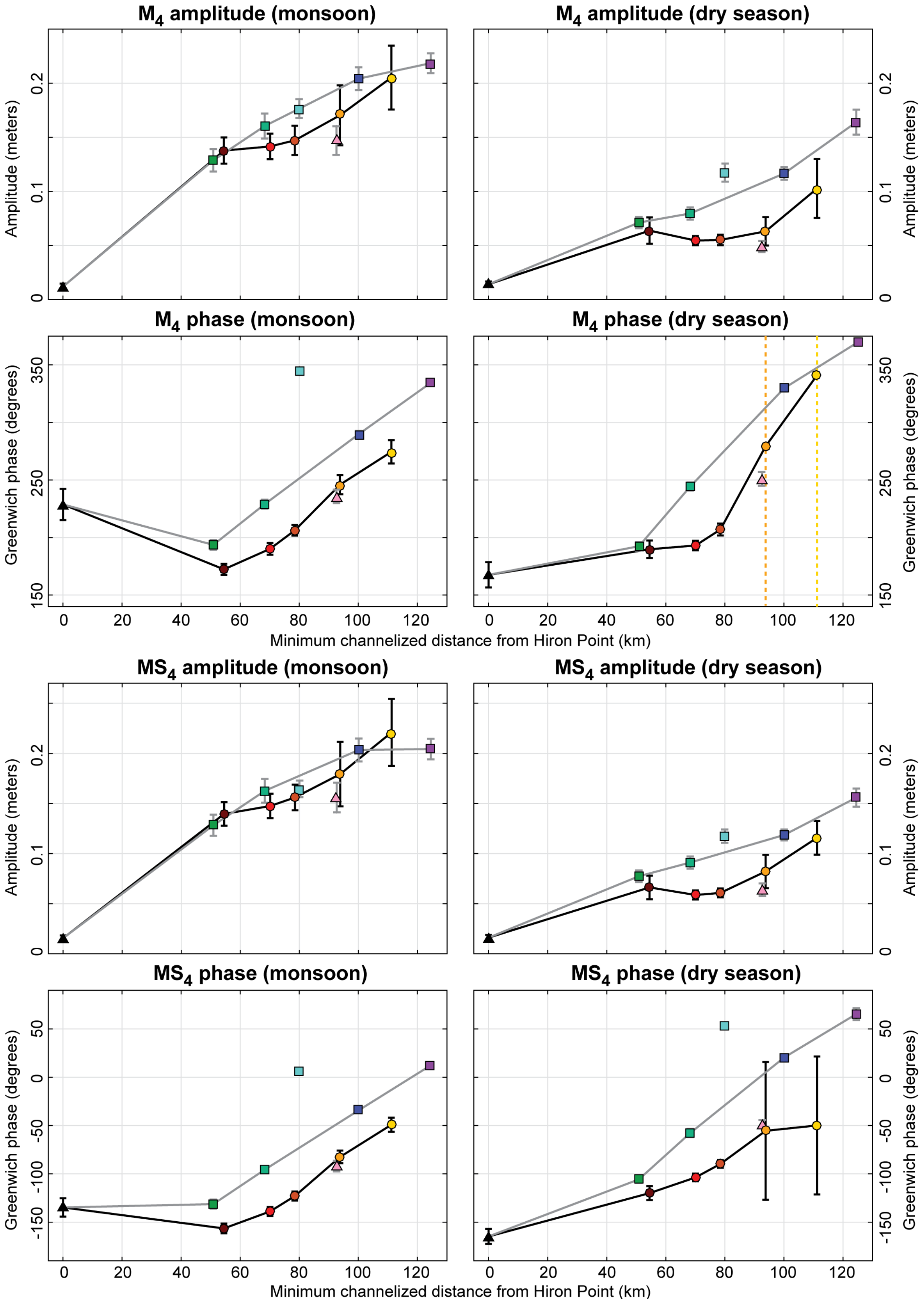

Figure B.9: *(Continued on following page.)*

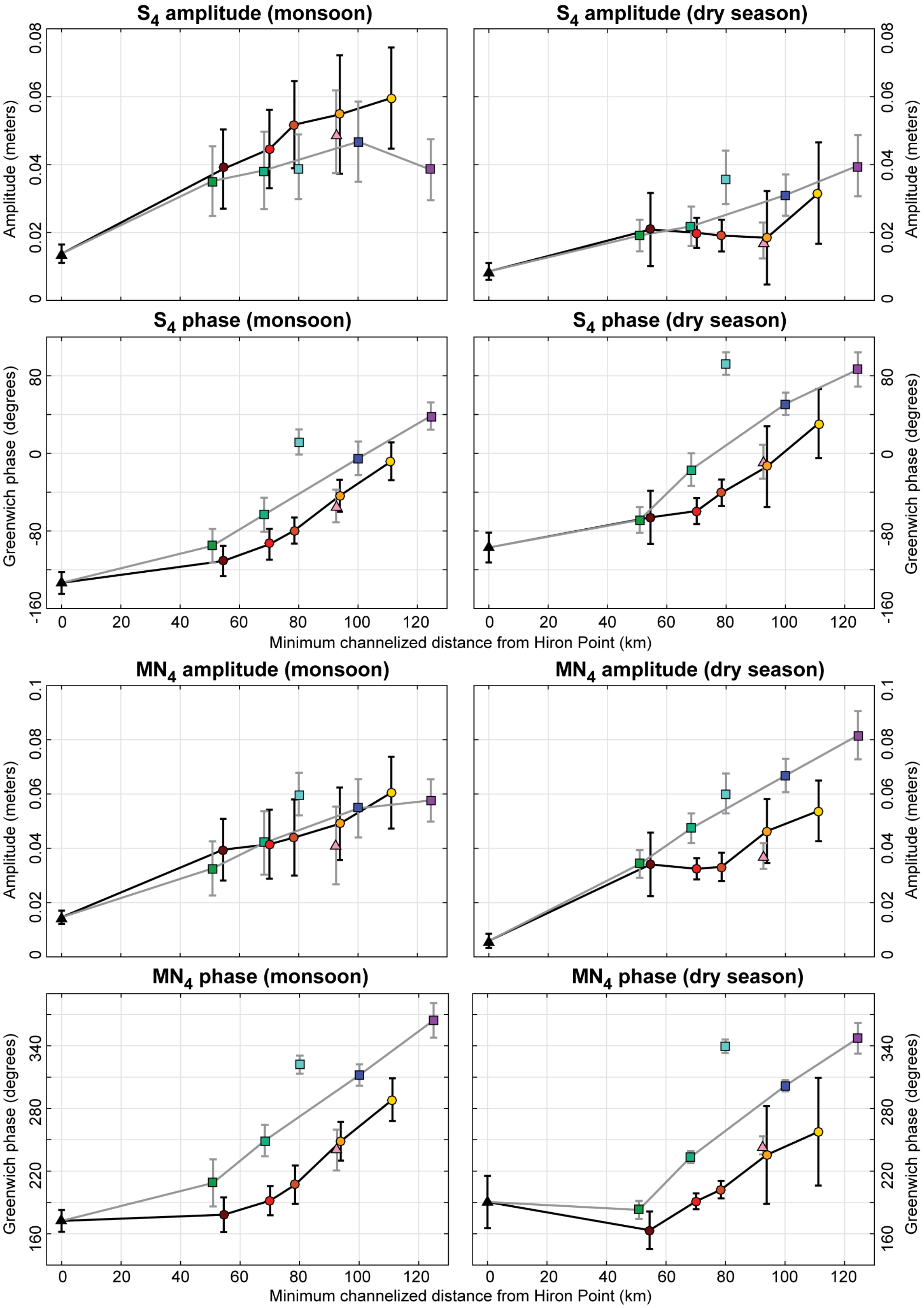

Figure B.9: *(Continued on following page.)*

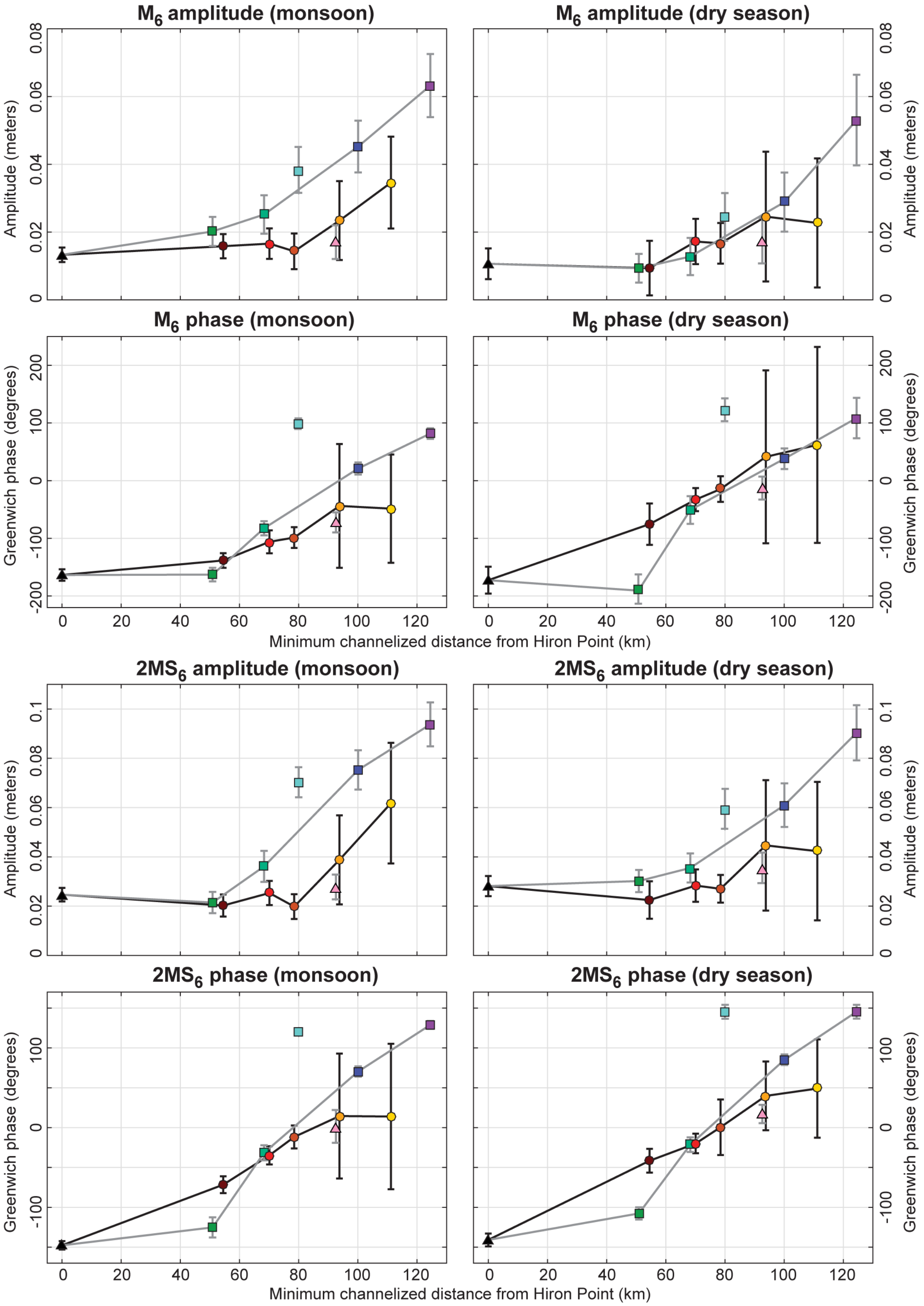

Figure B.9: *(Continued on following page.)*

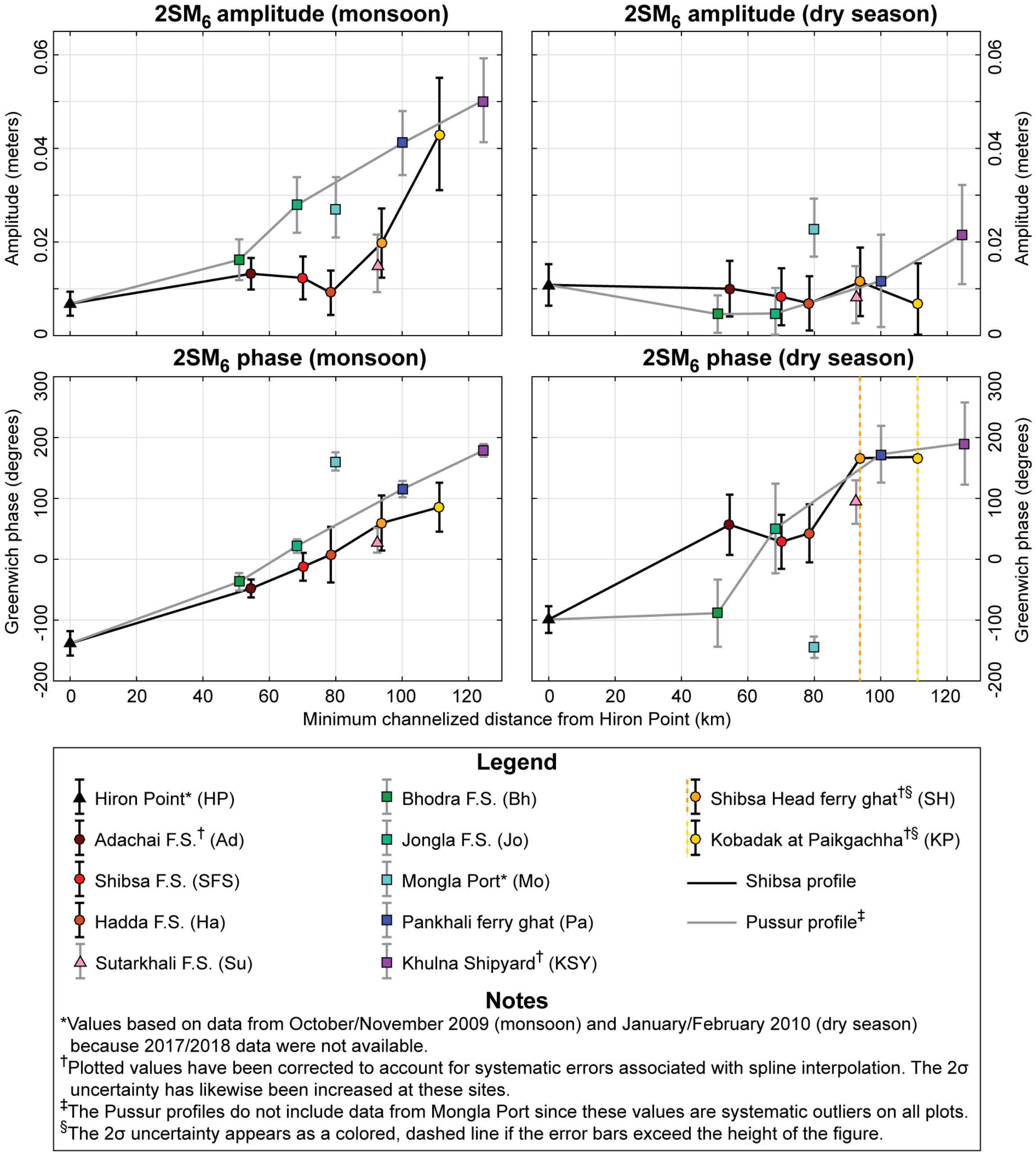

Notes

*Values based on data from October/November 2009 (monsoon) and January/February 2010 (dry season) because 2017/2018 data were not available.

†Plotted values have been corrected to account for systematic errors associated with spline interpolation. The 2σ uncertainty has likewise been increased at these sites.

‡The Pussur profiles do not include data from Mongla Port since these values are systematic outliers on all plots.

§The 2σ uncertainty appears as a colored, dashed line if the error bars exceed the height of the figure.

Figure B.9: Along-channel profiles of astronomical and shallow-water tidal constituents not discussed in the main text of Chapter 3. All values were produced using `UTide` for 30-day windows of data in the monsoon season (left) and dry season (right) and have been corrected to account for systematic errors associated with spline interpolation (see Section B.1.2).

REFERENCES

Abbas, B. M. (1966). Control of floods in East Pakistan. In *Scientific Problems of the Humid Tropical Zone Deltas and their Implications: Proceedings of the Dacca Symposium, February 24 to March 2, 1964*, pages 135–139, Paris. UNESCO.

Ali, A., Mynett, A. E., and Azam, M. H. (2007). Sediment dynamics in the Meghna Estuary, Bangladesh: A model study. *Journal of Waterway, Port, Coastal, and Ocean Engineering*, 133:255–263. doi.org/10.1061/(ASCE)0733-950X(2007)133:4(255).

Allison, M. A. and Kepple, E. B. (2001). Modern sediment supply to the lower delta plain of the Ganges-Brahmaputra River in Bangladesh. *Geo-Marine Letters*, 21:66–74. doi.org/10.1007/s003670100069.

Allison, M. A., Khan, S. R., Goodbred, S. L., and Kuehl, S. A. (2003). Stratigraphic evolution of the late Holocene Ganges-Brahmaputra lower delta plain. *Sedimentary Geology*, 155:317–342. doi.org/10.1016/S0037-0738(02)00185-9.

Angamuthu, B., Darby, S. E., and Nicholls, R. J. (2018). Impacts of natural and human drivers on the multi-decadal morphological evolution of tidally-influenced deltas. *Proceedings of the Royal Society A*, 474:26. doi.org/10.1098/rspa.2018.0396.

Anwar, M. S. and Takewaka, S. (2014). Analyses on phenological and morphological variations of mangrove forests along the southwest coast of Bangladesh. *Journal of Coastal Conservation*, 18:339–357. doi.org/10.1007/s11852-014-0321-4.

Aslan, A., White, W. A., Warne, A. G., and Guevara, E. H. (2003). Holocene evolution of the western Orinoco Delta, Venezuela. *GSA Bulletin*, 115:479–498. doi.org/10.1130/0016-7606(2003)115.

Aucan, J. and Ridd, P. V. (2000). Tidal asymmetry in creeks surrounded by saltflats and mangroves with small swamp slopes. *Wetlands Ecology and Mangement*, 8:223–231. doi.org/10.1023/A:1008459814925.

Auerbach, L. W., Goodbred Jr., S. L., Mondal, D. R., Wilson, C. A., Ahmed, K. R., Steckler, M. S., Small, C., Gilligan, J. M., and Ackerly, B. A. (2015). Flood risk of natural and embanked landscapes on the Ganges-Brahmaputra tidal delta plain. *Nature Climate Change*, 5:153–157. doi.org/10.1038/nclimate2472.

Bain, R. L., Hale, R. P., and Goodbred, S. L. (2019). Flow reorganization in an anthropogenically modified tidal channel network: An example from the southwestern Ganges-Brahmaputra-Meghna Delta. *Journal of Geophysical Research–Earth Surface*, 124:1–19. doi.org/10.1029/2018JF004996.

Baird, A. H., Bhalla, R. S., Kerr, A. M., Pelkey, N. W., and Srinivas, V. (2009). Do mangroves provide an effectie barrier to storm surges? *Proceedings of the National Academy of Sciences*, 106:E111. doi.org/10.1073/pnas.09008799106.

Bharati, L. and Jayakody, P. (2011). Hydrological impacts of inflow and land-use changes in the Gorai River catchment, Bangladesh. *Water International*, 36:357–369. doi.org/10.1080/02508060.2011.586200.

Bhuiyan, M. J. A. N. and Dutta, D. (2012). Assessing impacts of sea level rise on river salinity in the Gorai river network, Bangladesh. *Estuarine, Coastal and Shelf Science*, 96:219–227. doi.org/10.1016/j.ecss.2011.11.005.

Blanton, J. O., Lin, G., and Elston, S. A. (2002). Tidal current asymmetry in shallow estuaries and tidal creeks. *Continental Shelf Research*, 22:1731–1743. doi.org/10.1016/S0278-4343(02)00035-3.

Bolla Pittaluga, M., Coco, G., and Kleinhans, M. G. (2015). A unified framework for stability of channel bifurcations in gravel and sand fluvial systems. *Geophysical Research Letters*, 42:7521–7536. doi.org/10.1002/2015GL065175.

Bolle, A., Wang, Z. B., Amos, C., and De Ronde, J. (2010). The influence of changes in tidal asymmetry on residual sediment transport in the Western Scheldt. *Continental Shelf Research*, 30:871–882. doi.org/10.1016/j.csr.2010.03.001.

Bomer, E. J., Wilson, C. A., Hale, R. P., Hossain, A. N. M., and Rahman, F. M. A. (2019). Surface elevation and sedimentation dynamics in the Ganges-Brahmaputra tidal delta plain, Bangladesh: evidence for mangrove adaptation to human-induced hydrological disturbances. *Catena*. (Accepted).

Boon, J. D. (1973). Tidal dishcharge asymmetry in a salt marsh drainage system. *Limnology and Oceanography*, 20:71–80.

Brammer, H. (2012). *The Physical Geography of Bangladesh*. University Press Ltd., Dhaka.

Bricheno, L. M., Wolf, J., and Islam, S. (2016). Tidal intrusion within a mega delta: An unstructured grid modelling approach. *Estuarine, Coastal, and Shelf Science*, 182:12–26. doi.org/10.1016/j.ecss.2016.09.014.

Brown, J. M. and Davies, A. G. (2010). Flood/ebb tidal asymmetry in a shallow sandy estuary and the impact on net sand transport. *Geomorphology*, pages 431–439. doi.org/10.1016/j.geomorph.2009.08.006.

Buschman, F. A., Hoitink, A. J. F., van der Vegt, M., and Hoekstra, P. (2009). Subtidal water level variation controlled by river flow and tides. *Water Resources Research*, 45:1–12. doi.org/10.1029/2009WR008167.

Buschman, F. A., Hoitink, A. J. F., van der Vegt, M., and Hoekstra, P. (2010). Subtidal flow division at a shallow tidal junction. *Water Resources Research*, 46:1–12. doi.org/10.1029/2010WR009266.

Buschman, F. A., van der Vegt, M., Hoitink, A. J. F., and Hoekstra, P. (2013). Water and suspended sediment division at a stratified tidal junction. *Journal of Geophysical Research–Oceans*, 118:1459–1472. doi.org/10.1002/jgrc.20124.

Cai, H., Savenije, H. H. G., Jiang, C., Zhao, L., and Yang, Q. (2016). Analytical approach for determining the mean water level profile in an estuary with substantial freshwater discharge. *Hydrology and Earth System Sciences*, 20:1177–1195. doi.org/10.5194/hess-20-1177-2016.

Cai, H., Toffolon, M., Savenije, H. H. G., Yang, Q., and Garel, E. (2018). Frictional interactions between tidal constituents in tide-dominated estuaries. *Ocean Science*, 14:769–782. doi.org/10.5194/os-14-769-2018.

Chatterjee, M., Shankar, D., Sen, G. K., Sanyal, P., Sundar, D., Michael, G. S., Chatterjee, A., Amol, P., Mukherjee, D., Suprit, K., Mukherjee, A., Vijith, V., Chatterjee, S., Basu, A., Das, M., Chakraborti, S., Kalla, A., Kanta Misra, S., Mukhopadhyay, S., Mandal, G., and Sarkar, K. (2013). Tidal variations in the Sundarbans estuarine system, India. *Journal of Earth System Science*, 122:899–933. doi.org/10.1007/s12040-013-0314-y.

Chen, C. L. (1991). Unified theory on power laws for flow resistance. *Journal of Hydraulic Engineering*, 117(3):371–389. doi.org/10.1061/(ASCE)0733-9424(1991).

Chen, Y., Li, Y., Cai, T., Thompson, C., and Li, Y. (2016). A comparison of biohydrodynamic interaction within mangrove and saltmarsh boundaries. *Earth Surface Processes and Landforms*, 41:1967–1979. doi.org/10.1002/esp.3964.

Codiga, D. L. (2011). Unified Tidal Analysis and Prediction Using the UTide Matlab Functions. Technical Report 2011-01, Graduate School of Oceanography, University of Rhode Island, Narragansett, RI. www.po.gso.uri.edu/pub/downloads/codiga/pubs/2011Codiga-UTide-Report.pdf.

Collins, L. M., Collins, J. N., and Leopold, L. B. (1987). Geomorphic processes of an estuarine tidal marsh: Preliminary results and hypotheses. *International Geomorphology, 1986: Proceedings of the First International Conference on Geomorphology*, pages 1049–1072.

D'Alpaos, A., Lanzoni, S., Marani, M., and Rinaldo, A. (2010). On the tidal prism-channel area relations. *Journal of Geophysical Research–Earth Surface*, 115:1–13. doi.org/10.1029/2008JF001243.

Dashtgard, S. E., MacEachern, J. A., Frey, S. E., and Gingras, M. K. (2012). Tidal effects on the shoreface: Towards a conceptual framework. *Sedimentary Geology*, 279:42–61. doi.org/10.1016/j.sedgeo.2010.09.006.

Davies, J. L. (1964). A morphogenic approach to world shorelines. *Zeitschrift fuer Geomorphologie*, 8:127–142.

Deb, M. and Ferreira, C. M. (2018). Simulation of cyclone-induced storm surges in the low-lying delta of Bangladesh using coupled hydrodynamic and wave model (SWAN + ADCIRC). *Journal of Flood Risk Management*, 11:S750–S765. doi.org/10.1111/jfr3.12254.

Defense Mapping Agency (1991). *Bay of Bengal, Bangladesh and India, Raimangal River to Elephant Point [Map no. 63330, scale 1:300,000].* U.S. Defense Mapping Agency Hydrographic/Topographic Center, Washington, D.C., 9th edition.

Díez-Minguito, M., Baquerizo, A., Ortega-Sánchez, M., Navarro, G., and Losada, M. A. (2012). Tide transformation in the Guadalquivir estuary (SW Spain) and process-based zonation. *Journal of Geophysical Research–Oceans*, 117:1–14. doi.org/10.1029/2011JC007344.

Dronkers, J. (1986). Tidal asymmetry and estuarine morphology. *Netherlands Journal of Sea Research*, 20:117–131.

Dronkers, J. J. (1964). *Tidal Computations in Rivers and Coastal Waters.* North-Holland Publishing Company, Amsterdam.

Dury, G. H. (1971). Channel characteristics in a meandering tidal channel: Crooked River, Florida. *Geografiska Annaler*, 53:188–197. doi.org/10.2307/520788.

Dyer, K. R. (1973). *Estuaries: A Physical Introduction*. John Wiley & Sons, London.

Edmonds, D. A., Slingerland, R., Best, J., Parsons, D., and Smith, N. (2010). Response of river-dominated delta channel networks to permanent changes in river discharge. *Geophysical Research Letters*, 37:1–5. doi.org/10.1029/2010GL043269.

Edmonds, D. A. and Slingerland, R. L. (2008). Stability of delta distributary networks and their bifurcations. *Water Resources Research*, 44:1–13. doi.org/10.1029/2008WR006992.

Ericson, J. P., Vörösmarty, C. J., Dingman, S. L., Ward, G., and Meybeck, M. (2006). Effective sea-level rise and deltas: Causes of change and human dimension implications. *Global and Planetary Change*, 50:63–82. doi.org/10.1016/j.gloplacha.2005.07.004.

Fagherazzi, S. (2008). Self-organization of tidal deltas. *Proceedings of the National Academy of Sciences*, 105:18692–18695. doi.org/10.1073/pnas.0806668105.

Fagherazzi, S., Hannion, M., and D'Odorico, P. (2008). Geomorphic structure of tidal hydrodynamics in salt marsh creeks. *Water Resources Research*, 44:12. doi.org/10.1029/2007WR006289.

Feagin, R. A., Mukherjee, N., Shanker, K., Baird, A. H., Cinner, J., Kerr, A. M., Koedam, N., Sridhar, A., Arthur, R., Jayatissa, L. P., Seen, D. L., Menon, M., Rodriguez, S., Shamsuddoha, M., and Dahdouh-Guebas, F. (2010). Shelter from the storm? Use and misuse of coastal vegetation bioshields for managing natural disasters. *Conservation Letters*, 3:1–11. doi.org/10.1111/j.1755-263X.2009.00087.x.

Flinchem, E. P. and Jay, D. A. (2000). An introduction to wavelet transform tidal analysis methods. *Estuarine, Coastal and Shelf Science*, 51:177–200. doi.org/10.1006/ecss.2000.0586.

Fofonoff, N. P. and Millard, R. C. (1983). Algorithms for Computation of Fundamental Properties of Seawater. Technical Report 44, UNESCO, Paris. unesdoc.unesco.org/images/0005/000598/059832EB.pdf.

Foreman, M. G. G. (1977). Manual for Tidal Heights Analysis and Prediction. Technical Report 77-10, Institute of Ocean Sciences, Patricia Bay. www.pac.dfo-mpo.gc.ca/SCI/osap/publ/online/heights.pdf.

Foreman, M. G. G. and Neufeld, E. T. (1991). Harmonic tidal analyses of long time series. *International Hydrographic Review*, LXVIII:85–108.

Fortunato, A. B. and Oliveira, A. (2005). Influence of intertidal flats on tidal asymmetry. *Journal of Coastal Research*, 21:1062–1067. doi.org/10.2112/03-0089.1.

Friedrichs, C. T. and Aubrey, D. G. (1988). Non-linear tidal distortion in shallow well-mixed estuaries: a synthesis. *Estuarine, Coastal and Shelf Science*, 27:521–545. doi.org/10.1016/0272-7714(88)90082-0.

Friedrichs, C. T. and Aubrey, D. G. (1994). Tidal propagation in strongly convergent channels. *Journal of Geophysical Research-Oceans*, 99:3321–3336.

Gallo, M. and Vinzon, S. (2005). Generation of overtides and compound tides in the Amazon estuary. *Ocean Dynamics*, 55:441–448. doi.org/10.1007/s10236-005-0003-8.

Gao, S. and Collins, M. (1994). Tidal inlet equilibrium in relation to cross-sectional area and sediment transport patterns. *Estuarine, Coastal and Shelf Science*, 38:157–172. doi.org/10.1006/ecss.1994.1010.

Garel, E. and Cai, H. (2018). Effects of tidal-forcing variations on tidal properties along a narrow convergent estuary. *Estuaries and Coasts*, 41:1924–1942. doi.org/10.1007/s12237-018-0410-y.

Giese, B. S. and Jay, D. A. (1989). Modelling tidal energetics of the Columbia River Estuary. *Estuarine, Coastal and Shelf Science*, 29:549–571. doi.org/10.1016/0272-7714(89)90010-3.

Giosan, L., Constantinescu, S., Clift, P. D., Tabrez, A. R., Danish, M., and Inam, A. (2006). Recent morphodynamics of the Indus delta shore and shelf. *Continental Shelf Research*, 26:1668–1684. doi.org/10.1016/J.CSR.2006.05.009.

Godin, G. (1972). *The Analysis of Tides*. University of Toronto Press, Toronto.

Goodbred, S. L. and Saito, Y. (2012). Tide-dominated deltas. In Davis Jr., R. and Dalrymple, R., editors, *Principles of Tidal Sedimentology*, pages 129–150. Springer, New York.

Gräwe, U., Burchard, H., Müller, M., and Schuttelaars, H. M. (2014). Seasonal variability in M_2 and M_4 tidal constituents and its implications for the coastal residual sediment transport. *Geophysical Research Letters*, 41:5563–5570. doi.org/10.1002/2014GL060517.

Guo, L., van der Wegen, M., Jay, D. A., Matte, P., Wang, Z. B., Roelvink, D., and He, Q. (2015). River-tide dynamics: Exploration of nonstationary and nonlinear tidal behavior in the Yangtze River estuary. *Journal of Geophysical Research-Oceans*, 120:1–23. doi.org/10.1002/2014JC010491.

Guo, L., van der Wegen, M., Roelvink, J. A., and He, Q. (2014). The role of river flow and tidal asymmetry on 1-D estuarine morphodynamics. *Journal of Geophysical Research-Earth Surface*, 119:2315–2334. doi.org/10.1002/2014JF003110.

Hale, R., Bain, R., Goodbred, S. L., and Best, J. (2019a). Observations and scaling of tidal mass transport across the lower Ganges-Brahmaputra delta plain: Implications for delta management and sustainability. *Earth Surface Dynamics*, 7:231–245. doi.org/10.5194/esurf-2018-66.

Hale, R. P., Wilson, C. A., and Bomer, E. J. (2019b). Seasonal variability of forces controlling sedimentation in the Sundarbans National Forest, Bangladesh. *Frontiers in Earth Science*, 7:1–13. doi.org/10.3389/feart.2019.00211.

Hoitink, A. J. F. and Jay, D. A. (2016). Tidal river dynamics: Implications for deltas. *Reviews of Geophysics*, 54:240–272. doi.org/10.1002/2015RG000507.

Hoitink, A. J. F., Wang, Z. B., Vermeulen, B., Huismans, Y., and Kästner, K. (2017). Tidal controls on river delta morphology. *Nature Geoscience*, 10:637–645. doi.org/10.1038/ngeo3000.

Hood, W. G. (2010). Delta distributary dynamics in the Skagit River Delta (Washington, USA): Extending, testing, and applying avulsion theory in a tidal system. *Geomorphology*, 123:154–165. doi.org/10.1016/j.geomorph.2010.07.007.

Horstman, E. M., Dohmen-Janssen, C. M., Narra, P. M. F., van den Berg, N. J. F., Siemerink, M., and Hulscher, S. J. M. H. (2014). Wave attenuation in mangroves: A quantitative approach to field observations. *Coastal Engineering*, 94:47–62. doi.org/10.1016/j.coastaleng.2014.08.005.

Hunt, J. N. (1964). Tidal oscillations in estuaries. *Geophysical Journal of the Royal Astronomical Society*, 8. doi.org/10.1111/j.1365-246X.1964.tb03863.x.

Jan, S., Chern, C.-S., Wang, J., and Chao, S.-Y. (2004). The anomalous amplification of M_2 tide in the Taiwan Strait. *Geophysical Research Letters*, 31:1–4. doi.org/10.1029/2003GL019373.

Jarrett, J. T. (1976). Tidal Prism-Inlet Area Relationships (GITI Report 3). Technical report, Army Corps of Engineers, Fort Belvoir, VA.

Jay, D. A. (1991). Green's Law revisited: Tidal long-wave propagation in channels with strong topography. *Journal of Geophysical Research–Oceans*, 96:20585–20598. doi.org/10.1029/91JC01633.

Jay, D. A. and Flinchem, E. P. (1999). A comparison of methods for analysis of tidal records containing multi-scale non-tidal background energy. *Continental Shelf Research*, 19:1695–1732. doi.org/10.1016/S0278-4343(99)00036-9.

Jena, B. K., Sivakholundu, K. M., and Rajkumar, J. (2018). A description of tidal propagation in Hooghly estuary using numerical and analytical solutions. *Ocean Engineering*, 169:38–48. doi.org/10.1016/j.oceaneng.2018.09.009.

Kästner, K., Hoitink, A. J. F., Vermeulen, B., Geertsema, T. J., and Ningsih, N. S. (2017). Distributary channels in the fluvial to tidal transition zone. *Journal of Geophysical Research–Earth Surface*, 122:696–710. doi.org/10.1002/2016JF004075.

Kim, Y. H. and Voulgaris, G. (2005). Effect of channel bifurcation on residual estuarine circulation: Winyah Bay, South Carolina. *Estuarine, Coastal and Shelf Science*, 65:671–686. doi.org/10.1016/j.ecss.2005.07.004.

Kleinhans, M. G., Cohen, K. M., Hoekstra, J., and Ijmker, J. M. (2011). Evolution of a bifurcation in a meandering river with adjustable channel widths, Rhine delta apex, The Netherlands. *Earth Surface Processes and Landforms*, 36:2011–2027. doi.org/10.1002/esp.2222.

Kleinhans, M. G., Ferguson, R. I., Lane, S. N., and Hardy, R. J. (2013). Splitting rivers at their seams: bifurcations and avulsions. *Earth Surface Processes and Landforms*, 38:47–61. doi.org/10.1002.esp.3268.

Krien, Y., Mayet, C., Testut, L., Durand, F., Tazkia, A. R., Islam, A. K. M. S., Gopalakrishna, V. V., Becker, M., Calmant, S., Shum, C. K., Khan, Z. H., Papa, F., and Ballu, V. (2016). Improved bathymetric dataset and tidal model for the northern Bay of Bengal. *Marine Geodesy*, 39:422–438. doi.org/10.1080/01490419.2016.1227405.

Langbein, W. B. (1963). The hydraulic geometry of a shallow estuary. *International Association of Scientific Hydrology Bulletin*, 8:84–94. doi.org/10.1080/02626666309493340.

Le Provost, C. (1990). The geoid and mean sea level. *The International Hydrographic Review*, LXVII:171–175.

Le Provost, C. (1991). Generation of overtides and compound tides. In Parker, B. B., editor, *Tidal Hydrodynamics*, pages 269–296. John Wiley & Sons, Inc., New York.

LeBlond, P. H. (1979). Forced fortnightly tides in shallow rivers. *Atomsphere-Ocean*, 17:253–264. doi.org/10.1080/07055900.1979.9649064.

Leffler, K. E. and Jay, D. A. (2009). Enhancing tidal harmonic analysis: Robust (hybrid L_1/L_2) solutions. *Continental Shelf Research*, 29:78–88. doi.org/10.1016/j.csr/2008/1004.1011.

Lentsch, N., Finotello, A., and Paola, C. (2018). Reduction of deltaic channel mobility by tidal action under rising relative sea level. *Geology*, 46:599–602. doi.org/10.1130/G45087.1.

Leonardi, N., Canestrelli, A., Sun, T., and Fagherazzi, S. (2013). Effect of tides on mouth bar morphology and hydrodynamics. *Journal of Geophysical Research–Oceans*, 118:4169–4183. doi.org/10.1002/jgrc.20302.

Lessa, G. C. (2000). Morphodynamic controls on tides and tidal currents in two macrotidal shallow estuaries, NE Australia. *Journal of Coastal Research*, 16:976–989.

Lewis, M., Bates, P., Horsburgh, K., Neal, J., and Schumann, G. (2013). A storm surge inundation model of the northern Bay of Bengal using publicly available data. *Quarterly Journal of the Royal Meteorological Society*, 139:358–369. doi.org/10.1002/qj.2040.

Li, L., Guan, W., Hu, J., Cheng, P., and Wang, X. H. (2018). Responses of water environment to tidal flat reduction in Xiangshan Bay: Part 1 hydrodynamics. *Estuarine, Coastal and Shelf Science*, 206:14–26. doi.org/10.1016/j.ecss.2017.11.003.

Li, L., Wang, X. H., Williams, D., Sidhu, H., and Song, D. (2012). Numerical study of the effects of mangrove areas and tidal flats on tides: A case study of Darwin Harbour, Australia. *Journal of Geophysical Research–Oceans*, 117:12. doi.org/10.1029/2011JC007494.

Liu, J. T. and Aubrey, D. G. (1993). Tidal residual currents and sediment transport through multiple tidal inlets. In Aubrey, D. G. and Giese, G. S., editors, *Formation and Evolution of Multiple Tidal Inlets (Coastal and Estuarine Studies series)*, volume 44, pages 113–157. American Geophysical Union, Washington, D.C. doi.org/10.1029/CE044p0113.

Losada, M. A., Díez-Minguito, M., and Reyes-Merlo, M. A. (2017). Tidal-fluvial interaction in the Guadalquivir River Estuary: Spatial and frequency-dependent response of currents and water levels. *Journal of Geophysical Research–Oceans*, 122:847–865. doi.org/10.1002/2016JC011984.

Mariotti, G. and Fagherazzi, S. (2011). Asymmetric fluxes of water and sediments in a mesotidal mudflat channel. *Continental Shelf Research*, 31:23–36. doi.org/10.1016/j.csr.2010.10.014.

Marra, W. A., Parsons, D. R., Kleinhans, M. G., Keevil, G. M., and Thomas, R. E. (2014). Near-bed and surface flow division patterns in experimental river bifurcations. *Water Resources Research*, 50:1506–1530. doi.org/10.1002/2013WR014215.

Maza, M., Lara, J. L., and Losada, I. J. (2015). Tsunami wave interaction with mangrove forests; a 3-D numerical approach. *Coastal Engineering*, 98:33–54. doi.org/10.1016/j.coastaleng.2015.01.002.

Mazda, Y., Kanazawa, N., and Wolanski, E. (1995). Tidal asymmetry in mangrove creeks. *Hydrobiologia*, 295:51–58. doi.org/10.007/BF00029110.

Miori, S., Hardy, R. J., and Lane, S. N. (2012). Topographic forcing of flow partition and flow structures at river bifurcations. *Earth Surface Processes and Landforms*, 37:666–679. doi.org/10.1002/esp.3204.

Mirza, M. M. Q. (1998). Diversion of the Ganges water at Farakka and its effects on salinity in Bangladesh. *Environmental Management*, 22:711–722. doi.org/10.1007/s002679900141.

Mondal, D. R., McHugh, C. M., Mortlock, R. A., Steckler, M. S., Mustaque, S., and Akhter, S. H. (2018). Microatolls document the 1972 and prior earthquakes along the southeast coast of Bangladesh. *Tectonophysics*, 745:196–213. doi.org/10.1016/j.tecto.2018.07.020.

Mullarney, J. C., Henderson, S. M., Reyns, J. A. H., Norris, B. K., and Bryan, K. R. (2017). Spatially varying drag within a wave-exposed mangrove forest and on the adjacent tidal flat. *Continental Shelf Research*, 147:102–113. doi.org/10.1016/j.csr/2017.06.019.

Müller, M., Cherniawsky, J. Y., Foreman, M. G. G., and von Storch, J. S. (2012). Global M_2 internal tide and its seasonal variability from high resolution ocean circulation and tide modeling. *Geophysical Research Letters*, 39:1–6. doi.org/10.1029/2012GL053320.

Müller, M., Cherniawsky, J. Y., Foreman, M. G. G., and von Storch, J. S. (2014). Seasonal variation of the M_2 tide. *Ocean Dynamics*, 64:159–177. doi.org/10.1007/s10236-013-0679-0.

Myrick, R. M. and Leopold, L. B. (1963). Hydraulic Geometry of a Small Tidal Estuary. Technical Report 422-B, United States Government Printing Office, Washington, D.C. pubs.usgs.gov/pp/0422b/report.pdf.

Nidzieko, N. J. (2010). Tidal asymmetry in estuaries with mixed semidiurnal/diurnal tides. *Journal of Geophysical Research*, 115:1–13. doi.org/10.1029/2009JC005864.

Nidzieko, N. J. and Ralston, D. K. (2012). Tidal asymmetry and velocity skew over tidal flats and shallow channels within a macrotidal river delta. *Journal of Geophysical Research*, 117:1–17. doi.org/10.1029/2011JC007384.

Norris, J. M. (2001). Policy and Technical Guidance on Discharge Measurements Using Acoustic Doppler Current Profilers. Technical Report 2002.02, USGS Office of Surface Water, Reston, VA. water.usgs.gov/admin/memo/SW/sw02.02.html.

O'Brien, M. P. (1931). Estuary tidal prisms related to entrance areas. *Civil Engineering*, 1:738–739. doi.org/10.1002/jgrf.20128.

O'Brien, M. P. (1969). Equilibrium flow areas of inlets in sandy coasts. *Journal of Waterways and Harbors Division, Proceedings of the American Society of Civil Engineers*, 95:43–52.

Orescanin, M. M., Elgar, S., and Raubenheimer, B. (2016). Changes in bay circulation in an evolving multiple inlet system. *Continental Shelf Research*, 124:13–22. doi.org/10.1016/j.csr.2016.05.005.

Parker, B. B. (1984). *Frictional Effects on the Tidal Dynamics of a Shallow Estuary*. PhD thesis, The Johns Hopkins University, Baltimore.

Parker, B. B. (1991). The relative importace of the various nonlinear mechanisms in a wide range of tidal interactions. In Parker, B. B., editor, *Tidal Hydrodynamics*, pages 237–268. John Wiley & Sons, Inc., New York.

Passalacqua, P., Lanzoni, S., Paola, C., and Rinaldo, A. (2013). Geomorphic signatures of deltaic processes and vegetation: The Ganges-Brahmaputra-Jamuna case study. *Journal of Geophysical Research, Earth Surface*, 118:1838–1849. doi.org/10.1002/jgrf.20128.

Paul, B. K. (2009). Why relatively fewer people died? The case of Bangladesh's Cyclone Sidr. *Natural Hazards*, 50:289–304. doi.org/10.1007/s11069-008-9340-5.

Paul, G. C., Ismail, A. I. M., Rahman, A., Karim, M. F., and Hoque, A. (2016). Development of tide-surge interaction model for the coastal region of Bangladesh. *Estuaries and Coasts*, 39:1582–1599. doi.org/10.1007/s12237-016-0110-4.

Pawlowicz, R., Beardsley, B., and Lentz, S. (2002). Classical tidal harmonic analysis including error estimates in MATLAB using T_TIDE. *Computers and Geosciences*, 28:929–937. doi.org/10.1016/S0098-3004(02)00013-4.

Pethick, J. (1980). Velocity surges and asymmetry in tidal channels. *Estuarine and Coastal Marine Science*, 11:331–345.

Pethick, J. (1994). Estuaries and wetlands: Functions and form. In Falconer, R. A. and Goodwin, P., editors, *Wetland Management: Proceedings of the International Conference of the Institution of Civil Engineers, 2-3 June 1994*, pages 75–87. Thomas Telford Ltd., London.

Pethick, J. (2012). Assessing changes in the landform and geomorphology due to sea level rise in the Bangladesh Sundarbans. Technical report, World Bank.

Pethick, J. and Orford, J. D. (2013). Rapid rise in effective sea-level in southwest Bangladesh: Its causes and contemporary rates. *Global Planetary Change*, 111:237–245. doi.org/10.1016/j.gloplacha.2013.09.019.

Pierik, H. J., Stouthamer, E., Schuring, T., and Cohen, K. M. (2018). Human-caused avulsion in the Rhine-Meuse delta before historic embankment (The Netherlands). *Geology*, 46:935–938. doi.org/10.1130/G45188.1.

Pritchard, M. and Green, M. (2017). Trapping and episodic flushing of suspended sediment from a tidal river. *Continental Shelf Research*, 143:286–294. doi.org/10.1016/j.csr.2016.07.007.

Quartel, S., Kroon, A., Augustinus, P. G. E. F., Van Santen, P., and Tri, N. H. (2007). Wate attenuation in coastal mangroves in the Red River Delta, Vietnam. *Journal of Asian Earth Sciences*, 29:576–584. doi.org/10.1016/j.jseaes.2006.05.008.

Rahman, M. (2017). Study on morphological change and navigation problems of Pussur River in Bangladesh. Master's thesis, Khulna University of Engineering and Technology.

Rahman, M. M., Paul, G. C., and Hoque, A. (2017). A shallow water model for computing water level due to tide and surge along the coast of Bangladesh using nested numerical schemes. *Mathematics and Computers in Simulation*, 132:257–276. doi.org/10.1016/j.matcom.2016.08.007.

Reed, M. J. (2015). Polder 32: Riverbank Morphology in Southwestern Bangladesh. Master's thesis, University of Illinois at Champaign-Urbana.

Rogers, K. G., Goodbred Jr, S. L., and Mondal, D. R. (2013). Monsoon sedimentation on the 'abandoned' tide-influenced Ganges-Brahmaputra delta plain. *Estuarine, Coastal and Shelf Science*, 131:297–309. doi.org/10.1016/j.ecss.2013.07.014.

Rossi, V. M., Kim, W., López, J. L., Edmonds, D., Geleynse, N., Olariu, C., Steel, R. J., Hiatt, M., and Passalacqua, P. (2016). Impact of tidal currents on delta-channel deepening, stratigraphic architecture, and sediment bypass beyond the shoreline. *Geology*, 44:927–930. doi.org/10.1130/G38334.1.

Sakib, M., Nihal, F., Haque, A., Rahman, M., and Ali, M. (2015). Sundarban as a buffer against storm surge flooding. *World Journal of Engineering and Technology*, 3:1–6. doi.org/10.4236/wjet.2015.33C009.

Sassi, M. G., Hoitink, A. J. F., de Brye, B., Vermeulen, B., and Deleersnijder, E. (2011). Tidal impact on the division of river discharge over distributary channels in the Mahakam Delta. *Ocean Dynamics*, 61:2211–2228. doi.org/10.1007/s10236-011-0473-9.

Sassi, M. G., Hoitink, A. J. F., Vermeulen, B., and Hidayat, H. (2013). Sediment discharge division at two tidally influenced river bifurcations. *Water Resources Research*, 49:2119–2134. doi.org/10.1002/wrcr.20216.

Savenije, H. H. G. (2005). *Salinity and Tides in Alluvial Estuaries*. Elsevier, New York.

Savenije, H. H. G., Toffolon, M., Haas, J., and Veling, E. J. M. (2008). Analytical description of tidal dynamics in convergent estuaries. *Journal of Geophysical Research–Oceans*, 113:1–18. doi.org/10.1029/2007JC004408.

Schulz, E., Schuttelaars, H. M., Gräwe, U., and Burchard, H. (2015). Impact of the depth-to-width ratio of periodically stratified tidal channels on the estuarine circulation. *Journal of Physical Oceanography*, 45:2048–2069. doi.org/10.1175/JPO-D-14-0084.1.

Seminara, G., Lanzoni, S., Tambroni, N., and Toffolon, M. (2010). How long are tidal channels? *Journal of Fluid Mechanics*, 643:479–494. doi.org/10.1017/S0022112009992308.

Shaha, D. C. and Cho, Y. K. (2016). Salt plug formation caused by decreased river discharge in a multi-channel estuary. *Scientific Reports*, 6. doi.org/10.1038/srep27176.

Shampa, M. I. M. P. (2012). Tidal river management (TRM) for selected coastal area of Bangladesh to mitigate drainage congestion. *International Journal of Scientific and Technology Research*, 1:1–6.

Shetye, S. R., Gouveia, A. D., Singbal, S. Y., Naik, C. G., Sundar, D., Michael, G. S., and Nampoothiri, G. (1995). Propagation of tides in the Mandovi-Zuari estuarine network. *Proceedings of the Indian Academy of Sciences (Earth and Planetary Sciences)*, 104:667–682. doi.org/10.1007/BF02839302.

Simons, D. B. and Sentürk, F. (1992). *Sediment Transport Technology: Water and Sediment Dynamics*. Water Resources Publications, Littleton, CO.

Sindhu, B. and Unnikrishnan, A. S. (2013). Characteristics of tides in the Bay of Bengal. *Marine Geodesy*, 36:377–407. doi.org/10.1080/1490419.2013.781088.

Snyder, R. L., Sidjabat, M., and Filloux, J. H. (1979). A study of tides, setup ad bottom friction in a shallow semi-enclosed basin. Part II: Tidal model and comparison with data. *Journal of Physical Oceanography*, 9:170–188. doi.org/10.1175/1520-0485(1979)009.

Song, D., Yan, Y., Wu, W., Diao, X., Ding, Y., and Bao, X. (2016). Tidal distortion caused by the resonance of sexta-diurnal tides in a micromesotidal embayment. *Journal of Geophysical Research–Oceans*, 121:7599–7618. doi.org/10.1002/2016JC012039.

Speer, P. E. (1984). *Tidal Distortion in Shallow Estuaries*. PhD thesis, WHOI-MIT Joint Program in Oceanography, Woods Hole.

Speer, P. E. and Aubrey, D. G. (1985). A study of non-linear tidal propagation in shallow inlet/estuarine systems. Part II: Theory. *Estuarine, Coastal and Shelf Science*, 21:207–224. doi.org/10.1016/0272-7714(85)90097-6.

Syvitski, J. P. M., Kettner, A. J., Overeem, I., Hutton, E. W. H., Hannon, M. T., Brakenridge, G. R., Day, J., Vörösmarty, C., Saito, Y., Giosan, L., and Nicholls, R. J. (2009). Sinking deltas due to human activities. *Nature Geoscience*, 2:681–686. doi.org/10.1038/NGEO629.

Syvitski, J. P. M. and Saito, Y. (2007). Morphodynamics of deltas under the influence of humans. *Global and Planetary Change*, 57:261–282. doi.org/10.1016/j.gloplacha.2006.12.001.

Teh, S. Y., Koh, H. L., Liu, P. L.-F., Ismail, A. I. M., and Lee, H. L. (2009). Analytical and numerical simulation of tsunami mitigation by mangroves in Penang, Malaysia. *Journal of Asian Earth Sciences*, 36:34–46. doi.org/10.1016/j.jseaes.2008.09.007.

Tejedor, A., Longjas, A., Zaliapin, I., and Foufoula-Georgiou, E. (2015). Delta channel networks: 2. Metrics of topologic and dynamic complexity for delta comparison, physical inference, and vulnerability assessment. *Water Resources Research*, 51:4019–4045. doi.org/10.1002/2014WR016604.

Todeschini, I., Toffolon, M., and Tubino, M. (2008). Long-term morphological evolution of funnel-shape tide-dominated estuaries. *Journal of Geophysical Research–Oceans*, 113:14. doi.org/10.1029/2007JC004094.

Toffolon, M. and Savenije, H. H. G. (2011). Revisiting linearized one-dimensional tidal propagation. *Journal of Geophysical Research–Oceans*, 116:1–13. doi.org/10.1029/2010JC006616.

Toffolon, M. and Todeschini, I. (2006). Channel competition in tidal flats. In Parker, G. and García, M. H., editors, *River, Coastal and Estuarine Morphodynamics: RCEM 2005–Proceedings of the 4th IAHR Symposium on River, Coastal and Estuarine Morphodynamics*, pages 653–651, London. CRC Press.

Toublanc, F., Brenon, I., Coulombier, T., and Le Moine, O. (2015). Fortnightly tidal asymmetry inversions and perspectives on sediment dynamics in a macrotidal estuary (Charente, France). *Continental Shelf Research*, 94:42–54. doi.org/10.1016/j.csr.2014.12.009.

van Rijn, L. C. (2010). Tidal phenomena in the Scheldt Estuary (Report #1202016-000). Technical report, Deltares, Delft.

Warner, J. C., Schoellhamer, D., and Schladow, G. (2003). Tidal truncation and barotropic convergence in a channel network tidally driven from opposing entrances. *Estuarine, Coastal and Shelf Science*, 56:629–639. doi.org/10.1016/S0272-7714(02)00213-5.

Waterhouse, A. F., Valle-Levinson, A., and Winant, C. D. (2011). Tides in a system of connected estuaries. *Journal of Physical Oceanography*, 41:946–959. doi.org/10.1175/2010JPO4504.1.

Wells, J. T. (1995). Tide-dominated estuaries and tidal rivers. In Perillo, G. M. E., editor, *Geomorphology and Sedimentology of Estuaries*, chapter 6, pages 179–295. Elsevier, Amsterdam.

Wilson, C., Goodbred, S., Small, C., Gilligan, J., Sams, S., Mallick, B., and Hale, R. (2017). Widespread infilling of tidal channels and navigable waterways in human-modified tidal deltaplain of southwest Bangladesh. *Elementa*, 5. doi.org/10.1525/elementa.263.

Wilson, C. and Goodbred, S. L. (2015). Construction and maintenance of the Ganges-Brahmaputra-Meghna delta: linking process, morphology, and stratigraphy. *Annual Reviews of Marine Science*, 7:67–88. doi.org/10.1145/annurev-marine-010213-135032.

Winterwerp, J. and Giardino, A. (2012). Assessment of increasing freshwater input on salinity and sedimentation in the Gorai river system; report to World Bank. Technical report, Deltares, Delft. doi.org/10.13140/2.1.1504.1286.

Wright, L. D., Coleman, J. M., and Thom, B. G. (1973). Processes of channel development in a high-tide-range environment: Cambridge Gulf-Ord River Delta, western Australia. *The Journal of Geology*, 81:15–41. doi.org/10.1086/627805.

Yanagisawa, H., Koshimura, S., Goto, K., Miyagi, T., Imamura, F., Ruangrassamee, A., and Tanavud, C. (2009). The reduction effects of mangrove forest on a tsunami based on field surveys at Pakarang Cape, Thailand and numerical analysis. *Estuarine, Coastal and Shelf Science*, 81:27–37. doi.org/10.1016/j.ecss.2008.10.001.

Zeff, M. L. (1988). Sedimentation in a salt marsh-tidal channel system, southern New Jersey. *Marine Geology*, 82:33–48. doi.org/10.1016/0025-3327(88)90005-9.

Zeff, M. L. (1999). Salt marsh tidal channel morphometry: Applications for wetland creation and restoration. *Restoration Ecology*, 7:205–211. doi.org/10.1046/j.1526-100X.1999.72013.x.

Zhang, K., Liu, H., Li, Y., Xu, H., Shen, J., Rhome, J., and Smith, T. J. (2012). The role of mangroves in attenuating storm surges. *Estuarine, Coastal and Shelf Science*, 102–103:11–23. doi.org/10.1016/j.ecss.2012.02.021.

Zhang, W., Feng, H., Hoitink, A. J. F., Zhu, Y., Gong, F., and Zheng, J. (2017). Tidal impacts on the subtidal flow division at the main bifurcation in the Yangtze River Delta. *Estuarine, Coastal and Shelf Science*, 196:301–314. doi.org/10.1016/j.ecss.2017.07.008.

Zhang, Y., Wang, C.-Y., Fu, L.-Y., Zhao, B., and Ma, Y. (2019). Unexpected far-field hydrological response to a great earthquake. *Earth and Planetary Science Letters*, 519:202–212. doi.org/10.1016/j.epsl.2019.05.007.